2013

Single Molecule and Nanoparticle Imaging in Biophysical, Surface, and Photocatalysis Studies

Ji Won Ha
Iowa State University

Recommended Citation
Ha, Ji Won, "Single Molecule and Nanoparticle Imaging in Biophysical, Surface, and Photocatalysis Studies" (2013). *Graduate Theses and Dissertations*. 13494.
https://lib.dr.iastate.edu/etd/13494

Single Molecule and Nanoparticle Imaging in Biophysical, Surface, and Photocatalysis Studies

by

Ji Won Ha

A dissertation submitted to the graduate faculty

in partial fulfillment of the requirements for the degree of

DOCTOR OF PHILOSOPHY

Major: Analytical Chemistry

Program of Study Committee:
Ning Fang, Major Professor
Jacob W. Petrich
Emily Smith
Wenyu Huang
Ian C. Schneider

Iowa State University
Ames, Iowa
2013

Dedicated to my family

"Be anxious for nothing, but in everything by prayer and supplication with thanksgiving let your requests be made known to God. And the peace of God, which surpasses all comprehension, will guard your hearts and your minds in Christ Jesus."

- Philippians 4:6 ~7 -

TABLE OF CONTENT

CHAPTER 1. GENERAL INTRODUCTION

Dissertation Organization

This dissertation begins with a general introduction (chapter 1), followed by 6 chapters presented as six scientific manuscripts including introduction, experimental section, results and discussion, cited literature, and figures. Chapter 2 reports a differential interference contrast (DIC) polarization anisotropy that was successfully used for rotational tracking of gold nanorods attached onto a kinesin-driven microtubule. Chapter 3 describes a dual-wavelength detection of single gold nanorods rotating on a live cell membrane. Both transverse and longitudinal surface plasmon resonance (SPR) modes were used for tracking the rotational motions during a fast dynamic process under a DIC microscope. Chapter 4 presents a novel method to determine the full three-demensional (3D) orientation of single plasmonic gold nanorods rotating on live cell membranes by combining DIC polarization anisotropy with an image pattern recognition technique. Chapter 5 reports polarization- and wavelength-sensitive DIC microscopy imaging of 2-μm long gold nanowires as optical probes in biological studies. Chapter 6 demonstrates a new method to track 3D orientation of single gold nanorods supported on a gold film without angular degeneracy. The idea is to use the interaction (or coupling) of gold nanorods with gold film, yielding characteristic scattering patterns such as a doughnut shape. Chapter 7 describes imaging of photocatalytic activity, polarity and selectivity on single Au-CdS hybrid nanocatalysts using a high-resolution super-localization fluorescence imaging technique.

Introduction

Optical imaging is of great importance in biophysical, surface, and photocatalysis studies. With the advances of single molecule microscopy and spectroscopy it has become possible to observe the nanoscale behavior of single molecules in real time, which completely removes the ensemble averaging to show the actual distribution of values from individual molecules.[1]

In single molecule fluorescence microscopy, fluorescent molecules and quantum dots have been extensively used as optical probes in biological studies.[2] However, the fluorescent molecules and quantum dots suffer from photobleaching and photoblinking.[3] Recently, gold (Au) nanoparticles have gained much interests as an alternative to the fluorescent probes due to their photo-stability, thus allowing the nanoparticles to be observed for an indefinitely long time without photobleaching.[2] Furthermore, they are biocompatible and exhibit unique optical and chemical properties with a wide range of functionalities. To date, Au nanoparticle probes have found a wide spectrum of applications that include targeted drug delivery, cellular imaging, etc.[2, 4-6] In particular, anisotropic-shaped gold nanorods (AuNRs) have been utilized as orientation probes in single particle orientation and rotational tracking (SPORT) in biophysical studies.[7-10]

The most commonly used optical method to detect single Au nanoparticles is scattering-based dark-field (DF) microscopy.[7, 11] It is notable that Au nanoparticles are strong scatterers of visible light due to surface plasmon resonance (SPR) the coherent oscillation of free electrons in conduction band induced by interacting with light.[12, 13] However, since the scattering cross-sections of Au nanoparticles decrease with the sixth power of the radius (R) of a nanoparticle, these methods are limited to the visualization of rather large nanoparticle beyond 20 nm in diameter.[14] Recently, absorption-based methods have been developed to overcome the limitation of scattering-based methods.[8, 15-17] In this approach, photothermal effect is used to detect single Au nanoparticles down to 5 nm in diameter with a signal-to-noise ratio larger than 10. In addition, differential interference contrast (DIC) microscopy that works on the principle of interferometry can also be used as a powerful method to image single Au nanoparticles down to 20 nm in diameter.[18]

In this dissertation, I will first provide a general introduction to various single molecule and nanoparticle imaging techniques to detect fluorescent dyes and plasmonic gold nanoparticles. I will then provide an overview of my research projects about single molecule and nanoparticle imaging in biophysical, surface, and photocatalysis studies. This dissertation mainly focused on the use of DIC microscopy and total internal reflection (TIR) microscopy.

1. Single Molecule Fluorescence Imaging

1.1. Fluorescent Optical Probes

A variety of fluorophores have been widely used as optical probes in biological studies. The fluorophores were first extracted from natural products. Later, there have been many efforts to sythesize and develop new fluorescent probes such as more stable fluorophores derived from fuorescein isothiocyanate (FITC),[19] quantum dots (Qdots)[20, 21] and derivatives of green fluorescent protein (GFP)[22].

1.2. Wide-field Fluorescence Imaging Techniques

The simplest method to observe single-molecule fluorescence is to use wide-field fluorescence microscopy. As the name implies, a laser is used to illuminate an area several microns in diameter. The excitation light is eliminated through proper filtering, which allows the single molecule fluorescence to be sent to a two-dimensional (2D) array detector, usually a CCD camera. Performing single molecule fluorescence imaging in this fashion has two major advantages: many individual fluorophores can be observed simultaneously, and the position of fluorophores can be monitored dynamically, allowing us to observe translation of single molecules in real time. There are two popular techniques for wide-field single molecule imaging: epi-fluorescence and total internal reflection fluorescence (TIRF) microscopy.

1.2.1. Epi-fluorescence Microscopy

Figure 1 shows a simplified diagram of an epi-fluorescence microscope for single molecule fluorescence imaging. In epi-fluorescence microscopy, all parts of the sample in the illumination light path are excited simultaneously. Light of the excitation is focused on the sample through the microscope objective. The fluorescence emitted by the sample is focused onto the CCD camera through the same objective lens, which for greatest sensitivity will have a very high numerical aperture. Since most of the excitation light is transmitted through the sample, only reflected excitatory light reaches the objective together with the emitted light and, hence, the epi-fluorescence microscope gives a high signal-to-noise ratio. The remaining excitation light from fluorescent light is rejected by appropriate long pass filters or notch filters.

1.2.2. Total Internal Reflection Fluorescence (TIRF) Microscopy

A TIRF microscope makes use of an optical effect that can be adapted to observe fluorescent events occurring at the interface between two media of different refractive indices. Excitation light incident upon such a boundary, at an angle greater than the critical angle, undergoes total internal reflection (TIR). The electromagnetic field of the total internal reflected light extends into the sample beyond the interface, extending only a few hundred nanometres into the second medium of lower refractive index. This evanescent field (EF) decreases exponentially in intensity along the z-axis of penetration. The EF is used to excite only fluorophores that are sufficiently close to the interface. Fluorophores outside the EF do not generate fluorescent photons and have negligible interference to the image background. Therefore, a TIRF microscope leads to significantly improved signal-to-noise ratio together with the spatial resolution.

Two common approaches have been used to configure a TIRF microscope**:** the objective-type and the prism-type.[23] In the objective-type configuration (Figure 2A), the direction of the incident excitation light into the interface and the collection of fluorescence signals are carried out through the same objective lens with a numerical aperture usually larger than 1.45. In the prism-type configuration (Figure 2B), the excitation light is directed into the prism in a different light path, and the objective is only used to collect fluorescence light emitted from the sample. The prism-type TIRF microscope is usually cheaper than the objective-type counterpart, and it is much more convenient to adjust the incident angle in a prism-type TIRF microscope.

1.3. Super-Resolution Fluorescence Imaging Techniques

Far-field fluorescence microscopy allows one to observe molecules, cells and tissues. However, the spatial resolution of wide-field optical microscopy and visible light is limited by the diffraction of light to ~250 nm. Recently, several types of super-resolution fluorescence imaging techniques have been developed to break the diffraction limit of light. In this dissertation, I will focus on two super-resolution imaging techniques: stimulated emission depletion (STED) microscopy and stochastic optical reconstruction microscopy (STORM). These techniques make it possible to achieve the spatial resolution of 20-50 nm in the far-field.

1.3.1. Stimulated Emission Depletion (STED) Microscopy

STED microscopy was developed by Stefan W. Hell in 1994.[24] Figure 3 shows an experimental setup for STED. When a fluorophore is excited by light at its absorption wavelength, the fluorophore enters a high energy state. If the excited fluorophore is irradiated with red-shifted de-excitation light at its emission wavelength, the molecule immediately returns to the ground state. Thus, the fluorophore is switched off. This process is called stimulated emission which is the core principle of STED.

The STED microscope depends on pairs of synchronized laser pulses. Excitation is performed by a subpicosecond laser pulse that is tuned to the absorption spectrum of the fluorophore. The excitation pulse is focused into the sample, producing an ordinary diffraction limited spot of excited molecules. The excitation pulse is immediately followed by a depletion laser pulse, called 'STED-pulse'. The STED pulse is red-shifted in frequency to the emission spectrum of the fluorophore, so that its lower energy photons act ideally only on the excited molecules, quenching them to the ground state by stimulated emission. The net effect of the STED pulse is that the affected excited molecules cannot fluoresce because their energy is dumped and lost in the STED pulse. By spatially arranging the STED pulse in a doughnut mode, only the molecules at the periphery of the spot are ideally quenched. In the center of the doughnut, where the STED pulse is vanishing, fluorescence ideally remains unaffected.

The spatial resolution of around 20-50 nm can be achieved in STED and, hence, biological structures smaller than the diffraction limit of light can be resolved.[25, 26] However, to optimize the effectiveness of STED, the destructive interference in the center of the focal spot needs to be as close to perfection as possible.

1.3.2. Stochastic Optical Reconstruction Microscopy (STORM)

Stochastic Optical Reconstruction Microscopy (STORM, developed by Xiaowei Zhuang)[27, 28], Photoactivated Localization Microscopy (PALM, developed by Eric Betzig)[29], and fluorescence Photo-activation Localization Microscopy (fPALM, developed by Samuel T. Hess)[30] are super-resolution imaging techniques that utilize sequential activation and time-resolved localization of photoswitchable fluorophores to create high resolution images. These three methods were published independently in 2006 and their principle is identical.

Figure 4 shows an experimental setup for STORM. The STORM is based on high-accuracy localization of photoswitchable fluorophores. In each imaging cycle, only a fraction of the fluorophores are turned on, allowing their positions to be determined with nanometer accuracy by fitting the image of flurophores with Gaussin fuction.[31]

Therefore, many cycles are requied to give all the fluorophores a chance to be turned on, and the fluorophore positions obtained from a series of imaging cycles are used to reconstruct the final image (Figure 5).

The resolution of STORM can be 20-30 nm in lateral direction and 50-60 nm in axial direction.[28] However, the major disadvantages of STORM includes a lack of temporal resolution, a need of special photoswitchable dyes, etc.

2. Single Nanoparticle Imaging

2.1. Plasmonic Gold Nanoparticle Optical Probes

Gold nanoparticles have recently attracted much attention as optical probes for the following reasons. First, gold nanoparticles can be synthesized with control over size and shape. Second, gold nanoparticles can be conveniently functionalized with surface modification. Third, gold nanoparticles have excellent biocompatibility, making them suitable probes in biological studies. Finally, gold nanoparticles provide the unique optical properties that result from surface plasmon resonance collective oscillation of the conduction-band electrons with the incident light. For example, the light scattering is orders of magnitude greater than that of a nonmetallic object of the same size.

Among the gold nanoparticles, AuNRs are of great interest as optical probes in orientation sensing due to their anisotropic shape-induced optical properties.[7] The anisotropic AuNRs possess two geometrically confined LSPR bands: the longitudinal LSPR along the long axis and the transverse LSPR along the short axis.[8] The single dipolar character of the plasmon bands enables AuNRs to be used as orientation probes in ways similar to fluorescent molecular dipoles.[7, 8]

2.2. Single Nanoparticle Imaging Techniques

2.2.1. Bright-Field Microscopy

Bright-field (BF) microscopy is the simplest type of optical microscopy. BF microscopy relies on transmitted light for illumination of the sample. The objects that strongly absorb light will appear as dark spots on a bright, non-absorbing background. However, the major limitation is low contrast for weakly absorbing samples including biological samples. To overcome this limitation, it is usually required to stain biological samples in order to achieve better contrast under a BF microscope.

Gold nanoparticles have large absorption and scattering cross-sections. Thus, BF microscopy have been typically used to detect gold nanoparticles of 40 nm in diameter with a good signal-to-noise ratio at video rate.[32] However, BF microscopy has not been used as frequently as dark-field microscopy in recent studies.

2.2.2. Dark-Field Microscopy

Dark-field (DF) microscopy was invented by Richard Adolf Zsigmondy in 1923. A schematic configuration of DF microscopy is shown in Figure 6. In DF microscopy, the numerical aperture of the condenser is larger than that of the objective. In addition, there is an annular stop in the condenser which blocks the central part of the illumination light beam coming from the base of the microscope. When there is no sample on the microscope stage, the entire field of view appears dark. When a sample is placed on the stage, the scattered light from the sample is collected by the objective lens. In the DF image, the structures of the sample appear bright against the dark background. DF microscopy allows low contrast samples in BF microscopy to be detected with good signal-to-noise ratios. For example, gold nanoparticles larger than 20 nm in diameter can be detected readily in DF microscopy.[33] However, DF microscopy also has its own drawbacks. For example, to increase the signal, the sample needs to be illuminated by a strong light source, which can cause potential photo-damage to the sample. Furthermore, DF microscopy is limited by the scattering of many biological components that can lead to a large background in biological studies.[34]

2.2.3. Differential Interference Contrast (DIC) Microscopy

Nomarski or DIC microscopy is another optical microscopy technique that can be used to image single gold nanoparticles. Compared to BF and DF microscopies, DIC microscopy adopts a much more sophisticated scheme. A schematic configuration of DIC microscopy is shown in Figure 7. In DIC microscopy, light from the lamp is passes through a polariser located beneath the condenser. The polarised light then passes though a first Nomarski prism that splits the entering beam of light into two beams in slightly different directions but vibrating perpendicular to each other, and therefore unable to recombine to cause interference. The distance between the two beams is called the shear distance, and is always less than the resolving ability of the objective, to prevent the appearance of double images. The split beams enter and pass through the sample where their paths are altered by the sample's varying thickness, slopes, and refractive indices. When the parallel beams enter the objective, they are focused above the rear focal plane where they enter a second Nomarski prism that recombines the two beams at a defined distance outside of the prism. This removes the shear and the original path difference between the beam pairs. However, the parallel beams are no longer the same length because of path changes caused by the sample. In order for the parallel beams to interfere with each other, the vibrations of the beams of different path length must be brought into the same plane and axis. This is accomplished by placing a second polariser (or analyzer). The light then proceeds toward the eyepiece where it can be observed as differences in intensity and colour. DIC microscopy causes one side of an object to appear bright (or coloured) while the other side appears darker (or a different colour).

2.2.4. Photothermal Effect-Based Imaging

Gold nanoparticles excited near their plasmon resonance have a relatively large absorption cross-section and exhibit a fast electron-phonon relaxation time in the picosecond range**.** This makes them very efficient light absorbers. Since the luminescence yield of the nanoparticles is extremely weak, almost all the absorbed energy is converted into heat. The increase of temperature induced by this absorption induces a local variation of the refraction index. This photothermal effect was first used to detect gold nanoparticles by a photothermal interference contrast (PIC) method developed by Boyer *et al.*[15] With PIC method, images of gold nanoparticles down to 5 nm in diameter were recorded with a signal-to-noise ratio larger than 10. However, when high NA objectives are used, a linearly polarized beam becomes depolarized in the focal region after the refraction by the objective. In other words, if the incident electric field is along the x direction, the diffracted field includes an x component as well as y and z components. Such an effect of depolarization degrade the quality of the overlap between the two arms of the interferometer. As a consequence, PIC required high laser intensities, which for biological applications can be a serious limitation.

Berciaud *et al.* recently developed another photothermal method, called photothermal heterodyne imaging (PHI).[16, 17] The experimental setup is shown in Figure 8. This method does not suffer from the previous limitations. The sensitivity of PHI is two orders of magnitude above the earlier method. PHI uses a combination of two laser beams: an intensity-modulated heating beam, close-to-resonance, and an off-resonance probe beam. They are overlaid and focused on the sample by means of an air spaced objective. The probe beam was circularly polarized and the heating beam was linearly polarized. This method depends on the strong optical absorption of a metal particle at its plasmon resonance that gives rise to a change in temperature around the particle when it is illuminated by a heating laser beam. This temperature change leads to a variation of the local index of refraction. The time modulated-index of refraction profile produces a frequency shifted scattered field which is detected by its beatnote with the reflected probe field on a fast photodiode and the beat signal is easily extracted by lock-in amplifier. Therefore, the signal is directly proportional to the absorption cross section of the nanoparticle. Since the PHI signal is directly proportional to the power absorbed by the nanoparticles, this method was used to perform absorption spectroscopy studies of individual gold nanoparticles down to 5 nm in diameter.

3. Single Molecule and Nanoparticle Imaging in Biophysical, Surface, and Photocatalysis Studies

3.1. Single Molecule and Nanoparticle Imaging in Biophysical Studies

Single molecule and nanoparticle imaging has been used to study a variety of biological processes in living cells. This dissertation focuses on the use of single AuNRs along with optical microscopy techniques in biophysical studies, including diffusion of the nanoparticles on cell membranes. AuNRs have been studied under BF microscopy,[32] DF microscopy,[7, 35, 36] and photothermal heterodyne imaging[8, 15]. However, the applicability of the aforementioned microscopy techniques for biological studies is challenging due to the following reasons. The BF microscopy typically has low contrast with most biological samples and, hence, staining is often required to increase contrast. The DF method in biological imaging is limited by the scattering of many biological components resulting in a large background. The photothermal heterodyne imaging is limited by raster scanning of the sample to collect image and two heating and probe beams that could damage biological samples. Differential interference contrast microscopy makes it possible to overcome the limitations in the aforementioned imaging techniques and it is better suited to detect motions of plasmonic AuNRs in live cells.[18, 37] DIC microscopy works on the principle of interferometry to obtain information about the optical path difference between two orthogonally polarized beams separated by a Nomarski prism. The interference nature makes it insensitive to the scattered light from surrounding cellular components and keeps its high-throughput capability with high contrast images.

AuNRs have been extensively explored in biophysical studies with DIC microscopy and they have been successfully used as optical probes in single particle orientation and rotational tracking (SPORT).[9, 10, 38-41] Sun *et al*. reported that DIC microscopy-based SPORT technique could be used for the most direct measurement of the microtubule's rotation.[10] AuNRs (10 nm × 35 nm) were attached to the microtubules through the strong biotin-neutravidin linkage. These AuNRs were small enough to avoid obstructing the rotation of the microtubules. The rotation was detected by monitoring the periodic DIC signal changes corresponding to the orientation changes of the AuNRs.

However, there are two major drawbacks of the DIC microscopy-based SPORT. First, the bright and dark intensities were directly used to determine the AuNR orientation in the earlier reports[9, 10] and, hence, the precision coule be affected by intensity instabilities resulted from focus drift, etc., an alternative method using DIC polarization anisotropy to overcome the weakness is demonstrated in Chapter 2. The DIC polarization anisotropy is conveniently computed from the orthogonally polarized bright and dark intensities. DIC polarization anisotropy using an intensity ratio instead of absolute intensities is less affected by intensity instabilities and it provides more accurate, reproducible and reliable angle measurements in biophysical studies. DIC polarization anisotropy has been successfully used to reveal the unidirectional clockwise circular translocation of a AuNR attached to a kinesin-driven microtubule and to precisely determine the real-time orientation of the AuNR during the dynamic process.[38] Second, the angular degeneracy caused by two-fold symmetry of a AuNR limited the applications in single particle orientation and rotational tracking. That is, it is challenging to differenciate the orientation angles between θ and $-\theta$ (or $\pi-\theta$) relative to the polarization directions. In Chapter 4, the angular degeneracy is overcome by combining DIC polarization anisotropy with a image pattern recognition technique. The full 3D orientation of a AuNR could be determined in DIC microscopy. Furthermore, 360° orientations and rotational directions of a transferrin-modified AuNR rotating on a live cell membrane were successfully tracked in real time.[40]

3.2. Single Molecule and Nanoparticle Imaging in Surface Studies

Single molecule and nanoparticle imaging is of great importance in surface studies, including the interaction between functionalized nanoparticles and a large variety of functional surfaces. Marchuk *et al*. used dual-color TIR scattering microscopy to probe the interactions of plasmonic AuNRs with functional surfaces.[42] By using both the short and long axis surface plasmon resonance scattering enhancement, both in-plane and out-of-plane AuNR motion relative to the sample surface can be resolved. Furthermore, conformations of surface-bound anisotropic nanoparticles were resolved by combining with super-localization through point spread function fitting.

In Chapter 6, another TIR scattering-based focused orientation and position imaging (FOPI) was developed for surface studies.[43] In this method, plasmonic AuNRs are supported on a 50-nm thick gold film. The scattering patterns of AuNRs on the gold substrate are affected by the strong interaction of the excited dipole in the AuNR with the image dipole in the gold substrate. The characteristic scattering field distribution allowed for high-throughput determination of the full 3D spatial orientation of AuNRs within a single frame without suffering from angular degeneracy. Therefore, the FOPI method using the interaction (or coupling) of AuNRs with their surrounding environment can be an outstanding tool in single-particle rotational tracking and sensing applications to study interactions between functionalized nanoparticles and a large variety of functional surfaces.

3.3. Single Molecule and Nanoparticle Imaging in Photocatalysis Studies

Photocatalysis studies at the single particle and single molecule levels have recently attracted significant attentions, and single-particle catalysis using imaging techniques such as scattering-based DF microscopy[44-46], and single-molecule TIRF microscopy[47-53] has been demonstrated. Furthermore, high-resolution super-localization TIRF imaging in single-particle catalysis has also been carried out by several groups.[53-56] Zhou *et al.* employed super-localization TIRF imaging to study the surface reactivity of Au nanorod catalysts.[53] Cremer *et al.* reported high-resolution reactivity mapping of epoxidation reactions catalyzed by mesoporous titanosilicates.[55]

More recently, super-localization TIRF imaging of single metal-semiconductor heterostructures has been demonstrated by Tachikawa *et al.*; in this report, single-molecule super-resolution imaging of active sites on single Au-TiO_2 hybrid particles was carried out using an oxidation-reduction (redox)-responsive fluorescent dye.[54] Despite the recent study of photocatalysis by metal-semiconductor heterostructures at the single-particle level, their mechanisms of action and many of their photocatalytic properties remain largely unanswered, even though it is still necessary to develop metal-semiconductor heterostructures that can be widely used under visible light. Further, our understanding of the identity of the surface active sites and factors affecting the catalytic efficiency in these hybrid materials is still very limited.

In Chapter 7, to address the challenges, CdS semiconductor nanorods decorated with Au nanoparticles were synthesized in our collaborator Dr. Javie Vela's laboratory and studied at the single-particle level with millisecond time resolution. High-resolution super-localization TIRF imaging was used to unveil the nature and photocatalytic properties of the photo-generated carriers and redox active sites in Au-CdS hybrid heterostructures, using single-molecule detection following the oxidation of non-fluorescent amplex red to highly fluorescent resorufin.

References

1. Moernera, W. E.; Fromm, D. P. *Rev. Sci. Instrum.* **2003,** *74*, 3597–3619.

2. Murphy, C. J.; Gole, A. M.; Stone, J. W.; Sisco, P. N.; Alkilany, A. M.; Goldsmith, E. C.; Baxter, S. C. *Acc. Chem. Res.***2008,** *41*, 1721–1730.

3. Hardman, R. *Environ. Health Perspect.* **2006,** *114*, 166–172.

4. Wax, A.; Sokolov, K. *Laser & Photonics Reviews* **2009,** *3*, 146–158.

5. Love, S. A.; Marquis, B. J.; Haynes, C. L. *Appl. Spectroscopy* **2008,** *62*, 346A–362A.

6. Sperling, R. A.; Rivera Gil, P.; Zhang, F.; Zanella, M.; Parak, W. J. *Chem. Soc. Rev.* **2008,** *37*, 1896–1908.

7. Sönnichsen, C.; Alivisatos, A. P. *Nano Lett.* **2004,** *5*, 301–304.

8. Chang, W.-S.; Ha, J. W.; Slaughter, L. S.; Link, S. *Proc. Nat. Acad. Sci. U.S.A.* **2010**, *107*, 2781–2786.

9. Gu, Y.; Sun, W.; Wang, G.; Fang, N. *J. Am. Chem. Soc.* **2011,** *133*, 5720– 5723.

10. Wang, G.; Sun, W.; Luo, Y.; Fang, N. *J. Am. Chem. Soc.* **2010,** *132*, 16417–16422.

11. Hu, M.; Novo, C.; Funston, A.; Wang, H.; Staleva, H.; Zou, S.; Mulvaney, P.; Xia, Y.; Hartland, G. V. *J. Mater. Chem.* **2008,** *18*, 1949–1960.

12. Link, S.; Mohamed, M. B.; El-Sayed, M. A. *J. Phys. Chem. B* **1999,** *103*, 3073–3077.

13. Link, S.; El-Sayed, M. A. *J. Phys. Chem. B* **2005,** *109*, 10531–10532.

14. van Dijk, M. A.; Tchebotareva, A. L.; Orrit, M.; Lippitz, M.; Berciaud, S.; Lasne, D.; Cognet, L.; Lounis, B. *Phys. Chem. Chem. Phys.* **2006,** *8*, 3486–3495.

15. Boyer, D.; Tamarat, P.; Maali, A.; Lounis, B.; Orrit, M. *Science* **2002,** *297*, 1160–1163.

16. Berciaud, S.; Cognet, L.; Blab, G. A.; Lounis, B. *Phys. Rev. Lett.* **2004**, *93*, 257402.

17. Berciaud, S.; Lasne, D.; Blab, G. A.; Cognet, L.; Lounis, B. *Phys. Rev. B* **2006,** *73*, 045424.

18. Sun, W.; Wang, G.; Fang, N.; Yeung, E. S. *Anal. Chem.* **2009,** *81*, 9203–9208.

19. Berlier, J. E.; Rothe, A.; Buller, G.; Bradford, J.; Gray, D. R.; Filanoski, B. J.; Telford, W. G.; Liu, J. X.; Cheung, C. Y.; Chang, W.; Hirsch, J. D.; Beechem, J. M.; Haugland, R. P. *Journal of Histochemistry & Cytochemistry* **2003,** *51*, 1699–1712.

20. Walling, M.; Novak, J.; Shepard, J. R. E. *International Journal of Molecular Sciences* **2009,** *10*, 441–491.

21. Jaiswal, J. K.; Goldman, E. R.; Mattoussi, H.; Simon, S. M. *Nat. Meth.* **2004,** *1*, 73–78.

22. Tsien, R. Y. *Annual Review of Biochemistry* **1998,** *67*, 509–544.

23. Schneckenburger, H. *Current Opinion in Biotechnology* **2005,** *16*, 13–18.

24. Hell, S. W.; Wichmann, J. *Opt. Lett.* **1994,** *19*, 780–782.

25. Willig, K. I.; Rizzoli, S. O.; Westphal, V.; Jahn, R.; Hell, S. W. *Nature* **2006,** *440*, 935–939.

26. Eggeling, C.; Ringemann, C.; Medda, R.; Schwarzmann, G.; Sandhoff, K.; Polyakova, S.; Belov, V. N.; Hein, B.; von Middendorff, C.; Schonle, A.; Hell, S. W. *Nature* **2009,** *457*, 1159–1162.

27. Rust, M. J.; Bates, M.; Zhuang, X. *Nat. Meth.* **2006,** *3*, 793–796.

28. Huang, B.; Wang, W.; Bates, M.; Zhuang, X. *Science* **2008,** *319*, 810–813.

29. Betzig, E.; Patterson, G. H.; Sougrat, R.; Lindwasser, O. W.; Olenych, S.; Bonifacino, J. S.; Davidson, M. W.; Lippincott-Schwartz, J.; Hess, H. F. *Science* **2006,** *313*, 1642–1645.

30. Hess, S. T.; Girirajan, T. P. K.; Mason, M. D. *Biophysical journal* **2006,** *91*, 4258–4272.

31. Dempsey, G. T.; Bates, M.; Kowtoniuk, W. E.; Liu, D. R.; Tsien, R. Y.; Zhuang, X. *J. Am. Chem. Soc.* **2009,** *131*, 18192–18193.

32. Saxton, M. J.; Jacobson, K. *Annual Review of Biophysics and Biomolecular Structure* **1997,** *26*, 373–399.

33. Lee, K. J.; Nallathamby, P. D.; Browning, L. M.; Osgood, C. J.; Xu, X.-H. N. *ACS Nano* **2007,** *1*, 133–143.

34. L Li, H.-W.; McCloskey, M.; He, Y.; Yeung, E. *Anal. Bioanal. Chem.* **2007,** *387*, 63–69.

35. Xiao, L.; Qiao, Y.; He, Y.; Yeung, E. S. *Anal. Chem.* **2010,** *82*, 5268–5274.

36. Xiao, L.; Qiao, Y.; He, Y.; Yeung, E. S. *J. Am. Chem. Soc.* **2011,** *133*, 10638–10645.

37. S Stender, A. S.; Marchuk, K.; Liu, C.; Sander, S.; Meyer, M. W.; Smith, E. A.; Neupane, B.; Wang, G.; Li, J.; Cheng, J.-X.; Huang, B.; Fang, N. *Chem. Rev.* **2013**, *113*, 2469–2527.

38. Ha, J. W.; Sun, W.; Wang, G.; Fang, N. *Chem. Commun.* **2011,** *47*, 7743–7745.

39. Ha, J. W.; Sun, W.; Stender, A. S.; Fang, N. *J. Phys. Chem. C* **2012,** *116*, 2766–2771.

40. Xiao, L.; Ha, J. W.; Wei, L.; Wang, G.; Fang, N. *Angew. Chem. Int. Ed.* **2012,** *51*, 7734–7738.

41. Gu, Y.; Sun, W.; Wang, G.; Jeftinija, K.; Jeftinija, S.; Fang, N. *Nat. Commun.* **2012,** DOI: 10.1038/ncomms2037.

42. Marchuk, K.; Ha, J. W.; Fang, N. *Nano Lett.* **2013,** *13*, 1245–1250.

43. Ha, J. W.; Marchuk, K.; Fang, N. *Nano Lett.* **2012,** *12*, 4282–4288.

44. Novo, C.; Funston, A. M.; Mulvaney, P. *Nat. Nanotechnol.* **2008,** *3*, 598–602.

45. Tang, M. L.; Liu, N.; Dionne, J. A.; Alivisatos, A. P. *J. Am. Chem. Soc.* **2011,** *133*, 13220–13223.

46. Liu, N.; Tang, M. L.; Hentschel, M.; Giessen, H.; Alivisatos, A. P. *Nat. Mater.* **2011,** *10*, 631–636.

47. De Cremer, G.; Sels, B. F.; De Vos, D. E.; Hofkens, J.; Roeffaers, M. B. J. *Chem. Soc. Rev.* **2010,** *39*, 4703–4717.

48. Chen, P.; Zhou, X.; Shen, H.; Andoy, N. M.; Choudhary, E.; Han, K.-S.; Liu, G.; Meng, W. *Chem. Soc. Rev.* **2010,** *39*, 4560–4570.

49. Tachikawa, T.; Majima, T. *Chem. Soc. Rev.* **2010,** *39*, 4802–4819.

50. Xu, W.; Kong, J. S.; Yeh, Y.-T.; Chen, P. *Nat. Mater.* **2008,** *7*, 992–996.

51. Xu, W.; Kong, J. S.; Chen, P. *Phys. Chem. Chem. Phys.* **2009,** *11*, 2767–2778.

52. Xu, W.; Jain, P. K.; Beberwyck, B. J.; Alivisatos, A. P. *J. Am. Chem. Soc.* **2012,** *134*, 3946–3949.

53. Zhou, X.; Andoy, N. M.; Liu, G.; Choudhary, E.; Han, K.-S.; Shen, H.; Chen, P. *Nat. Nanotechnol.* **2012,** *7*, 237–241.

54. Tachikawa, T.; Yonezawa, T.; Majima, T. *ACS Nano* **2012,** *7*, 263–275.

55. De Cremer, G.; Roeffaers, M. B. J.; Bartholomeeusen, E.; Lin, K.; Dedecker, P.; Pescarmona, P. P.; Jacobs, P. A.; De Vos, D. E.; Hofkens, J.; Sels, B. F. *Angew. Chem. Int. Ed.* **2010,** *49*, 908–911.

56. Roeffaers, M. B. J.; De Cremer, G.; Libeert, J.; Ameloot, R.; Dedecker, P.; Bons, A.-J.; Bückins, M.; Martens, J. A.; Sels, B. F.; De Vos, D. E.; Hofkens, J. *Angew. Chem. Int. Ed.* **2009,** *48*, 9285–9289.

Figures and Captions

Note: In the following figures schematics are not drawn to scale.

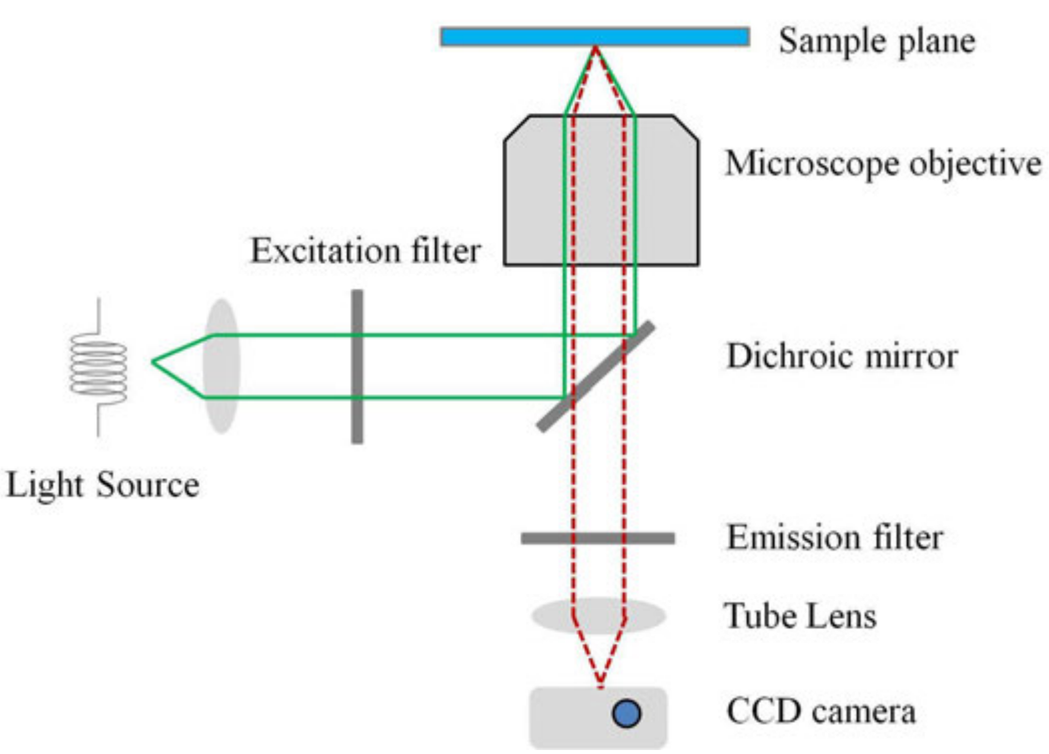

Figure 1. Experimental setup for epi-fluorescence microscopy.

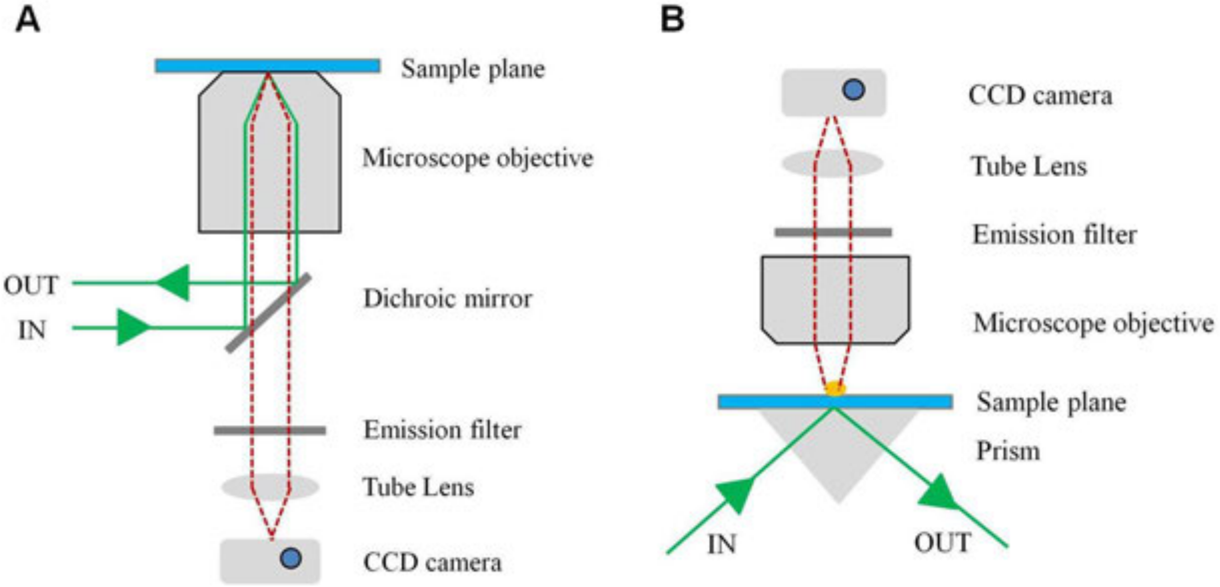

Figure 2. Experimental setup for TIRF microscopy. (A) Objective-type TIRF microscopy. (B) Prism-type TIRF microscopy.

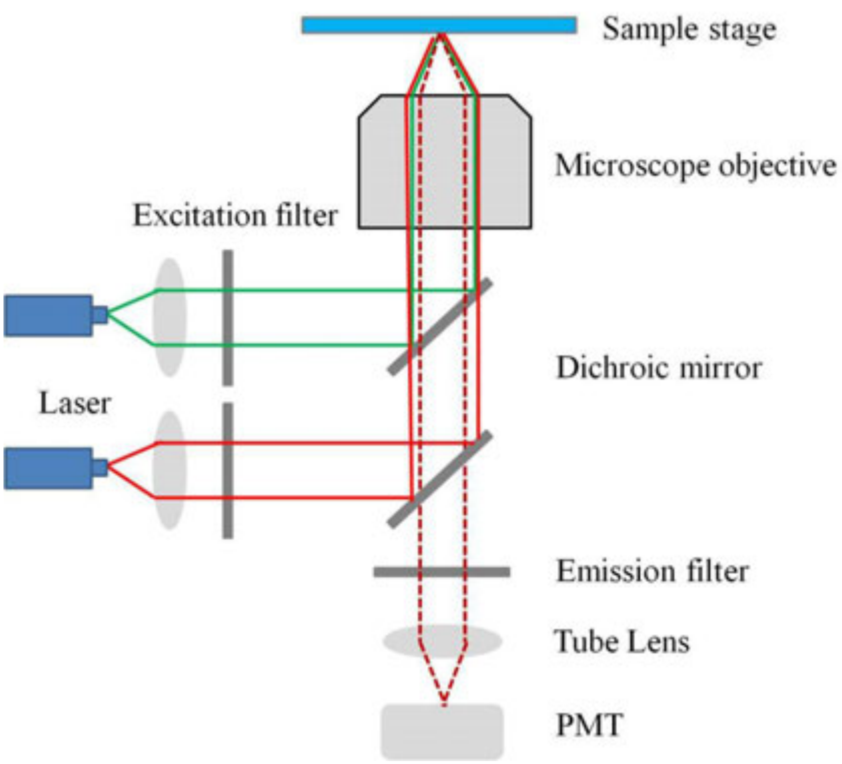

Figure 3. Experimental setup for STED.

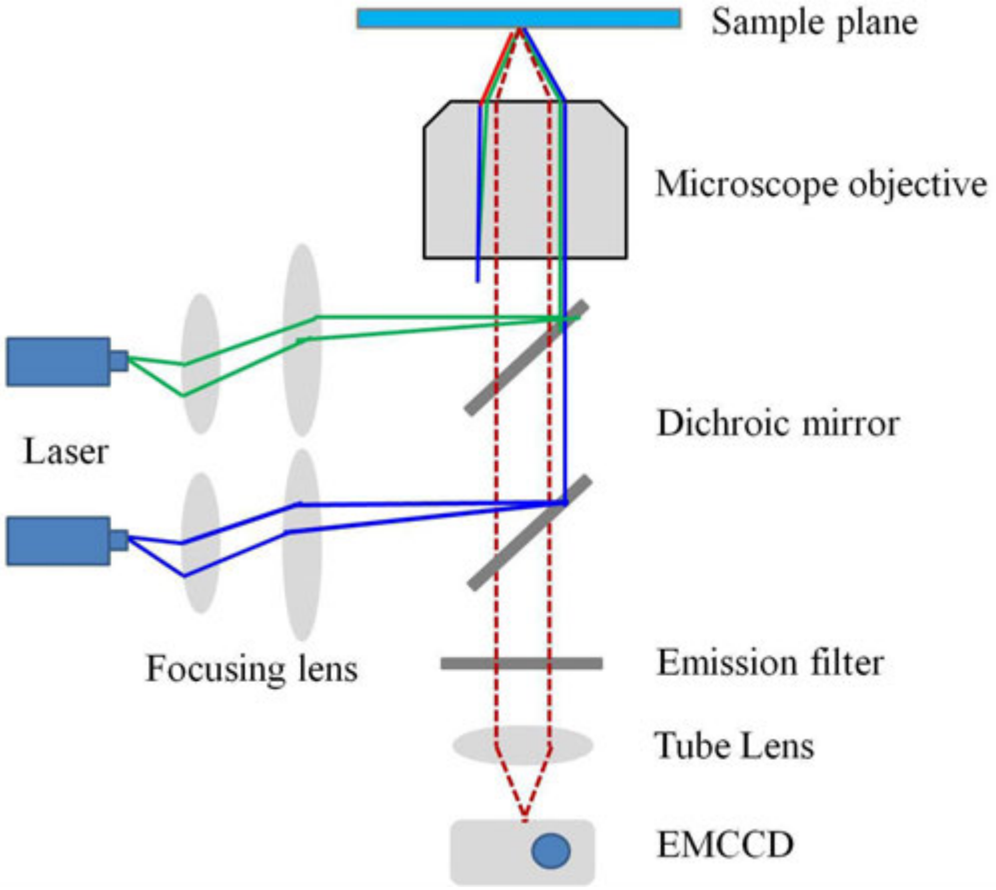

Figure 4. Experimental setup for STORM.

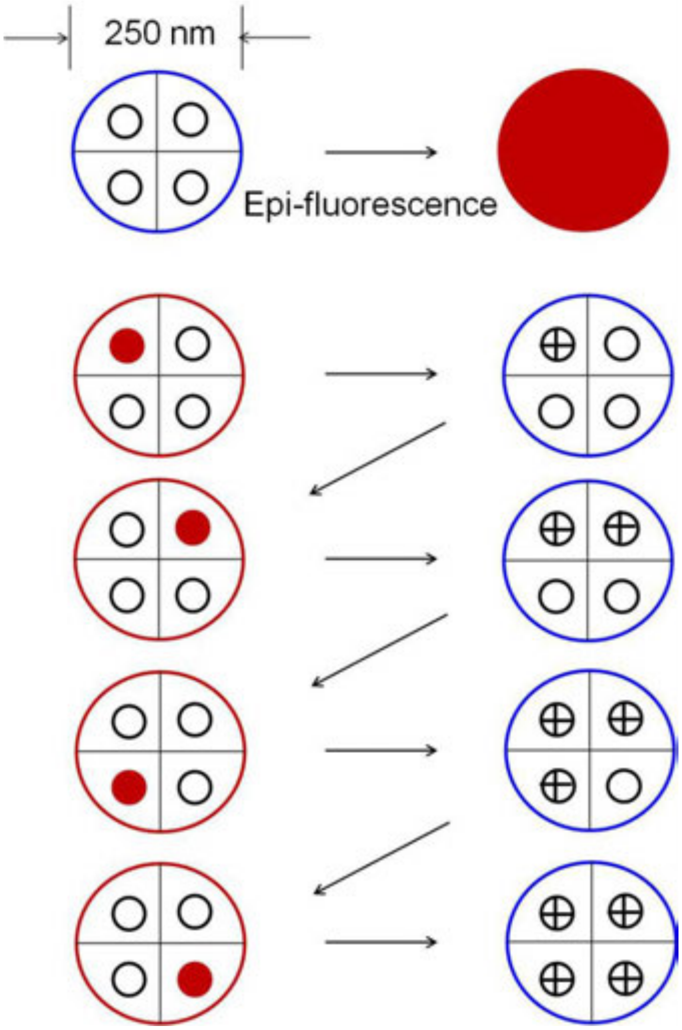

Figure 5. Principle of STORM. When four fluorescent molecules are located within 250 nm (diffraction limit) and are excited simultaneously, they cannot be distinguished. But, the fluorescent dyes are controlled to be excited one by one in STORM. The center position of each dye is localized through 2D Gaussian fitting.

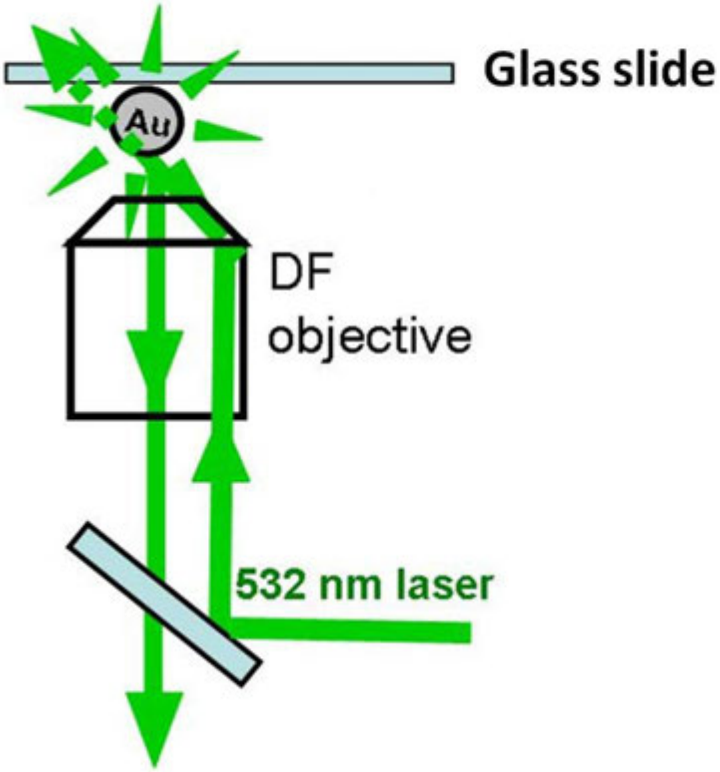

Figure 6. Schematic of the experimental setups for laser DF microscopy. Gold (Au) nanoparticles are deposited onto the surface of a glass slide. The 532 nm laser is directed through the outer ring of a dark-field objective. The scattered light by the NPs is collected in reflection mode using the same objective.

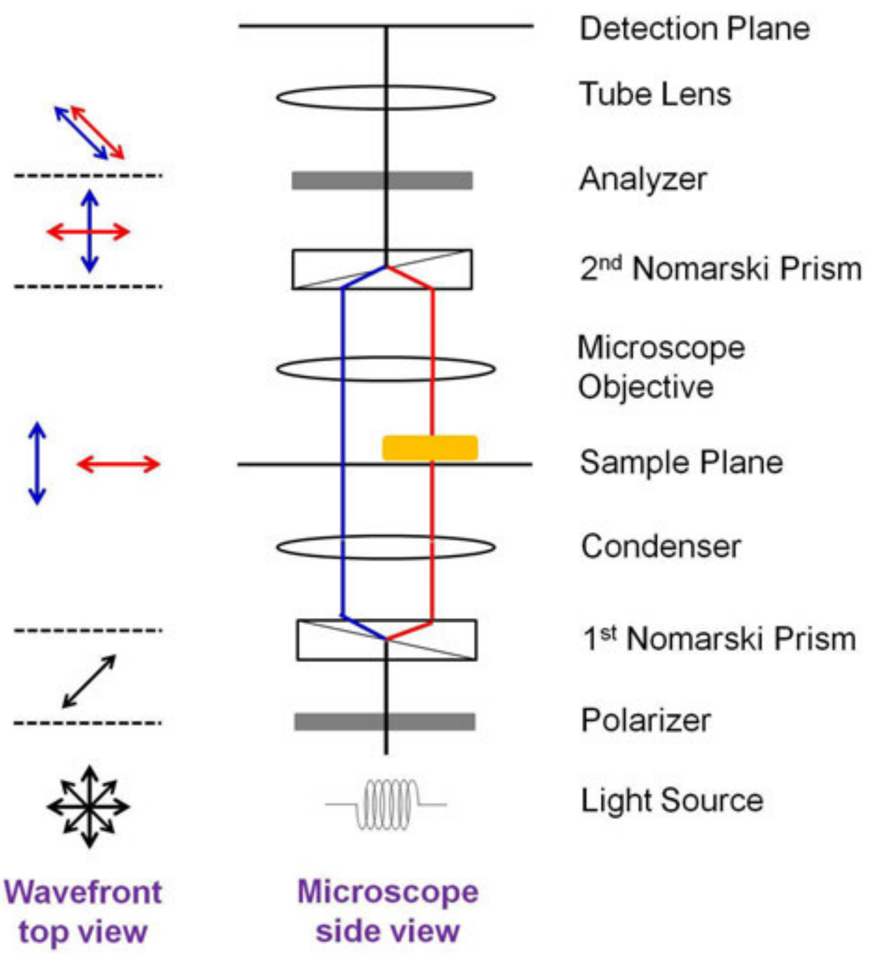

Figure 7. The optical path and wavefront in the DIC microscope. The blue- and red- lines represent the optical path of two orthogonal beams split by the first Nomarski prism.

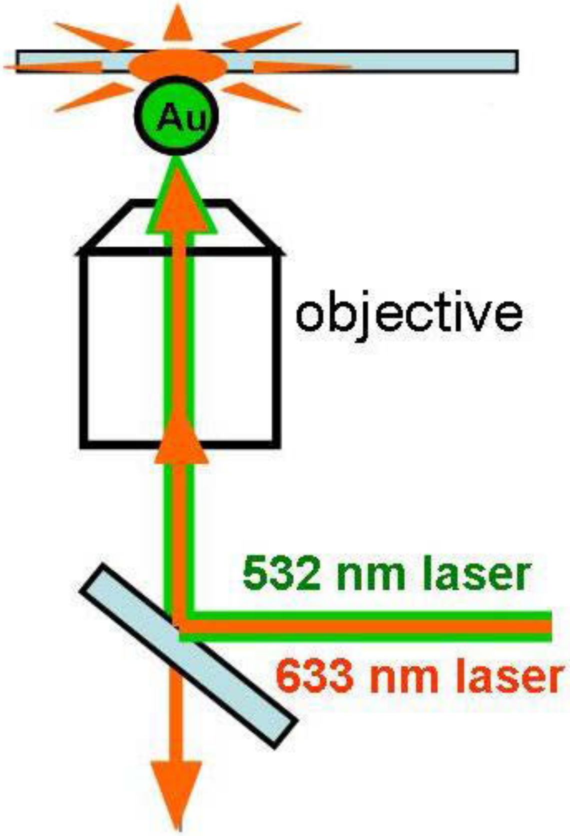

Figure 8. Schematic of the experimental setups for photothermal heterodyne imaging. Two laser beams (heating beam and probe beam) are overlaid and focused on the sample. The 532 nm laser is used to heat the nanoparticles. The change in refractive index due to the local change in temperature is detected by the 633-nm probe beam.

CHAPTER 2. DIFFERENTIAL INTERFERENCE CONTRAST POLARIZATION ANISOTROPY FOR TRACKING ROTATIONAL DYNAMICS OF GOLD NANORODS

Ji Won Ha, Wei Sun, Gufeng Wang, and Ning Fang*

A paper published in *Chemical Communications* 2011, 47, 7743-7745.

Reproduced by permission of the Royal Society of Chemistry (RSC)

* Corresponding author

Abstract

We describe differential interference contrast (DIC) polarization anisotropy for tracking rotational dynamics of gold nanorod (AuNR) probes. DIC polarization anisotropy enabled us to reveal the unidirectional clockwise circular translocation of an AuNR attached to a kinesin-driven microtubule and to precisely determine the real-time orientation of the AuNR during the dynamic process.

Introduction

Rotational tracking is of great importance for scientists to understand certain functions and mechanisms of biomolecules, such as RNA folding,[1] rotational motion of ATPase,[2] and structural and rotational dynamics of myosin V.[3] Fluorescent molecules have been wieldy used in biological systems for this purpose due to their polarized emission upon the excitation by polarized light.[1-6] Fluorescence anisotropy is commonly used to measure the extent of polarization of the emission.[5-7] The high autofluorescence background and short observation time due to photobleaching and photoblinking are generally considered the major drawbacks of fluorescence polarization in live cell imaging.

More recently, gold nanorods (AuNRs) have been gaining much attention as ideal probes under a variety of imaging tools for orientation sensing due to their anisotropic shape, photostability,[8] and excellent biocompatibility.[9] In dark-field scattering-based methods, Sönnichsen and Alivisatos placed a beam splitter to separate the scattering light from AuNRs into two orthogonal polarization directions.[10,11] Polarization anisotropy was then calculated to extract information on the AuNR orientation. However, the scattering-based methods are challenging for identifying AuNRs from cellular components and other debris that scatter light. Moreover, it is difficult to detect particles smaller than 20 nm in diameter since the scattering cross section decreases as $1/R^6$, where R is the radius of a particle.[12] Highly sensitive absorption-based photothermal imaging has also been utilized to determine the AuNR orientation, and photothermal polarization anisotropy was employed for determining the orientation angle with two orthogonally polarized intensities.[13] However, this method requires switching between two laser excitation sources to obtain two orthogonal intensities for AuNRs and raster scanning of the sample to collect an image, which limit its applicability for studies of fast dynamics in biological systems.

We have introduced a differential interference contrast (DIC) microscopy-based single particle orientation and rotation tracking (SPORT) method to resolve the rotational motions of AuNRs.[14] In the previous study we used the bright and dark intensities directly to determine the AuNR orientation. The precision of the orientation angle determination was related to the precision of the DIC intensity measurement. In practice, however, the precision might be affected by intensity fluctuations of the light source, the slight movement of AuNRs in the vertical direction, etc. Therefore, in this paper we demonstrate an improved, alternative approach by using DIC polarization anisotropy computed from the orthogonally polarized dark and bright intensities. DIC polarization anisotropy using an intensity ratio instead of absolute intensities is less affected by intensity instabilities and it allows for more accurate, reproducible and reliable angle measurements in dynamic studies. It is notable that DIC polarization anisotropy has several advantages over the conventional fluorescence, scattering and absorption-based polarization methods. DIC polarization anisotropy is simpler with respect to instrumentation, easier and more convenient in terms of operation, and capable of getting simultaneous images of both the nanorod probes and cellular components.[15]

Experimental Section

Differential Interference Contrast (DIC) Microscope. An upright Nikon Eclipse 80i microscope was used in this study. The DIC mode used a pair of Nomarski prisms, two polarizers, a quarter-wave plate, a Plan Apo oil-immersion objective (100×, N.A. = 1.40) to collect the signals from the samples, and an oil-immersion condenser (N.A. = 1.40). A Photometrics CoolSnap ES CCD camera (1392 × 1040 imaging array, 6.45 μm × 6.45 μm pixel size) was employed to record highly detailed DIC images of gold nanorods (AuNRs). An Andor iXon^{EM}+ CCD camera (512 × 512 imaging array, 16 μm × 16 μm pixel size) was used to capture fast dynamics of AuNRs on kinesin-driven microtubules. The DIC imaging at 720 nm close to the longitudinal surface plasmon resonance (SPR) of AuNRs was carried out by inserting a 720 nm band-pass filter into the light path in the microscope. The band-pass filter was obtained from Thorlabs (Newton, NJ) and it has central wavelength of 720 nm and a full width at half-maximum (FWHM) of 10 nm.

Sample preparation of immobilized AuNRs. AuNRs (25 × 73 nm) were purchased from Nanopartz (Salt Lake, UT). The AuNR colloid solution was first diluted with 18.2-MΩ pure water to a proper concentration. Then the diluted solution was sonicated for 15 min at room temperature. After sonication, 6 μL of the diluted solution was placed onto a pre-cleaned slide which is then covered with a 22 × 22 mm No. 1.5 coverslip (Corning, NY). The positively charged AuNRs were immobilized onto the negatively charged surface of the coverslip by electrostatic forces.

Polarization-dependent DIC imaging of immobilized AuNRs. The sample glass slide was placed on a 360° rotating mirror holder affixed onto the microscope stge. By rotating the mirror holder 5° or 10° per step, the nanorods were positioned in different orientations, and DIC images at 720 nm were taken with the Photometrics CoolSnap ES CCD camera. The collected images were analyzed by MATLAB and NIH ImageJ.

Preparation of kinesin motor proteins and microtubules. BL21 (DE3) *E. coli* bacteria with the full-length His-tagged kinesin plasmid were obtained from Dr. William O. Hancock at Pennsylvania State University. The *E. coli* bacteria were induced to express kinesin with isopropyl β-D-1-thiogalactopyranoside (IPTG). Then, the kinesin was purified on a Ni-nitrilotriacetic acid (NTA) agarose column according to published protocol.[1] All the tubulin proteins, GTP and taxol were purchased from Cytoskeleton

(Denver, CO). Tubulin proteins were mixed and aliquoted with ratio as following: 86 % unlabeled tubulin, 7 % Rhodamine labeled tubulin and 7 % biotinylated tubulin. Microtubules were prepared by applying published protocols.[2,3] 10 μL BRB80 buffer supplemented with 9 μM tubulin, 4 mM $MgCl_2$, 0.5 mM GTP and 10 μM taxol inside was incubated at 37 °C for 3 hrs; microtubules were then diluted and stabilized in 100 μL BRB80 buffer supplemented by 10 μM taxol.

Microtubules gliding on the kinesin-coated substrate. Two strips of double-sided tape were placed on a clean glass slide to serve as the spacers, and one clean coverslip was then placed on top to form a chamber. Penta-His antibodies in BRB80 was allowed to flow into the chamber. After 5 min a 0.5 mg/mL casein (Sigma, St. Louis, MO) in BRB80 was introduced to prevent nonspecific protein binding. After 5 min BRB80 solution containing 0.2 mg/mL casein, 0.2 mM MgATP and kinesin (with a His-tag) was introduced into the chamber to replace the previous liquid. The kinesin motors bind specifically to the antibodies by their His-tags. A futher 5 min later BRB80 solution containing 0.2 mg/mL casein, 0.2 mM MgATP, 10 μM Taxol and microtubules was flowed into the chamber and the microtubules were allowed to bind to the motors for 5 min. Subsequently, BRB80 solution containing 0.2 mg/mL casein, 0.2 mM MgATP, 10 μM Taxol and neutravidin-modified AuNR (10 × 35 nm, Nanopartz) was flowed into the chamber and was kept at room temperature for 7 min. The neutravidin-modified AuNR was firmly attached to the microtubule surface through multiple strong biotin-neutravidin linkages. Finally, the chamber was filled with a motility solution containing BRB80, 0.2 mg/mL casein, 1 mM MgATP, 10 μM Taxol, and an oxygen scavenger mixture [50

μg/mL glucose oxidase (Sigma), 4 μg/mL catalase (Sigma), 1% (w/v) glucose (Sigma) and 0.1% (v/v) β-mercaptoethanol (Fluka)]. DIC imaging of AuNRs attached to microtubules was performed by observing the sample slide under a DIC microscope. A video (32 frames per second) was captured with an Andor iXon^{EM}+ CCD camera. MATLAB and NIH ImageJ were used to analyze and process the collected video.

Results and Discussion

We first calculated the DIC polarization anisotropy for AuNRs (25 × 73 nm) immobilized on a glass slide and illuminated at 720 nm that is close to the longitudinal surface plasmon resonance (SPR) wavelength. It is worthwhile to note that the working principle of DIC microscopy is well suitable for measuring polarization anisotropy. In a DIC microscope, the incident light beam is split by the first Nomarski prism into two beams in the orthogonal bright and dark polarization directions. Each of the two orthogonally polarized beams generates an independent intermediate image of the sample. For anisotropic AuNRs, the longitudinal SPR mode is excited differently by the two polarized beams, resulting in two different intermediate images. After the two split beams are recombined by the second Nomarski prism and interfere with each other after passing through a polarizer, distinctive DIC contrast patterns are created for AuNRs in different orientations relative to the two polarization directions.

Figure 1 shows polarization-dependent DIC images of the immobilized AuNRs. The orientation of AuNR is defined as the angle θ between the AuNR's long axis and the dark polarization axis as shown in Figure 1A. The darkest DIC intensity for NR 1 highlighted in the green square in Figure 1A was observed when its long axis was aligned with the dark polarization axis (red arrow, $\theta = 0°$). After a 90° rotation of the sample slide, the long axis of NR 1 was aligned with the bright polarization axis (blue arrow, $\theta = 90°$) to generate the brightest intensity in Figure 1B.

A complete AuNR rotation study was carried out by rotating the stage by 5° or 10° per step to position NR 1 in different orientations. The normalized DIC bright (blue) and dark (red) intensities at 720 nm were plotted as a function of orientation angle in Figure 2A. The bright and dark intensities are anti-correlated, that is, an increase in the bright intensity is accompanied by a decrease in the dark intensity, and vice versa. Figure 2B is the polar plot that elucidates the polarization-dependent DIC imaging for NR 1. The two periodic patterns at 720 nm show a shift of ~90°.

DIC polarization anisotropy P is defined in Eq. 1:

$$P = \frac{I_{\mathrm{B,N}} - I_{\mathrm{D,N}}}{I_{\mathrm{B,N}} + I_{\mathrm{D,N}}} \qquad (1)$$

where $I_{\mathrm{B,N}}$ and $I_{\mathrm{D,N}}$ are the normalized bright and dark intensities at the longitudinal SPR wavelength, respectively. Figure 2C shows the polarization anisotropy P for NR 1 as a function of orientation angle. The P values are in the range of -1 to +1 depending on the AuNR's orientation relative to the bright and dark polarization directions as illustrated in Figure 2D.

We have shown in the previous work that the DIC bright (or dark) intensity of an AuNR is proportional to the fourth power of the sine (or cosine) of the orientation angle θ.[14] Therefore, the P values can be calculated directly for any given θ using Eq. 2:

$$P = \frac{\sin^4(\theta) - \cos^4(\theta)}{\sin^4(\theta) + \cos^4(\theta)} \tag{2}$$

As shown in Figure 2C, the experimental P values obtained from Eq. 1 agree well with the theoretical P values calculated from Eq. 2, which validates that DIC polarization anisotropy allows for accurate measurements of orientation angles of AuNRs.

We further derived Eq. 3 that relates DIC polarization anisotropy P to the orientation angle θ:

$$\begin{aligned} \theta &= \mathrm{acos}\left(\sqrt{\frac{A - \sqrt{A^2 - 2A}}{2}}\right), \quad P < 0 \\ \theta &= \mathrm{acos}\left(\sqrt{\frac{A + \sqrt{A^2 - 2A}}{2}}\right), \quad P > 0 \end{aligned} \tag{3}$$

where A is defined as $(P\text{-}1)/P$. Therefore, we are able to deduce the orientation angle θ backward from the measurement of DIC polarization anisotropy.

The next crucial step is to verify that DIC polarization anisotropy can be used to study rotational dynamics at sub-micrometer scale. Kinesin-induced gliding of microtubule was chosen as the model system. In our previous work, AuNRs with an average size of 10 × 35 nm were employed to reveal the axial rotation of non-13-protofilament microtubules and the non-rotation of 13-protofilament microtubules on the kinesin-coated surface.[14] In the present study, a circular movement of an AuNR of similar size attached to a curved microtubule gliding on the kinesin-coated surface was recorded at video-rate (32 frames/s), and the DIC polarization anisotropy for the AuNR was analyzed.

The control over activity, speed, and directionality of kinesin-driven microtubules is important to utilize them as a principal molecular transport mechanism for nanotechnology applications. It has been shown that when a moving microtubule bumped against the wall, it could change the direction to move along the wall.[16] In addition, an applied electric field was able to control the transport speed and produce the circular translocation of microtubules.[17,18] In the present study, we analyzed the shape-induced circular movement of microtubule on the kinesin-coated surface, which serves as a convenient and useful model system. A curved microtubule was produced from taxol-stabilized microtubules by the hydrolysis of GTP in β-tubulin as time passes.[19]

Figure 3A shows successive DIC images of the AuNR that was firmly attached to the microtubule through the strong biotin-neutravidin binding. The DIC polarization anisotropy measurement allowed us to reveal the unidirectional clockwise circular movement (illustrated in Figure 3B) of the kinesin-driven microtubule. The angular velocity of the microtubule taking on the circular movement was 10.1 rad·s^{-1}. No axial rotation of the microtubule was detected. This circular movement, which was caused by the curve shape of the microtubule, gave rise to the periodic bright and dark intensity changes. The darkest intensity was found in Frames No. 4 and 15 when the AuNR's long axis was parallel to the dark axis, while the brightest intensity was found in Frame No.10 when the AuNR's long axis was nearly perfectly aligned with the bright axis. Figure 3C shows a time trace of the anti-correlated DIC intensities in the bright (blue) and dark (red) polarization directions. The DIC polarization anisotropy *P* values computed using Eq. 1 were distributed between -1 and +1 as demonstrated in Figure 3D. Figures 3C and 3D that were obtained for the dynamic process are nearly identical to Figures 2A and 2C that were obtained for the rotation of immobilized nanorods. Clearly, DIC polarization anisotropy allows us to precisely determine real-time orientation during the dynamic process.

Conclusions

In conclusion, DIC microscopy is an excellent tool to measure polarization anisotropy for tracking rotational dynamics of AuNR probes. DIC polarization anisotropy can be conveniently obtained from the bright and dark intensities of a single DIC image of AuNR. The usefulness of DIC polarization anisotropy was verified by precise tracking of an AuNR firmly attached to a kinesin-driven microtubule taking on a circular movement. DIC polarization anisotropy is proved to be an accurate and reliable measurement of AuNR orientation for SPORT.

References

1. Zhuang, X.; Bartley, L. E.; Babcock, H. P.; Russell, R.; Ha, T.; Herschlag, D.; Chu, S. *Science* **2000**, *288*, 2048.
2. Nishizaka, T. *et al*., *Nat. Struct. Mol. Biol*., **2004**, *11*, 142.
3. Toprak, E. *et al*., *Proc. Natl. Acad. Sci. U.S.A.*, **2006**, *103*, 6495.
4. Moerner, W. E.; Orrit, M. *Science* **1999**, *283*, 1670.
5. Forkey, J. N.; Quinlan, M. E.; Goldman, Y. E. *Prog. Biophys. Mol. Biol*., **2000**, *74*, 1.
6. Khatua, S.; Guerrero, J. M.; Claytor, K.; Vives, G.; Kolomeisky, A. B.; Tour, J. M.; Link, S. *ACS Nano* **2009**, *3*, 351.
7. Chung, I.; Shimizu, K. T.; Bawendi, M. G. *Proc. Natl. Acad. Sci. U.S.A*., **2003**, *100*, 405.

8. Sperling, R. A.; Gil, P. R.; Zhang, F.; Zanella, M.; Parak, W. *Chem. Soc. Rev.*, **2008**, *37,* 1896.

9. Murphy, C. J.; Gole, A. M.; Stone, J. W.; Siscot, P. N.; Alkilany, A. M.; Goldsmith, E. C.; Baxter, S. C. *Acc. Chem. Res.*, **2008**, *41*, 1721.

10. Sönnichsen, C.; Alivisatos, A. P. *Nano Lett.*, **2005**, *5*, 301.

11. Pierrat, S.; Hartinger, E.; Faiss, S.; Janshoff, A.; Sönnichsen, C. *J. Phys. Chem. C.*, **2009**, *113,* 11179.

12. Van Dijk, M. A.; Tchebotareva, A. L.; Orrit, M.; Lippitz, M.; Berciaud, S.; Lasne, D.; Cognet, L.; Lounis, B. *Phys. Chem. Chem. Phys*., **2006**, *8*, 3486.

13. Chang, W. -S.; Ha, J. W.; Slaughter, L. S.; Link, S. *Proc. Natl. Acad. Sci. U.S.A*., **2010**, *107*, 2781.

14. Wang, G.; Sun, W.; Luo, Y.; Fang, N. *J. Am. Chem. Soc*., **2010**, *132*, 16417.

15. Sun; W.; Wang, G.; Fang, N.; Yeung, E. S. *Anal. Chem.*, **2009**, *81*, 9203.

16. Hiratsuka, Y.; Tada, T.; Oiwa, K.; Kanayama, T.; Uyeda, T. Q. P. *Biophys. J.*, **2001**, *81*, 1555.

17. Dujovne, I.; van den Heuvel, M.; Shen, Y.; de Graaff, M.; Dekker, C. *Nano Lett.*, **2008**, *8*, 4217.

18. Kim, T.; Kao, M.; Hasselbrink, E. F.; Meyhlofer, E. *Nano Lett.*, **2007**, *7*, 211.

19. Hyman, A. A. *et al*., *Curr. Biol.*, **2007**, *17*, 1765.

Figures and Captions

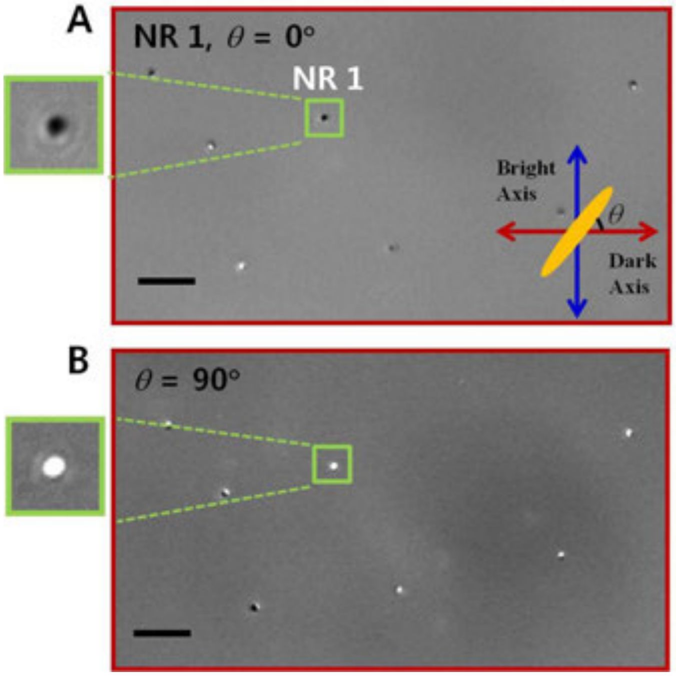

Figure 1. Polarization-dependent DIC images of AuNRs with an average size of 25 × 73 nm. (A) DIC image of a group of AuNRs. (B) DIC image of the same AuNRs after a 90° rotation of the sample slide. Higher magnification views of the NR 1 are displayed. The scale bar represents 2 μm.

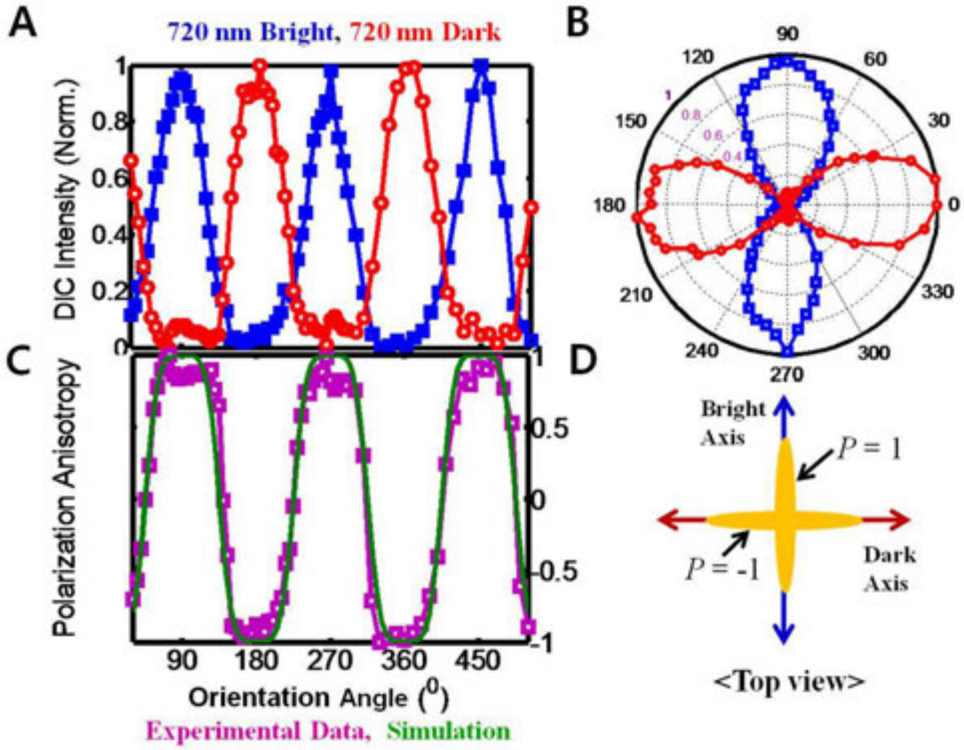

Figure 2. DIC polarization anisotropy for NR 1 highlighted in Figure 1. (A) The normalized bright and dark intensities change periodically when the stage rotates by 5° or 10 ° per step. (B) Polar plot for the bright and dark intensities of NR 1. (C) Polarization anisotropy *P* for NR 1. The experimental *P* values are compared to the calculated *P* values (green curve) as a function of orientation angle. (D) Schematic of *P* values at two special cases ($\theta = 0°$ and $\theta = 90°$).

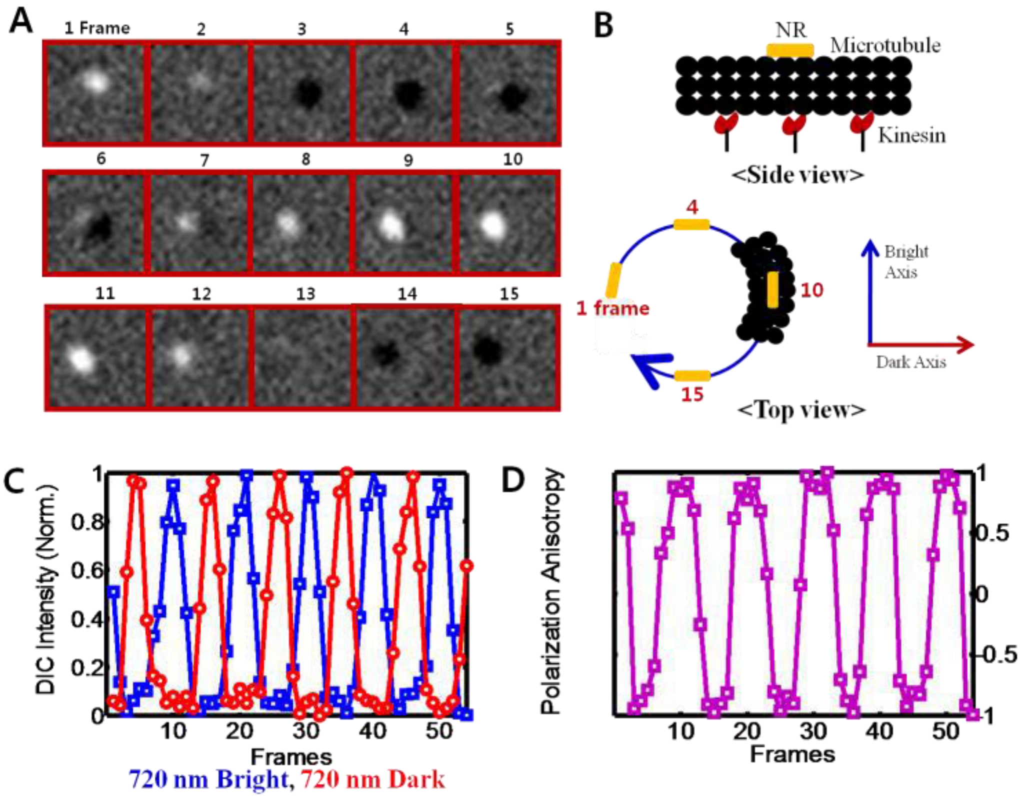

Figure 3. Dynamics tracking of an AuNR attached on a kinesin-driven microtubule with DIC polarization anisotropy. The average size of the AuNRs used in this experiment was 10 × 35 nm. (A) Successive DIC images of the AuNR as a function of time. (B) Schematic of a piece of gliding microtubule that shows rotational translocation. (C) Time traces of measured and normalized DIC intensities in the two orthogonal polarization directions for the AuNR firmly attached to the rotating microtubule. (D) Polarization anisotropy for the AuNR.

Supplementary Materials

Calculation of the orientation angle θ from the polarization anisotropy P. Two orthogonal intensities from bright and dark polarization directions are obtained in DIC microscopy. We have shown that the DIC bright intensity of an AuNR is proportional to the fourth power of the sine of the orientation angle θ between the long axis of a NR and the dark axis.[4] In addition, the DIC dark intensity is proportional to the fourth power of the cosine of the orientation angle θ. Therefore, the normalized bright and dark intensities ($I_{B,N}$, $I_{D,N}$) as a function of the orientation angle θ can be written as

$$I_{B,N}(\theta) = \sin^4(\theta)$$
$$I_{D,N}(\theta) = \cos^4(\theta)$$

DIC polarization anisotropy P is defined as

$$P = \frac{I_{B,N} - I_{D,N}}{I_{B,N} + I_{D,N}}$$

Therefore, the polarization anisotropy P can be rewritten as

$$P = \frac{\sin^4(\theta) - \cos^4(\theta)}{\sin^4(\theta) + \cos^4(\theta)}$$

The orientation angle θ can be expressed in terms of P and the following relationship for the orientation angle θ as a function of P was finally obtained.

$$\theta = \operatorname{acos}\left(\sqrt{\frac{A-\sqrt{A^2-2A}}{2}}\right), \qquad P<0$$

$$\theta = \operatorname{acos}\left(\sqrt{\frac{A+\sqrt{A^2-2A}}{2}}\right), \qquad P>0$$

where A is defined as $(P\text{-}1)/P$.

CHAPTER 3. DUAL-WAVELENGTH DETECTION OF ROTATIONAL DIFFUSION OF SINGLE ANISOTROPIC NANOCARRIERS ON LIVE CELL

Ji Won Ha, Wei Sun, Anthony S. Stender, and Ning Fang*

A paper published in *Journal of Physical Chemistry C* 2012, 116, 2766-2771.

* Corresponding author

Abstract

Single particle rotational tracking is of great importance to monitor orientation changes of biomolecules and to understand their functions and mechanisms in biological systems. Differential interference contrast (DIC) microscopy has found to be an excellent tool to measure polarization anisotropy for tracking rotational dynamics of gold nanorod (AuNR) probes. DIC polarization anisotropy can be conveniently obtained from the bright and dark intensities of a single DIC image of AuNR. Here, DIC microscopy-based dual-wavelength detection of rotational motions of AuNRs at both transverse and longitudinal surface plasmon resonance (SPR) wavelengths is demonstrated. The transverse SPR mode was successfully used to track fast rotational dynamics of individual AuNRs on live cell membranes. This is important since the transverse SPR mode is mostly insensitive to the medium refractive index, AuNR aspect ratio, and the adsorption of biomolecules. DIC polarization anisotropy was simultaneously obtained from the two SPR wavelengths during the dynamic process. Both wavelengths showed good agreement and provided accurate and reliable measurement of AuNR orientation.

Introduction

Nanocarriers provide a novel platform for specific delivery of therapeutic agents across cell membranes.[1,2] Cell-surface receptors are considered the potential targets in these drug delivery systems.[1] Over the past decade, various nanometer-scale drug carriers have been designed and explored based on different nanomaterials, including: polymers, liposomes, nanotubes, polymeric micelles, dendrimers, magnetic nanoparticles, and silica nanoparticles.[3-8]

Recently, gold nanorods (AuNRs) have gained interest as potential non-toxic and site-specific nanocarriers for several reasons. First, AuNRs can be synthesized with control over average size, size distribution, and particle shape, all of which are key factors associated with cellular uptake mechanisms and improved penetration into cells.[9] In addition, surfaces of AuNRs can be conveniently functionalized with surface chemistry.[10-12] Furthermore, AuNRs have excellent biocompatibility,[13] making them suitable carriers in drug delivery systems. Finally, anisotropic AuNRs offer the unique scattering, absorption, and photothermal properties that result from surface plasmon resonance (SPR) collective oscillation of the conduction-band electrons with the incident light.[14,15] The dissipation of absorbed energy as heat by near-infrared light can be employed to actively release drugs[16,17] and kill cancer cells.[18]

Although there has been much progress on AuNR carriers, the detailed mechanisms of cellular uptake, drug delivery, and penetration into cells are still poorly understood. Therefore, there exists a need to fully elucidate the detailed mechanisms for the more efficient design and modification of AuNR carriers. Since the mechanisms are closely related to the rotational dynamics of AuNRs delivered onto cell membranes, it is truly vital to develop convenient and powerful methods to track real-time rotational motions of AuNRs in and on living cells. Rotational tracking of individual AuNRs has been carried out under scattering-based dark-field (DF) microscopy[19-21] and absorption-based photothermal imaging.[22] Although these methods have been successfully used to reveal well-defined rotational motions, there are some limitations on their application to the studies of fast dynamics in cells.

Recently, we introduced Nomarski-type differential interference contrast (DIC) microscopy-based single particle orientation and rotational tracking (SPORT) technique[23] and DIC polarization anisotropy[24] for an accurate and reliable measurement of AuNR orientation. We successfully used the DIC polarization anisotropy to track rotational dynamics of an AuNR firmly attached to a kinesin-driven microtubule upon the longitudinal SPR excitation at video-rate.[24] However, it is worth noting that the longitudinal SPR mode is very sensitive to the surrounding environment.[25] Therefore, it is beneficial if the transverse SPR excitation, which is less sensitive to the environment, can provide sufficient contrast in probing fast rotational dynamics of AuNRs in biological systems.

In this paper we report an improved dual-wavelength SPORT technique. We used two SPR excitation wavelengths of 540 nm (transverse SPR mode) and 720 nm (longitudinal SPR mode) simultaneously to resolve rotational dynamics of AuNRs with an average size of 25 nm × 73 nm. We demonstrate simultaneous polarization anisotropy measurement of individual AuNRs taking on fast rotational motions on live cell membranes with a dual-view DIC microscope operated at the two SPR wavelengths.

Experimental Section

DIC Microscope. An upright Nikon Eclipse 80i microscope was used in this study. In the DIC mode, a set of two Nomarski prisms, two polarizers, a quarter-wave plate were installed. The samples were illuminated through an oil-immersion condenser (N.A. = 1.40), and the optical signals were collected by a Plan Apo oil-immersion objective (100×,N.A. = 1.40). DIC images at a selected wavelength were collected by inserting the corresponding band-pass filters of 540 nm and 720 nm into the light path in the microscope. The filters with a full width at half-maximum (FWHM) of 10 nm were purchased from Thorlabs (Newton, NJ). An Andor iXon^{EM}+ 897 camera was used to capture rotational dynamics of AuNRs on the cell membrane at 32 frames s^{-1}. A Hamamatsu ORCA-Flash 2.8 CMOS camera was used to image AuNRs immobilized on a pre-cleaned glass slide.

Sample Preparation and DIC Imaging of Immobilized AuNRs. AuNRs with an average size of 25 nm × 73 nm were purchased from Nanopartz (Salt Lake City, UT). The AuNR colloid solution was first diluted with 18.2-MΩ pure water to a proper concentration. Then the diluted solution was sonicated for 10 minutes at room temperature. After sonication, 6 μL of the diluted solution was placed onto a pre-cleaned slide which was then covered with a 22 mm × 22 mm No. 1.5 coverslip (Corning, NY). The positively charged AuNRs were immobilized on the negatively charged surface of the coverslip by electrostatic forces. The sample glass slide was placed on a 360° rotating microscope stge. By rotating the stage 5° or 10° per step, the AuNRs were positioned in different orientations. DIC images were taken with the Hamamatsu CMOS camera. The collected images were analyzed with MATLAB and NIH ImageJ.

Polarization-sensitive DF Scattering Imaging of Immobilized AuNRs. In DF mode we used a Nikon Plan Fluor 100× 0.5-1.3 oil iris objective and a Nikon DF condenser with a 1.43-1.20 N.A. in oil. To perform the polarization-dependent DF scattering imaging of immobilized AuNRs, we placed a polarizer into the beam path and rotated the polarizer to change the polarization direction from 0° to 360° in 10° increments. DF Scattering images were taken with the Hamamatsu CMOS camera. The collected images were also analyzed with MATLAB and NIH ImageJ.

Dual-wavelength DIC Imaging of Immobilized AuNRs. A DIC microscope was operated at two wavelengths simultaneously by using a Photometrics dual-view filter (Tucson, AZ) installed in the light path as shown in Figure S1. We used a 565 nm dichroic filter and two sets of band-pass filters for 540 nm and 720 nm.

Cell Culture, Sample Preparation, and DIC Imaging of AuNRs. A 549 human lung cancer cell line was purchased from American Type Culture Collection (CCL-185, ATCC, Manassas, VA). The cells were placed in a T25 cell culture flask (Corning) and grown in cell culture medium supplemented with 10 % fetal bovine serum (FBS) in a cell culture incubator (37 °C, 5 % CO_2). When subculturing, 150 μL of cell suspension solution was transferred to a 22 mm × 22 mm poly-L-lysine (PLL)-coated coverslip, housed in a 35-mm Petri dish (Corning). The Petri-dish was left in the incubator for 1 h to let the cells attach to the coverslip. After 1.5 mL of the cell culture medium with 10 % FBS supplement was added to immerse the coverslip, the Petri dish was left again in the incubator for 24 h. AuNRs were diluted in cell culture medium to the proper concentration and incubated with cells for 1 h. To achieve efficient targeting of AuNRs (25 nm × 73 nm) to a cell, transferrin molecules were conjugated to the surface of AuNRs. To stabilize the AuNRs in cell culture medium, polyethylene glycol (PEG) molecules were also conjugated on the AuNRs. The coverslip with cells was then put on a glass slide and was put under the dual-wavelength DIC microscope for observation.

Effect of the Thiol Molecules on the DIC and DF Intensities of Immobilized AuNRs. The AuNR colloid solution was diluted with ethanol (99.95%, Emerck) to a proper concentration. After sonication for 10 minutes, 10 μL of the diluted solution was placed onto a pre-cleaned slide which was then covered with a coverslip. DIC images (or DF images) of immobilized AuNRs were taken with the Hamamatsu CMOS camera. Then, 1 mM 1-decanethiol (Aldrich, USA) in ethanol was added to the one slide of the coverslip. After 20 minutes DIC images (or DF images) were taken for the same AuNRs. In DF microscopy, a transmission grating beam splitter with 70 lines/mm was placed in front of the Hamamatsu CMOS camera to measure the effect of the adsorption of the thiol molecules on the spectral shift of single AuNRs.

Results and Discussion

In DIC microscopy, the incident light beam is split into two orthogonal bright and dark polarization directions. In the previous study, we showed that DIC polarization anisotropy P is conveniently computed from the bright and dark intensities from the DIC image of a single AuNR. The DIC polarization anisotropy P is defined in eq 1:[24]

$$P = \frac{I_{\mathrm{B,N}} - I_{\mathrm{D,N}}}{I_{\mathrm{B,N}} + I_{\mathrm{D,N}}} \qquad (1)$$

where $I_{\mathrm{B,N}}$ and $I_{\mathrm{D,N}}$ are the normalized bright and dark intensities at the illumination wavelength, respectively.

In the present work, we first correlated the orientations of individual AuNRs (25 nm × 73 nm) measured by DIC polarization anisotropy with those determined from polarization-sensitive DF scattering imaging. Under the DIC microscope, we measured AuNRs immobilized on a glass slide with 720 nm excitation close to 706 nm the longitudinal SPR of the AuNRs in water (Figure S2). We then carried out polarization-dependent DF scattering imaging for the same AuNRs by rotating the polarizer from 0° to 360° in 10° increments.

It is well established that the scattering light from a single AuNR is strongly polarized along the long axis of the nanorod.[21] Figure 1 shows the correlated DIC and DF scattering images of the same AuNRs. We defined the orientation angles θ and ψ as illustrated in Figure 1A. The angle between the polarizing axis and the bright (or dark) axis is set to be 45°. The scattering intensities for the two AuNRs marked by the blue and red squares are plotted as a function of orientation angle ψ (Figure S3). For the two AuNRs, the orientation angle θ for AuNR 1 and AuNR 2 was θ_{DF}=61° and θ_{DF}=169°, respectively. Their almost orthogonal orientations can be clearly observed in the dark and bright DIC images in Figure 1A and we determined values of θ_{DIC}=64° for AuNR 1 and θ_{DIC}=161° for AuNR 2. Therefore, we found a good agreement in orientation angles measured by the two methods.

To confirm this with a statistically meaningful dataset, we obtained the correlated DIC and DF images (Figure S4) and measured the orientation angles for 20 additional AuNRs. Figure 2 shows the correlation of orientation angles determined independently by DIC polarization anisotropy and DF scattering. The good correlation between the orientation angles obtained from the two techniques validates that the orientation of single AuNRs can be accurately determined by DIC polarization anisotropy with 720 nm excitation.

We simulated the absorption spectra of AuNR with a varying refractive index (*n*) for the surrounding medium. λ_{max} of AuNR red-shifted with increasing *n* from air to oil (Figure S5), which is consistent with the previous reports.[14,25] It should be noted that the effect on the longitudinal SPR mode is much more pronounced as a function of *n*, clearly shown in the plot of λ_{max} *vs*. *n*. Moreover, the biomolecular biding event in complex biological systems such as living cells can result in a further longitudinal SPR peak shift since the adsorbed molecules have a higher *n* than the surrounding environment.[26] On the contrary, the transverse SPR mode of AuNR is much less sensitive to those and thus gives a more reliable measurement of the AuNR orientation in complex biological systems, providing a sufficiently high signal-to-noise ratio is obtainable

To test if the transverse SPR mode also provides accurate orientation measurements in a DIC microscope, we measured AuNRs fixed on a glass slide with both

540 nm and 720 nm excitation wavelengths. To investigate the dependence of DIC intensities of AuNRs on the orientation angle θ at the two SPR wavelengths, we rotated the sample by 5° or 10° increments per step. The bright and dark intensities for the AuNR in Figure 3A were anti-correlated for each wavelength. Furthermore, as expected, DIC intensities in the bright polarization direction from two SPR wavelengths were also anti-correlated as shown in Figure 3A, that is, an increase in the bright intensity at 720 nm excitation is accompanied by an decrease in the bright intensity at 540 nm, and vice versa. We calculated the experimental *P* values of the AuNR for the two SPR wavelengths. As shown in Figure 3B, the experimental *P* values for 720 nm agree well with both the *P* values for 540 nm and the calculated *P* values. Clearly, DIC polarization anisotropy using the transverse SPR excitation and the longitudinal SPR excitation simultaneously allows for accurate and reliable measurements of AuNR orientations.

It is crucial to confirm that the transverse SPR mode can be used to track rotational dynamics of AuNR in biological systems. Since AuNRs are considered an attractive candidate for nanocarriers in drug delivery systems, we chose AuNRs on live cell membranes as a model system. This model system is important because it will allow us to elucidate the mechanisms on cellular uptake, drug delivery, and endocytosis. We employed a dual-view DIC microscope as shown in Figure S1, which is operated at two SPR wavelengths simultaneously. The dual-wavelength DIC detection is necessary to allow the correlation of the two SPR wavelengths in the dynamic tracking experiment. To accomplish the aforementioned, we used a Photometrics dual-view filter with a 565 nm dichroic filter and two band-pass filters corresponding to the two SPR wavelengths.

We recorded a movie showing rotational dynamics of transferrin-modified AuNRs on a live cell membrane at 32 frames s^{-1} (Movie 2 in the Supporting Information). Figure 4A shows a dual-view DIC image of transferrin-modified AuNRs rotating on a live cell membrane, measured at 540 nm (left) and 720 nm (right) simultaneously. Such a measurement cannot be achieved by other optical methods, including DF scattering. The DIC polarization anisotropy of the AuNR rotating on a live cell membrane was computed for two wavelengths and randomly distributed between –1 and 1 as shown in Figure 4B. DIC images of the AuNR 4 at five chosen frames of 12, 16, 56, 80, and 115 for two SPR wavelengths are demonstrated in Figure 4B and anti-correlated images in the two SPR wavelengths are observed. It is worth noting that the experimental *P* values obtained from 720 nm excitation wavelength are in good agreement with those computed from 540 nm excitation wavelength during the dynamic process (Figure 4B). Therefore, the transverse SPR mode provides

The scattering cross-section decreases as $1/R^6$, where R is the radius of a gold nanosphere (AuNS), while absorption cross-section decreases as $1/R^3$ that scales with the volume of an AuNS.[27] In this respect, absorption is capable of giving much higher signal and resolution for AuNS less than 30 nm in diameter. In contrast, it is difficult to measure AuNS smaller than 30 nm in diameter with DF scattering-based method. A DIC microscopy works on the principle of interferometry to gain information about the optical path length of the sample. In the previous study, we performed the size dependence of DIC intensity of AuNS with diameters ranging from 20 nm to 80 nm at 550 nm.[28] Their contrast increased with an accelerating trend when their size increases. For AuNS smaller than 40 nm, they were detectable in the range between 510 nm and 560 nm. We found that DIC intensity (or contrast) decreases as ~$1/R^3$, which is similar to the trend shown in the absorption-based photothermal imaging method (Figure S6). Therefore, a DIC microscope provides a good sensitivity for measuring the smaller AuNS and it was allowed to detect AuNR (25 nm × 73 nm) rotating on a live cell membrane at 540 nm.

The longitudinal SPR wavelength at 720 nm provides much better signal of AuNR on a live cell membrane (Figure S7). However, the longitudinal SPR of AuNR is very sensitive to *n* of surrounding medium, aspect ratio (AR) of AuNR, and the adsorption of molecules, resulting in the spectral shift directly related to DIC signal.[14,25,26] This means that the excitation wavelength needs to be changed for measuring AuNRs with different ARs. Moreover, if biomolecules are bound to the surface of AuNR in complex biological systems, the longitudinal SPR peak will be shifted, which directly affects the signals from the AuNR. In this respect, it is advantageous to use the transverse SPR mode in studying fast rotational dynamics of AuNRs over time in biological systems.

To clearly demonstrate the need and advantage of using the transverse SPR mode, we carried out an experiment to see the biomolecular biding effect on the DIC intensities under a dual-view DIC microscopy. It is well known that 1-decanethiol has a strong preference for the adsorption onto the surface of AuNRs and it becomes dehydrogenated during the adsorption process.[29] Figure 5 demonstrates DIC images of immobilized AuNRs taken before (A) and 20 minutes after addition of 1-decanethiol (B). The DIC intensity of AuNR 5 at 540 nm were mostly insensitive to the adsorption of 1-decanethiol (Figure 5C). In contrast, DIC intensity of the AuNRs at 720 nm were much more sensitive to the addition of 1-decanethiol and it was 1.6 times increased for the AuNR 5 (Figure 5D). The change in the intensity at 720 nm can be explained by the spectral shift of longitudinal SPR peak, induced by the change in *n* with the adsorption of the thiol molecules onto the AuNRs.

The effect of the adsorption of the thiol molecules on the spectral shift of single AuNRs, which resulted in the change of the DIC intensities, was further studied by DF microscopy. We placed a transmission grating beam splitter with 70 lines/mm in front of the Hamamatsu CMOS camera. This transmission grating allowed one portion of the incoming scattering light to form the zero-order image and dispersed another portion of the light to form the wavelength-resolved first-order image. Both the zero-order and first-order images can be captured by the camera. It can be seen that the zero-order image from an individual AuNR is a focused spot and the first-order image is a long streak. If the number density of AuNR spots on the substrate is not very high, there will be no overlap between zero-order and first-order images of different AuNRs and they can be readily separated. Figure 6A shows the zero-order and the first-order images of AuNR 6 taken before and 20 minutes after addition of the 1-decanethiol. The longitudinal SPR wavelength of AuNR 6 was red-shifted by ~30 nm due to the adsorption of the thiol molecules after 20 minutes (Figure 6B). The red-shift is also observed by an eye in the corresponding first-order images of Figure 6A. We also found that the scattering intensity of AuNR 6 was decreased with the adsorption of the thiol molecules after 20 minutes (Figure 6C). This can be explained by chemical damping resulting from the adsorption of thiols onto the surface of the AuNR (chemical effect), which is poorly understood so far when comparing to other decay processes such as bulk metal damping, electron-surface scattering, and radiation damping.[30] Therefore, it is beneficial to use the transverse SPR mode in probing orientations of AuNRs over time in biological systems. To the best of our knowledge, this is the first report of the live-cell video-rate tracking of rotational dynamics of AuNRs using the transverse SPR mode.

Conclusions

The accurate AuNR orientation measurement by DIC polarization anisotropy was verified by the correlation between the orientation angles of randomly oriented AuNRs as determined by DIC polarization anisotropy and polarization-sensitive DF scattering imaging. More importantly, we introduced dual-view DIC microscopy-based polarization anisotropy measurement of rotational dynamics of individual AuNRs at both longitudinal and transverse SPR wavelengths. We demonstrated that DIC polarization anisotropy simultaneously obtained from the two SPR wavelengths showed a good agreement during the dynamic process of AuNRs on a live cell membrane. This verifies that the transverse SPR mode, which is much less sensitive to its surrounding medium and the adsorption of biomolecules, can be employed in DIC microscopy for probing the fast dynamics of individual AuNRs in biological systems. Therefore, we showed the possibilities of using the transverse SPR mode in a DIC microscope to track the fast rotational dynamics of individual AuNR in or on living cells.

References

1. Suri, S. S.; Fenniri, H.; Singh, B. *J. Occup. Med. Toxicol.*, **2007**, *2*, 16–21.
2. Ferrari, M. *Nat. Rev. Cancer*, **2005**, *5*, 161–171.
3. Xu, P. S.; Van Kirk, E. A.; Zhan, Y. H.; Murdoch, W. J.; Radosz, M.; Shen, Y. Q. *Angew. Chem. Int. Ed.* **2007**, *46*, 4999–5002.

4. Kisak, E. T.; Coldren, B.; Evans, C. A.; Boyer, C.; Zasadzinski, Z. A. *Curr. Med. Chem*. **2004**, *11*, 199–219.

5. Wu, W., Wieckowski, S.; Pastorin, G.; Benincasa, M.; Klumpp, C.; Briand, J. –P.; Gennaro, R.; Prato, M.; Bianco, A. *Angew. Chem. Int. Ed*. **2005**, *44*, 6358–6362.

6. Paleos, C. M.; Tsiourvas, D.; Sideratou, Z.; Tziveleka, L. *Biomacromolecules* **2004**, *5*, 524–529.

7. Veiseh, O.; Gunn, J. W.; Zhang, M. *Adv. Drug. Deliv. Rev*. **2010**, *62*, 284–304.

8. Cho, Y.; Shi, R.; Borgens, R. B.; Ivanisevic, A. *Nanomedicine* **2008**, *3*, 507–519.

9. Gole, A.; Murphy, C. J. *Chem. Mater.* **2004**, *16*, 3633–3640.

10. Shiotani, A.; Mori, T.; Niidome, T.; Niidome, T.; Katayama, Y. *Langmuir* **2007**, *23*, 4012–4018.

11. Yu, C.; Varghese, L.; Irudayaraj, J. *Langmuir* **2007**, *23*, 9114–9119.

12. Thierry, B.; Ng, J.; Krieg, T.; Griesser, H. J. *Chem. Commun.* **2009**, 1724–1726.

13. Murphy, C. J.; Gole, A. M.; Stone, J. W.; Sisco, P. N.; Alkilany, A. M.; Goldsmith, E. C.; Baxter, S. C. *Acc. Chem. Res.* **2008**, *41*, 1721–1730.

14. Link, S.; Mohamed, M. B.; El-Sayed, M. A. *J. Phys. Chem. B* **1999**, *103*, 3073–3077.

15. Oyelere, A. K.; Chen, P. C.; Huang, X.; El-Sayed, H. E.; El-Sayed, M. A. *Bioconjugate Chem.* **2007**, *18*, 1490–1497.

16. Wijaya, A.; Schaffer, S. B.; Pallares, I. G.; Hamad-Schifferli, K. *ACS Nano* **2009**, *3*, 80–86.

17. Takahashi, H.; Niidome, Y.; Yamada, S. *Chem. Commun*. **2005**, 2247–2249.

18. Huang, X.; Jain, P. K.; El-Sayed, I. H.; El-Sayed. M. A. *Lasers Med. Sci*. **2008**, *23*, 217–228.

19. Sönnichsen, C.; Alivisatos, A. P. *Nano Lett.* **2005**, *5*, 301–304.

20. Pierrat, S.; Hartinger, E.; Faiss, S.; Janshoff, A.; Sönnichsen, C. *J. Phys. Chem. C.* **2009**, *113*, 11179–11183.

21. Xiao, L.; Qiao, Y.; He, Y.; Yeung, E. S. *Anal. Chem.* **2010**, *82*, 5268–5274.

22. Chang, W. –S.; Ha, J. W.; Slaughter, L. S.; Link, S. *Proc. Natl. Acad. Sci. U.S.A*. **2010**, *107*, 2781–2786.

23. Wang, G.; Sun, W.; Luo, Y.; Fang, N. *J. Am. Chem. Soc*. **2010**, *132*, 16417–16422.

24. Ha, J. W.; Sun, W.; Wang, G.; Fang, N. *Chem. Commun*. **2011**, *47*, 7743–7745.

25. Lee, K. S.; El-Sayad, M. A. *J. Phys. Chem. B* **2005**, *109*, 20331–20338.

26. Willets, K. A.; Van Duyne, R. P. *Annu. Rev. Phys. Chem*. **2007**, *58*, 267–297.

27. van Dijk, M. A.; Tchebotareva, A. L.; Orrit, M.; Lippitz, M.; Berciaud, S.; Lasne, D.; Cognet, L.; Lounis, B. *Phys. Chem. Chem. Phys*. **2006**, *8*, 3486–3495.

28. Sun, W.; Wang, G.; Fang, N.; Yeung, E. S. *Anal. Chem*. **2009**, *81*, 9203–9208.

29. Subramanian, R.; Lakshminarayanan, V. *Electrochimica Acta* **2000**, *45*, 4501–4509.

30. Hu, M.; Novo, C.; Funston, A.; Wang, H.; Staleva, H.; Zon, S.; Mulvaney, P.; Xia, Y.; Hartland, G. V. *J. Mater. Chem*. **2008**, *18*, 1949–1960.

Figures and Captions

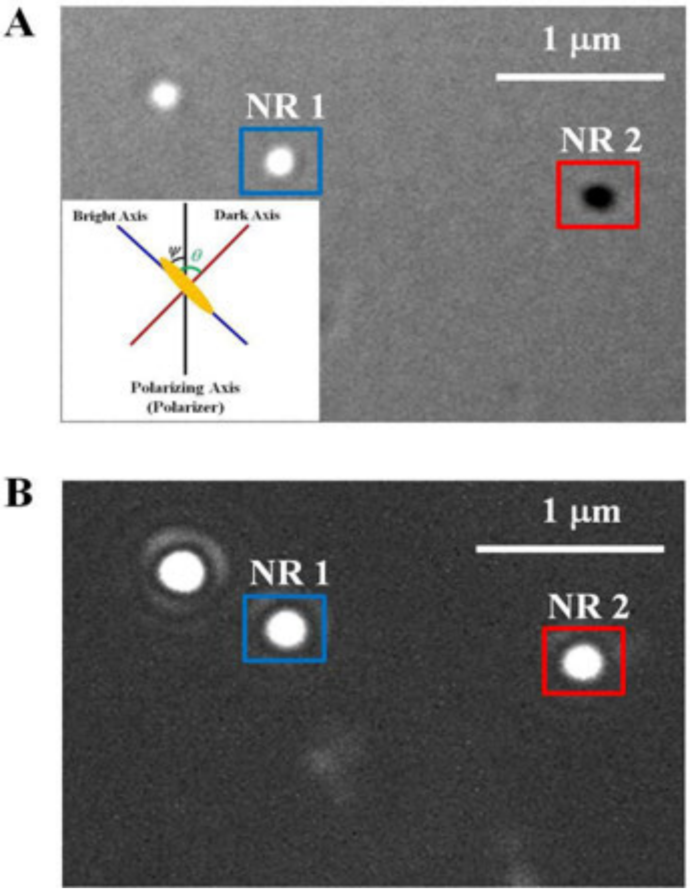

Figure 1. Correlated DIC (A) and DF scattering (B, without polarizer) images of AuNRs with an average size of 25 nm × 73 nm. The inset in Figure 1A shows a schematic of θ and ψ in the coordinate plane.

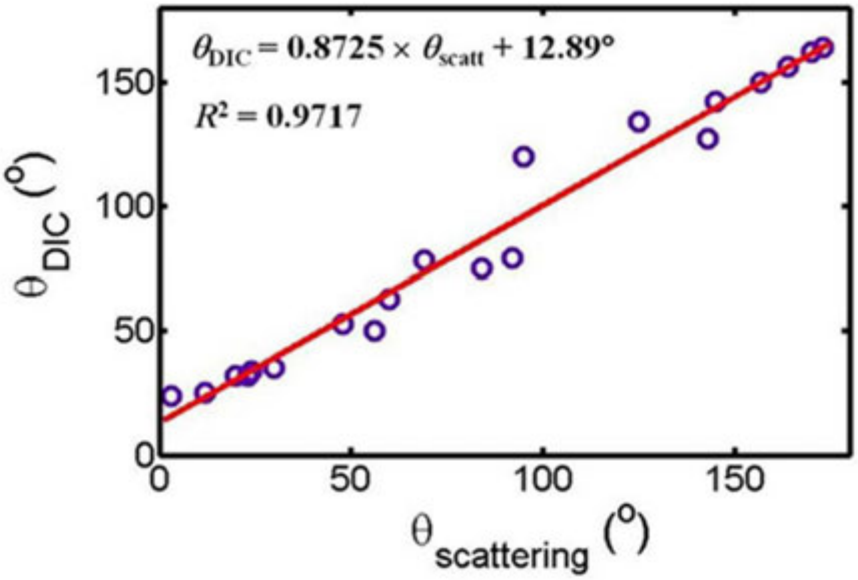

Figure 2. Correlation of orientation angles for 20 AuNRs. AuNR orientations obtained from the DIC polarization anisotropy with 720 nm excitation are in good agreement with the angles determined from DF scattering imaging.

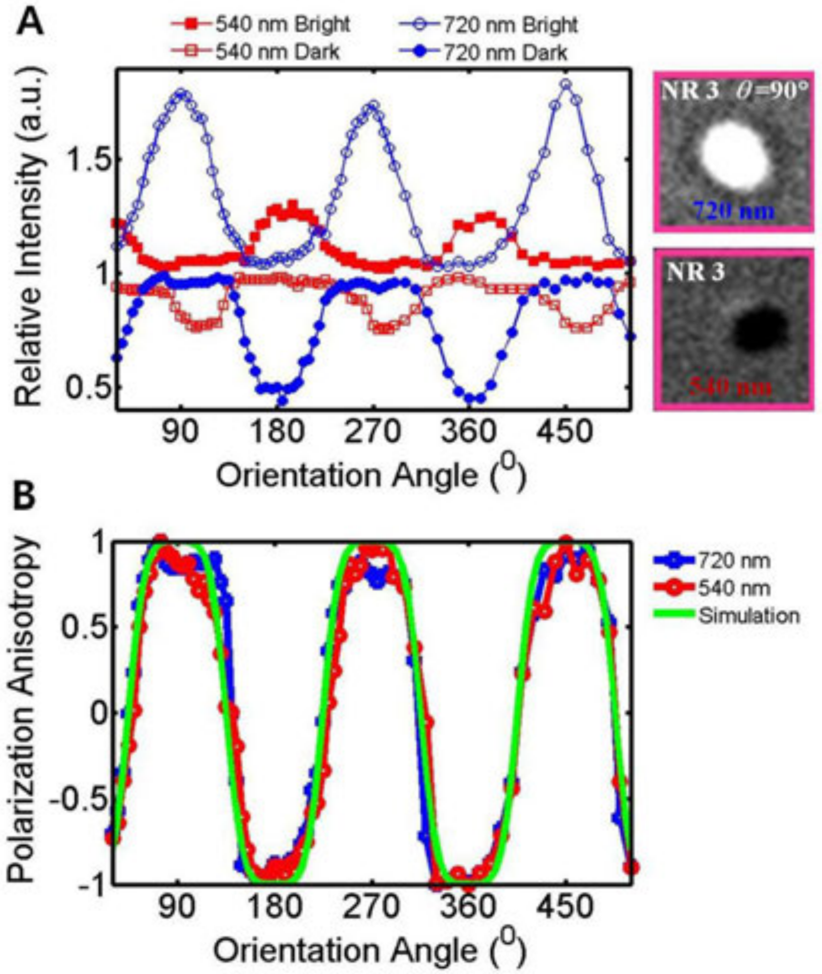

Figure 3. (A) Periodic changes of the bright and dark intensities for the AuNR 3 at two SPR wavelengths. DIC images of the AuNR 3 at θ of 90° are displayed. (B) Polarization anisotropy P for the AuNR 3. The experimental P values for the two SPR wavelengths are compared to the calculated P values as a function of orientation angle θ.

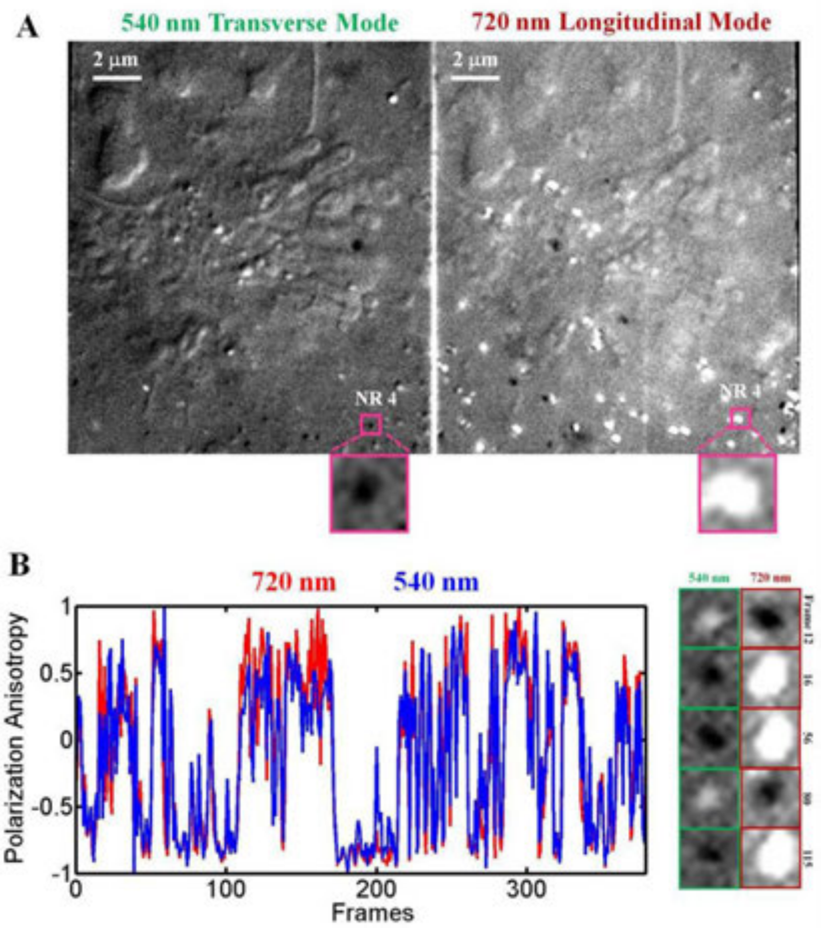

Figure 4. (A) Dual-view DIC image of AuNRs rotating on a live cell membrane. The AuNRs were measured at two SPR wavelengths of 540 nm (left) and 720 nm (right) simultaneously during the fast dynamic process. AuNR 4 is highlighted with a pink square. (B) Polarization anisotropy *P* computed from 720 nm (red) and 540 nm wavelength (blue) for the AuNR 4. DIC images of the AuNR 4 at five chosen frames of 12, 16, 56, 80, and 115, for the two SPR wavelengths are displayed.

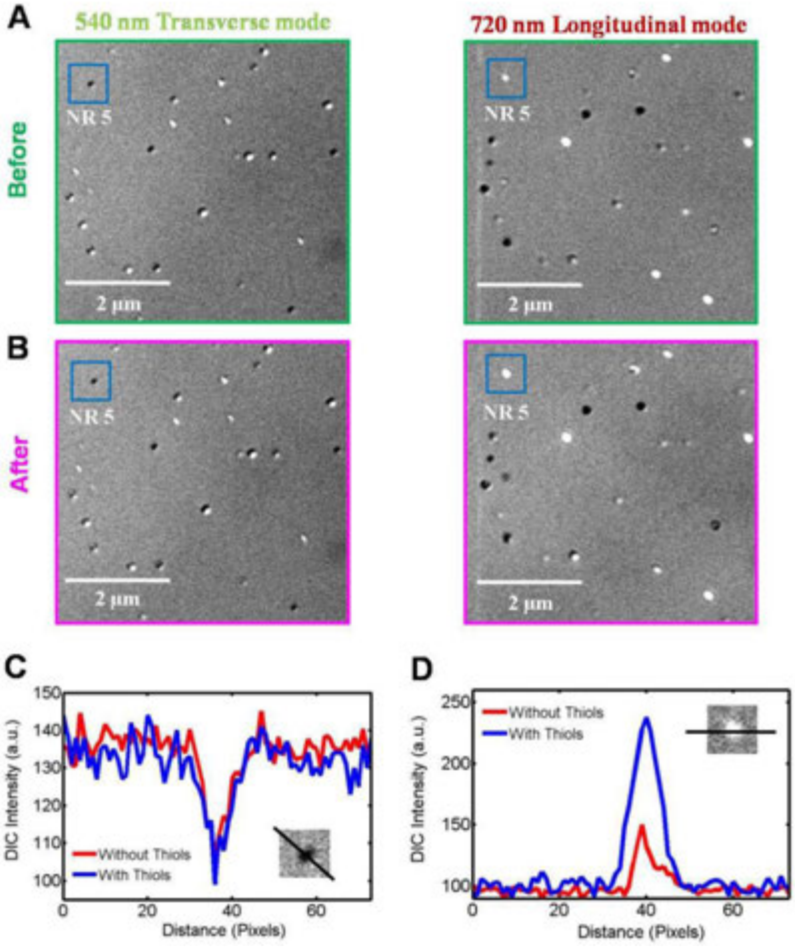

Figure 5. (A) Dual-view DIC image of AuNRs fixed on a glass substrate before addition of 1-decanethiol. The AuNRs were measured at two SPR wavelengths of 540 nm (left) and 720 nm (right) simultaneously. (B) Dual-view DIC image of the same AuNRs, taken 20 minutes after addition of 1-decanethiol. (C, D) Change in the intensity of AuNR 5 before (red) and after addition of the 1-decanethiol (blue), measured at 540 nm (C) and 720 nm (D). Inset images show the direction of the line scan across the AuNR for obtaining the intensity profiles.

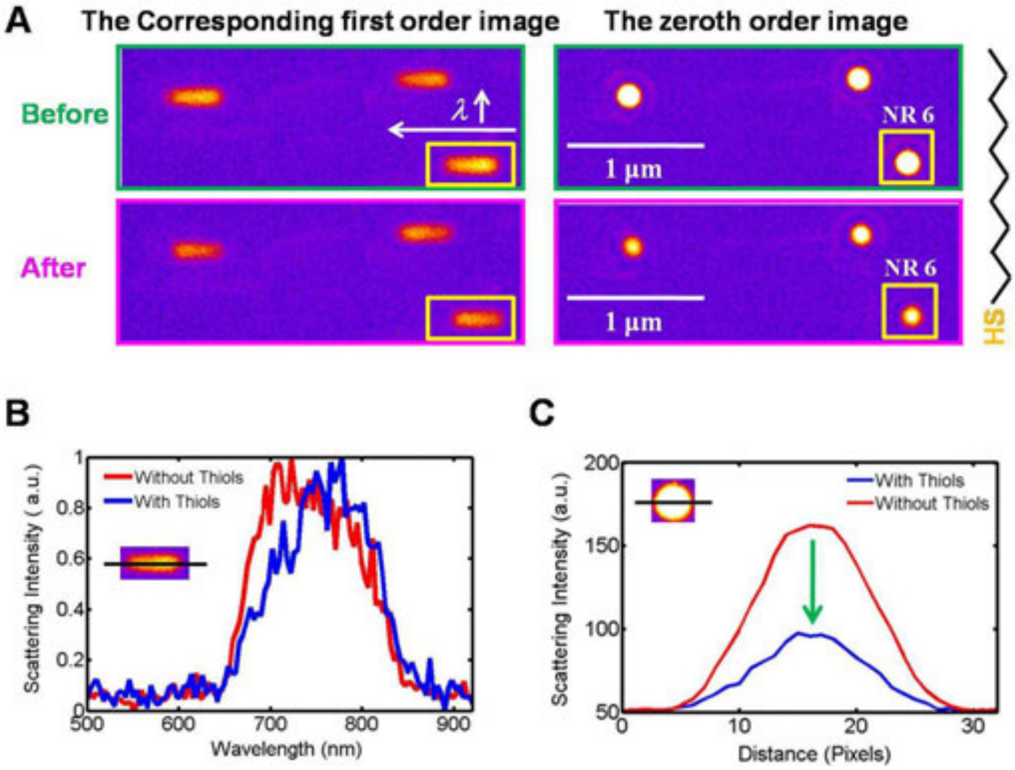

Figure 6. (A) Zeroth- and first-order DF scattering image of single AuNRs before (top, green) and after addition of 1-decanethiol (bottom, pink). The λ increases from right to left in the first-order image. (B) Normalized- and overlaid-scattering spectra of the AuNR 6 taken before (red) and after addition of 1-decanethiol (blue). (C) Change in scattering intensities of AuNR 6 after addition of 1-decanethiol. Inset images show the direction of the line scan for obtaining the intensity profiles.

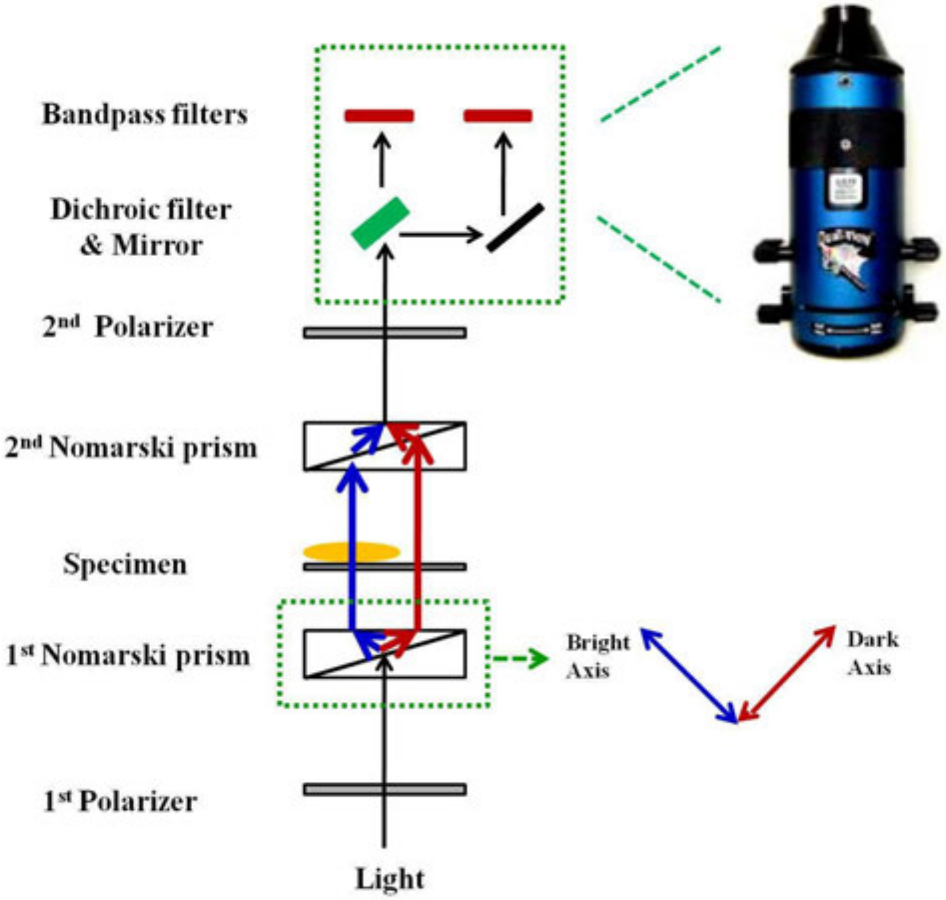

Figure S1. Setup for dual-view DIC microscopy used in this experiment. A MAG Biosystems dual-view filter with a 565 nm dichroic filter and two bandpass filters corresponding to the two SPR wavelengths of 540 nm and 720 nm are used.

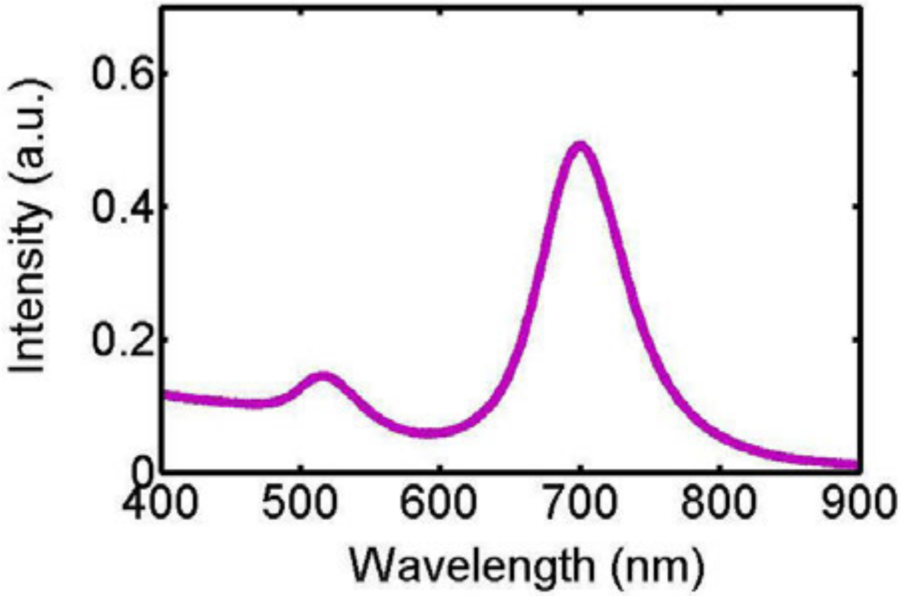

Figure S2. Ensemble extinction spectrum of AuNRs (25 nm × 75 nm) measured in water. Two broad transverse and longitudinal SPR bands appear at 520 nm and 706 nm, respectively.

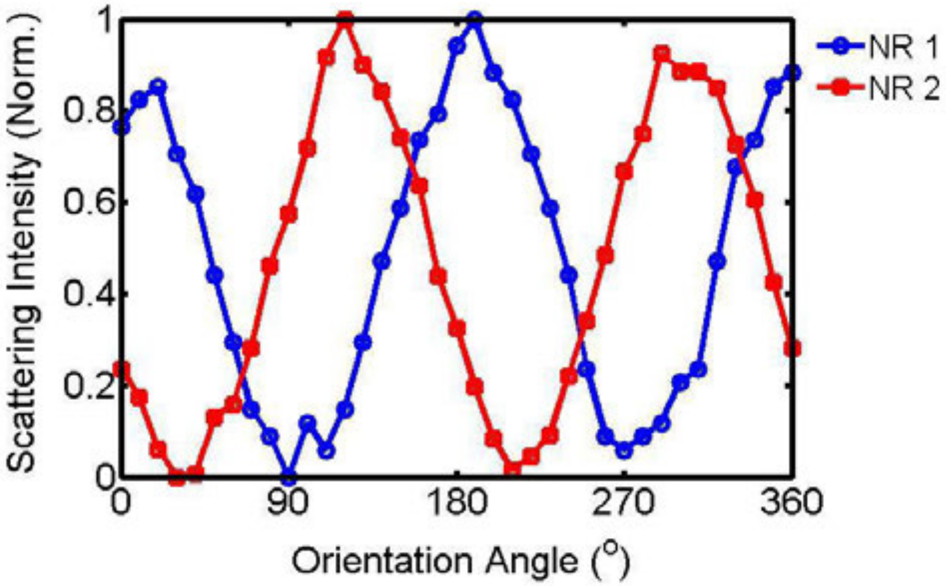

Figure S3. Scattering intensity traces for AuNR 1 (blue) and AuNR 2 (red) as a function of orientation angle ψ. We changed the polarization from 0° to 360° in 10° increments.

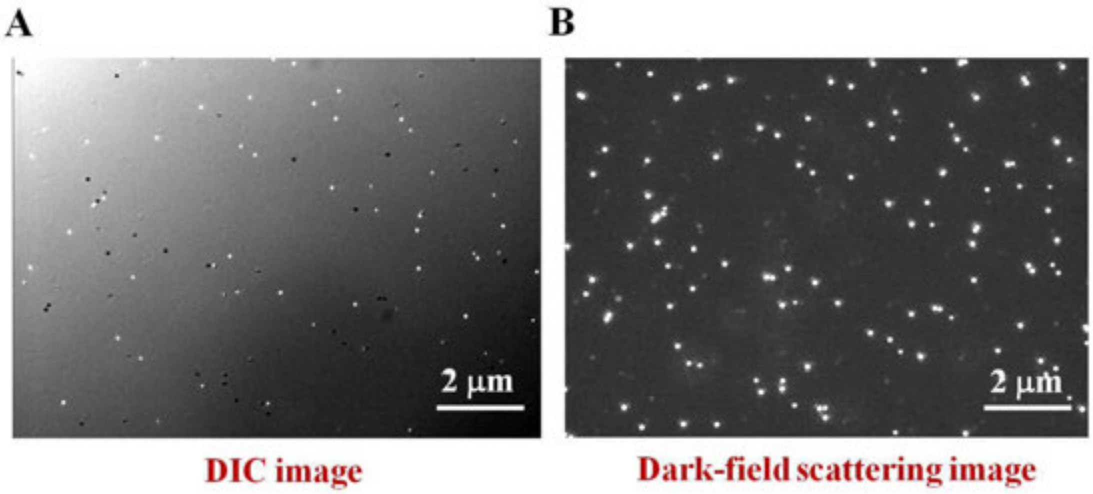

Figure S4. Correlated DIC (A) and DF (B, without polarizer) images for same AuNRs. The DIC image was taken at 720 nm excitation. 20 AuNRs in the image were used for the correlation of orientation angles determined from DIC polarization anisotropy and polarization-sensitive DF scattering imaging.

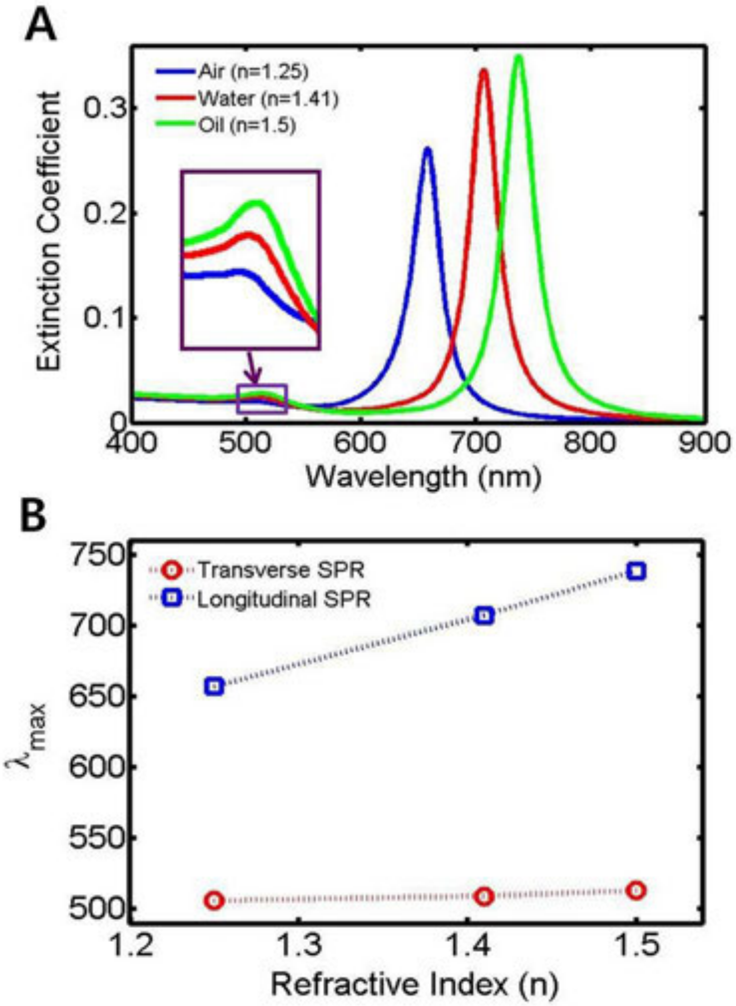

Figure S5. (A) Simulated absorption spectra of AuNR with changing the refractive index (n) of surrounding medium. (B) The absorption maximum (λ_{max}) as a function of n for the longitudinal SPR mode (blue) and the transverse SPR mode (red). λ_{max} of AuNR red-shifts with increasing n from air (n=1.25, an average between air and glass) to oil (n=1.5). The aspect ratio was fixed at a value of 3 same as the average aspect ratio of AuNRs measured in this study.

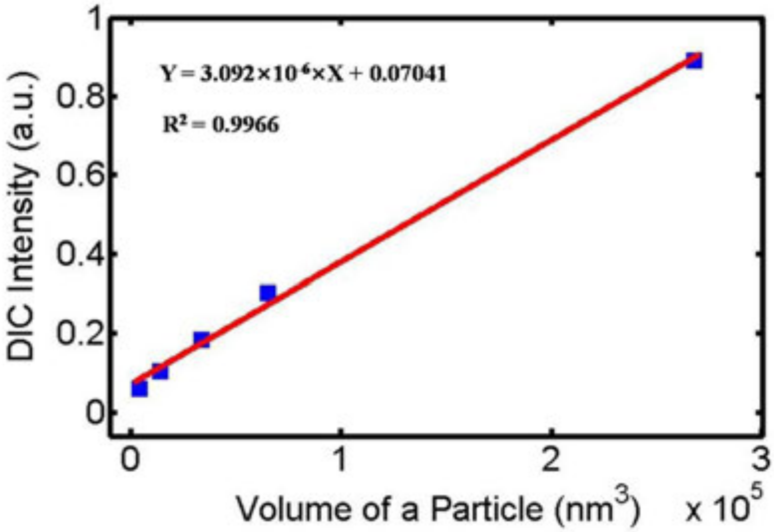

Figure S6. Size dependence of DIC intensity of gold nanospheres (AuNSs) with diameters of 20 nm, 30 nm, 40 nm, 50 nm, 80 nm. The AuNSs were measured at 550 nm. DIC intensities for each size are as follows: 20 nm - 0.061, 30 nm - 0.104, 40 nm - 0.183, 50 nm - 0.304, 80 nm - 0.891. The R^3 dependence of DIC intensity on size is shown, where R is the radius of a particle. Red-line is a linear fit to data points.

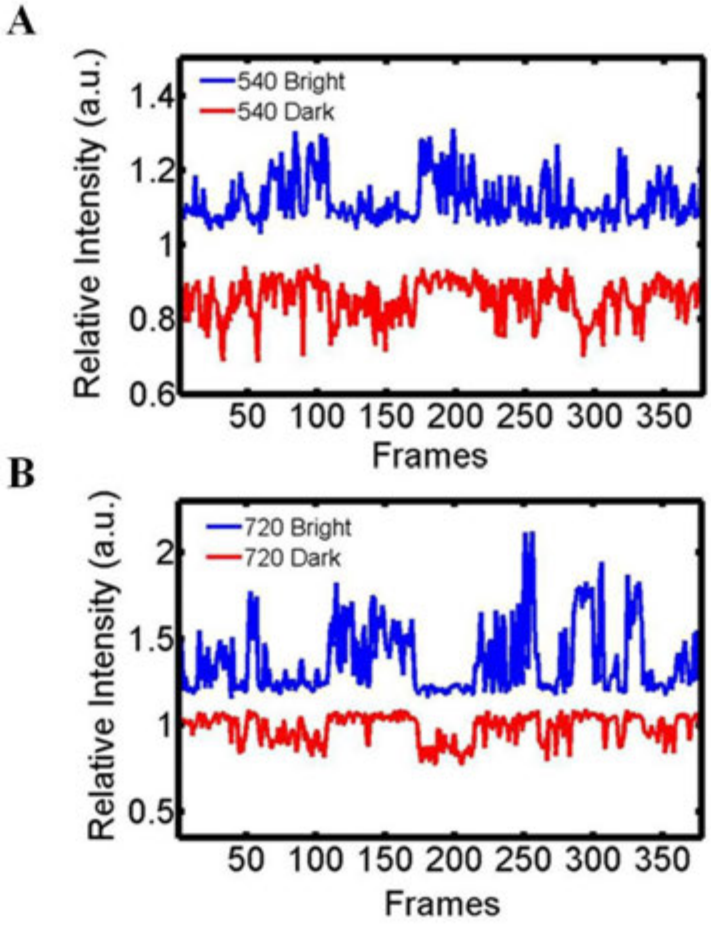

Figure S7. Time traces of measured DIC intensities in the bright (blue) and dark (red) polarization directions for the AuNR 4 in Figure 4 during the rotational dynamic process. DIC intensities were measured at two SPR wavelengths of 540 nm (A) and 720 nm (B) simultaneously. The bright and dark intensities are anti-correlated for each wavelength.

Supplementary Materials

Calculation of Optical Absorption Spectra of AuNRs. We used Gans theory with the known dielectric function for gold to simulate the optical absorption spectra of randomly oriented AuNR colloids by varying the refractive index of surrounding medium (n). According to Gans theory, the extinction coefficient γ of randomly oriented particles in the dipole approximation is given by

$$\gamma = \frac{2\pi N V \varepsilon_m^{3/2}}{3\lambda} \sum_j \frac{(1/P_j^2)\varepsilon_2}{(\varepsilon_1 + \frac{1-P_j}{P_j}\varepsilon_m)^2 + \varepsilon_2^2} \qquad (1)$$

N: the number of particles per unit volume

V: the volume of each particle

ε_m: the dielectric constant of the surrounding medium, ε_m is equal to n^2

λ: the wavelength of the interacting light

ε_1 and ε_2: the real and complex part of the material dielectric function

P_j: the depolarization factors for the three axes A, B, C of the rod with $A>B=C$

$$P_A = \frac{1-e^2}{e^2}\left[\frac{1}{2e}\ln\left(\frac{1+e}{1-e}\right)-1\right] \qquad (2)$$

$$P_B = P_C = \frac{1-P_A}{2} \qquad (3)$$

$$e = \sqrt{1-\left(\frac{B}{A}\right)^2} \qquad (4)$$

Eq 1 for γ was plotted as a function of n while the aspect ratio (A/B) of AuNRs was fixed to a value of 3 same as the average aspect ratio of AuNRs measured in this study.

Determination of Orientation Angle θ from DIC Polarization Anisotropy *P*. In DIC microscopy we obtain two orthogonal intensities in the bright and dark polarization directions at the illumination wavelength. In the previous study, we derived an equation that relates DIC polarization anisotropy *P* to the orientation angle θ of AuNRs:

$$\begin{aligned} \theta &= \operatorname{acos}\left(\sqrt{\frac{A-\sqrt{A^2-2A}}{2}}\right), \qquad P<0 \\ \theta &= \operatorname{acos}\left(\sqrt{\frac{A+\sqrt{A^2-2A}}{2}}\right), \qquad P>0 \end{aligned} \tag{5}$$

where *A* is defined as (*P*-1)/*P*. Therefore, we used eq 5 to deduce the orientation angle θ backward from the measurement of DIC polarization anisotropy *P*. It is worthwhile to note that DIC polarization anisotropy *P* is distributed from -1 to 1 and we cannot distinguish the orientation angle between π-θ and θ having a same *P* value. However, by correlating with the orientation angles of individual 20 AuNRs determined from DF scattering imaging, we were able to overcome the limitation and determine the true orientation angles from 0° to 180° by DIC polarization anisotropy.

CHAPTER 4. DETERMINING THE FULL THREE-DIMENSIONAL ORIENTATION OF SINGLE ANISOTROPIC NANOPARTICLES BY DIFFERENTIAL INTERFERENCE CONTRAST MICROSCOPY

Lehui Xiao,[+] Ji Won Ha,[+] Lin Wei, Gufeng Wang, and Ning Fang*

A paper published in *Angewandte Chemie Internatial Edition* 2012, 51, 7734-7738.

Reproduced by permission of the Wiley-VCH

[+] These authors contributed equally to this work

* Corresponding author

Abstract

Plasmonic gold nanorods (AuNRs) have been used as orientation probes in optical imaging because of their shape-induced anisotropic optical properties.[1] However, current optical imaging techniques lack the capability to decipher the full three dimensional (3D) orientation of *in-focus* gold nanorods in the four quadrants of the Cartesian plane. Resolving the mirror angles and determining the accurate rotational modes of the gold nanorod are critical in biological observations because the chirality of biological macromolecules and their assemblies, e.g., right- or left-handed helices, is fundamental in biology. Herein, we overcome this limitation by combining differential interference contrast (DIC) microscopy image pattern recognition with DIC polarization anisotropy analysis to resolve the exact azimuthal angles (from 0° to 360°) as well as the polar angles of tilted AuNRs that are positioned in the focal plane of the objective lens without sacrificing the spatial and temporal resolution. The rotational direction of individual in-focus AuNRs can thus be tracked dynamically. Finally, we successfully monitored the

real-time rotational behavior of transferrin-modified gold nanorods on live cell membranes.

Introduction

Many biological processes involve rotational motion at the nanoscale, e.g., RNA folding,[2] walking of molecular motors,[3] twisting of dynamin assembly,[4] and self-rotation of ATPase,[5] etc. Tracking the rotational motion with optical probes is of great importance to understanding these processes in biological and engineered environments. Fluorescence anisotropy has been commonly attempted to probe the rotational motion of biomolecules using organic dyes, conjugated polymers, and inorganic semiconductor nanocrystals.[6] Nevertheless, the major disadvantages of current fluorescent orientation probes are stochastic transition between on and off states,[7] high photobleaching tendency,[7a,8] and less-than-desirable biocompatibility,[9] limiting their use in biological systems.

Recently, AuNRs are gaining considerable attention as suitable orientation probes because of their shape-induced anisotropic optical properties,[1a-c] large scattering and absorption cross-sections resulted from the surface plasmon resonance (SPR) effect, high photo- and chemical-stability, and excellent biocompatibility.[10] Scattering- and absorption-based polarization anisotropy measurements of AuNRs have been carried out under dark-field (DF) microscopy[1a] and photothermal heterodyne imaging.[1d] These methods were successfully used to measure the orientation of AuNRs. However, in these methods, only in-plane orientation information is effectively obtained while the out-of-plane orientation is still ambiguous. Furthermore, their applicability for studies of fast dynamics in live cells is limited. It is challenging for DF microscopy to differentiate AuNRs from other highly scattering cellular components. Photothermal heterodyne imaging requires rapid scanning of the sample to collect an image and comprehensive intensity and polarization modulation of the heating beam.

DIC microscopy is better suited to probe orientation and rotational motion of nanoobjects in live cells when used in combination with plasmonic AuNRs.[1e] DIC microscopy resolves the optical path difference between two mutually orthogonally polarized beams separated by a shear distance along the optical axis of a Nomarski prism (Figure S1). The interference nature makes it insensitive to the scattered light from surrounding cellular components and keeps its high-throughput capability. Therefore, the DIC microscopy-based single particle orientation and rotational tracking (SPORT) technique is more applicable to the studies of fast rotational dynamics in live cells.

When plasmonic nanoparticles are illuminated under an optical microscope, the incident electromagnetic wave is commonly attenuated through absorption and scattering.[11] The attenuation at a given wavelength is quantified by the corresponding cross-section. Typically, when a AuNR is excited by monochromatic light at the longitudinal SPR wavelength, the scattered electromagnetic field can be simplified as generated from a single dipole with the oscillation direction along its principal axis, provided that the nanorod is much smaller than the wavelength of light.[11] The DIC image of AuNR is resulted from the interference of two mutually shifted, phase-delayed, and orientation-dependent scattering images. Quantitatively, the relative bright and dark intensities of AuNR can be simplified into Eq. 1 (see details in Supporting Information):

$$I_{\mathrm{B}} - I_0 \propto \cos^2(\varphi)\sin^2(\theta) \quad (1)$$

$$I_0 - I_{\mathrm{D}} \propto \sin^2(\varphi)\sin^2(\theta)$$

where I_0 is the background intensity, I_{B} and I_{D} are the bright and dark intensities, respectively, and φ and θ are the azimuthal and polar angles defined in Figure 1A. The bright and dark intensities are the projections of the dipole onto the bright and dark polarization directions, respectively. Therefore, the angular-dependent DIC intensities can be used to extract the information on the AuNR's orientation. The DIC polarization anisotropy P, which is defined in Eq. 2,[12] can be conveniently computed from the orthogonally polarized bright and dark intensities in a DIC image at the longitudinal SPR wavelength:

$$P = \frac{I_{\mathrm{B,N}} - I_{\mathrm{D,N}}}{I_{\mathrm{B,N}} + I_{\mathrm{D,N}}} \qquad (2)$$

where $I_{\mathrm{B,N}}$ and $I_{\mathrm{D,N}}$ are normalized relative bright and dark intensities (Eq. 1), respectively. Obviously, the DIC polarization anisotropy is only dependent on the azimuthal angle of φ, while the sum value of the relative bright and dark intensities is purely related with the polar angle of θ. By determining the DIC polarization anisotropy and sum value of the bright and dark parts from the DIC image, the rotational dynamics of individual AuNR then could be readily quantified. Further error estimation for the azimuthal and polar angle determination based on the above calculations is shown in Figure S2.

The mirror effect in angular determination for a AuNR is currently the major challenge of the previously reported DIC microscopy-based technique[1e,12] as well as other polarization-based techniques for resolving the exact 3D orientation of AuNRs in the focal plane of the objective lens. In the previous study,[1e] we used the absolute bright and dark intensities directly to determine the AuNR orientation, which could only resolve the orientation angle from one of the four quadrants, that is, from 0° to 90°. In addition, although the DIC polarization anisotropy using an intensity ratio instead of absolute intensities provides a more reliable and accurate angle measurements of a AuNR in dynamic studies, it still cannot distinguish those mirror orientation angles (i.e. φ, π-φ, $\pi+\varphi$ and 2π-φ are having the same DIC polarization anisotropy value) with respect to the polarization directions of a AuNR.[12,13] Therefore, it is infeasible to rapidly distinguish the ambiguous rotational motions, e.g., clockwise or counter-clockwise, of a AuNR in the focal plane. However, the rotational direction is important to unveil the underlying mechanisms of many biological processes as chiral biological macromolecules and their assemblies, e.g., right- or left-handed helices, are involved.

In the present study, we for the first time overcome the limitation described above by combining DIC image pattern recognition with DIC polarization anisotropy measurement. We demonstrate that the full 3D orientation information can be extracted for in-focus AuNRs that are tilted with respect to the horizontal object plane.

Experimental Section

Principle of a DIC Microscopy-Based SPORT of Anisotropic AuNR Probes. In DIC microscopy, the incident beam is split into two orthogonally polarized beams in the two bright and dark polarization directions by the first Nomarski prism as shown in Figure S1. When two beams pass through the sample, they generate image contrasts for optical path length gradients in the sample. Therefore, each of the two orthogonally polarized beams generates an independent intermediate image. One such image is shifted laterally by ~100 nm and then overlapped with the other to generate the final interference image. For anisotropic shape of AuNRs, the two intermediate images are different because the two illumination beams are phase-delayed to different extents, depending on the orientation of the AuNR relative to the two polarization directions. Therefore, the DIC images of AuNRs appear as diffraction-limited spots with disproportionate bright and dark parts and they show different bright and dark intensities depending on the AuNR orientation. The azimuthal angle of AuNRs is defined as the angle φ between the long axis of a AuNR and the bright axis as shown in Figure S1. The darkest intensity is observed when a AuNR is parallel to the dark polarization axis. When we rotate a rotational stage by 90°, the bright part of DIC image changes to the brightest intensity meaning that it is parallel to the bright polarization axis. The bright and dark intensities are changed periodically as a function of the orientation angle φ and the intensities from bright and dark polarization directions are anti-correlated.

Optical Microscopy. All optical microscopy experiments were performed on an upright Nikon Eclipse 80i microscope in this study. There is no change in the light path or other optical components. The DIC modules are commercially available and they include a pair of Nomarski prisms (for 100×), two standard polarizers, a quarter-wave plate, a Plan Apo oil-immersion objective (100×, N.A. = 1.40), and an oil-immersion condenser (N.A. = 1.40). Band-pass filters (532 nm, 700 nm) with a full width at half-maximum (FWHM) of 10 nm were obtained from Semrock (Newton, NJ) and inserted into the light path in the microscope. A Hamamatsu complementary metal oxide semiconductor (CMOS) camera was employed to record highly detailed DIC images of AuNRs and to record fast dynamics of AuNRs rotating on live cell membranes. In the DF mode, a Nikon Plan Fluor 100× 0.5-1.3 oil iris objective and a Nikon DF oil condenser were adopted.

Sample Preparation and DIC Imaging of AuNRs. AuNRs with an average size of 25 nm × 73 nm were purchased from Nanopartz (Salt Lake, UT). The AuNR colloid solution was first diluted with 18.2-MΩ pure water to a proper concentration. Then the diluted solution was sonicated for 15 min at room temperature. We made a solution containing 1 μm microspheres, 60 nm Au nanospheres, and AuNRs. For the orientation study of AuNRs lying flat on the horizontal plane, a sample was prepared by spin casting of the solution on the pre-cleaned glass slide. Then, a 22 mm × 22 mm No. 1.5 coverslip (Corning, NY) was covered on the glass slide. For the orientation study of AuNRs that are tilted, the AuNRs were embedded in gel-matrix. All gels were prepared by dissolving the desired quantity of gel powder (w/w, 2%) in distilled water by boiling for 5 min on a hotplate. We, then, added the solution containing AuNRs into gels. A sample was prepared by spin casting of the mixture on the well-cleaned glass slide.

The sample glass slide was placed on a 360° rotating mirror holder affixed onto the microscope stge. By rotating the mirror holder 5° per step, the AuNRs were positioned in different orientations. DIC images at 532 nm and 700 nm were taken with the Hamamatsu CMOS camera. In the case of the tilted AuNRs, after rotating by 5° per step we obtained a DIC image stack by scanning in the z-direction that allows us to find the exact focal plane of AuNRs embedded in gel matrix. The collected images and movies were analyzed with MATLAB and NIH ImageJ.

Cell Culture and Sample Preparation of AuNRs on Cell Membranes. A549 human lung cancer cell line (CCL-185) was purchased from American Type Culture Collection (Manassas, VA). The cells were placed in a T25 cell culture flask (Corning) and grown in cell culture medium supplemented with 10 % fetal bovine serum (FBS) in a cell culture incubator (37 °C, 5 % CO_2). When subculturing, 150 μL of cell suspension solution was transferred to a 22 mm × 22 mm poly-L-lysine (PLL)-coated coverslip, housed in a 35-mm Petri dish (Corning). The Petri-dish was left in the incubator for 1 h to let the cells attach to the coverslip. After 1.5 mL of the cell culture medium with 10 % FBS supplement was added to immerse the coverslip, the Petri dish was left again in the incubator for 24 h. AuNRs were diluted in cell culture medium to the proper concentration and incubated with cells for 1 h.

For nanorod modification, a NHS-PEG disulfide linker (Sigma-Aldrich) was used to functionalize the surface of AuNRs with transferrin (Sigma-Aldrich). The NHS-PEG disulfide linker has both disulfide and succinimidyl functionalities for respective chemisorption onto gold and facile covalent coupling of transferrin. Briefly, excessive surfactant was first removed from 1.0 mL AuNR solution by centrifugation at 2000 g for 10 min and the particles were resuspended in 1.0 mL of 2 mM borate buffer. A proper amount of fresh NHS-PEG disulfide solution (in dimethyl sulfoxide) was added to reach a final thiol concentration of 0.2 mM and reacted with AuNRs for 2 h. The solution was then cleaned up by centrifugation and resuspended in 2 mM borate buffer. For transferrin-modified AuNRs, 20 μg of transferrin was added to the gold colloidal solution and reacted for 8 h. The AuNRs were then blocked by adding 100 μL of 10% BSA solution (2 mM borate buffer) for over 8 h. Before use, the colloidal AuNR probes were cleaned up by centrifugation and resuspended in 500 μL of 1% BSA (2 mM borate buffer). The coverslip with cells was put on a glass slide to form the sample slide for imaging.

Orientation of AuNRs Lying Flat on Glass Substrate. We made a solution containing 1 μm microspheres (position reference), 60 nm Au nanospheres (focal plane reference), and AuNRs with an average size of 25 nm × 73 nm. A sample was prepared by spin casting the solution on the pre-cleaned glass slide. This sample preparation strategy ensures the AuNRs lay flat on the glass slide surface. DIC images were taken for the sample at two SPR wavelengths of 532 nm and 700 nm and wavelength-dependent DIC images of AuNRs and Au nanospheres are shown in Figure S6A, allowing us to conveniently identify single AuNRs. The DIC contrast for the AuNR highlighted with green frame is rather weak under the transverse SPR wavelength of 532 nm, while it is greatly enhanced under the longitudinal SPR wavelength of 700 nm. In contrast with the AuNR, Au nanosphere squared with black generated a strong DIC contrast at 532 nm excitation and a very weak contrast at 700 nm. To explore the relationship between DIC image patterns and orientations of AuNRs, a 360° rotation study at 700 nm excitation was carried out by rotating the stage by 5° per step to position the highlighted AuNR in different orientations. The 60 nm Au nanospheres were used as a standard to fix the focal plane after rotating each 5° of the stage and they were measured with 532 nm excitation. The brightest DIC intensity for the AuNR is observed when its long axis is aligned with the bright axis, while the darkest DIC intensity is obtained when it is rotated by additional

90°. We found that the image patterns are changed periodically according to variation in the orientation of the AuNR (Figure S6B). A complete set of DIC images for the AuNR as a function of frames is shown in Figure S7. The orientation angle φ of the AuNR in Frame 1 is around 0° giving the brightest intensity. The normalized bright and dark DIC intensities for the AuNR were well fitted with functions of $\cos^2(\varphi)$ and $\sin^2(\varphi)$, respectively (Figure S8). We further computed the polarization anisotropy P values for the AuNR at each frame. The P values for the AuNR were plotted as a function of frames and were distributed from -1 to +1 depending on the AuNR's orientation relative to the bright and dark polarization directions (Figure S6C).

Procedure for Determining the Orientation of AuNRs in the DIC Image. A DIC image of a AuNR was taken. DIC polarization anisotropy P can be computed from two orthogonal intensities in the bright and dark polarization directions in DIC microscopy and it is used to obtain the orientation angle φ of a AuNR. Due to the optical symmetry effect of P value, the calculated orientation angle φ is between 0° and 90°. For AuNRs that are tilted, there are four points with the same P value. It is notable that there are four distinctive image patterns corresponding to each point as demonstrated in Figure 1. Therefore, after obtaining the orientation angle φ, a DIC image pattern of a AuNR was compared with the unique DIC image patterns library of single AuNR in order to resolve the true orientation angle φ in the four quadrants. Finally, Equations (S11) and (S12) are used to determine the polar angle θ. The angular determination accuracies for azimuthal and polar angles are shown in Figure S2.

Results and Discussion

The light scattered by a tilted anisotropic AuNR has a skewed electromagnetic field distribution containing full-space angular information, which, however, is not resolvable in a single focused fluorescence or DF image. Thus, defocused orientation imaging techniques have been employed to determine 3D orientations of out-of-focus nanoprobes within a single frame.[1b,3,14] The defocused imaging techniques are based on the electric dipole approximation and the fact that the dipole radiation exhibits an angular anisotropy. When a nanoprobe is positioned outside of the focal plane, the intensity distribution of the blurred image provides information about the nanoprobe's emission dipole orientation; however, the standard defocused imaging technique doesn't always yield orientation accurately due to largely reduced signal intensity and it is usually required to switch back and forth between focused and defocused imaging for getting the orientation and localization information simultaneously with precision, which sacrifices the temporal resolution in dynamic tracking experiments. As demonstrated by Toprak *et al*., the temporal resolution was only 1-2 frames per second (fps) due to the much reduced signal intensity from the defocused imaging mode.[3] Therefore, the standard defocused imaging strategy is more suitable for the characterization of static events. On the contrary, in DIC microscopy, the final image is generated from the interference of two mutually shifted, phase-delayed, and orientation-dependent scattering images. Thus, the electromagnetic field distribution is artificially encoded into the DIC point spread function, resulting in identifiable orientation-dependent DIC image patterns for AuNRs in the focal plane. To demonstrate this, we studied the DIC images of tilted AuNRs (25 nm × 73 nm) embedded in 2% agarose gel matrix. The polar angle θ of AuNR 1 (Figure 1B) was first determined to be 14° by using the defocused DF imaging technique (Figure S3).[1b] We, then, obtained the corresponding DIC images of the same AuNRs at 700 nm excitation (Figure 1B). A 360° rotation study was carried out by rotating the stage by 5° per step to position AuNR 1 in different orientations. The exact focal plane of the AuNR was found by scanning in the z-direction with a vertical step size of 69 nm. Based on the positions and intensities of the bright and dark parts in each frame, four distinctive image patterns are found to represent the nanorod orientations in the four quadrants (R1 to R4) of the Cartesian plane (Figure 1C). Figure S4 shows the complete set of DIC images of AuNR 1 at 72 orientations from 0° to 360° with an interval of 5°. The normalized bright and dark DIC intensities for AuNR 1 can be fitted well with the functions in Eq. 1 (Figure S5), thus indicating the good reliability of the dipole approximation applied in this work. Figure 1D shows a plot of the polarization anisotropy as a function of frame for AuNR 1.

The DIC image patterns of AuNRs change as a function of orientation angle because the spatial distribution of the scattered electromagnetic field from AuNRs is closely related with the orientation angles of AuNRs. The light scattered by the tilted AuNR 1 is projected onto slightly different positions on the DIC images after interference to generate different image patterns. The trend in the pattern changes for AuNR 1 is consistent with other AuNRs that are tilted. To further confirm AuNR 1 was a single nanoparticle instead of an aggregate, we determined its scattering spectrum with a transmission grating beam splitter with 70 lines/mm in front of the Hamamatsu complementary metal oxide semiconductor (CMOS) camera in DF mode. This transmission grating allowed one portion of the incoming scattering light to form the zeroth-order image and dispersed another portion of the light to form the wavelength-resolved first-order image. Both the zeroth-order and first-order images can be captured by the camera. The measured longitudinal SPR peak of AuNR 1 appears at 708 nm, which agrees well with the simulated spectrum (Figure 1E). The demonstrated ability to readily distinguish the orientations in the four quadrants (R1 to R4) using the DIC image patterns allows us to resolve the exact azimuthal angle (from 0° to 360°) of an in-focus AuNR in a single DIC image by combining with DIC polarization anisotropy measurement. It is worth noting that the DIC image pattern recognition is only used to identify the exact quadrant in which the AuNR is located. Thus, the strategy of integrating the pattern recognition technique and DIC polarization anisotropy is principly more reliable and accurate than the previously demonstrated standard defocused imaging methods which are based solely on matching the measured image pattern with a set of simulated defocused PSFs.

Further investigation revealed that the distinctively different DIC image patterns can only be generated for AuNRs that are tilted (neither totally lying flat on the horizontal plane nor standing straight up along its long axis) in the 3D space. For the AuNRs that were set flat on a pre-cleaned glass slide by spin casting, the bright and dark DIC intensities are also changed periodically as it rotates from 0° to 360° (Figures S6 and S7) and show good fits to the functions in Eq. 1 (Figure S8). However, these image patterns are similar in all four quadrants and thus cannot be used to differentiate the angular mirror effect. The difference in image patterns increases as the polar angle θ decreases from 90°, and the cutoff polar angle θ to show sufficient difference is estimated to be 70° (Figure S9).

To further demonstrate the usefulness of this technique, we tracked rotational dynamics of AuNRs on live cell membranes. Functional AuNRs are considered efficient delivery cargoes in biological applications.[10] Tracking rotational and translational dynamics of individual AuNRs on live cell membranes will lead to a better understanding of drug delivery mechanisms and other cellular processes, such as endocytosis.[15] In this regard, transferrin-modified AuNRs rotating on live cell membranes were chosen as a model system to verify the applicability of this method toward resolving fast rotational dynamics in biological systems.

We recorded image stacks that show rotational motions of a AuNR (AuNR 2) on a live cell membrane at a temporal resolution of 100 ms (Figure 2A). On the fluidic and uneven cell membrane, AuNR 2 was more often tilted to give rise to the required image patterns for azimuthal orientation identification within 0° - 360°. 30 consecutive frames (Figure 2B) were chosen from a movie that displays clear transitions among different image intensities and patterns when AuNR 2 was tilted. DIC polarization anisotropy was computed for the 30 images to extract the azimuthal angle φ. Based on the pattern recognition technique, then the DIC image patterns were used to resolve the true orientation angle φ in the four quadrants, and finally, the sum value of the bright and dark parts was used to determine the polar angle θ (Figure 2C). As illustrated in the polar plot of Figure 2D, in frames 1-11, AuNR 2 experienced reversible rocking motion between R1 and R2. In frame 12, it rotated to R2 and showed a continuous anticlockwise rotation until frame 27. A reminiscent rocking motion was shown again after that. It is worthy of note that these interesting angular rotational information only could be resolved by the methdology with full 3D angular resovability.

Conclusions

In summary, a novel optical rotational tracking method with the capability of full-space orientation resolvability for individual in-focus nanoprobes without sacrificing spatial and temporal resolution was demonstrated to overcome the limitations of current polarization anisotropy techniques. The applicability and usefulness of our method toward *in vivo* studies in biological systems was also verified by the precise tracking of 3D orientation angles of AuNRs rotating on live cell membranes. Deciphering the full 3D orientation information of the probe or nano-cargo in a dynamic fashion will shed new light on physical and biological processes with characteristic rotational motions, such as the detailed working mechanisms of molecular nanomachines and relevant assisting proteins during the internalization of functional drug delivery vectors.[3,4] Using this new method, further studies to elucidate the comprehensive interaction mechanisms between the functionalized nano-cargoes and the membrane receptors in live cells are underway. Detailed in-situ conformational information on how they bind on the cell membrane, how they move and rotate during the endocytosis process in live cells at single particle level would provide new avenues for the development of new generation of high efficient drug and gene delivery carriers.[15b,16]

References

1. a) Sönnichsen, C.; Alivisatos, A. P. *Nano Lett.* **2005**, *5*, 301–304; b) Xiao, L.; Qiao, Y. X.; He, Y.; Yeung, E. S. *Anal. Chem.* **2010**, *82*, 5268–5274; c) Xiao, L.; Qiao, Y.; He, Y.; Yeung, E. S. *J. Am. Chem. Soc.* **2011**, *133*, 10638–10645; d) Chang, W. -S.; Ha, J. W.; Slaughter, L. S.; Link, S. *Proc. Natl. Acad. Sci. USA* **2010**, *107*, 2781–2786; e) Wang, G.; Sun, W.; Luo, Y.; Fang, N. *J. Am. Chem. Soc.* **2010**, *132*, 16417–16422.

2. Zhuang, X.; Bartley, L. E.; Babcock, H. P.; Russell, R.; Ha, T.; Herschlag, D.; Chu, S. *Science* **2000**, *288*, 2048–2051.

3. Toprak, E.; Enderlein, J.; Syed, S.; McKinney, S. A.; Petschek, R. G.; Ha, T.; Goldman, Y. E.; Selvin, P. R. *Proc. Natl. Acad. Sci. USA* **2006**, *103*, 6495–6499.

4. Roux, A.; Uyhazi, K.; Frost, A.; De Camilli, P. *Nature* **2006**, *441*, 528–531.

5. Nishizaka, T.; Oiwa, K.; Noji, H.; Kimura, S.; Muneyuki, E.; Yoshida, M.; Kinosita, K. Jr. *Nat. Struct. Mol. Biol.* **2004**, *11*, 142–148.

6. Forkey, J. N.; Quinlan, M. E.; Goldman, Y. E. *Prog. Biophys. Mol. Biol.* **2000**, *74*, 1–35.

7. a) Moerner, W. E.; Orrit, M. *Science* **1999**, *283*, 1670–1676; b) Nirmal, M.; Dabbousi, B. O.; Bawendi, M. G.; Macklin, J. J.; Trautman, J. K.; Harris, T. D.; Brus, L. E. *Nature* **1996**, *383*, 802–804.

8. Xie, X. S.; Dunn, R. C. *Science* **1994**, *265*, 361–364.

9. Derfus, A. M.; Chan, W. C. W.; Bhatia, S. N. *Nano Lett.* **2004**, *4*, 11–18.

10. Murphy, C. J.; Gole, A. M.; Stone, J. W.; Sisco, P. N.; Alkilany, A. M.; Goldsmith, E. C.; Baxter, S. C. *Acc. Chem. Res.* **2008**, *41*, 1721–1730.

11. Bohren, C. F.; Huffman, D. R. *Absorption and scattering of light by small particles*, (Wiley, New York, 1983).

12. Ha, J. W.; Sun, W.; Wang, G.; Fang, N. *Chem. Commun.* **2011**, *47*, 7743–7745.

13. Ha, J. W.; Sun, W.; Stender, A.; Fang, N. *J. Phys. Chem. C.* **2012**, *116*, 2766–2771.

14. a) Böhmer, M.; Enderlein, J. *J. Opt. Soc. Am. B.* **2003**, *20*, 554–559; b) Enderlein, J.; Böhmer, M. *Opt. Lett.* **2003**, *28*, 941–944; c) Lieb, M. A.; Zavislan, J. M.; Novotny, L. *J. Opt. Soc. Am. B.* **2004**, *21*, 1210–1215.

15. a) Ewers, H.; Smith, A. E.; Sbalzarini, I. F.; Lilie, H.; Koumoutsakos, P.; Helenius, A. *Proc. Natl. Acad. Sci. USA* **2005**, *102*, 15110–15115; b) Xiao, L.; Wei, L.; Liu, C.; He, Y.; Yeung, E. S. *Angew. Chem. Int. Ed. Engl.* **2012**, *51*, 4181–4184.

16. Shi, X.; von dem Bussche, A.; Hurt, R. H.; Kane, A. B.; Gao, H. *Nat. Nanotech.* **2011**, *6*, 714–719.

Figures and Captions

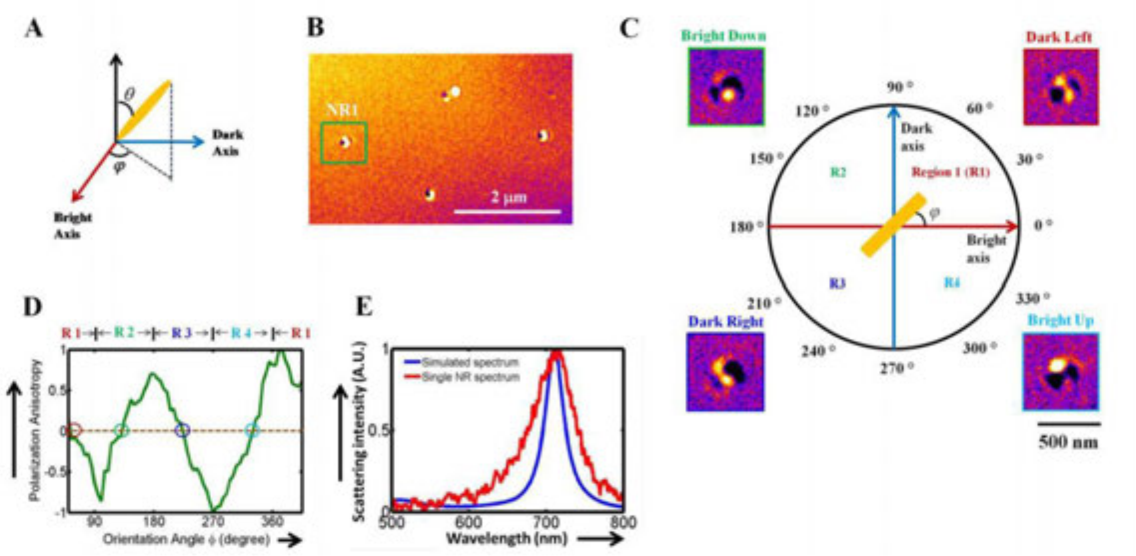

Figure 1. Orientation of AuNRs that are tilted in gel matrix with polar angle around 14°. (A) Scheme of azimuthal and polar angles in the Cartesian coordinate. (B) DIC image under 700 nm illumination. (C) Changes in DIC image pattern of AuNR 1 highlighted in (B) as a function of azimuthal angles. Four different image patterns appear for the tilted AuNR 1: the dark part on the left (R1), bright part down (R2), dark part right (R3), and bright part up (R4). (D) DIC Polarization anisotropy *P* for AuNR 1 (green curve) as a function of azimuthal angle φ. The dotted line is drawn at $P = 0$ and there are four points of contact at this *P* value. The corresponding images at each point of contact for four frames at $P = 0$ are shown in (C). (E) The measured (red) and simulated (blue) scattering spectra of AuNR 1.

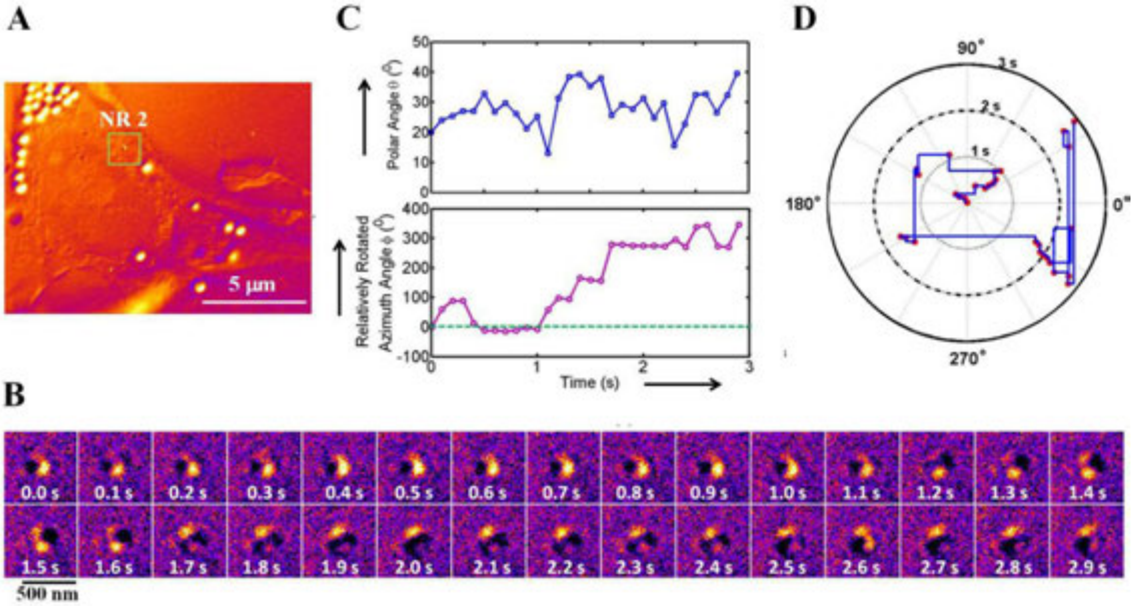

Figure 2. Dynamic rotational movements of single AuNR on a live cell membrane. (A) DIC image of the live cell and AuNR 2. (B) 30 consecutive images of AuNR 2 chosen from a movie. (C) Determined relatively rotated azimuthal angle φ and polar angle θ for AuNR 2 throughout the 30 consecutive frames. (D)The rotational track of azimuthal angle φ as a function of time for the image sequence of (B).

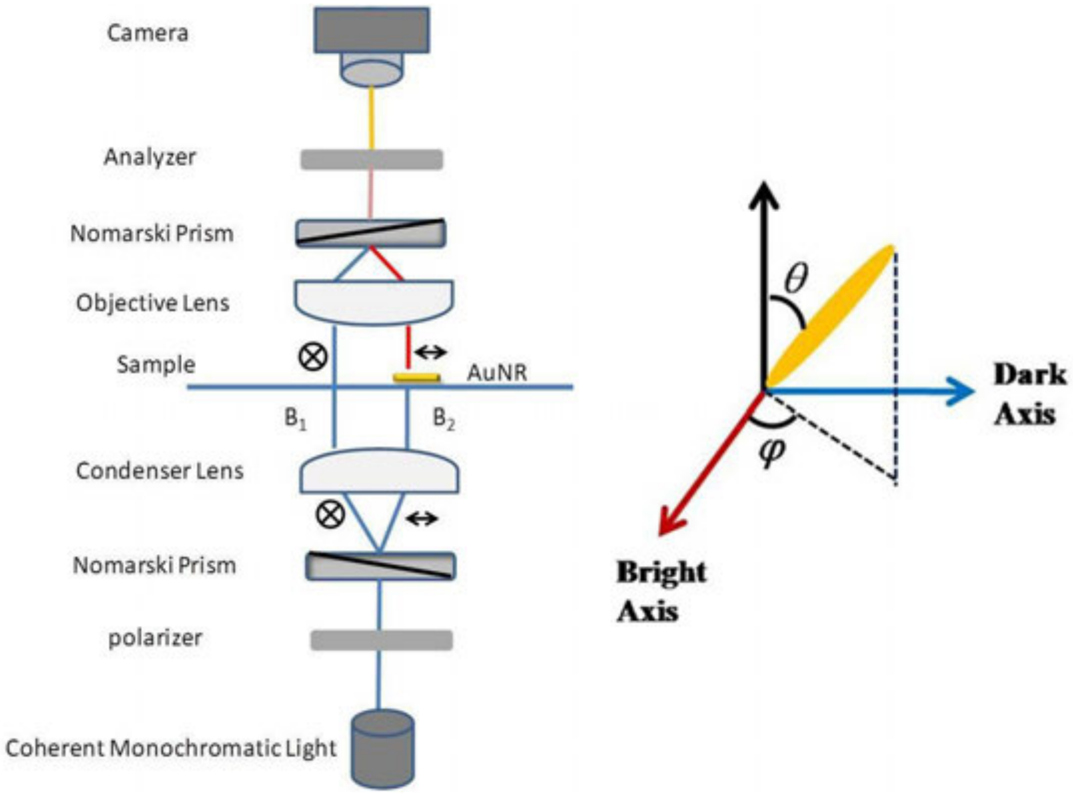

Figure S1. The light path scheme of DIC setup and the coordinate system used in this paper. The incident beam is split by the first Nomarski prism into two orthogonally polarized beams in the bright and dark polarization directions.

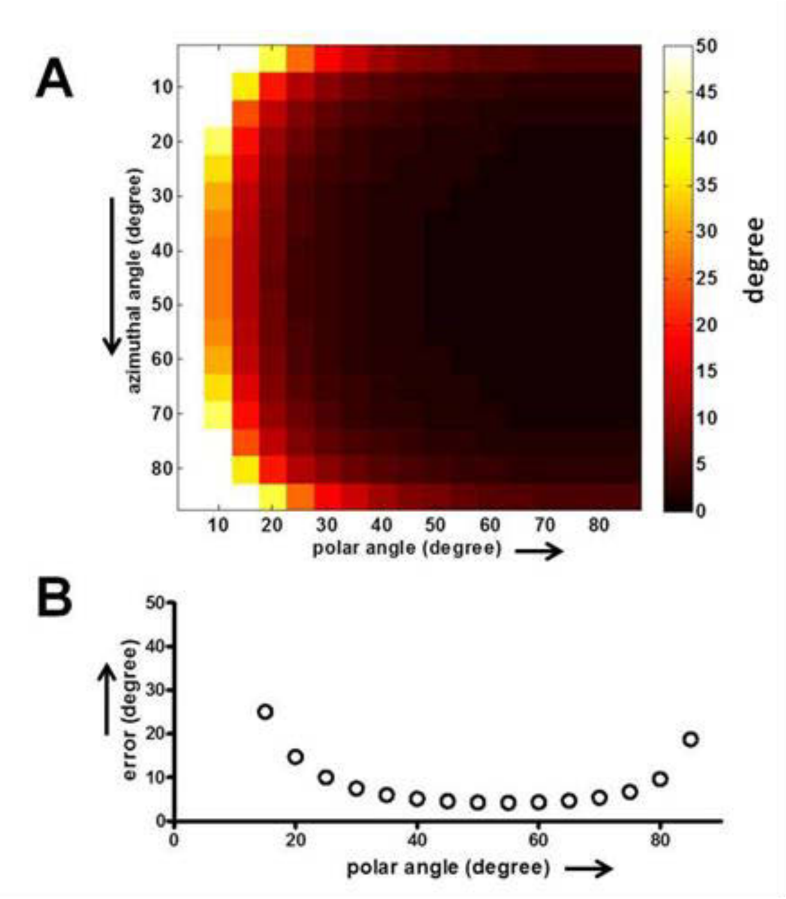

Figure S2. The azimuthal angle determination accuracy at different polar angles (A) and the polar angle determination accuracy (B). The error S_φ for azimuthal angle is estimated by

$$S_\varphi = \sqrt{\left(\frac{\partial f(I_{B,N},I_{D,N})}{\partial I_{B,N}}\right)^2 \times S^2_{I_{B,N}} + \left(\frac{\partial f(I_{B,N},I_{D,N})}{\partial I_{D,N}}\right)^2 \times S^2_{I_{D,N}}} \quad ,$$

where $f(I_{B,N},I_{D,N}) = \varphi = \frac{\arccos(P)}{2}$, $S_{I_{B,N}}$ and $S_{I_{D,N}}$ are the intensity measurement errors from the bright and dark channels. Similarly, the polar angle determination accuracy also can be estimated based on $\theta = \arcsin(\sqrt{I_{B,N} + I_{D,N}})$. In our current imaging setup, the error for intensity measurement from the bright and dark channels are ~2 %. The color scale bar shows an angle accuracy in degrees.

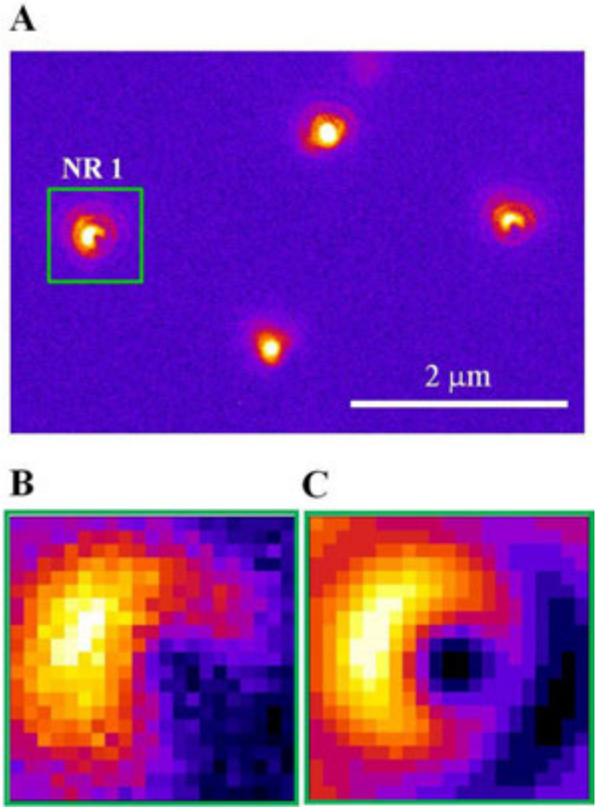

Figure S3. Orientation of AuNRs embedded in gel matrix. (A) Typical defocused DF image of AuNRs in gel matrix. The sample was illuminated at the longitudinal SPR wavelength. (B) Measured and enlarged DF image of AuNR 1 highlighted with a green square. (C) Simulated DF image that shows the corresponding best-fit from library. The calculated polar angle θ of AuNR 1 is around 14°.

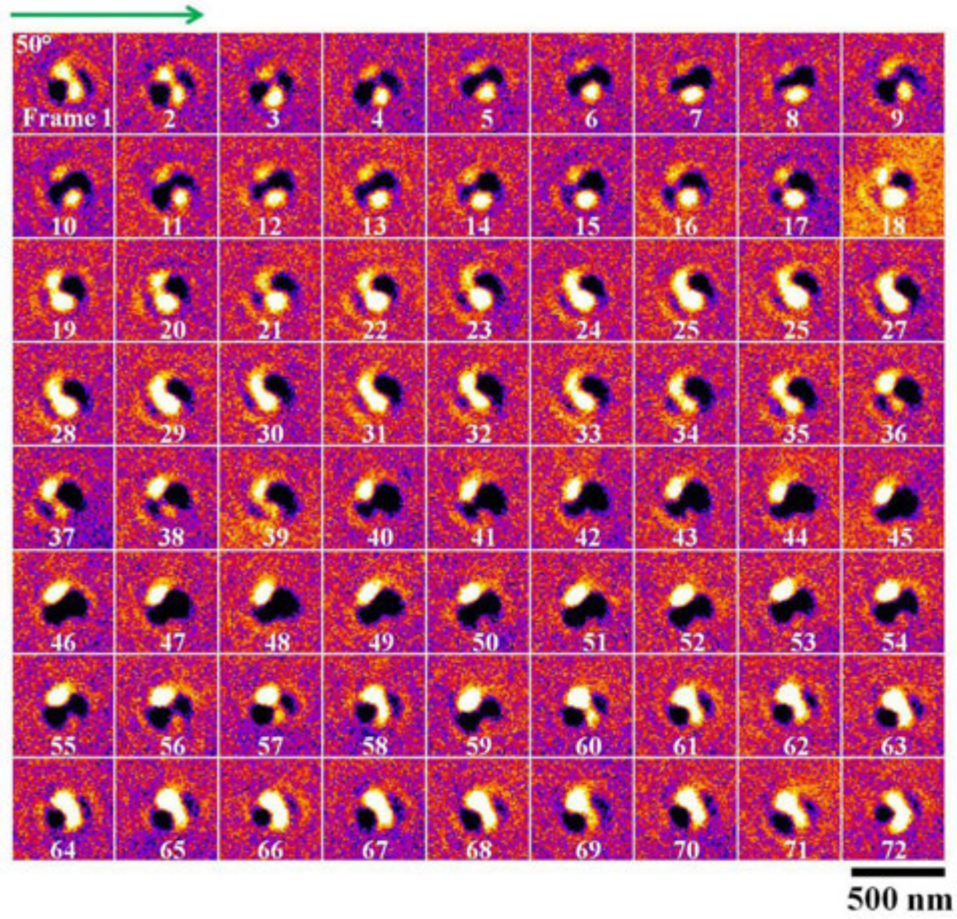

Figure S4. A complete set of DIC images of AuNR 1 in Figure 1 at 72 orientations from 0° to 360° with an increment of 5° (one frame). The azimuthal angle in Frame 1 is around 50° and the polar angle is around 14°. There are four distinctive image patterns for AuNR 1 that is tilted. These images can be grouped into four sets (18 frames each), which represent the four quadrants of the Cartesian plane.

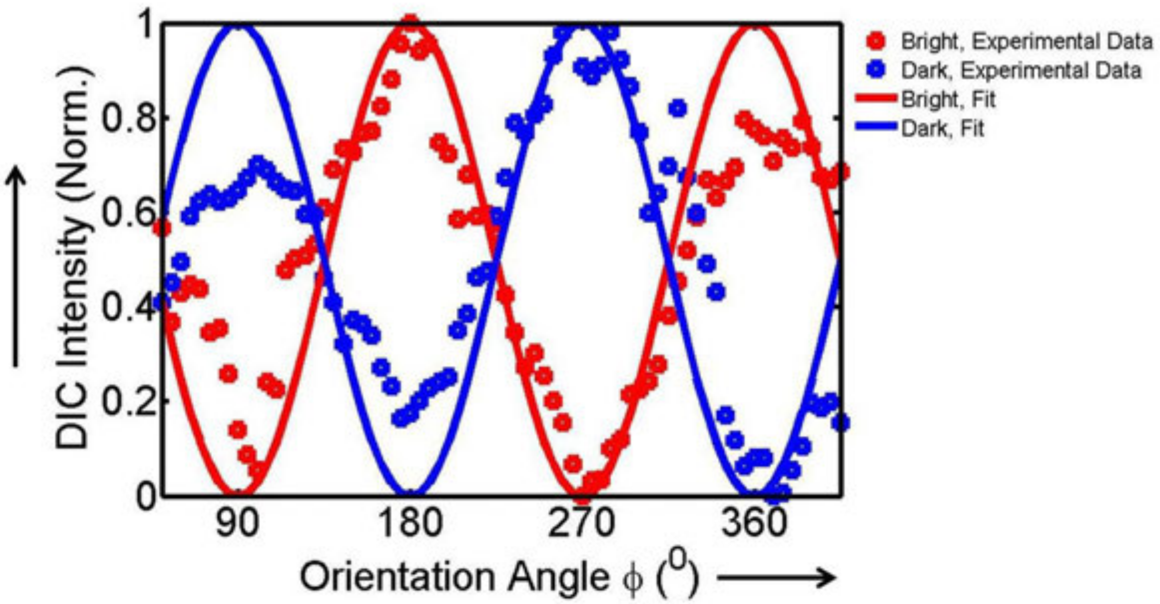

Figure S5. DIC intensity profiles of the tilted AuNR 1 in gel matrix as a function of azimuthal orientation angle *φ*. The normalized bright and dark DIC intensities for AuNR 1 were fitted with functions in Eq. 1. Since the collected scattering signal from the tilted AuNR embedded in gel matrix was attenuated to some extent in contrast to that from the AuNR adsorbed on glass slide surface, slight errors could be noted on the sample rotating measurements. However, the curves can still be fitted well with the functions.

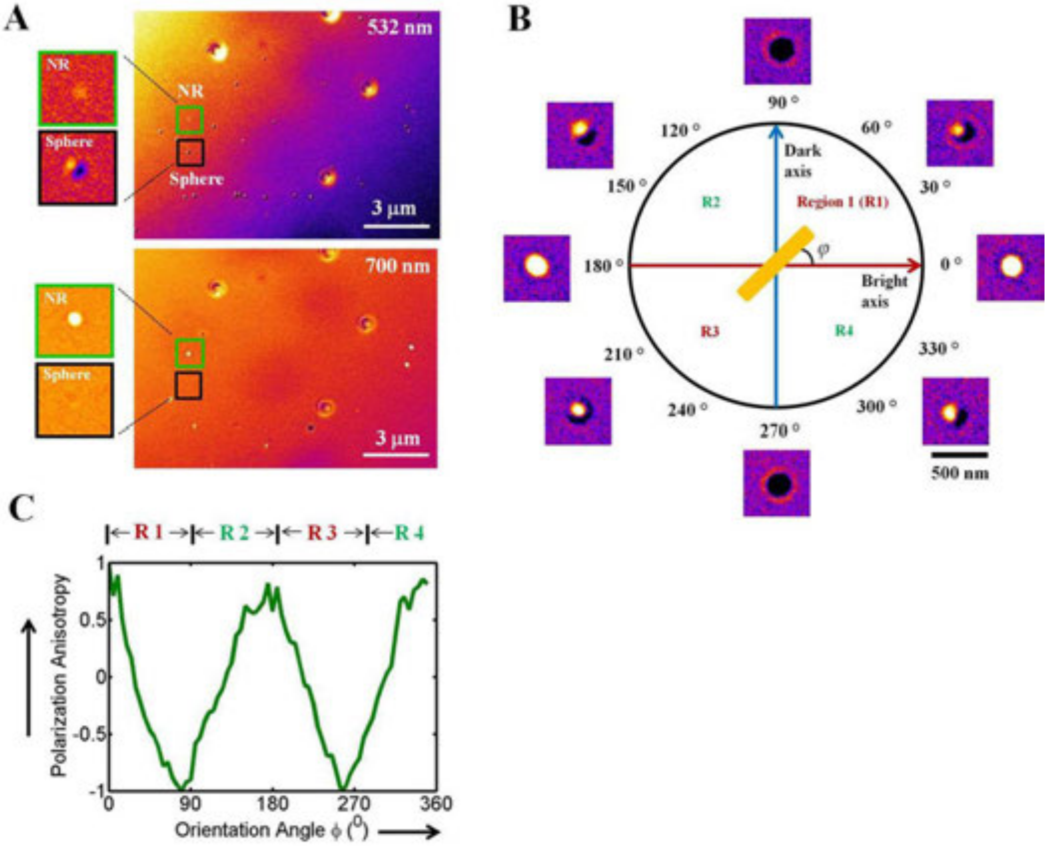

Figure S6. Orientation of single AuNR lying flat on a glass slide. (A) DIC images of AuNRs and Au nanospheres at two SPR wavelengths of 532 nm and 700 nm. (B) Change in DIC image pattern of the highlighted AuNR as a function of orientation angles. Brightest intensity is obtained in Frame 1, meaning the azimuthal angle of the AuNR in this frame is around 0°. Each frame corresponds to 5°. (C) DIC polarization anisotropy *P* for the AuNR.

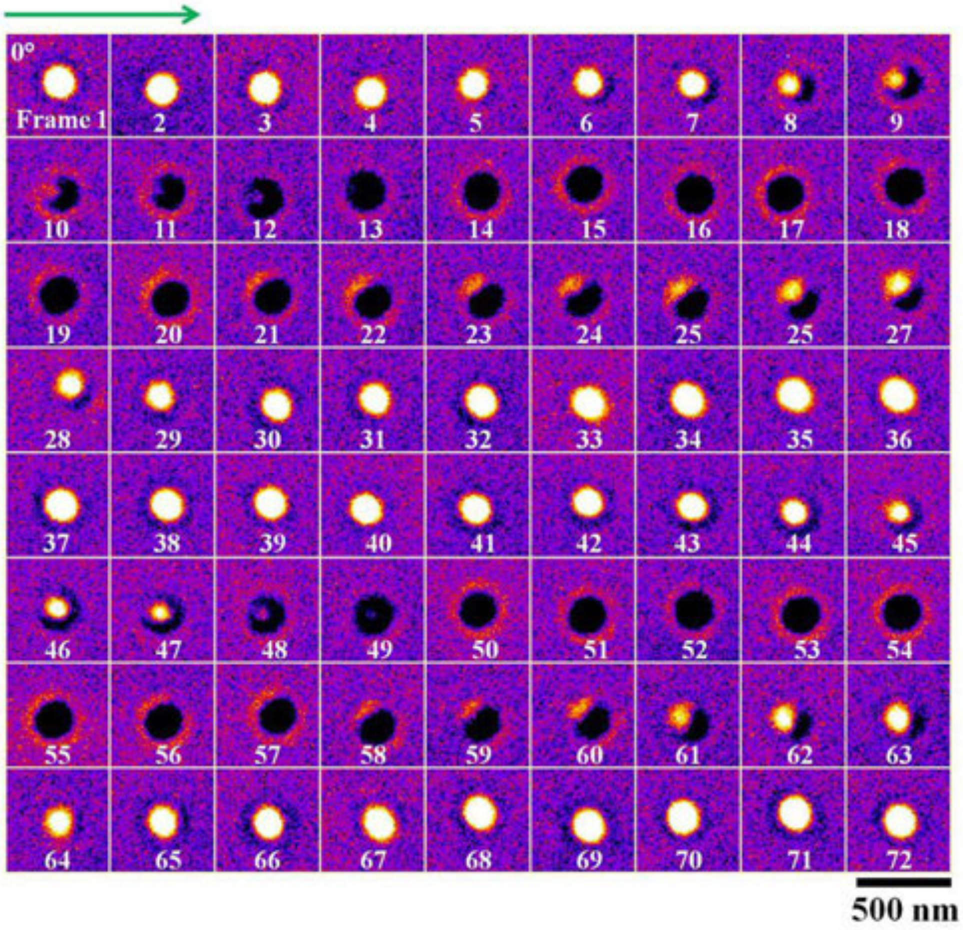

Figure S7. A complete set of DIC images of the highlighted AuNR lying flat on the horizontal plane in Figure S6. The orientation angle in Frame 1 is around 0°.

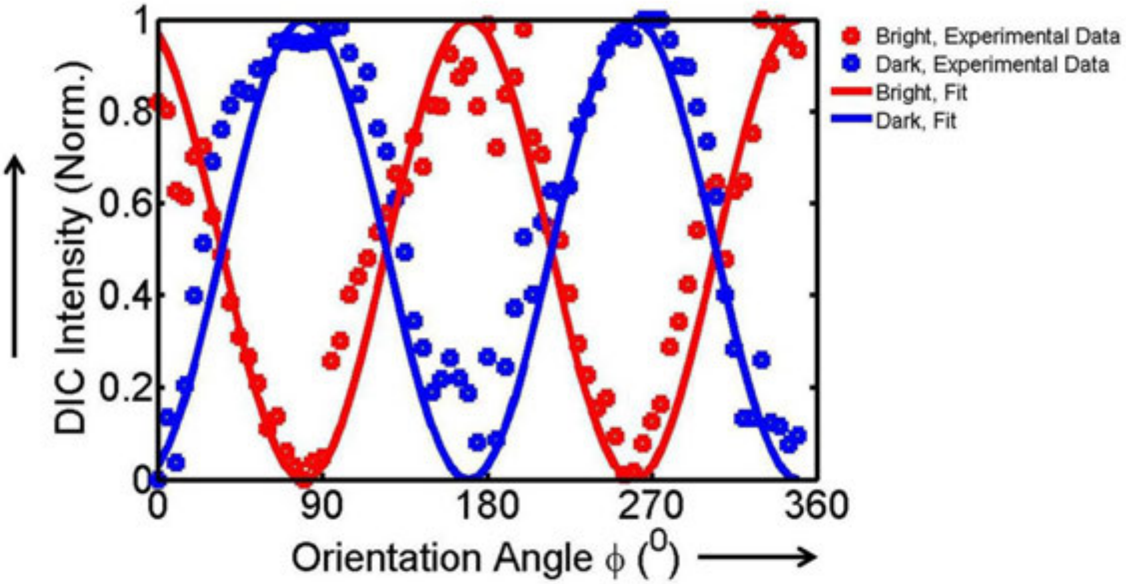

Figure S8. DIC intensities of the highlighted AuNR in Figure S6 for bright and dark polarization directions as a function of orientation angle φ. The normalized bright and dark DIC intensities for the AuNR were fitted with functions in Eq. 1.

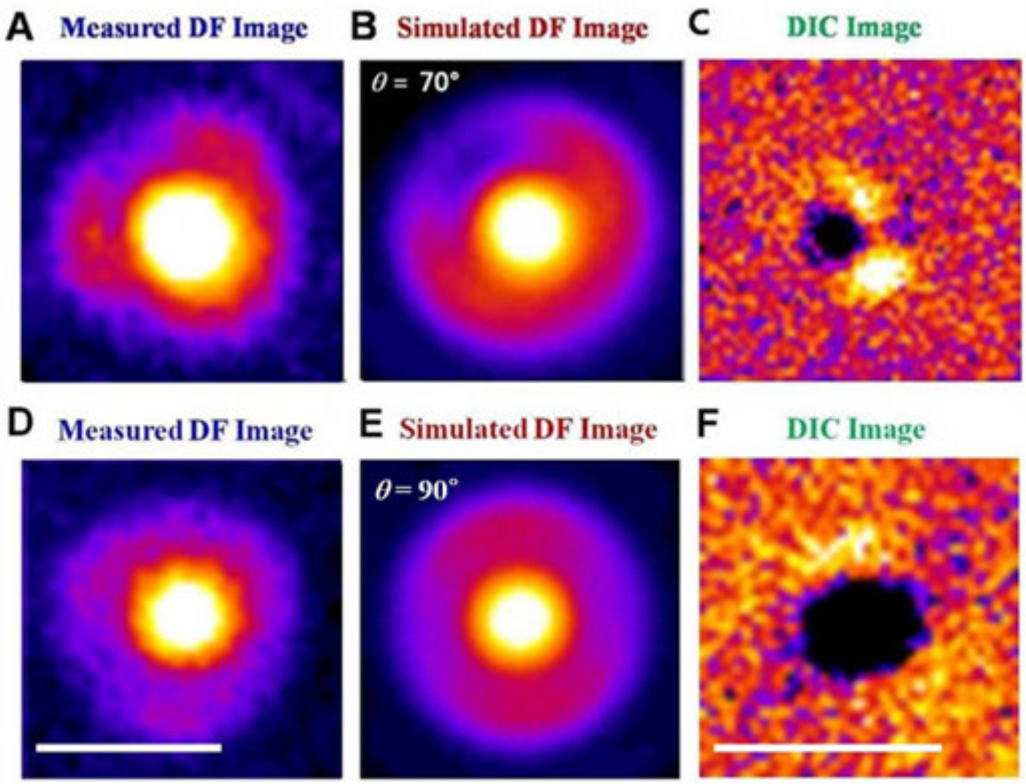

Figure S9. (A) Measured defocused DF image of a AuNR embedded in gel matrix. (B) The corresponding best-fit simulated DF image. The calculated polar angle θ is 70°. (C) DIC image of the same AuNR that is tilted. (D, E) Measured (D) and simulated (E) DF images of another AuNR that was set almost flat on a glass slide. The calculated polar angle θ is around 90°. (F) DIC image of the same AuNR lying flat on a glass slide. Scale bars correspond to 500 nm.

Supplementary Materials

Scattering Contribution to DIC Image of Single AuNRs. A typical imaging light path and coordinate system for DIC microscope is shown in Figure S1. A beam of light is transmitted through a polarizer/Nomarski prism/condenser set to generate two beams of light (B_1 and B_2). These two beams are separated by a certain distance (usually a few hundred nanometers) along the shear direction. The phase difference of these two wavefronts is called bias retardation. Usually, to increase the image contrast, additional bias retardation can be introduced by insertion of a quarterwave plate or an adjustment at the primary Wollaston (or Nomarski) prism ($\Delta\omega$). Given these two beams directly pass through the sample plane without additional phase retardation (no sample case), the measured interference intensity (background) by the CCD camera could be written as

$$I_o = T^2 + S^2 - 2TS\cos(\Delta\gamma + \Delta\omega)$$

(S5)

where T and S are the amplitude of the first and second beams, respectively.[3] Since there is no sample in the image plane, the amplitudes of these two beams are identical.

When one of these two beams (i.e., B_2 vibrates along x-axis) confronts with plasmonic gold nanorods (AuNR), the incident beam will be attenuated via absorption and scattering. Since the absorption part decays in a non-irradiative way (i.e. dissipates in thermal energy), only the scattering part contributes to the final interference image in DIC microscopy. Given the AuNR is excited by a coherent monochromatic light at close to the longitudinal resonance wavelength, the scattered electromagnetic field from AuNR can be further simplified into a single scattering dipole with the oscillation direction along its long axis. Therefore, the scattering dipole moment induced by beam B_2 could be described as

$$\vec{p} = \varepsilon_m \alpha E_o \cos(\varphi)\sin(\theta)\hat{e}_p$$

(S6)

where ε_m is the permittivity of the surrounding, E_o is the amplitude of the incident electrical field, φ and θ are the azimuthal and polar angle of AuNR, α is the polarizability of the nanoparticle. For AuNR, α equals

$$\alpha = 4\pi xyz \frac{\varepsilon_1 - \varepsilon_m}{3\varepsilon_m + 3P_A(\varepsilon_1 - \varepsilon_m)}$$

(S7)

where ε_1 is the permittivity of AuNR, x, y and z are the semiaxes of AuNR (x > y = z), and P_A (the depolarization factor) is determined by Eq. S2.

It is worthwhile to note that, in DIC microscopy, only the component with the same polarization direction as beam B_2 can be combined together with the other polarized probe beam (B_1). Thus, the effective scattering field from the AuNR that forms the differential interference image could be considered as the projection of the scattering dipole into the x axis again

$$\vec{p}_x = |p|\cos(\varphi)\sin(\theta)\hat{e}_x \quad .$$

(S8)

Then, the effective scattering component is

$$E_s = \frac{e^{ikz}}{-ikz}\frac{ik^3}{4\pi\varepsilon_m}\hat{e}_z \times (\hat{e}_z \times \vec{p}_x)$$

(S9)

where k is the wave number, z is the observation distance.

From Equations (S5) and (S9), we can readily determine the interference intensity of the bright part of the DIC image when beam B_2 confronts with a AuNR on the sample plane by

$$I_B = |E_o|^2 (t^2 + \sigma^2 \cos(\varphi)^4 \sin(\theta)^4 - 2t\sigma \cos(\varphi)^2 \sin(\theta)^2 \cos(\Delta\gamma + \Delta\omega + \Delta\zeta)) \qquad \text{(S10)}$$

where t is the transmission efficiency of the first beam, σ describes the scattering efficiency of AuNR, $\Delta\zeta$ is the phase delay caused by AuNR. The first term on the right describes the background signal from the first beam. The second term denotes the scattering component from AuNR which becomes comparable or even smaller than the shot noise of the first term for the case of small size particles.[4] The third term is scattering determined, but it is linearly enhanced by the first term. If $\Delta\omega$ is set properly, the contrast can be enhanced through reducing the background intensity I_0. Therefore, the relative interference signal from the bright part is proportional to

$$I_B - I_0 \propto \cos^2(\varphi)\sin^2(\theta)$$

(S11)

Similarly, the corresponding relative dark part interference intensity can be written as

$$I_0 - I_D \propto \sin^2(\varphi)\sin^2(\theta)$$

(S12)

CHAPTER 5. DIFFERENTIAL INTERFERENCE CONTRAST MICROSCOPY IMAGING OF MICROMETER-LONG PLASMONIC NANOWIRES

Ji Won Ha, Kuangcai Chen, and Ning Fang*

A paper published in *Chemical Communications* (DOI: 10.1039/C3CC46871B).

Reproduced by permission of The Royal Society of Chemistry (RSC)

* Corresponding author

Abstract

Micrometer-long metallic nanowires are promising optical probes in biological studies because of direct observation of their motions under an optical microscope. Differential interference contrast (DIC) microscopy is an excellent imaging technique that allows us to track motions of such probes either on the cell membrane or in the intracellular microenvironment. However, the optical properties of the nanowires have not been explored in DIC microscopy, and their DIC image patterns and intensities as a function of orientation angle remain unanswered. Herein, we present polarization- and wavelength-sensitive optical properties of 2 μm-long gold nanowires much larger than the wavelength of incident light. We demonstrate that DIC intensities from bright and dark polarization directions are anti-correlated for surface plasmon resonance wavelengths and that DIC polarization anisotropy can be used as a fast and reliable method to analyze rotational dynamics of the gold nanowires on synthetic membranes without angular degeneracy. These results have a potential impact on the use of micrometer-long gold nanowires as optical probes in biological studies.

Introduction

Micrometer-long metallic nanowires much larger than the wavelength of incident light are promising optical probes in biological studies.[1] However, the use of metallic nanowires in live cell studies has not been extensively explored due to biocompatibility and cytotoxicity issues. Lately, with much progress in surface modifications of the metallic nanoparticles,[2-7] there has been renewed interest in using micrometer-long metallic nanowires in biological studies including gene delivery,[8] biosensing,[9,10] and endocytosis[11,12]. Micrometer-long multi-segment nanowires were used as barcodes for biological multiplexing.[13,14] Moreover, micrometer-long nickel nanowires were used to manipulate live cells through magnetic field.[15,16] Kuo *et al.* demonstrated that serum-coated gold nanowires with lengths up to a few micrometers can be readily internalized by cells with the least toxicity.[12]

A great advantage of using micrometer-long Au nanowires in live cell studies is that it is possible to directly visualize their motions either on cell membrane or in the intracellular microenvironment through an optical microscope. In order words, we can directly differentiate their clockwise or counter-clockwise rotations, which is critical in biological studies. Scattering- and absorption-based optical microscopes can be used to observe plasmonic nanoparticles under dark-field (DF) microscopy[17-19] and photothermal heterodyne imaging[20,21]. However, their applicability for studies of fast dynamics in live cells is limited. The scattering-based DF method in biological imaging is limited by the scattering of many biological components resulting in a large background. The absorption-based photothermal heterodyne imaging is limited by raster scanning of the sample to collect an image and two heating and probe beams that could damage biological samples. Differential interference contrast (DIC) microscopy enables us to overcome the limitations in both DF and photothermal techniques and it is better suited to observe motions of plasmonic nanoparticles in live cells.[22,23] DIC microscopy resolves the optical path difference between two orthogonally polarized beams separated by a Nomarski prism. The interference nature makes it insensitive to the scattered light from surrounding cellular components and keeps its high-throughput capability.

Gold nanorods (AuNRs) much smaller than the wavelength of light have been extensively explored in biophysical studies with DIC microscopy and they have been successfully used as optical probes in single particle orientation and rotational tracking (SPORT).[24-28] Very recently, DIC microscopy-based SPORT technique using the AuNR probes was used to directly visualize the rotational dynamics of cargos at pauses during axonal transport.[29] However, micrometer-long Au nanowires have not been studied under a DIC microscope, and their optical properties remain unanswered. More specifically, our understanding of the dependence of DIC image patterns (or intensities) of these Au nanowires on polarization and wavelength of light is still limited. In this context, it is desirable to elucidate the optical properties of Au nanowires with DIC microscopy for the development of nanowire-based probing systems, and to demonstrate the feasibility of Au nanowires as optical probes in dynamic and biological studies.

Here, we report the optical properties of 2-µm long Au nanowires under a DIC microscope. We performed a 360° rotational study to clarify the effect of polarization of light on the DIC image patterns and intensities at three chosen surface plasmon resonance (SPR) wavelengths. Furthermore, we demonstrate the feasibility and usefulness of the Au nanowires as optical probes in dynamic and biological studies by combining with DIC polarization anisotropy. To the best of our knowledge, this is the first report to present the optical properties of micrometer-long Au nanowires under a DIC microscope, and to track their rotational motions on synthetic membranes by the DIC polarization anisotropy.

Experimental Methods

Differential Interference Contrast Microscopy. Differential interference contrast (DIC) microscopy was preformed with an upright Nikon Eclipse 80i microscope in this study. The DIC mode used a pair of Nomarski prisms, two polarizers, a quarter-wave plate, a Plan Apo oil-immersion objective (100×, N.A. = 1.40), and an oil-immersion condenser (N.A. = 1.40). Band-pass filters (520 nm, 550 nm, 640 nm) with a full width at half-maximum (FWHM) of 10 nm were obtained from Thorlab (Newton, NJ, USA) and inserted into the light path in the microscope. A Hamamatsu CMOS camera (ORCA-Flash 2.8) was employed to record highly detailed DIC images of Au nanowires and to record dynamics of Au nanowires rotating on synthetic membranes.

Sample Preparation and DIC Imaging of Au Nanowires. Au nanowires with an average size of 2000 nm × 75 nm were purchased from Nanopartz (A14-2000, Loveland, CO). The Au nanowire colloid solution was first sonicated for 15 min at room temperature. We made a solution containing 80-nm Au nanospheres and the Au nanowires. The 80-nm Au nanospheres were purchased from BBI (WI, USA). A sample was prepared by spin casting the solution on the pre-cleaned glass slide. Then, a 22 mm × 22 mm No. 1.5 coverslip (Corning, NY) was covered on the glass slide.

The sample glass slide was placed on a 360° rotating mirror holder affixed onto the microscope stge. By rotating the mirror holder 10° per step, the Au nanowires were positioned in different orientations. The 80-nm Au nanospheres were used as a standard to fix the focal plane after rotating each 10° of the stage. To excite the Au nanowire with different SPR wavelenghts, band-pass filters (520 nm, 550 nm, 640 nm) were inserted into the light path in the microscope. DIC images were taken with the Hamamatsu CMOS camera. The collected images and movies were analyzed with MATLAB and NIH ImageJ.

Preparation of Synthetic Lipid Bilayers on Glass Slides. The phospholipid 1-palmitoyl-2-oleoyl-sn-glycero-3-phosphocholine (POPC, Avanti Polar Lipids) solution in chloroform was first dried by a nitrogen steam and followed by at least 3 hr drying under vacuum at room temperature to remove the residual chloroform. The dried lipids were stored in a -20°C freezer.

Phosphate buffered saline (1× PBS, pH 7.4) was used to bring the final concentration to 0.5 mg/mL. The cloudy solution containing multilamellar vesicles was obtained after swelling in the PBS buffer solution for 30 min with several times vortexing. The suspension solution was then forcing through a 100 nm pore size polycarbonate membrane at least 21 times to prepare the solution with large unilamellar vesicles using a mini-extruder (Avanti Polar Lipids, Alabaster, AL). The resulted solution was kept in a 4°C fridge.

The planar bilayer was formed by incubating the large unilamellar vesicles solution on a freshly cleaned glass slide in a chamber created by two double-sided tapes and a clean coverslip for 10 min. After that, PBS was used to remove the excess lipids. Au nanowire solution was then introduced into the chamber with the membrane for DIC imaging.

Results and Discussion

Au nanowires used here were purchased from Nanopartz (A14-2000, Loveland, CO). Figure 1A shows a transmission electron microscopy (TEM) image of the Au nanowires chemically prepared. The mean length and diameter of Au nanowires are 2000 nm and 75 nm, respectively. Figure 1B shows a UV-Vis spectrum of these Au nanowires dispersed in water. As the length increases, the dipole plasmon mode red-shifts while more extinction peaks appear at shorter wavelengths, which correspond to the longitudinal higher-order multipole modes.[30,31] In addition, the transverse mode blue-shifts to slightly shorter wavelengths.[30] As shown in Figure 1B, the transverse SPR mode appears around 520 nm and the prominent higher-order multipole modes are observed in the visible spectrum at around 550 nm and 640 nm. Therefore, we chose three SPR wavelengths of 520 nm, 550 nm, and 640 nm to study the optical properties of the Au nanowires at the single-particle level. A sample was prepared by spin casting a solution containing Au nanowires on a pre-cleaned glass slide to position the Au nanowires relatively flat to the surface as they were fixed to the slide. The concentration of Au nanowires on the glass surface was controlled to be 1 μm^{-2} in order to facilitate single particle characterization and to minimize inter-particle SPR coupling resulting in the spectral shift.

In the present study, DIC microscopy is used to measure single Au nanowires at the three SPR wavelengths. In a DIC microscope, the incident plane-polarized beam is split into two orthogonally polarized mutually coherent beams pertaining to the bright (blue-line) and dark (red-line) polarization directions by the first Nomarski prism (Figure S1). After the beams pass through the sample, they are recombined by the second Nomarski prism and interfere with each other. This interference at recombination is sensitive to their optical path length difference. As the two split beams pass through the sample, they generate image contrasts dependent upon optical path length gradients in the sample.

We first studied the optical properties of Au nanowires at the transverse SPR mode of 520 nm. Figure 2A shows a DIC image of the immobilized single Au nanowires on a glass slide measured with 520-nm excitation. The orientation of Au nanowire is defined as the orientation angle φ between the nanowire's long axis and the bright axis as shown in Figure 2B. A 360° rotational study was carried out by rotating the stage by 10° per step to position Au nanowire 1 in different orientations. In this study, Au nanospheres with a diameter of 80 nm were used as a standard to find the focal plane after each 10° rotation of the stage. Interestingly, a totally bright DIC image for Au nanowire 1 highlighted with the white square in Figure 2A was observed when its long axis was aligned with the bright polarization axis (blue-arrow, φ=0° in Figure 2B). After a 90° rotation of the sample slide, the long axis of the nanowire 1 was aligned with the dark polarization axis (red-arrow, φ=90°) to generate a totally dark image (Figure 2B). Figure S2 shows the complete set of DIC images of Au nanowire 1 from 0° to 360° with an interval of 10°. It is worthwhile to note that this is consistent with the polarization-dependent DIC images of short AuNRs (25 nm × 73 nm, Figure S3). DIC intensities from bright and dark polarization directions at 520 nm are plotted as a function of orientation angle in Figure 2C. The DIC intensities change periodically in both polarization directions when the stage rotates by 10° per step. The bright and dark intensity curves are anti-correlated, that is, an increase in the bright intensity is accompanied by a decrease in the dark intensity, and vice versa (Figures 2C and S4). The normalized bright and dark DIC intensities for Au nanowire 1 are well fitted with functions of $\sin^4(\varphi)$ and $\cos^4(\varphi)$, respectively (Figure S4). Therefore, Figures 2C and S2 elucidate the polarization-sensitive DIC images and intensities for 2-μm long Au nanowires at 520 nm, which is similar to the trend in short AuNRs. However, we found that there is a clear and significant difference between short AuNRs and long Au nanowires. A DIC image of short AuNR aligned with the bright polarization axis ($\varphi = 0°$) and measured at the transverse SPR wavelength shows a totally dark image yielding the lowest intensity in the bright polarization axis.[24] However, DIC image of Au nanowire aligned with the bright polarization axis ($\varphi = 0°$) and measured at 520 nm shows a totally bright image giving the highest intensity in the bright polarization axis. This result suggests that for Au nanowire at the orientation angle $\varphi = 0°$, DIC intensity from multipole mode (or bright polarization axis) is greater than that from the transverse mode (or dark polarization axis) at the excitation wavelength of 520 nm.

Besides the transverse SPR mode, we further measured single Au nanowires randomly orientated on a glass slide at higher-order multipole SPR wavelengths of 550 nm and 640 nm. Figure 3A shows a DIC image of the immobilized single Au nanowires measured at 550 nm. A 360° rotational study was carried out by rotating the stage by 10°

per step. We found that polarization- and wavelength-sensitive DIC images and intensities of single Au nanowires as shown in Figure 3. Similar to the DIC images at 520 nm (Figure 2), a totally bright DIC image for Au nanowire 2 highlighted with the green square in Figure 3A was observed when its long axis was aligned with the bright polarization axis (Figure 3B) for both wavelengths. However, as the orientation angle φ was increased from 0° to 90°, the bright image turned to dark images because the long axis is getting aligned with the dark polarization axis. Figures S5 and S6 show the complete set of DIC images of Au nanowire 2 from 0° to 360° with an interval of 10° for both 550 nm (Figure S5) and 640 nm (Figure S6). DIC intensities from bright and dark polarization directions at both wavelengths are plotted as a function of orientation angle in Figure 3C. The bright and dark DIC intensities are anti-correlated for both wavelengths. However, it should be noted that the DIC intensities for two different SPR wavelengths are different, and 550-nm illumination provided higher contrast (or intensity) than that of 640-nm illumination (Figure 3C). We ensured that the transmission of two band-pass filters of 550 nm and 640 nm used in this study is almost same (Figure S7). Therefore, the difference in the DIC intensities of the same nanowire for two wavelengths can be explained by the fact that 2-μm long Au nanowires absorb more light at 550 nm than 640 nm as supported in Figure 1B. To quantitatively compare, we further obtained relative modulation depth in the intensity profiles for both wavelengths (Figure 3D). When the modulation depth at 550 nm was 1, the relative modulation depth at 640 nm was determined to be 0.46 for Au nanowire 2. We further measured 10 more individual nanowires and an average relative modulation depth at 640 nm was found to be 0.45 (Figure S8). This result clearly suggests that a 550-nm excitation can provide DIC images with higher contrast and intensities for the nanowires. Therefore, we chose 550-nm wavelength to visualize Au nanowires for the following single particle tracking experiments.

Although Au nanowires are directly visualized under a DIC microscope, a fast and reliable method to analyze their motions dynamically is still required. Since the normalized bright and dark DIC intensities for Au nanowire 2 at 550 nm are anti-correlated and well fitted with functions of $\sin^4(\varphi)$ and $\cos^4(\varphi)$ (Figure 4A), DIC polarization anisotropy is expected to be used. The DIC polarization anisotropy P can be conveniently obtained from the bright and dark intensities of a single DIC image of the nanoprobe. DIC polarization anisotropy using an intensity ratio instead of absolute intensities is less affected by intensity instabilities so that it leads to more accurate, reproducible and reliable angle measurements.[26-28] DIC polarization anisotropy is defined in the following equation 1.

$$P = \frac{I_{\mathrm{B,N}} - I_{\mathrm{D,N}}}{I_{\mathrm{B,N}} + I_{\mathrm{D,N}}} \qquad (1)$$

where $I_{\mathrm{B,N}}$ and $I_{\mathrm{D,N}}$ are the normalized bright and dark intensities, respectively. In this study, DIC polarization anisotropy were computed from the orthogonally polarized bright and dark intensities of Au nanowire 2 at 550 nm. Figure 4B shows the polarization anisotropy P for Au nanowire 2 as a function of orientation angle φ. The P values are in the range of -1 to +1 depending on the Au nanowire's orientation relative to the bright and dark polarization directions as illustrated in Figure 4B. Since the DIC bright (or dark) intensity of a Au nanowire is proportional to the fourth power of the sine (or cosine) of the orientation angle φ, the P values can be calculated directly for any given φ using the following equation 2.

$$P = \frac{\sin^4(\varphi) - \cos^4(\varphi)}{\sin^4(\varphi) + \cos^4(\varphi)} \qquad (2)$$

As shown in Figure 4B, the experimental P values obtained from equation 1 agree well with the theoretical P values calculated from equation 2, which validates that DIC polarization anisotropy enables accurate measurements of orientation angle of micrometer-long Au nanowires. The orientation angle φ can be deduced backward from the measurement of P values.[26]

We then tried to demonstrate the feasibility of the DIC polarization anisotropy in dynamic studies with single Au nanowire probes. In the present study, single Au nanowires rotating on synthetic lipid bilayers (or membranes) were chosen as a model system to verify the applicability of the DIC polarization anisotropy together with Au nanowire probes in dynamic biological systems. Cetyltrimethyl ammonium bromide (CTAB)-coated Au nanowires freely diffusing in solution when introduced into a chamber can be bound to the membrane through non-specific binding. We recorded movies that show rotational motions of surface-bound Au nanowires at temporal resolution of 100 ms (Figure 5A). Movie S1 displays rotational motions of surface-bound Au nanowire 3 in Figure 5A. The nanowire 3 shows random in-plane rotations on the membrane, giving rise to bright and dark DIC images over time. 16-consecutive frames from the movie were chosen as an example to show the change in the DIC image patterns (Figure 5B). All the frames are provided in Figure S9. From the rotational motions of the nanowire 3, we can imagine that there is one fixed binding site at around its center on the membrane as depicted in Figure 5C. Figure 5D shows DIC intensities in the bright (blue) and dark (red) polarization directions during the dynamic process and they are anti-correlated. DIC polarization anisotropy was then computed for all the frames to extract orientation angle φ (Figure 5D). The calculated P values are randomly distributed between -1 and 1 as a function of time. This means that this nanowire 3 with one fixed binding site has high freedom of rotation on the membrane.

Another conformation is to have one fixed binding site at the end of a nanowire. In this case, the nanowire can also have high freedom of rotation, resulting in the randomly distributed P values between -1 and 1. Movie S2 shows rotational motions of Au nanowire 4 with one fixed binding site at the end of the nanowire. As expected, the P values are randomly distributed between -1 and 1 as a function of time (Figure S10C). All the frames in the movie are provided in Figure S11.

Furthermore, single Au nanowires can be bound to the membrane with multiple binding sites. Movie S3 shows rotational motions of Au nanowire 5 with multiple fixed binding sites on the membrane. From the movie, we can observe much lower freedom of rotation of the nanowire. The little movement resulted in the P values fluctuating at around 0.1 as a function of time (Figure S12C). Figure S13 presents all the successive images from the movie. Therefore, we demonstrated that 2 μm-long Au nanowire probes can be potentially used as optical probes by combining with the DIC polarization anisotropy a fast and reliable method to track rotational motions in dynamic studies. It is also demonstrated that we can overcome the limitation of the angular degeneracy resulted from the 2-fold symmetry in polarization-based techniques through combining the DIC polarization anisotropy with micrometer-long Au nanowire probes. That is, it is possible to distinguish the rotational motions, such as clockwise or counter-clockwise, of an optical probe in the focal plane without angular degeneracy, which is critical in biological studies.

Conclusions

We demonstrated polarization- and wavelength-sensitive DIC images of 2 μm-long gold nanowires much larger than the wavelength of light. We found that the normalized DIC intensities from bright and dark polarization directions at SPR wavelengths are anti-correlated and well fitted with $\sin^4(\varphi)$ and $\cos^4(\varphi)$, respectively. Furthermore, the DIC polarization anisotropy was verified to be a reliable method to analyze rotational dynamics of Au nanowires. Therefore, the results show that micrometer-long Au nanowires could be potentially used as optical probes in biological studies, including gene delivery and endocytosis, through combining with a DIC microscope.

References

1. Yan, R.; Park, J.-H.; Choi, Y.; Heo, C.-J.; Yang, S.-M.; Lee, L. P.; Yang, P. *Nat. Nanotechnol.* **2012**, *7*, 191.
2. Nativo, P.; Prior, I. A.; Brust, M. *ACS Nano* **2008**, *2*, 1639.
3. You, C.-C.; Chompoosor, A.; Rotello, V. M. *Nano Today* **2007**, *2*, 34.
4. Bauer, L. A.; Reich, D. H.; Meyer, G. J. *Langmuir* **2003**, *19*, 7043.
5. Bauer, L. A.; Birenbaum, N. S.; Meyer, G. J. *J. Mater. Chem.* **2004**, *14*, 517.
6. Baruah, B.; Craighead, C.; Abolarin, C. *Langmuir* **2012**, *28*, 15168.

7. Sapsford, K. E.; Algar, W. R.; Berti, L.; Gemmill, K. B.; Casey, B. J.; Oh, E.; Stewart, M. H.; Medintz, I. L. *Chem. Rev.* **2013**, *113*, 1904.

8. Salem, A. K.; Searson, P. C.; Leong, K. W. *Nat. Mater.* **2003**, *2*, 668.

9. Dawson, K.; Baudequin, M.; O'Riordan, A. *Analyst* **2011**, *136*, 4507.

10. Lu, Y.; Yang, M.; Qu, F.; Shen, G.; Yu, R. *Bioelectrochemistry* **2007**, *71*, 211.

11. Chiung-Wen, K.; Jun-Jung, L.; Kung Hwa, W.; Peilin, C. *Nanotechnology* **2008**, *19*, 025103.

12. Kuo, C. W.; Lai, J. J.; Wei, K. H.; Chen, P. *Adv. Funct. Mater.* **2007**, *17*, 3707.

13. Keating, C. D.; Natan, M. J. *Adv. Mater.* **2003**, *15*, 451.

14. Hurst, S. J.; Payne, E. K.; Qin, L.; Mirkin, C. A. *Angew. Chem. Int. Ed.* **2006**, *45*, 2672.

15. Hultgren, A.; Tanase, M.; Chen, C. S.; Meyer, G. J.; Reich, D. H. *J. Appl. Phys.* **2003**, *93*, 7554.

16. Tanase, M.; Felton, E. J.; Gray, D. S.; Hultgren, A.; Chen, C. S.; Reich, D. H. *Lab Chip* **2005**, *5*, 598.

17. Sönnichsen, C.; Alivisatos, A. P. *Nano Lett.* **2004**, *5*, 301.

18. Xiao, L.; Qiao, Y.; He, Y.; Yeung, E. S. *Anal. Chem.* **2010**, *82*, 5268.

19. Xiao, L.; Qiao, Y.; He, Y.; Yeung, E. S. *J. Am. Chem. Soc.* **2011**, *133*, 10638.

20. Chang, W.-S.; Ha, J. W.; Slaughter, L. S.; Link, S. *Proc. Nat. Acad. Sci. U.S.A.* **2010**.

21. Boyer, D.; Tamarat, P.; Maali, A.; Lounis, B.; Orrit, M. *Science* **2002**, *297*, 1160.

22. Sun, W.; Wang, G.; Fang, N.; Yeung, E. S. *Anal. Chem.* **2009**, *81*, 9203.

23. Stender, A. S.; Marchuk, K.; Liu, C.; Sander, S.; Meyer, M. W.; Smith, E. A.; Neupane, B.; Wang, G.; Li, J.; Cheng, J.-X.; Huang, B.; Fang, N. *Chem. Rev.* **2013**, Article ASAP (DOI: 10.1021/cr300336e)

24. Wang, G.; Sun, W.; Luo, Y.; Fang, N. *J. Am. Chem. Soc.* **2010**, *132*, 16417.

25. Gu, Y.; Sun, W.; Wang, G.; Fang, N. *J. Am. Chem. Soc.* **2011**, *133*, 5720.

26. Ha, J. W.; Sun, W.; Wang, G.; Fang, N. *Chem. Commun.* **2011**, *47*, 7743.

27. Ha, J. W.; Sun, W.; Stender, A. S.; Fang, N. *J. Phys. Chem. C* **2012**, *116*, 2766.

28. Xiao, L.; Ha, J. W.; Wei, L.; Wang, G.; Fang, N. *Angew. Chem. Int. Ed.* **2012**, *51*, 7734.

29. Gu, Y.; Sun, W.; Wang, G.; Jeftinija, K.; Jeftinija, S.; Fang, N. *Nat. Commun.* **2012**, *3*, 1030.

30. Payne, E. K.; Shuford, K. L.; Park, S.; Schatz, G. C.; Mirkin, C. A. *J. Phys. Chem. B* **2006**, *110*, 2150.

31. Encina, E. R.; Coronado, E. A. *J. Phys. Chem. C* **2007**, *111*, 16796.

Figures and Captions

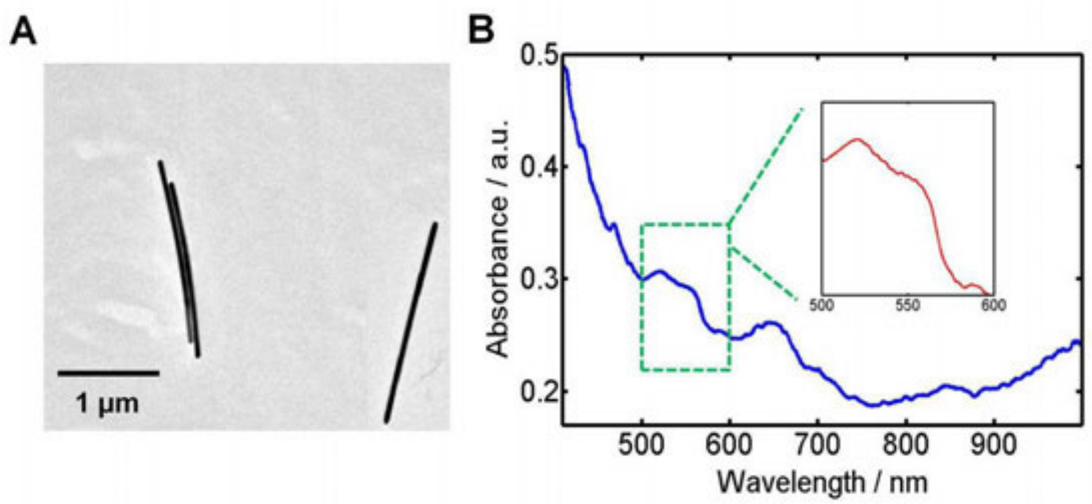

Figure 1. (A) TEM image of Au nanowires. The average length and width of nanowires are 2000 nm and 75 nm, respectively. (B) UV-Vis absorption spectrum of 2 µm-long Au nanowires in water. The transverse SPR peak appears at 520 nm, while the prominent higher-order multipole peaks appear at 550 nm and 640 nm.

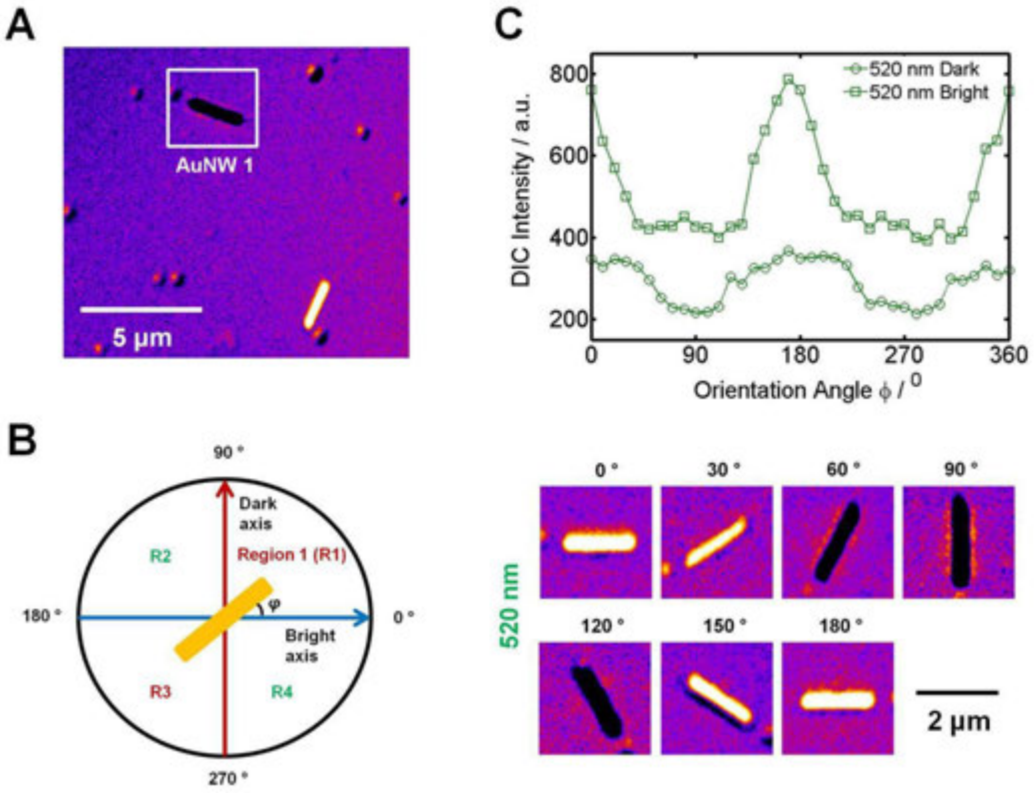

Figure 2. Polarization-dependent DIC images and intensities of 2 µm-long Au nanowires at the transverse SPR wavelength of 520 nm. (A) DIC image of single Au nanowires measured at 520 nm. 80-nm Au nanospheres were used as reference particles to find the focal plane. (B) Schematic diagram to show the definition of the orientation angle φ in the Cartesian coordinate. The blue-arrow shows the bright polarization axis, while the red-arrow shows the dark polarization direction axis. DIC images of Au nanowire 1 in (A) are shown as a function of orientation angle from 0° to 180° with an interval of 30°. (C) Change in the bright and dark DIC intensities of Au nanowire 1 as a function of orientation angle with an increment of 10°. DIC intensities are anti-correlated in two bright and dark polarization directions.

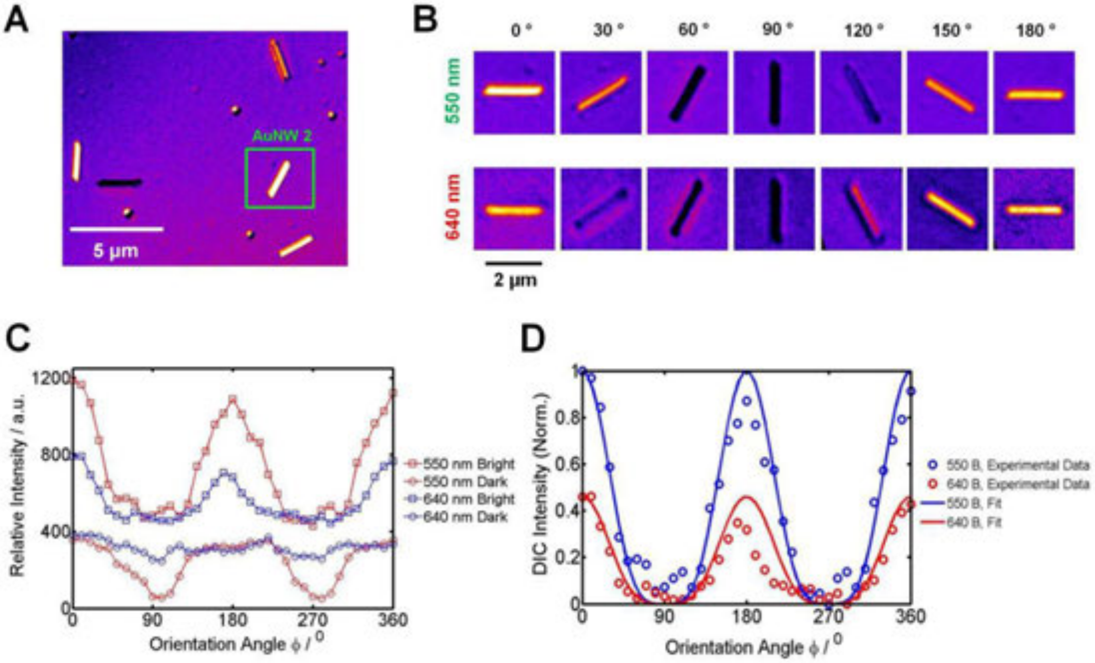

Figure 3. Polarization- and wavelength-dependent DIC images and intensities of 2 µm-long Au nanowires at the multipole SPR wavelengths of 550 nm and 640 nm. (A) DIC image of single Au nanowires measured at 550 nm. 80-nm Au nanospheres were used as reference particles to find the focal plane. (B) DIC images of Au nanowire 2 in (A) are shown as a function of orientation angle from 0° to 180° with an interval of 30°. (C) Change in the bright and dark DIC intensities of Au nanowire 2 as a function of orientation angle with an increment of 10° for two multipole wavelengths. DIC intensities are anti-correlated in two bright and dark polarization directions. (D) Comparison on the modulation depth of Au nanowire 2 at 550 nm (blue-curve) and 640 nm (red-curve). The relative modulation depth at 640 nm is determined to be 0.46 when it was 1 at 550 nm.

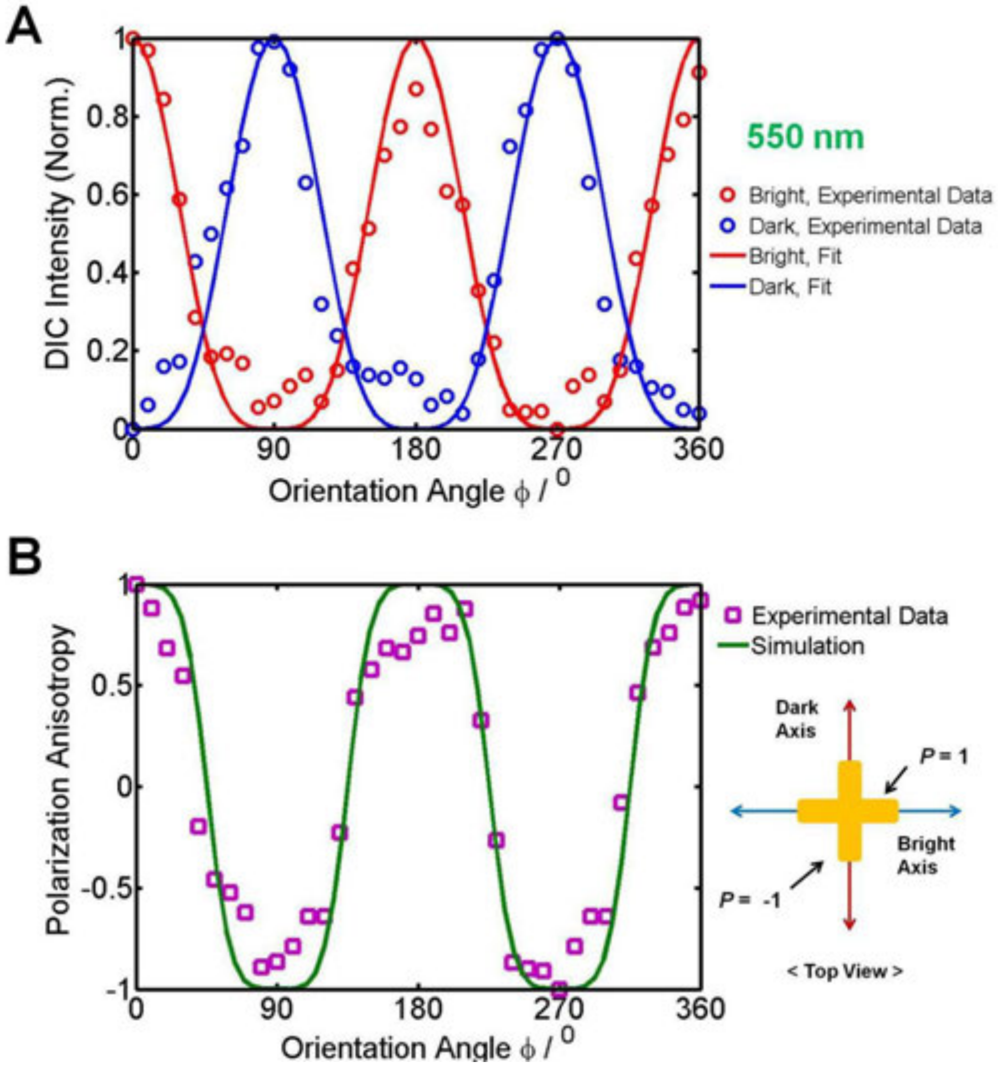

Figure 4. DIC polarization anisotropy for Au nanowire 2 in Figure 3 at 550 nm. (A) The normalized bright (red-circle) and dark (blue-circle) intensities for Au nanowire 2 as a function of orientation angle *φ*. The DIC intensities change periodically when the stage rotates by 10° per step. The normalized bright and dark intensities are fitted with $\sin^4(\varphi)$ and $\cos^4(\varphi)$, respectively. (B) DIC polarization anisotropy *P* for the nanowire 2. The experimental *P* values (pink-square) are compared to the calculated *P* values (green-curve) as a function of orientation angle. Schematic of *P* values at two special cases (P=1 at φ=0° and P=-1 at φ=90°).

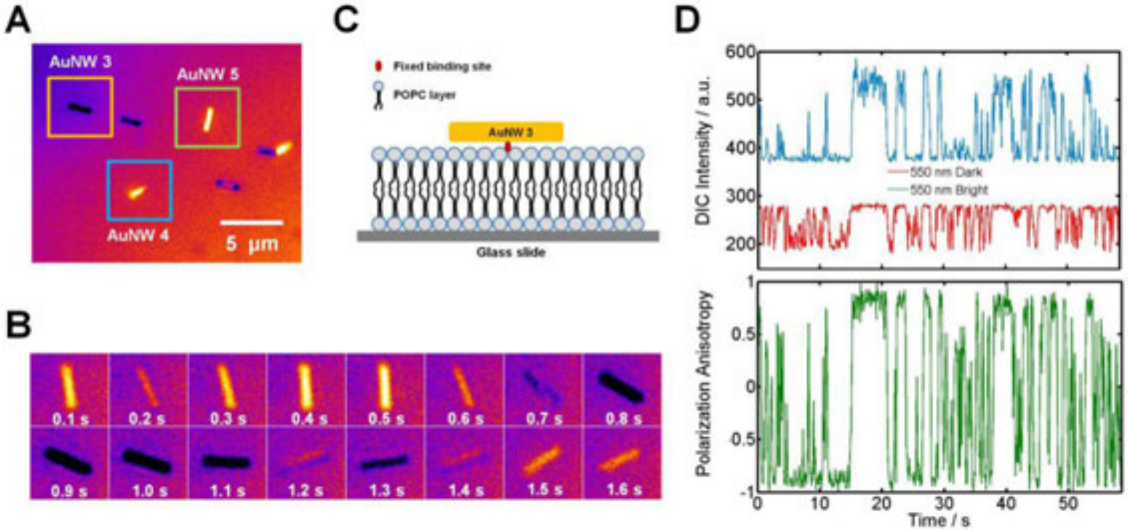

Figure 5. Dynamic tracking of 2-μm long Au nanowires on synthetic membranes with DIC polarization anisotropy. (A) DIC image of single Au nanowires bound onto the membrane. (B) 16-successive DIC images of the nanowire 3 as a function of time. Temporal resolution is 100 ms. (C) Schematic of the nanowire 3 that has one fixed binding site at around its center on the membrane. (D) Time traces of measured DIC intensities in the two orthogonal bright (bright-curve) and dark (red-curve) polarization directions for the nanowire 3 rotating on the membrane. DIC polarization anisotropy for the nanowire 3 is computed from the intensity traces as a function of time.

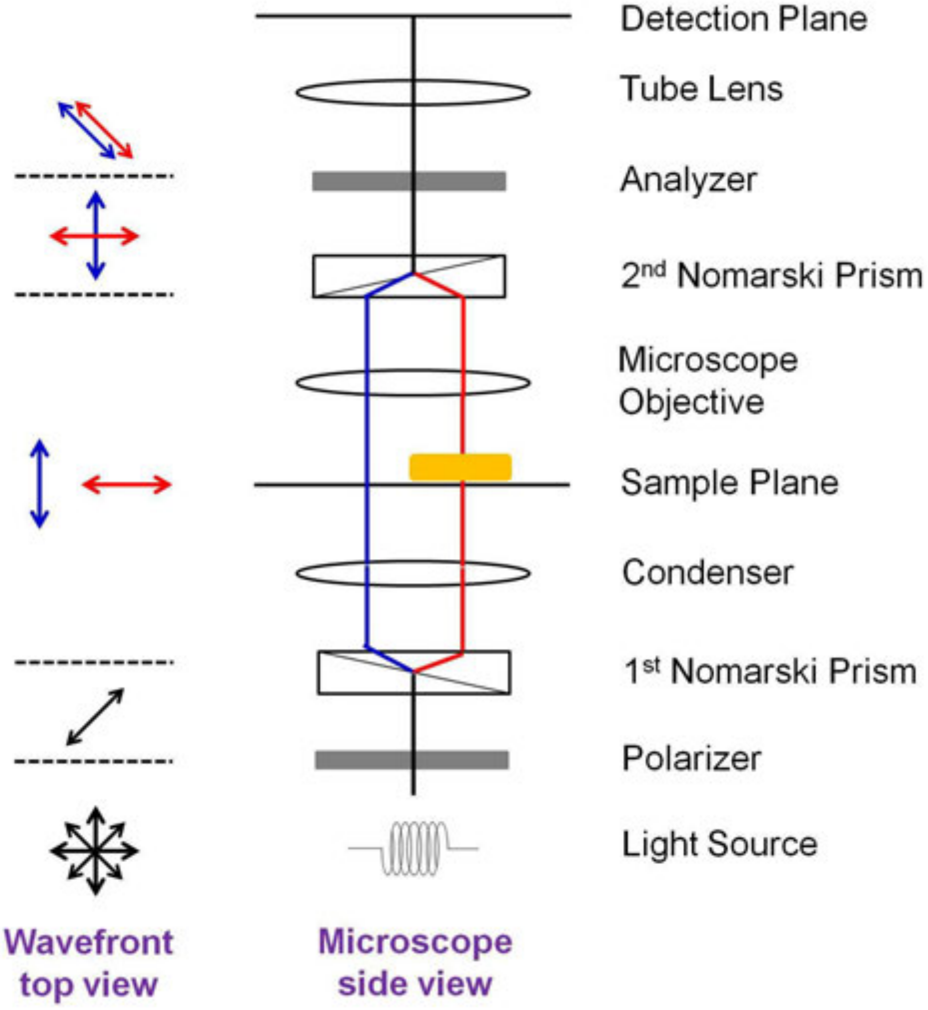

Figure S1. The optical path and wavefront in the DIC microscope. The blue- and red-lines represent the optical path of two orthogonal beams split by the first Nomarski prism.

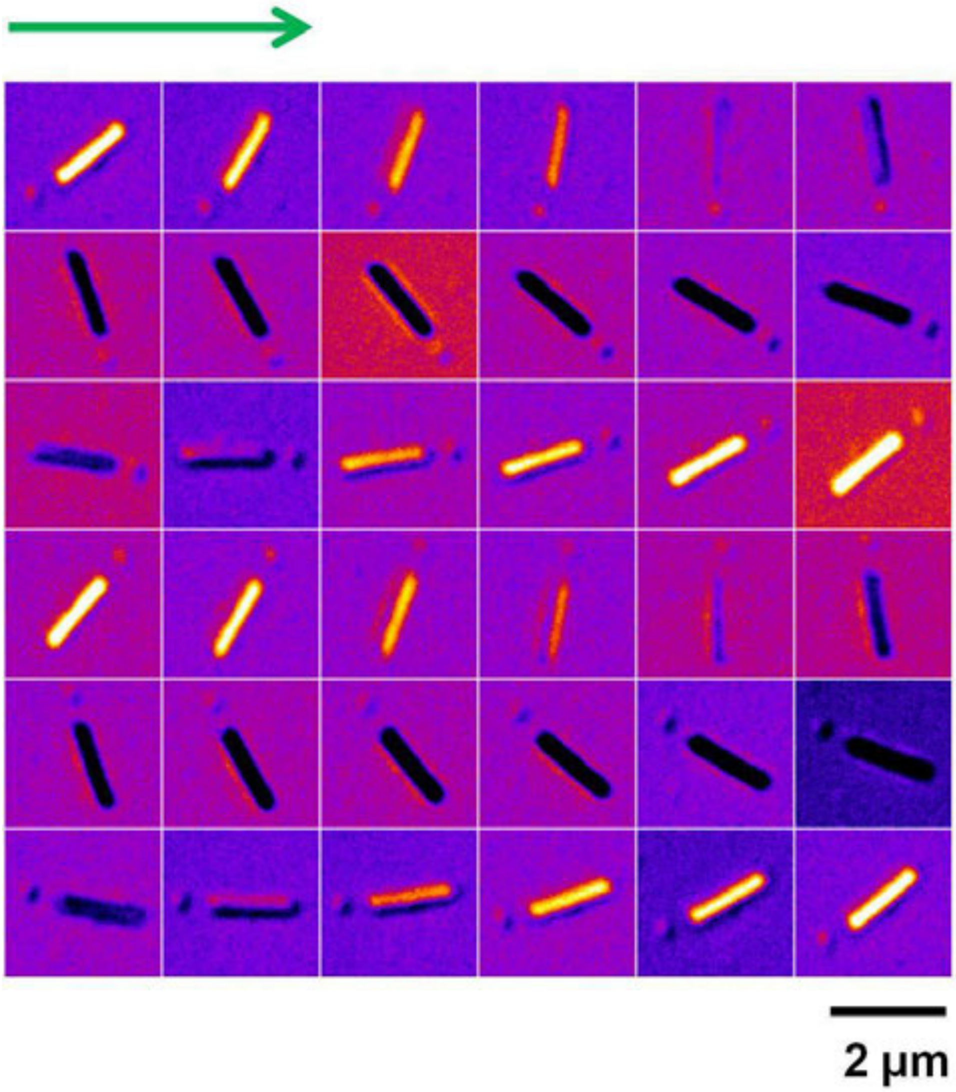

Figure S2. A complete set of DIC images of Au nanowire 1 in Figure 2 at 36 orientations from 0° to 360° with an increment of 10°. The nanowire is excited at 520 nm close to its transverse SPR mode. The image patterns are changed periodically as a function of angle.

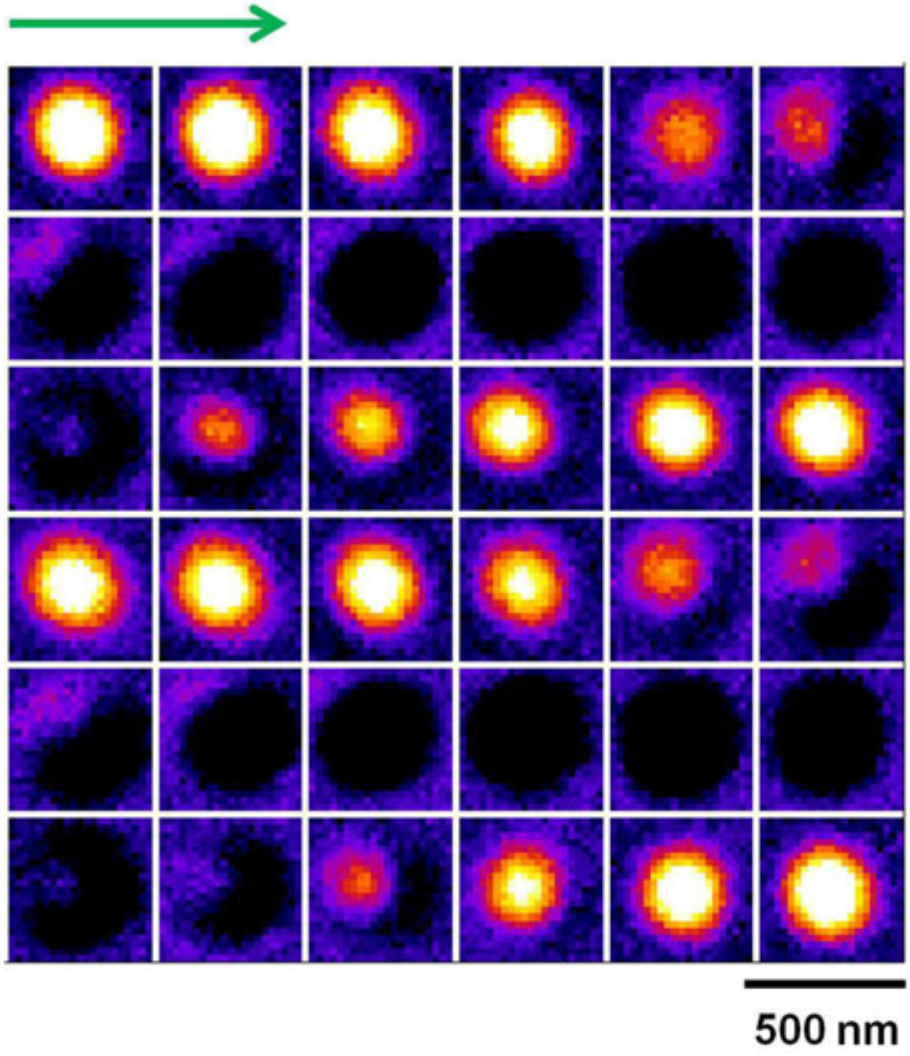

Figure S3. A complete set of DIC images of single Au nanorod (25 nm × 73 nm) at 36 orientations from 0° to 360° with an increment of 10°. The nanorod is excited at 700 nm close to its longitudinal SPR mode. The DIC image patterns change periodically as a function of orientation angle.

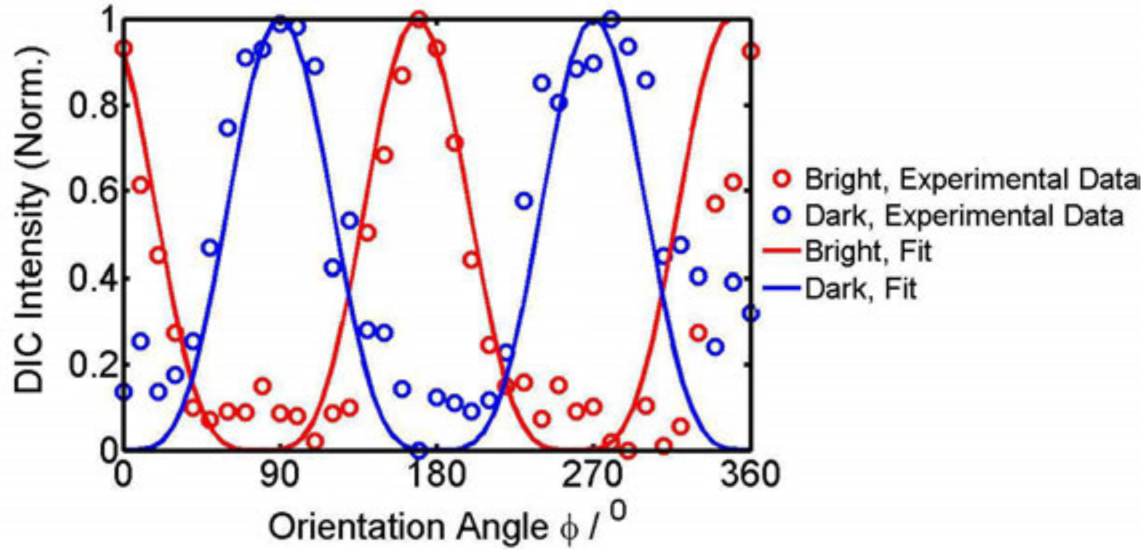

Figure S4. DIC Intensity profiles of the Au nanowire 1 in Figure 2 as a function of orientation angle φ. The normalized bright (red-curve) and dark (blue-curve) DIC intensities were fitted with functions of $\sin^2(\varphi)$ and $\cos^2(\varphi)$, respectively.

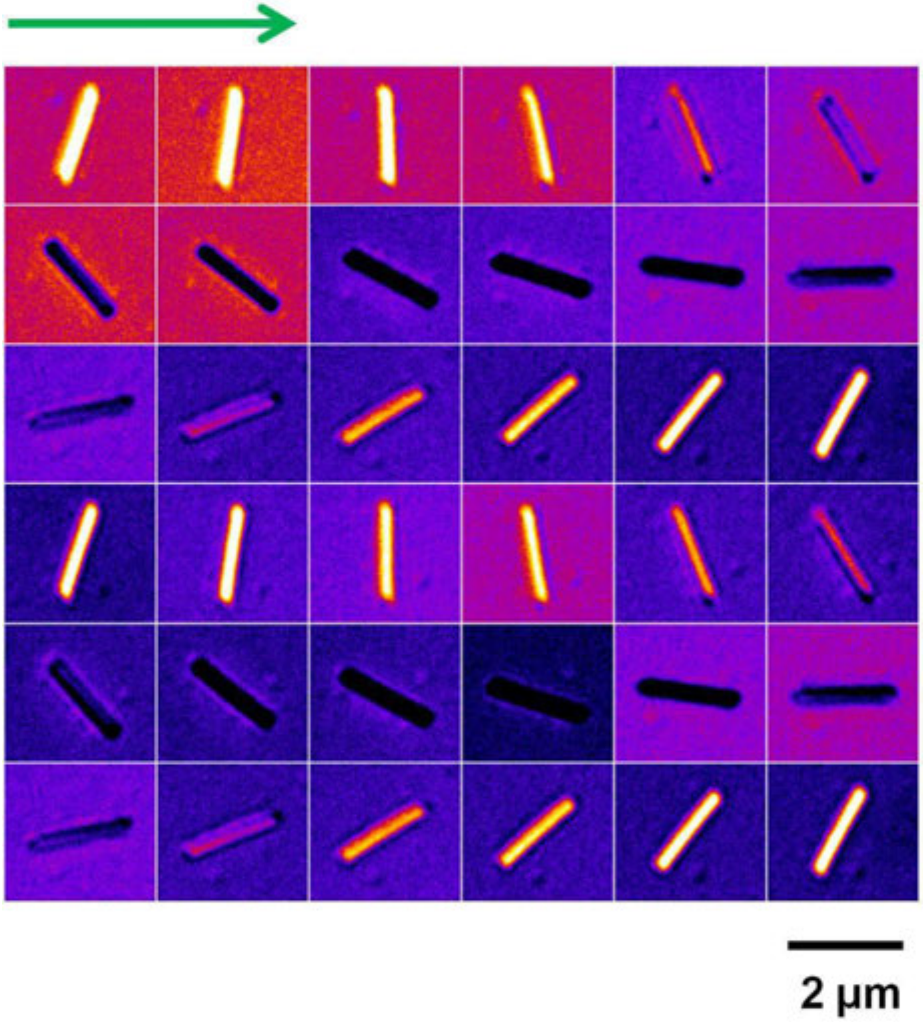

Figure S5. A complete set of DIC images of the highlighted Au nanowire 2 in Figure 3. The nanowire is excited at 550 nm. The image patterns are changed periodically as a function of orientation angle φ from 0° to 360° with an increment of 10°.

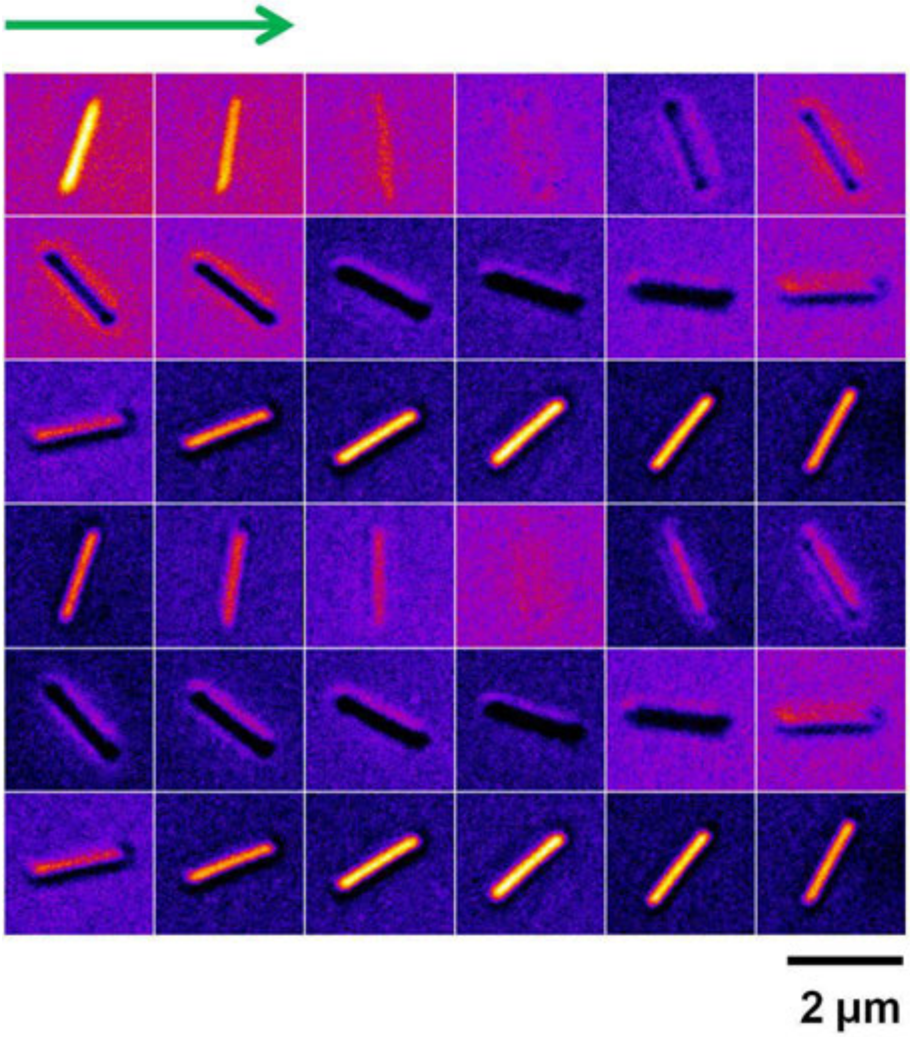

Figure S6. A complete set of DIC images of the highlighted Au nanowire 2 in Figure 3 at the excitation wavelength of 640 nm. The image patterns are changed periodically as a function of orientation angle φ from 0° to 360° with an increment of 10°.

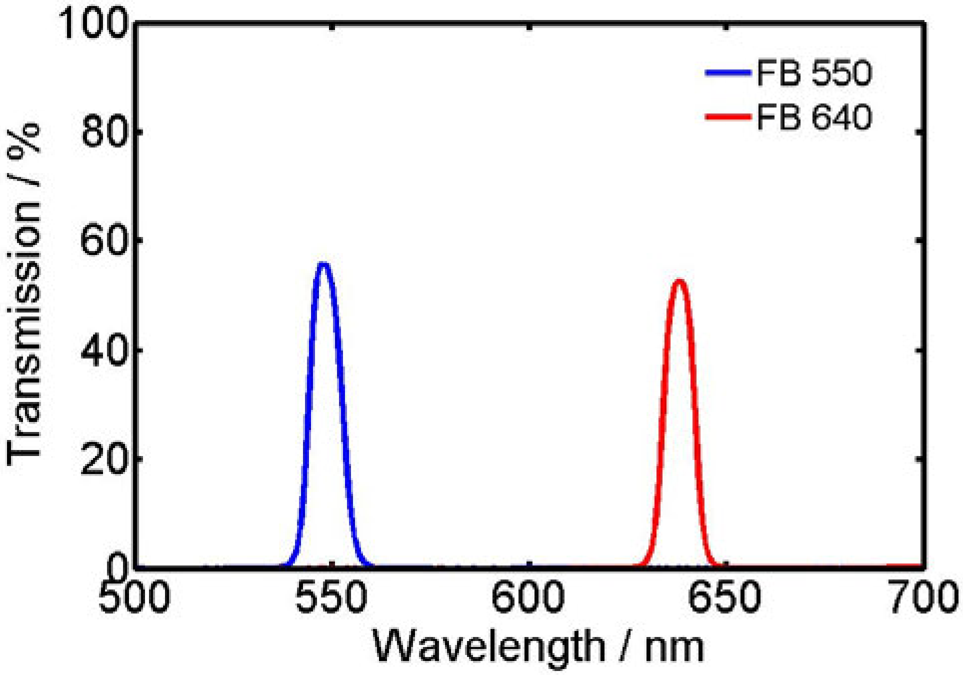

Figure S7. Transmission of two band-pass filters of 550 nm (blue-curve) and 640 nm (red-curve). The band width (FWHM) is 10 nm for both filters.

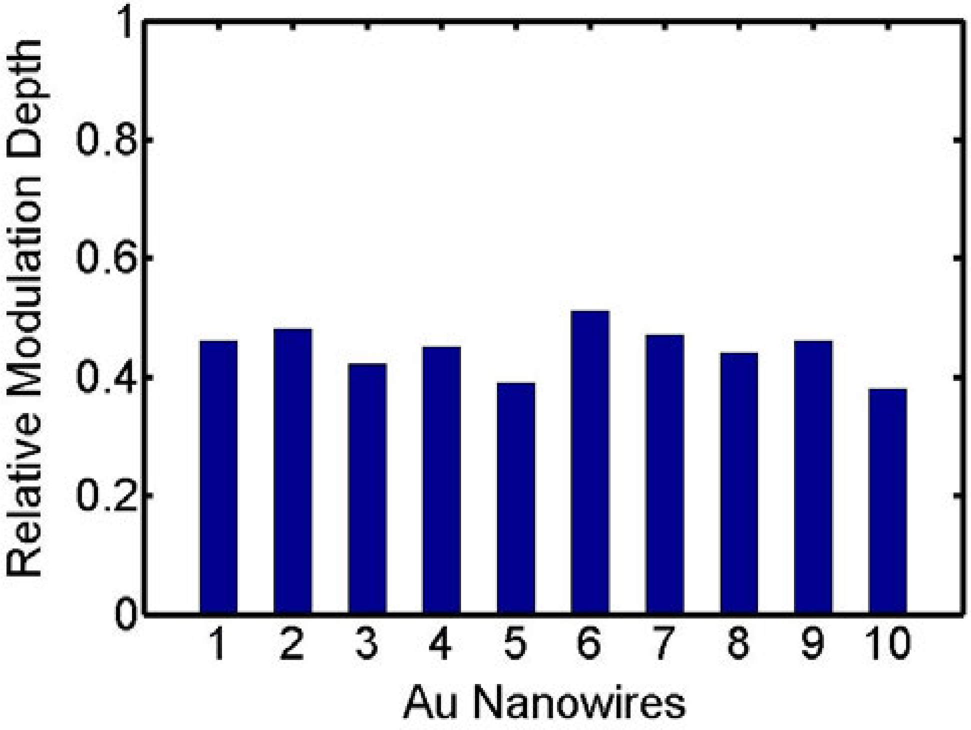

Figure S8. Relative modulation depth of individual Au nanowires at two SPR wavelengths of 550 nm and 640 nm. When the modulation depth at 550 nm was 1, the relative modulation depth at 640 nm was determined for each nanowire. The average relative modulation depth for 10 nanowires is 0.45.

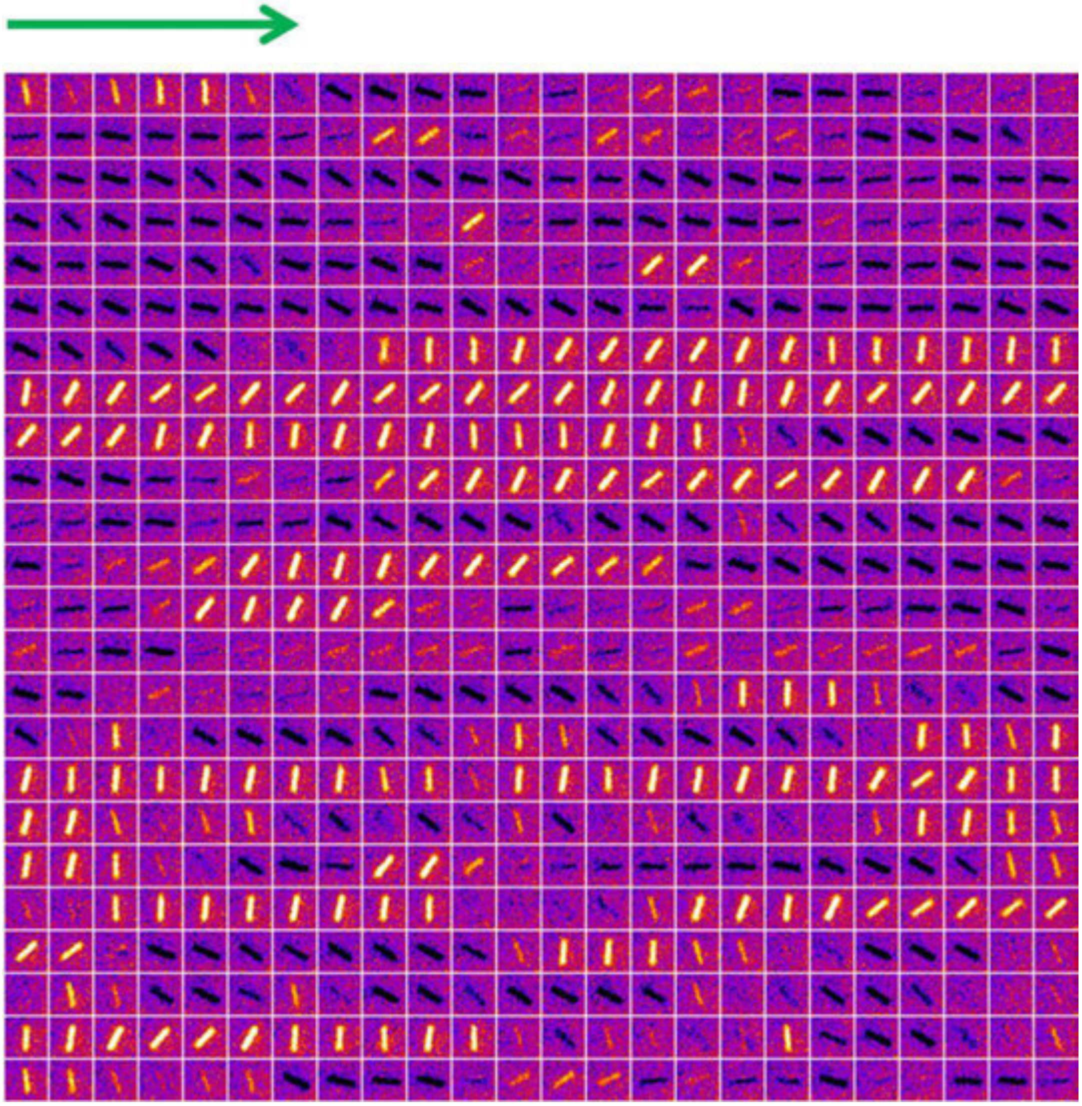

Figure S9. DIC images of the highlighted Au nanowire 3 in Figure 5 as a function of time. The successive images are from Movie S1 and are obtained by 550-nm excitation. Temporal resolution is 100 ms.

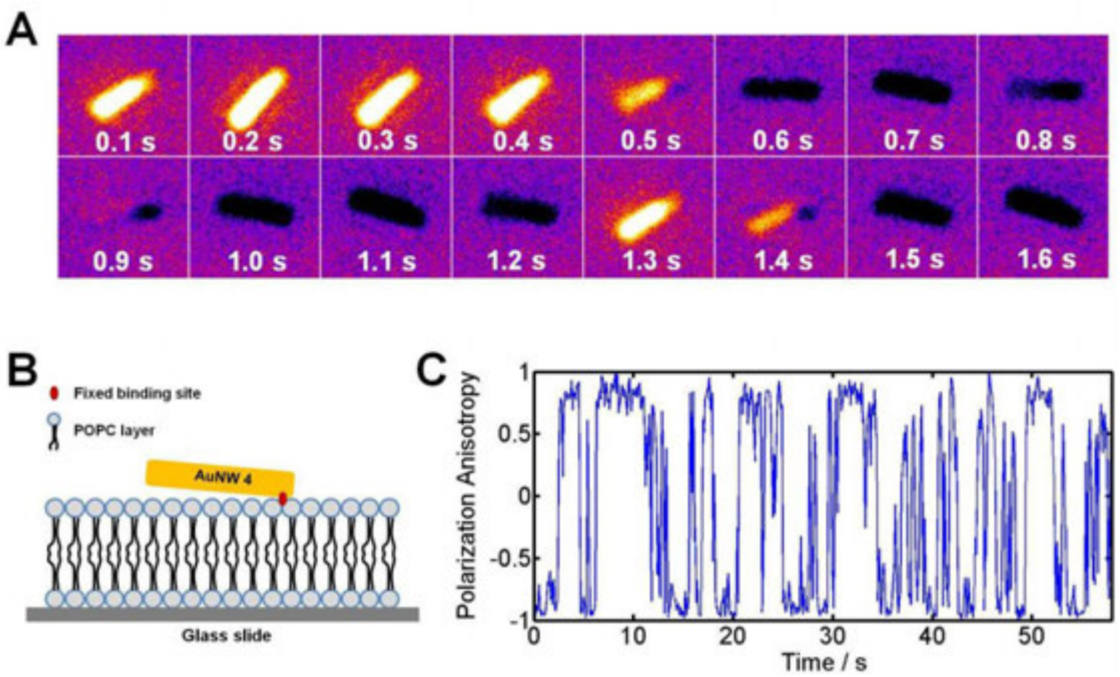

Figure S10. (A) 16-successive DIC images of the nanowire 4 in Figure 5 as a function of time. Temporal resolution is 100 ms. (B) Schematic of the nanowire 4 that has one fixed binding site at the end on the membrane. (C) DIC Polarization anisotropy for the nanowire 4 as a function of time.

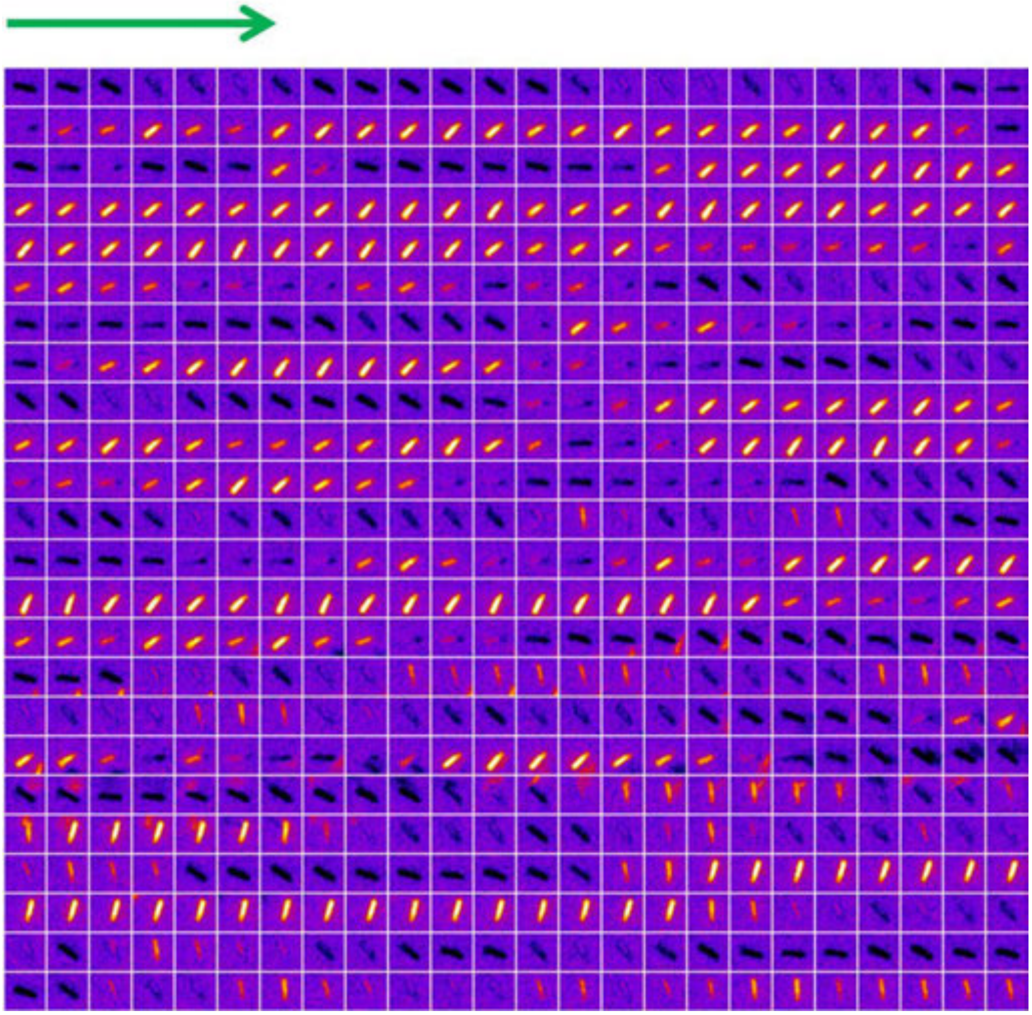

Figure S11. DIC images of the highlighted Au nanowire 4 in Figure 5 as a function of time. The successive images are from Movie S2 and are obtained by 550-nm excitation. Temporal resolution is 100 ms.

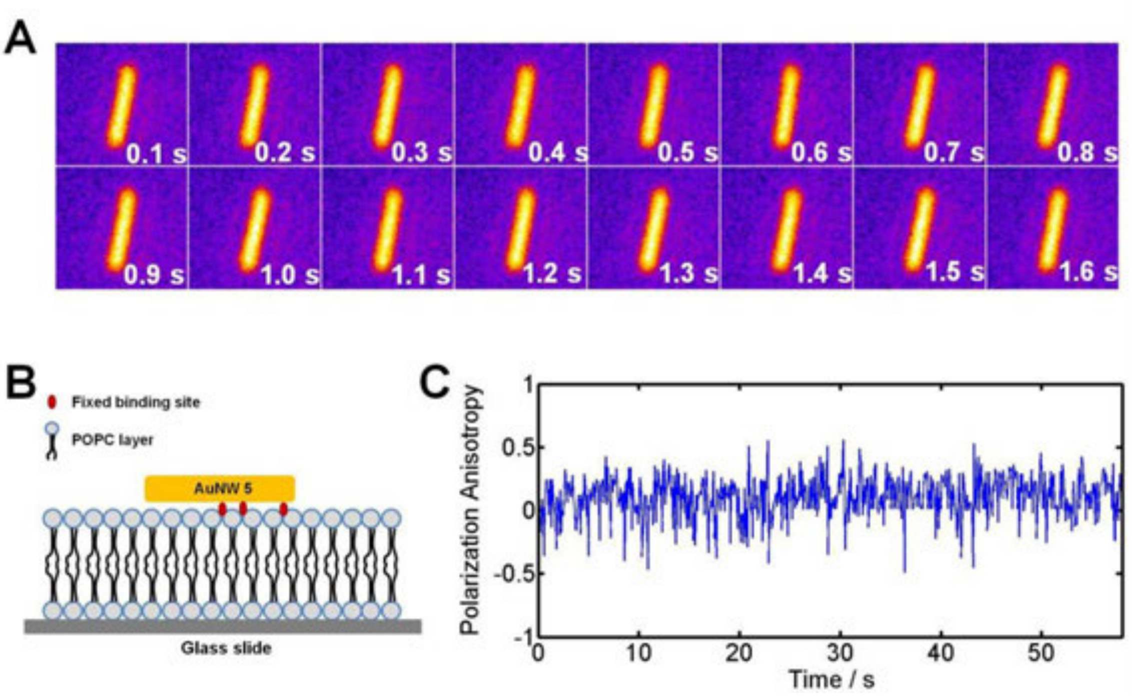

Figure S12. (A) 16-successive DIC images of the nanowire 5 in Figure 5 as a function of time. Temporal resolution is 100 ms. (B) Schematic of the nanowire 5 that has multiple fixed binding sites on the membrane. (C) DIC polarization anisotropy for the nanowire 5 as a function of time.

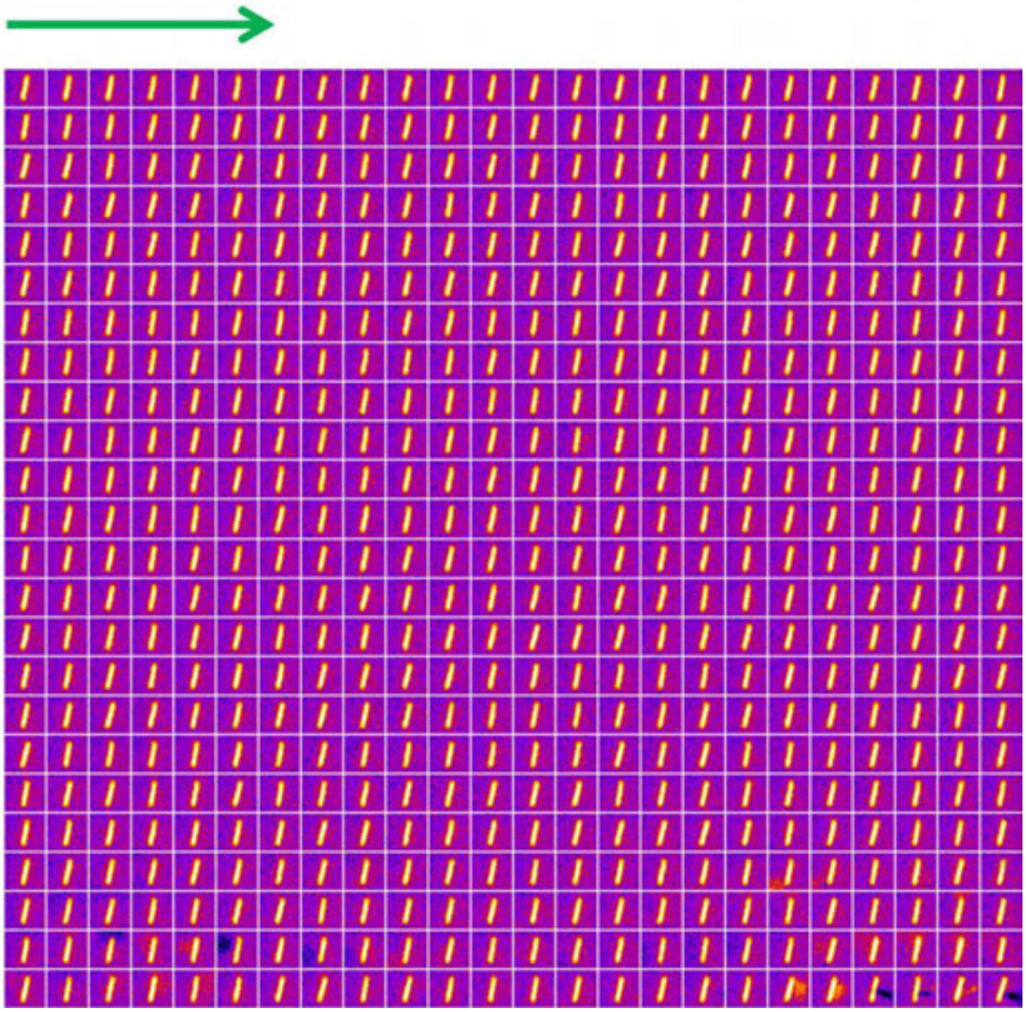

Figure S13. DIC images of the highlighted Au nanowire 5 in Figure 5 as a function of time. The successive images are from Movie S3 and are obtained by 550-nm excitation. Temporal resolution is 100 ms.

CHAPTER 6. FOCUSED ORIENTATION AND POSITION IMAGING (FOPI) OF SINGLE PLASMONIC NANOPARTICLES BY TOTAL INTERNAL REFLECTION SCATTERING MICROSCOPY

Ji Won Ha, Kyle Marchuk, and Ning Fang*

A paper published in *Nano Letters* 2012, 12, 4282-4288.

Reproduced by permission of The American Chemical Society (ACS)

* Corresponding author

Abstract

The defocused orientation and position imaging (DOPI) and polarization-based in-focus imaging techniques have been widely used for detecting rotational motions with anisotropic gold nanorods (AuNRs) as orientation probes. However, these techniques have a number of significant limitations, such as the greatly reduced signal intensity and relatively low spatial and temporal resolutions for *out-of-focus* AuNRs and the angular degeneracy for *in-focus* AuNRs. Herein, we present a total internal reflection (TIR) scattering-based focused orientation and position imaging (FOPI) of AuNRs supported on a 50-nm thick gold film, which enables us to overcome the aforementioned limitations. Imaging AuNRs under the TIR scattering microscope provides excellent signal-to-noise ratio and results in no deteriorating images. The scattering patterns of AuNRs on the gold substrate are affected by the strong interaction of the excited dipole in the AuNR with the image dipole in the gold substrate. The doughnut-shaped scattering field distribution allows for high-throughput determination of the full three-dimensional spatial orientation of *in-focus* AuNRs within a single frame without angular degeneracy. Therefore, the TIR

scattering-based FOPI method is demonstrated to be an outstanding candidate for studying dynamics of functionalized nanoparticles on a large variety of functional surfaces.

Introduction

Single molecule and particle rotational tracking with optical microscopy is of great significance to elucidate many important phenomena in biological and physical sciences. For example, the mechanistic functions of molecular nanomachines, such as ribozyme folding,[1] myosin walking,[2] dynamin assembly twisting,[3] and ATPase rotating,[4] have been imaged in real time. Fluorescence anisotropy utilizing dye molecules as orientation probes has been widely used to extract orientation and rotational information.[5-7] However, the time-dependent fluctuations in fluorescence signals and limited observation time for fluorescent molecules are generally considered the major drawbacks.[8-10] One solution to these issues is to replace fluorescent molecules with plasmonic gold nanorods (AuNRs) that possess shape-induced anisotropic optical properties,[11] large scattering and absorption cross-sections,[12] high-photostability,[12,13] and excellent biocompatibility.[14]

A few polarization-based optical imaging methods have been reported to resolve the orientation of individual AuNRs in the focal plane, including dark-field (DF) polarization microscopy,[11,15] photothermal heterodyne imaging (PHI),[16] and differential interference contrast (DIC) polarization anisotropy.[17-21] The core idea of these methods is to separate the light from a single AuNR into two orthogonal polarization directions and detect the signals in two channels. However, in these polarization-based *in-focus* measurements, only the in-plane orientation is effectively obtained while the out-of-plane orientation is either unattainable (such as in DF or PHI) or still ambiguous due to the much worse out-of-plane angular resolution (such as in DIC). Furthermore, the angular degeneracy, which refers to the inability to differentiate the nanorod orientations in the four quadrants of the Cartesian coordinate system due to the symmetric cylindrical shape, limits the applications in single particle orientation and rotational tracking (SPORT). The angular degeneracy for in-focus nanorods in DIC can be partially circumvented by combining DIC polarization anisotropy measurement with image pattern recognition to resolve the orientation of a AuNR that is tilted with respect to the horizontal object plane;[22] however, the relatively low signal intensity for a tilted nanorod leads to reduced angular resolution, and it is challenging to maintain the optimal tilted position of a nanorod during a dynamic process.

Besides the in-focus imaging techniques, the defocused orientation and position imaging (DOPI) techniques have been reported to have the capability of determining the 3D orientation of *out-of-focus* AuNR without angular degeneracy.[2,23-27] The DOPI techniques are based on the electron transition dipole approximation and the fact that the dipole radiation exhibits an angular anisotropy. The core idea is that the direct detection of the spatial distribution of the scattered or emitted field of single dipoles becomes possible when an aberration is deliberately applied to the imaging system. However, the DOPI techniques do not always yield the accurate orientation due to the greatly decreased signal intensity, and it is often required to switch back and forth between focused and defocused imaging to obtain more accurate orientation and position measurements.[2]

In the present study, we report a total internal reflection (TIR) scattering-based focused orientation and position imaging (FOPI) technique to overcome the aforementioned limitations of the existing in-focus polarization anisotropy and DOPI techniques. TIR fluorescence or scattering microscopy is a highly sensitive wide-field imaging technique with greatly reduced background noise.[28,29] We demonstrate that the scattered light from a single AuNR in the focal plane of the objective can be used directly to resolve the 3D spatial orientation without angular degeneracy using a single frame captured by a TIR scattering microscope. The core idea of the FOPI method is to use the effect of supporting substrate on the far-field scattering patterns of plasmonic nanoparticles.[30-37] For a single AuNR supported on a gold film, the in-plane (parallel to the film) dipole of the AuNR is damped by the image dipole in the gold film, while the out-of-plane (perpendicular to the film) dipole of the AuNR is enhanced. As a result, the point spread function (PSF) intensity distribution at the image plane has a characteristic doughnut shape. Interestingly, this doughnut-shaped far-field scattering pattern can also provide the 3D spatial orientation without suffering from the angular degeneracy, deteriorating image quality, or greatly reduced signal intensity.

Experimental Section

Materials and Sample Preparation. AuNRs with an average size of 25 nm × 60 nm were purchased from Nanopartz as a colloidal suspension (Salt Lake, UT). Two absorption peaks appear at 521 and 628 nm in the UV-Vis absorption spectrum (Figure S1), which was collected with a Varian Cary 300 UV-Vis spectrophotometer. The AuNR colloid solution was first diluted with 18.2-MΩ pure water to a proper concentration. The diluted solution was then sonicated for 15 min at room temperature. The sample was prepared by spin casting the diluted solution either on the pre-cleaned glass slide or on the gold film deposited on the cleaned glass slide. The concentration of AuNRs deposited on the gold film surface was controlled to be 1 μm^{-2} in order to facilitate single AuNR characterization and to minimize inter-particle SPR coupling resulting in the spectral shift. A 22 mm × 22 mm No. 1.5 coverslip (Corning, NY) was then placed on the glass slide. Finally, the sample slide was set on the prism surface for measurement.

Preparation of the Gold Film Substrate. The glass slides were thoroughly cleaned in an ultrasonic bath twice in Contrad 70 liquid detergent solution (Decon Laboratories, PA), four times in 18.2-MΩ pure water, and twice in pure ethanol. Each cleaning step lasted 20 min. After being blown dry with pure nitrogen gas, the glass slides were deposited with 50 nm gold by using an Airco Temscal BJD1800 electron beam evaporator (Berkeley, CA) equipped in Microelectronics Research Center (MRC) of Iowa State University.

Instrumentation and TIR Imaging of AuNRs. Figure S2 shows the schematic representation of the apparatus that is modified from the previously published configuration (Sun, W.; Marchuk, K.; Wang, G.; Fang, N. *Anal. Chem.* **2010**, *82*, 2441–2447). In order to reduce the sample drifting, the original microscope stage was replaced with a Sutter MP-285 motorized 3D translational stage (Novato, CA). An equilateral fused silica prism (Melles Griot, Albuquerque, NM) was housed in a homemade prism holder that was fixed on the Sutter stage. A 40-mW (max power) 647 nm solid-state continuous wave (CW) laser (Coherent, Santa Clara, CA) and a 100 W Xenon lamp were employed for excitation. The laser beam was first pointed to a periscope, passed through a Uniblitz mechanical shutter (model LS2Z2, Vincent Associates, Rochester, NY) and a focusing lens (15-cm focal length), and then directed toward the mirror of a galvanometer optical scanner (model 6220, Cambridge Technology, Cambridge, MA). The focusing lens was used to control the laser spot size in the imaging area. The mirror galvanometer is coupled to a high precision motorized linear stage (model MAA-PP, Newport, Irvine, CA) and directs the focused laser beam through the equilateral prism to the interface at different incident angles. A half-wave Fresnel rhomb retarder (Thorlabs, Newton, NJ) was placed in the beam path to switch from s- to p- polarizations. For both polarized excitations, the laser output power was adjusted to 1 mW. White light was directed through an optical fiber to the prism sidewall for illumination. The angle of incidence at the metal film is ~45°. A Nikon Plan Fluor 100× 0.7-1.3 oil iris objective with its NA set to 0.7 was utilized in this measurement. All the scattering images were captured with an Andor iXonEM+ 897 CCD camera (Belfast, Northern Ireland). The collected images were analyzed by MATLAB and NIH ImageJ (http://rsbweb.nih.gov/ij/).

Results and Discussion

The AuNRs used in this study have an average size of 25 nm × 60 nm (aspect ratio 2.4). In the UV-Vis absorption spectrum of this colloidal AuNR solution (Figure S1 in the Supporting Information), the peaks at 521 and 628 nm correspond to the transverse and longitudinal surface plasmon resonance (SPR) modes, respectively. The sample slides were prepared by placing the AuNRs either on a glass slide or on a gold film (~50 nm thick). The sample slides were index-matched with immersion oil on the top surface of a prism and illuminated by either a Xenon lamp (white light) or a 647-nm continuous wave laser using the TIR geometry (Figure S2). The experimental setup was modified from the previously published configuration.[38]

The SPR of 60-nm gold nanospheres in a uniform dielectric medium of air has a peak at 535 nm; in contrast, when the same nanosphere is placed on a gold film (~50 nm thick), the SPR peak is dramatically red-shifted to ~655 nm.[31] This spectral shift is consistent with the interaction between two closely spaced nanoparticles with the incident electric field polarized parallel to the line connecting the nanoparticle centers.[39,40] As an important consequence, the wavelength (647 nm) of the laser used in the present study is close to either the longitudinal SPR mode of AuNRs on a glass slide or the transverse SPR mode of AuNRs on a gold film.

Using the TIR geometry, a thin evanescent field (only a few hundred nanometers thick) is created at the interface of two media to excite the AuNRs on the sample slide. The coupling to the AuNRs allows the light to scatter into the far-field and be captured by a camera. To the best of our knowledge, this is the first report to acquire the detailed information on far-field scattering patterns of anisotropic AuNRs on different substrates by using a TIR scattering microscope.

Figure 1 shows a comparison of the scattering patterns of AuNRs on two different surfaces under TIR white light illumination. The scattering pattern appears as a solid bright spot (Figure 1B) when the AuNR is deposited on a glass slide, or a doughnut shape (Figure 1E) when the AuNR is deposited on a gold film. These distinctive scattering patterns are consistent with the previous report.[37] Intensity line sections are drawn across the center of the scattering patterns. We note that the background scattering of the gold film (Figure 1F) is about 3 times higher than that of the glass slide (Figure 1C), which can be explained by the fact that TIR illumination induces the resonances of both gold film and nanoparticles simultaneously.

AuNRs that are much smaller than the wavelength of the incident light can be considered electric point dipoles. According to the electrostatic approximation, the overall scattering electrical field from an anisotropic AuNR can be quantified through linear superposition of three independent scattering electric fields associated with three mutually orthogonal dipoles.[23,41] Therefore, the orientation of a single AuNR may be resolved by characterizing the scattering intensity distribution from each dipole. To clearly demonstrate this, the proof of concept experiments have been performed as described below under the TIR scattering microscope.

Using the 647-nm laser as the excitation source, we imaged the transverse SPR mode of AuNRs deposited on the gold film. The electric field associated with the incident light can be decomposed into s- (parallel to the substrate) and p- (perpendicular to the substrate) polarized components. These two electric field components selectively excite the AuNR's electric point dipoles that are oriented parallel (in-plane dipole) or perpendicular (out-of-plane dipole) to the gold substrate, as shown schematically in Figures 2A and 2C. A high-contrast doughnut-shaped intensity distribution is observed under p-polarized excitation (Figure 2B), while the scattering intensity decreases greatly when the same AuNR is imaged under s-polarized excitation (Figure 2D). The different scattering field distributions can be ascribed to the induced image charge model, which predicts that s- and p- polarized excitations result in destructive and constructive interference, respectively. In this study, p-polarized excitation selectively excites the AuNR's out-of-plane transverse dipole perpendicular to the substrate and creates an image charge dipole that is in phase with the AuNR's out-of-plane dipole, resulting in constructive interference. It should be noted that the doughnut-shaped scattering pattern is formed by the net out-of-plane transverse dipole and directly portrays the scattering intensity distribution from this dipole. On the other hand, s-polarized light selectively excites the AuNR's in-plane transverse dipole parallel to the substrate and induces an image charge dipole that is out of phase with the AuNR's in-plane dipole, resulting in destructive interference and a strongly damped far-field scattering intensity.

More interestingly, when a single AuNR is tilted from the surface and measured by p-polarized light, the net out-of-plane dipole torus is no longer circularly symmetric (Figure 2E). This yields a change in the doughnut-shaped scattering pattern (Figure 2F) and enables us to resolve the spatial orientation of the AuNR in the focal plane of the objective.

We can now account for the observed doughnut-shaped scattering pattern in Figure 1E. Unlike separated s- or p- polarized laser excitation, the total far-field scattering intensity from a single AuNR measured by TIR white light illumination is contributed from both the in-plane and out-of-plane dipoles. The observed scattering pattern depends on the relative magnitudes of the net in-plane and out-of-plane dipoles. In Figure 1E, the out-of-plane dipole makes the dominant contribution towards the final doughnut-shaped scattering field distribution.

The numerical aperture (NA) of the objective also has an influence on the scattering pattern and signal intensity. An objective with a smaller NA produces clearer scattering patterns with enhanced signal-to-noise ratio (SNR) due to the much decreased noise and background scattering (Figure S3, see details in the Supporting Information).

Therefore, a smaller NA value of 0.7 was used in all of the TIR scattering experiments with AuNRs on a gold film.

The DOPI techniques have been widely used to decipher the 3D orientation of AuNR from a single image.[2,23-27] To compare the DOPI techniques with the FOPI method presented in this paper, AuNRs supported on a glass slide were first visualized by s-polarized TIR excitation at 647 nm (close to the longitudinal SPR mode). The polar angle θ and the azimuthal angle φ of a AuNR in 3D space are defined in Figure 3A. The azimuthal angle φ can be in any of the four quadrants (Regions R1 to R4) of the Cartesian plane. As shown in Figure 3B, the scattered light from a nanorod in the focal plane of the objective is focused into a solid bright spot, which gives little information about the 3D orientation of the AuNR's emission dipole. However, when the AuNR is positioned at ~1 μm away from the focal plane, the intensity distribution of the blurred image provides information about the AuNR's emission dipole orientation (Figure 3C). The in-plane orientation angle φ can be readily extracted from the two-lobe scattering pattern exhibiting angular anisotropy. The out-of-plane polar angle θ was determined by using the program developed by Enderlein and Böhmer for simulating the characteristic intensity distribution from an emitter with three perpendicular emission dipoles of different emission strength.[24,25] The orientation of a AuNR on a glass substrate can be determined by referring to their corresponding field map. The best-fit simulated scattering pattern (Figure 3D) is obtained by adjusting the parameters defining the orientation angles and the emission strength of three mutually orthogonal oscillation dipoles of AuNR.

To gain the information on 3D orientation, the DOPI techniques sacrifice spatial resolution due to the greatly reduced image contrast and enlarged image size, and temporal resolution due to the requirement to switch back and forth between focused and defocused imaging for obtaining more accurate orientation and position. In contrast, it is notable that the FOPI method enables us to decipher the 3D spatial orientation of AuNRs located in the focal plane of the objective without suffering from the limitations of the DOPI techniques. To clearly support this claim, we imaged the transverse SPR mode of AuNR on the gold film by p-polarized TIR illumination at 647 nm. The intensity distribution of the focused doughnut-shaped scattering pattern (Figure 3F) provides the information about the AuNR's out-of-plane dipole orientation without introducing any image deterioration. Figure 3G shows the defocused image of the same AuNR with intentionally introduced aberrations. The defocused image is much broader and contains more lobes in the peripheral area. The polar and azimuthal angles of the AuNR are determined to be 88° and 46°, respectively, by comparing the measured scattering pattern (Figure 3F) with the best-fit simulated scattering pattern (Figure 3H) obtained from the same simulation program.[24,25]

It is worthwhile to point out two additional considerations of these image patterns. First, both focused (Figure 3F) and defocused (Figure 3G) scattering patterns provided the spatial orientation of AuNRs, which suggests another advantage of the FOPI method that the doughnut-shaped scattering pattern in FOPI is less sensitive to aberrations in the objective, e.g., a focus drift, than the DOPI techniques. Second, the TIR scattering microscope provides excellent SNR even at a low laser output power (~1 mW in our experiments): for AuNRs with an average size of 25 nm × 60 nm, the SNR is 248 in

Figure 3B for the excitation of the longitudinal SPR mode on a glass slide and 125 in Figure 3F for the excitation of the transverse SPR mode on a gold film.

Next, we compare the polarization-based in-focus imaging methods[11,15-21] with the FOPI method. The angular degeneracy resulted from the 2-fold symmetry of AuNR is considered a major drawback of the polarization-based methods (Figure S4). The FOPI technique overcomes this limitation and is capable of fast and high-throughput detection of 3D orientations of a large number of in-focus AuNRs without angular degeneracy. Figure S5 in the Supporting Information shows a typical FOPI image of randomly oriented AuNRs on a gold film, measured by p-polarized excitation. The diverse scattering patterns show that the orientations of these AuNRs are highly varied. Four single AuNRs having different azimuthal angles in the four quadrants of the Cartesian plane are randomly selected, and their 3D orientation angles are subsequently determined by fitting with the simulated patterns (Figure 4).

Conclusions

A high-throughput FOPI method with 3D orientation resolvability for single in-focus AuNRs supported on a gold film is demonstrated to overcome the limitations of both the polarization-based methods and the DOPI methods. Under p-polarized laser TIR excitation, AuNRs give rise to characteristic doughnut-shaped scattering patterns due to the strong coupling between the AuNR's out-of-plane transverse dipole and the induced image charge dipole in the gold substrate. The doughnut-shaped scattering patterns allow for direct and high-throughput detection of 3D orientations of in-focus AuNRs within a single frame without suffering from angular degeneracy or deterioration in image quality.

The FOPI method is introduced as a new approach using the interaction (or coupling) of AuNRs with their surrounding environment for determining the full 3D orientation of in-focus AuNRs, and it can be an outstanding tool in single-particle rotational tracking and sensing applications to study interactions between functionalized nanoparticles and a large variety of functional surfaces.

References

1. Zhuang, X.; Bartley, L. E.; Babcock, H. P.; Russell, R.; Ha, T.; Herschlag, D.; Chu, S. A. *Science* **2000**, *288*, 2048–2051.

2. Toprak, E.; Enderlein, J.; Syed, S.; McKinney, S. A.; Petschek, R. G.; Ha, T.; Goldman, Y. E.; Selvin, P. R. *Proc. Natl. Acad. Sci. U.S.A.* **2006**, *103*, 6495–6499.

3. Roux, A.; Uyhazi, K.; Frost, A.; De Camilli, P. *Nature* **2006**, *441*, 528–531.

4. Nishizaka, T.; Oiwa, K.; Noji, H.; Kimura, S.; Muneyuki, E.; Yoshida, M.; Kinosita, K. Jr. *Nat. Struct. Mol. Biol.* **2004**, *11*, 142–148.

5. Forkey, J. N.; Quinlan, M. E.; Goldman, Y. E. *Prog. Biophys. Mol. Biol.* **2000**, *74*, 1–35.

6. Khatua, S.; Guerrero, J. M.; Claytor, K.; Vives, G.; Kolomeisky, A. B.; Tour, J. M.; Link, S. *ACS Nano* **2009**, *3*, 351–356.

7. Chung, I.; Shimizu, K. T.; Bawendi, M. G. *Proc. Natl. Acad. Sci. U.S.A*. **2003**, *100*, 405–408.

8. Moerner, W. E.; Orrit, M. *Science* **1999**, *283*, 1670–1676.

9. Nirmal, M.; Dabbousi, B. O.; Bawendi, M. G.; Macklin, J. J.; Trautman, J. K.; Harris, T. D.; Brus, L. E. *Nature* **1996**, *383*, 802–804.

10. Xie, X. S.; Dunn, R. C. *Science* **1994**, *265*, 361–364.

11. Sönnichsen, C.; Alivisatos, A. P. *Nano Lett.* **2005**, *5*, 301–304.

12. Sperling, R. A.; Gil, P. R.; Zhang, F.; Zanella, M.; Parak, W. *Chem. Soc. Rev.* **2008**, *37*, 1896–1908.

13. Wu, X.; Yeow, E. K. L. *Nanotechnology* **2008**, *19*, 035706.

14. Murphy, C. J.; Gole, A. M.; Stone, J. W.; Sisco, P. N.; Alkilany, A. M.; Goldsmith, E. C.; Baxter, S. C. *Acc. Chem. Res.* **2008**, *41*, 1721–1730.

15. Xiao, L.; Qiao, Y.; He, Y.; Yeung, E. S. *J. Am. Chem. Soc.* **2011**, *133*, 10638–10645.

16. Chang, W. -S.; Ha, J. W.; Slaughter, L. S.; Link, S. *Proc. Natl. Acad. Sci. U.S.A.* **2010**, *107*, 2781–2786.

17. Ha, J. W.; Sun, W.; Wang, G.; Fang, N. *Chem. Commun.* **2011**, *47*, 7743–7745.

18. Ha, J. W.; Sun, W.; Stender, A. S.; Fang, N. *J. Phys. Chem. C* **2012**, *116*, 2766–2771.

19. Wang, G.; Sun, W.; Luo, Y.; Fang, N. *J. Am. Chem. Soc.* **2010**, *132*, 16417–16422.

20. Gu, Y.; Sun, W.; Wang, G.; Fang, N. *J. Am. Chem. Soc.* **2011**, *133*, 5720–5723.

21. Stender, A. S.; Wang, G.; Sun, W.; Fang, N. *ACS Nano* **2010**, *4*, 7667–7675.

22. Xiao, L.; Ha, J. W.; Wei, L.; Wang, G.; Fang, N. *Angew. Chem. Int. Ed.* **2012**, *accepted* (DOI: 10. 1002/anie.201202340).

23. Xiao, L.; Qiao, Y. X.; He, Y.; Yeung, E. S. *Anal. Chem.* **2010**, *82*, 5268–5274.

24. Böhmer, M.; Enderlein, J. *J. Opt. Soc. Am. B* **2003**, *20*, 554–559.

25. Enderlein, J.; Böhmer, M. *Opt. Lett*. **2003**, *28*, 941–944.

26. Lieb, M. A.; Zavislan, J. M.; Novotny, L. *J. Opt. Soc. Am. B* **2004**, *21*, 1210–1215.

27. Li, Q.; Xu, Y.; Chen, X. -J.; Dai, Q. -F.; Liu, H.; Lan, S.; Tie, S.; Wu, L. J. *ACS Nano* **2012**, *6*, 1268–1277.

28. Toshio, Y.; Yasushi, S.; Shigeru, M. *Nature Cell Biol.* **2000**, *2*, 168–172.

29. Marchuk, K.; Guo, Y.; Sun, W.; Vela, J.; Fang, N. *J. Am. Chem. Soc.* **2012**, *134*, 6108–6111.

30. Link, S.; El-Sayed, M. A. *J. Phys. Chem. B* **1999**, *103*, 4212–4217.

31. Mock, J. J.; Hill, R. T.; Degiron, A.; Zauscher, S.; Chilkoti, A.; Smith, D. R. *Nano Lett.* **2008**, *8*, 2245–2252.

32. Chen, S.-Y.; Mock, J. J.; Hill, R. T.; Chilkoti, A.; Smith, D. R.; Lazarides, A. A. *ACS Nano* **2010**, *4*, 6535–6546.

33. Hill, R. T.; Mock, J. J.; Urzhumov, Y.; Sebba, D. S.; Oldenburg, S. J.; Chen, S.-Y.; Lazarides, A. A.; Chilkoti, A.; Smith, D. R. *Nano Lett.* **2010**, *10*, 4150–4154.

34. Swanglap, P.; Slaughter, L. S.; Chang, W. -S.; Willingham, B.; Khanal, B. P.; Zubarev, E. R.; Link, S. *ACS Nano* **2011**, *5*, 4892–4901.

35. Chen, H.; Shao, L.; Ming, T.; Woo, K. C.; Man, Y. C.; Wang, J.; Lin, H. -Q. *ACS Nano* **2011**, *5*, 6754–6763.

36. Knight, M. W.; Wu, Y.; Lassiter, J. B.; Nordlander, P.; Halas, N. J. *Nano Lett.* **2009**, *9*, 2188–2192.

37. Chen, H.; Ming, T.; Zhang, S.; Jin, Z.; Yang, B.; Wang, J. *ACS Nano* **2011**, *5*, 4865–4877.

38. Sun, W.; Marchuk, K.; Wang, G.; Fang, N. *Anal. Chem.* **2010**, *82*, 2441–2447.

39. Slaughter, L. S.; Wu, Y.; Willingham, B. A.; Nordlander, P.; Link, S. *ACS Nano* **2010**, *4*, 4657–4666.

40. Liu, H.; Ng, J.; Wang, S. B.; Hang, Z. H.; Chan, C. T.; Zhu, S. N. *New J. Phys.* **2011**, *13*, 073040.

41. Link, S.; Mohamed, M. B.; El-Sayed, M. A. *J. Phys. Chem. B* **1999**, *103*, 3073–3077.

Figures and Captions

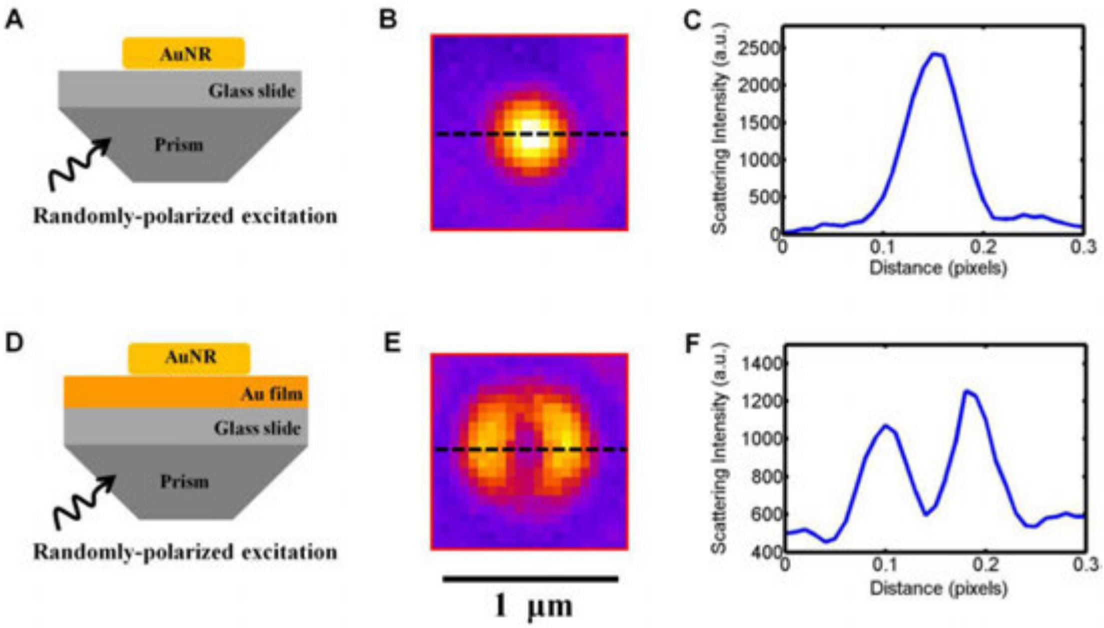

Figure 1. Influence of dielectric substrate on the far-field scattering patterns of AuNR under TIR white light illumination. (A) Schematic diagram, (B) scattering pattern and (C) intensity line-sectional profile for a single AuNR on a glass slide. (D-E) corresponding diagrams for a single AuNR on a gold film. The broken black lines in (B) and (E) indicate the intensity line sections.

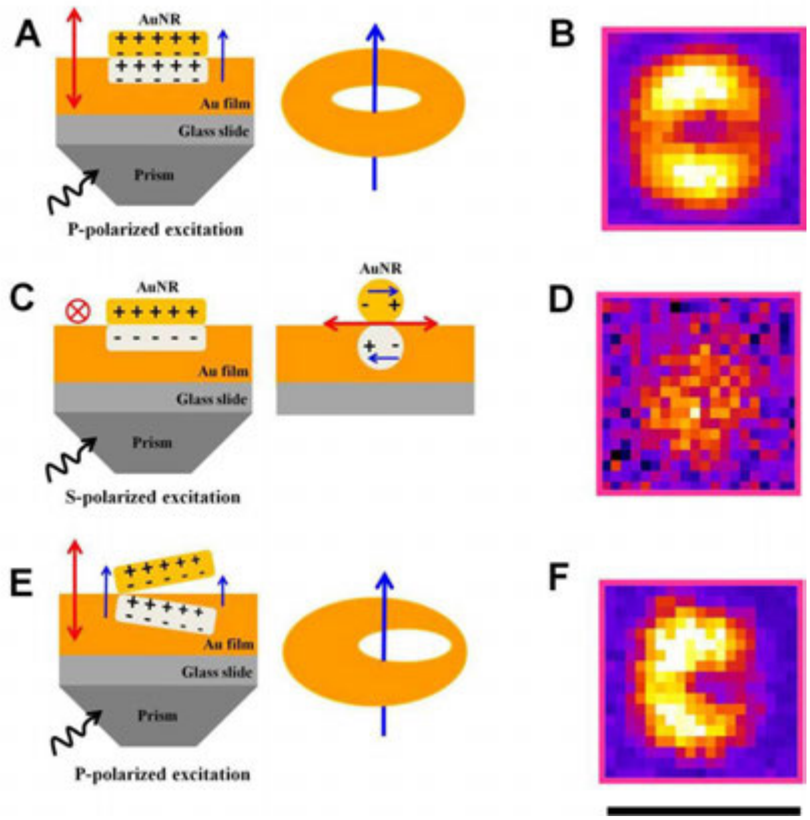

Figure 2. Far-field scattering patterns of a AuNR supported on a gold substrate under p- or s-polarized 647-nm laser excitation. (A) Schematic diagram for p-polarized excitation, and (B) the resulted doughnut-shaped scattering pattern. The dipole of the AuNR is perpendicular to the gold film and couples to the induced image dipole having the same direction, leading to constructive interaction. The radiation torus that is collected by the objective lens is illustrated. (C) Schematic diagram for s-polarized excitation, and (D) the significantly damped scattering intensity. The dipole of the AuNR parallel to the gold film is canceled out by the induced image dipole in the opposite direction. To clearly show the interaction of the AuNR dipole with the image dipole in the substrate, the AuNR is rotated by 90° in the schematic diagram. (E) Schematic diagram for a tilted AuNR under p-polarized excitation, and (F) the resulted scattering pattern. The net out-of-plane dipole torus is no longer circularly symmetric. The red arrows indicate the direction of the excitation polarizations, and the blue arrows indicate the dipoles. The scale bar represents 1 µm.

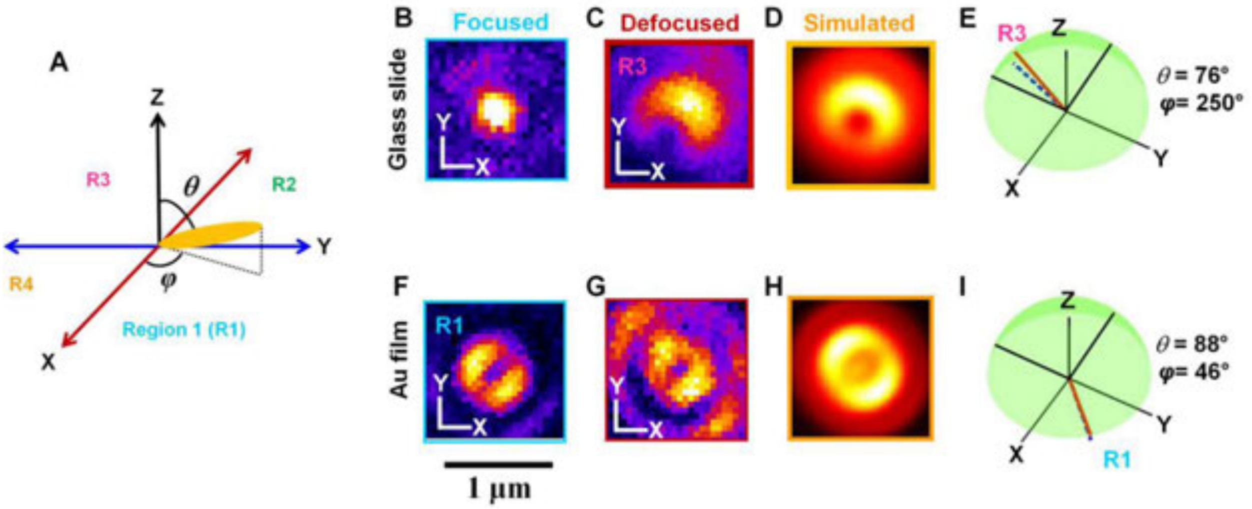

Figure 3. DOPI *vs*. FOPI. (A) Definitions of the polar angle θ and the azimuthal angle φ of a AuNR in 3D space. (B-E) Far-field scattering patterns of a AuNR on a glass slide under s-polarized excitation: focused image appearing as a solid bright spot (B), defocused image (C), the corresponding best-fit simulated scattering pattern (D), and the 3D illustration of the determined orientation ($\theta = 76°$ and $\varphi = 250°$) (E). (F-I) Far-field scattering patterns of a AuNR on a gold film under p-polarized excitation: a doughnut-shaped focused image (F), a defocused image (G), the corresponding best-fit simulated scattering pattern (H), and the 3D illustration of the determined orientations ($\theta = 88°$ and $\varphi = 46°$) (I). The defocusing distance is estimated to be ~1 μm. In (E) and (I), the red line shows the determined 3D orientation and the blue dotted line is the corresponding in-plane projection.

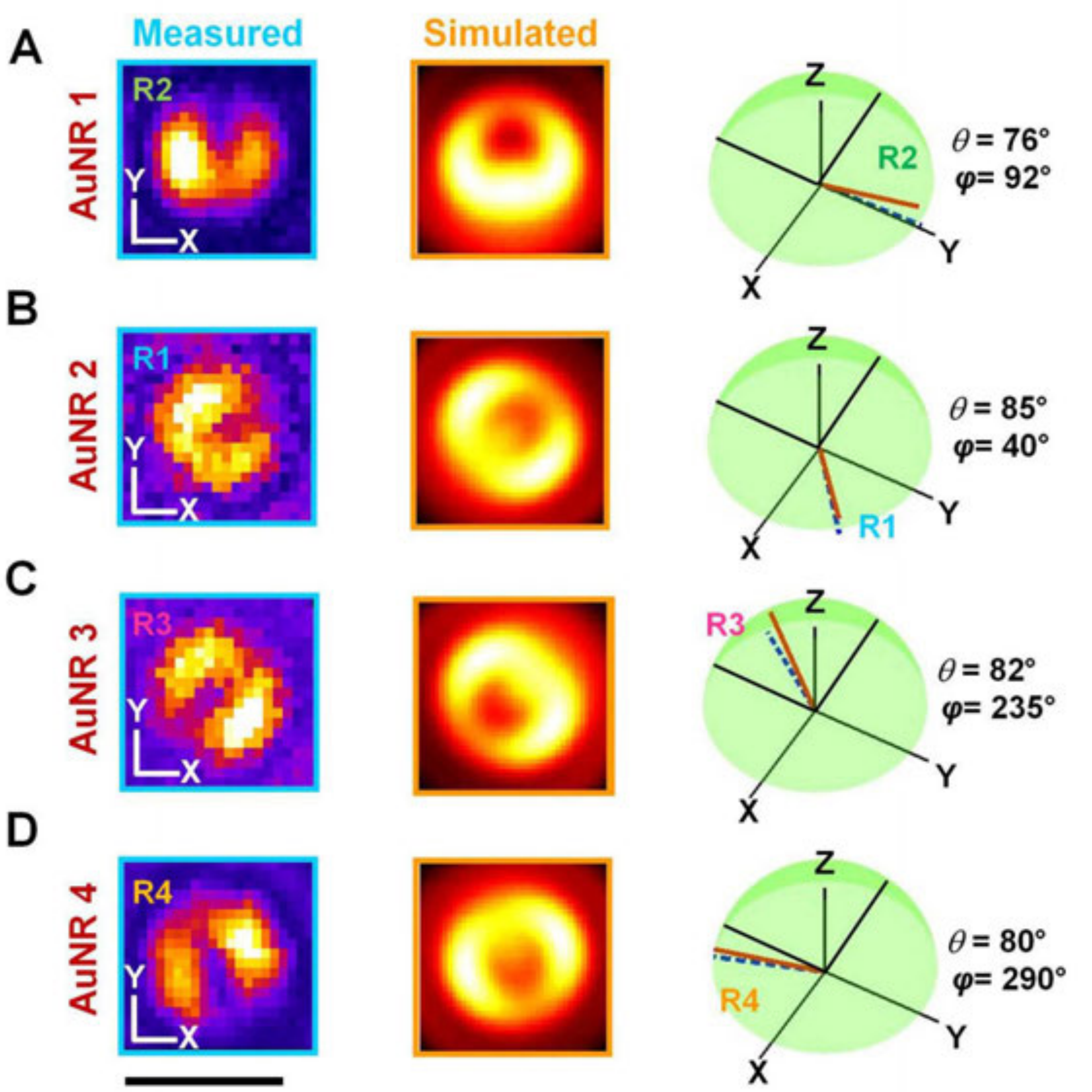

Figure 4. The measured (sky-blue) and best-matched simulation (orange) patterns from four randomly selected AuNRs in different orientations on a gold film. The simulated images match well with the measured patterns. The 3D spatial orientations of the four AuNRs determined through the pattern match analysis are illustrated. Note that the azimuthal angles are resolved without angular degeneracy in the four quadrants of the Cartesian plane. The scale bar represents 1 μm.

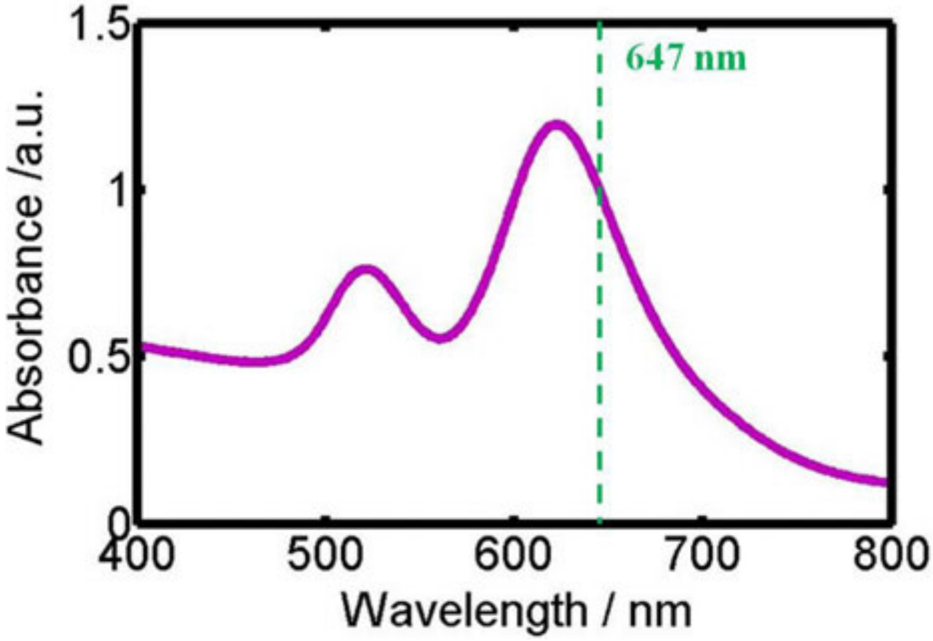

Figure S1. Ensemble absorption spectrum of AuNRs with an average size of 25 nm × 60 nm in aqueous solution. Two absorption peaks appear at 521 nm (transverse SPR) and 628 nm (longitudinal SPR). The green dotted line indicates the wavelength of laser excitation at 647 nm.

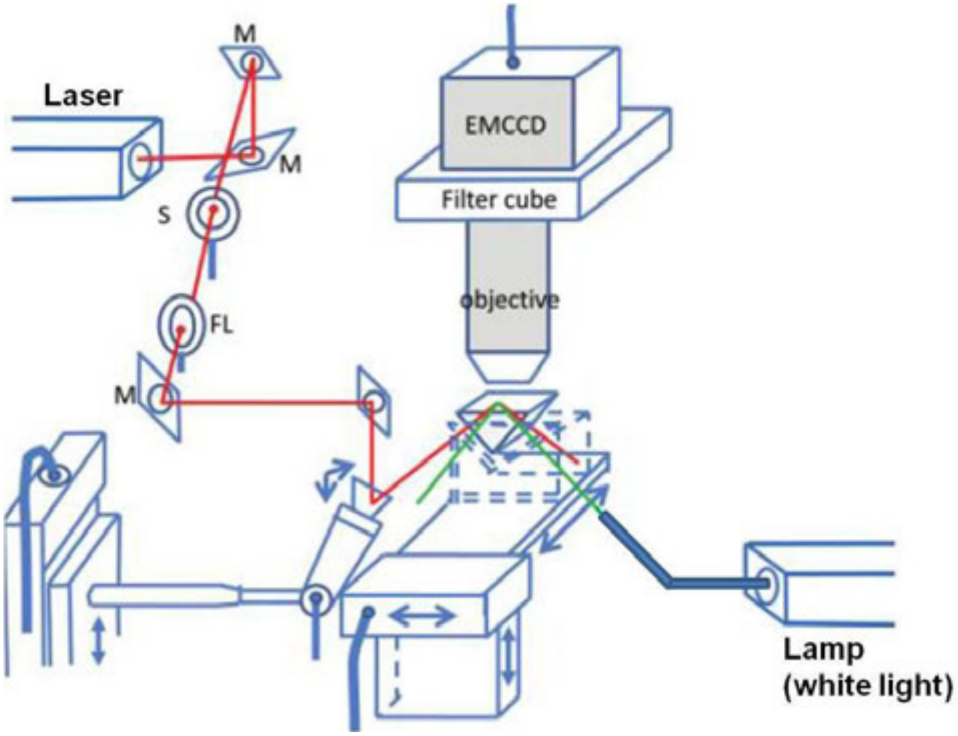

Figure S2. Schematic diagram of the automated prism-type scanning-angle total internal reflection (TIR) scattering microscope: M, mirror; S, mechanical shutter; FL, focusing lens. A half-wave Fresnel rhomb retarder is placed in the beam path to switch between s- and p- polarizations. Two excitation sources of a Xenon lamp (white light) and a 647 nm CW laser are used in this study.

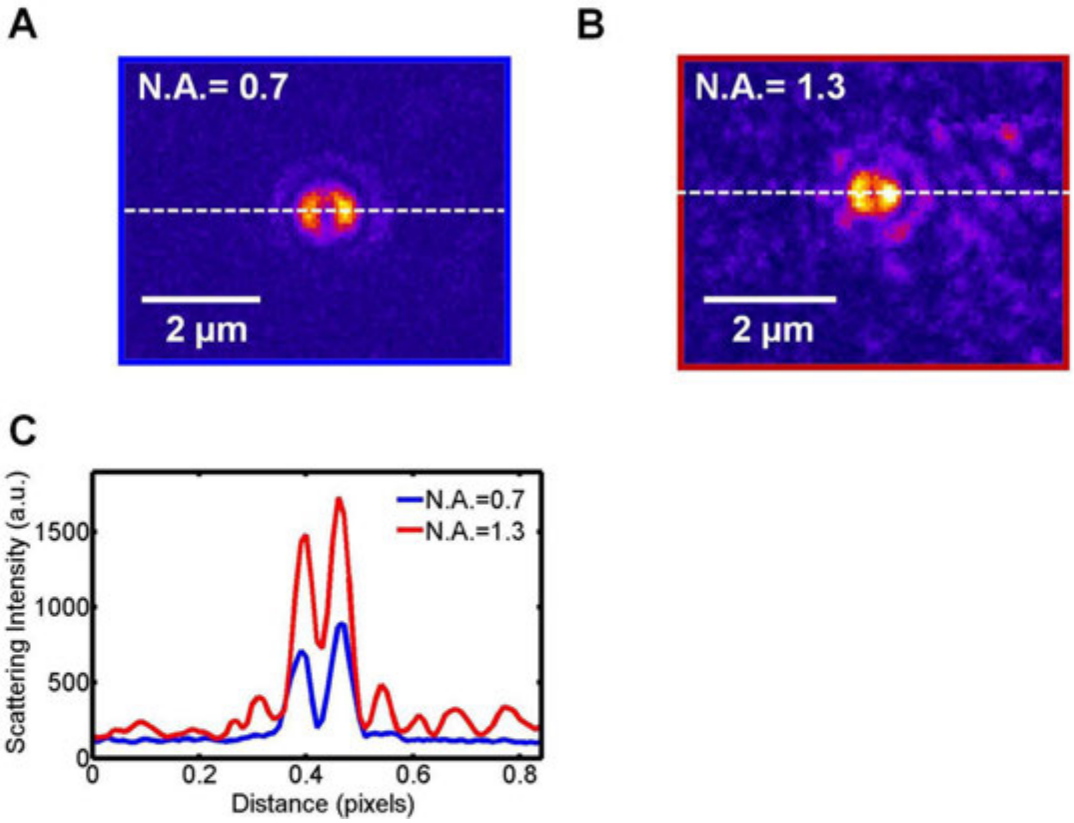

Figure S3. Effect of the numerical aperture (NA) of the objective on the scattering patterns of a AuNR on a gold substrate under p-polarized excitation at 647 nm. The NA was varied from 0.7 to 1.3. (A) Far-field scattering image of the AuNR with a smaller NA of 0.7. (B) Far-field scattering image of the same AuNR with a larger NA of 1.3. (C) Line-sectional profiles across the center of the scattering patterns of the AuNR with different NA of 0.7 (blue-curve) and 1.3 (red-curve). The smaller NA objective lens provides clearer scattering pattern (A) due to the decreased noise and background scattering (C).

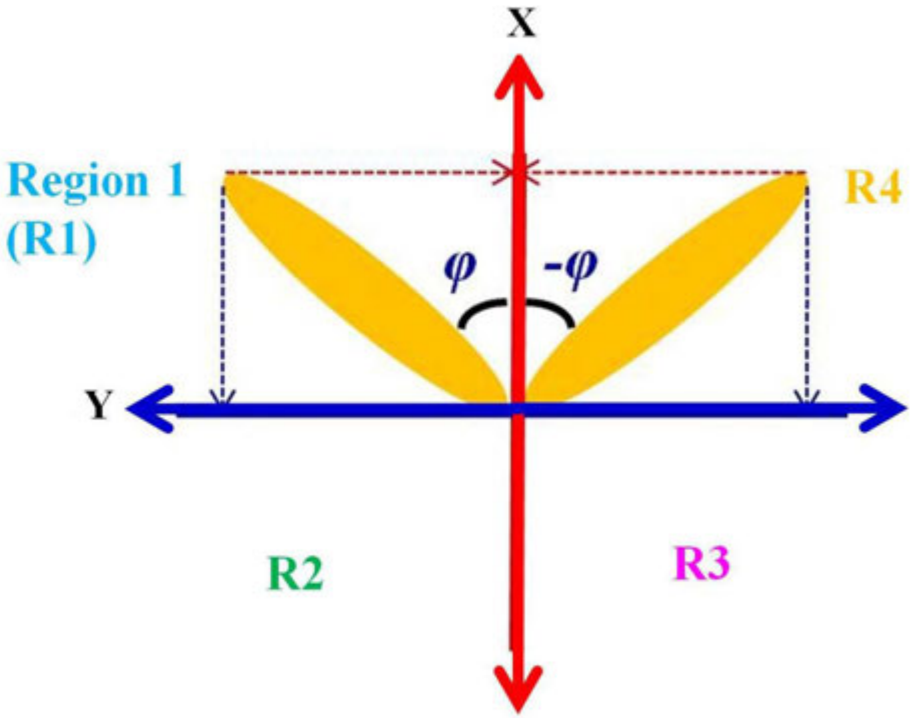

Figure S4. Schematic diagram to show angular degeneracy generally considered a major limitation of polarization-based techniques in single particle orientation tracking. The angular degeneracy is resulted from the 2-fold optical symmetry of a AuNR relative to the x-axis (red-arrow). We cannot distinguish the orientation angle between *φ* and -*φ* with the respect to x- axis.

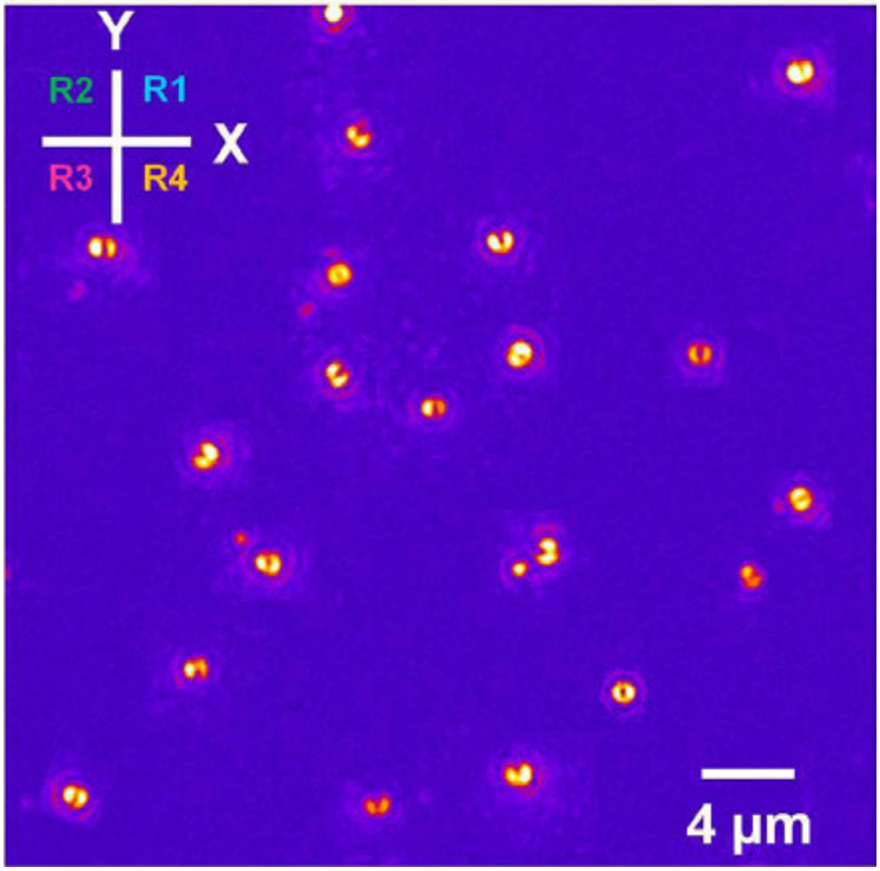

Figure S5. TIR scattering image of AuNRs with diverse orientations. The AuNRs are deposited on a gold film and measured by p-polarized excitation at 647 nm. The AuNRs' transverse (x-y) positions can be determined from cross-sectional profiles of the doughnut-shaped scattering patterns.

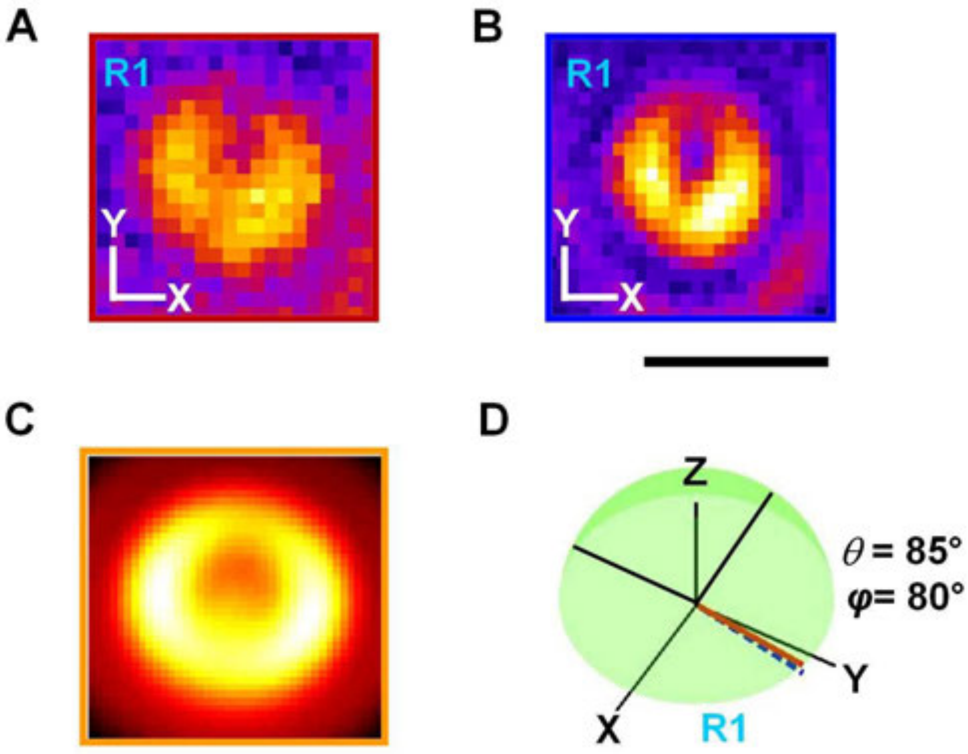

Figure S6. Far-field scattering patterns of the same AuNR on a gold film measured by TIR white light excitation (A) and p-polarized laser excitation at 647 nm (B). (C) The corresponding best-fit simulated scattering pattern. The orientation of AuNR for the simulation experiment is adjusted until it accords well with the experiment result. (D) The determined orientation angles of the AuNR are illustrated in 3D space: θ=85° and φ=80°. The red line indicates the AuNR. The blue-dotted line indicates the corresponding in-plane projection of the AuNR in R1. The scale bar represents 1 μm.

Supplementary Materials

Effect of Objective NA on Scattering Patterns of AuNRs in TIRS Microscopy.

The numerical aperture (NA) of the objective is an important parameter that influences far-field scattering patterns of AuNRs. It is defined by NA = $n \sin \theta$, where n is the refractive index of the medium, and θ is the half-angle of the maximum cone of light that can enter the objective. NA is closely associated with the resolving power of the objective. Therefore, an objective with a larger NA value will be able to visualize finer details than an objective with a smaller NA value. Furthermore, larger NA objectives collect more light and generally produce brighter images with more diffraction patterns. In the case of conventional DF illumination, when the NA value becomes greater than 1, a clear two-lobe pattern of out-of-focus AuNR appears and, therefore, the angular information can be resolved from the characteristic field distribution pattern.[2]

In this study, we investigate the influence of objective NA on the scattering pattern and signal intensity of a AuNR deposited on a gold film under p-polarized TIR illumination. Figure S3 shows the scattering patterns and signal intensities, as the NA of the objective in use is varied from 0.7 to 1.3. Figures S3A and S3B illustrate the far-field scattering images of the same AuNR taken at the different NA values of 0.7 (Figure S3A) and 1.3 (Figure S3B). With a NA value of 0.7, the doughnut-shaped pattern is broader and clearer than the pattern obtained with a larger NA value of 1.3. The intensity line sections (Figure S3C) show that the scattering intensity increases with the higher NA value of 1.3 as more light is collected; however, due to the increased background scattering and noise, the signal-to-noise (S/N) ratio is in fact decreased by a factor of ~4 as compared to that from the NA value of 0.7. These results suggest that the smaller NA value of 0.7 is more suitable for the TIR scattering experiments with AuNRs on a gold film.

White Light Excitation *vs.* p-polarized Laser Excitation. We compared white light TIR excitation with p-polarized laser TIR excitation at 647 nm for same AuNRs on a gold film in order to gain more insight into the scattering patterns containing the spatial orientation information. Figure S6 shows the doughnut-shaped far-field scattering patterns of the same AuNR on a gold film under either TIR white light (Figure S6A) or p-polarized laser (Figure S6B) illumination. As expected, the two scattering patterns are similar. Moreover, we found that p-polarized laser excitation produces the clearer two-lobe scattering intensity distribution, which is purely contributed from the out-of-plane dipole of AuNR (Figure S6B). Figure S6C is the best-fit scattering image and the 3D orientation angle of the AuNR was determined to have a polar angle θ of 85° and an azimuth angle φ of 80° in R1. Figure S6D depicts the 3D orientation of the AuNR in 3D space. These well-matched results show that both the in-plane projection information and the out-of-plane angle information can be directly resolved from the pattern match analysis.

CHAPTER 7. SUPER-RESOLUTION MAPPING OF PHTO-GENERATED ELECTRON AND HOLE SEPARATION IN SINGLE METAL-SEMICONDUCTOR NANOCATALYSTS

Ji Won Ha, T. P. A. Purnima, Rui Han, Bin Dong, Javier Vela,* and Ning Fang*

A manuscript submitted to *Journal of the American Chemical Society*.

* Corresponding author

Abstract

Metal-semiconductor heterostructures are promising visible light photocatalysts for many chemical reactions. However, little is known about the surface active sites and factors that control the catalytic activity and selectivity in these hybrid materials. Here, we use high-resolution super-localization imaging to reveal the nature and photocatalytic properties of the surface active sites on single Au-CdS hybrid nanocatalysts. We find that the excited surface plasmons in the metal play an important role in photocatalysis, and one must consider the photoinduced plasmonic effect together with the facets and defects of the metal. We demonstrate two distinct, incident energy-dependent charge separation mechanisms that result in completely opposite photo-generated active sites (e^- and h^+) and divergent energy flows on the hybrid nanocatalysts. Engineering the direction of energy flow at the nanoscale can provide an efficient way to overcome important challenges in photocatalysis, such as controlling catalytic activity and selectivity. These results bear enormous potential impact on the development of better visible light photocatalysts for solar-to-chemical energy conversion.

Introduction

Anisotropic semiconducting nanoparticles with high surface-to-volume ratios have gained much attention over the past decade as photocatalysts for many chemical reactions including photoelectrochemical hydrogen production[1-6] and photochemical degradation of organic pollutants.[7] Most semiconductor photocatalysts are currently based on wide-gap materials that have limited applicability outside of the UV range. However, UV light constitutes less than 5% of the solar spectrum; therefore, it is highly desirable to investigate photocatalysts with tunable activity that can be widely applied under visible light.

Metal-modified semiconductor nanorods are promising visible-active heterostructured photocatalysts for the following reasons: First, semiconductor nanorods, as compared to spherical semiconductors, provide the advantage of multiple exciton generation and more efficient photo-induced charge separation.[8,9] Second, the physical spatial separation of photo-generated electrons and holes in metal-semiconductor heterostructures can suppress recombination and enhance overall photocatalytic efficiency.[10] Third, recent advances in solution-phase synthesis enable the highly predictable and reliable fabrication of metal-semiconductor heterostructures with controlled size, shape, and composition tailored for specific applications.[11-13] Importantly, this unique ability to selectively build metal-semiconductor heterostructures with several morphologies and spatial relationships between their individual components can be used to engineer and direct energy flows at the nanoscale. This is a great advantage over their separate isolated components because one can conveniently tune the catalytic efficiency of the heterostructure by controlling the size, distribution and loading of metal particles.

In this context, it is important to elucidate the fundamental photocatalytic mechanisms operating on metal-semiconductor hybrid heterostructures in order to design and develop better (more active, selective and stable) photocatalysts.

The photocatalytic behavior of metal-semiconductor heterostructures active in the visible has been studied mainly at the ensemble level.[14-20] For example, Amirav *et al.* demonstrated photocatalytic hydrogen production using Pt-tipped CdS nanorod heterostructures;[18] notably, the catalytic properties were considerably influenced by the individual particle sizes, structures, etc. To surmount the challenge arising from the intrinsic heterogeneity associated from ensemble-averaged measurements, it is highly desirable and necessary to employ photocatalytic measurements at the single-particle level.

Recently, single-particle catalysis using methods such as electrochemical detection,[21] surface plasmon spectroscopy,[22-24] and single-molecule fluorescence microscopy[25-31] has been demonstrated. Novo *et al.* reported the direct observation of oxidation reactions on single Au nanocrystals using dark-field microscopy.[22] Xu *et al.* presented the catalytic properties of Au nanoparticles at the single-particle level using single-molecule fluorescence microscopy.[28,29] Furthermore, high-resolution super-localization fluorescence imaging in single-particle catalysis has also been carried out by several groups.[31-34] Zhou *et al.* employed super-localization fluorescence imaging to unveil the surface reactivity of Au nanorod catalysts, and found that surface defects play important roles in catalytic activity.[31] Cremer *et al.* reported high-resolution reactivity mapping of epoxidation reactions catalyzed by mesoporous titanosilicates.[33]

More recently, super-localization fluorescence imaging of single metal-semiconductor heterostructures has been demonstrated by Tachikawa *et al.*; in this report, single-molecule super-resolution imaging of active sites on single Au-TiO_2 hybrid particles were studied using an oxidation-reduction (redox)-responsive fluorescent dye.[32] Despite the recent study of photocatalysis by metal-semiconductor heterostructures at the single-particle level, their mechanisms of action and many of their photocatalytic properties such as selectivity remain largely unanswered, even though it is still necessary to develop metal-semiconductor heterostructures that can be widely used under visible light. Further, our understanding of the identity of the surface active sites and factors affecting the catalytic efficiency in these hybrid materials is still very limited. Therefore, the remaining grand challenges in this area are to investigate and develop highly-active metal-semiconductor heterostructures with tunable activity under visible light, to resolve the single surface active sites where individual photo-induced redox reactions occur on these photocatalytic structures, and to clarify the factors that control catalytic activity and selectivity in metal-semiconductor heterostructures.

To address the aforementioned challenges, we synthesized CdS semiconductor nanorods decorated with Au nanoparticles and studied the real-time redox photocatalysis of these hybrid heterostructures at the single-particle level with millisecond time resolution. We chose Au-CdS hybrid heterostructures as photocatalysts because they provide efficient light absorption and photocatalytic activity in the visible range.[35] We employ high-resolution super-localization fluorescence imaging to resolve the nature and photocatalytic properties of the photo-generated carriers and redox active sites (electrons,

e^- and holes, h^+) in Au-CdS hybrid heterostructures, using single-molecule detection following the oxidation of non-fluorescent amplex red to highly fluorescent resorufin.

Experimental Section

Single-molecule fluorescence measurements. Single-molecule fluorescence experiments were carried out on a prism-type dual-color total internal reflection fluorescence (TIRF) microscope. A 532-nm laser beam (10 mW) was focused onto the sample to directly excite both Au-CdS hybrid heterostructures and the resorufin product molecules. Besides the 532-nm laser, a 405-nm laser beam (5 mW) was also used to excite the Au-CdS heterostructures in this study. The fluorescence from resorufin product during the oxidation reactions was collected by a Nikon Plan Fluor 100× oil iris objective (NA=1.4) through a filter (532 LP, Chroma Technology Corp). All the fluorescence images were captured with an Andor iXonEM+ 897 CCD camera (Belfast, Northern Ireland). The collected movies and images were analyzed by MATLAB and NIH ImageJ (http://rsbweb.nih.gov/ij/). The fluorescence intensity trajectories were extracted from localized fluorescence spots individually across the entire movie. The intensity of each bright spot in an image was obtained by integrating the signal counts over an area of ~1 μm^2.

Results and Discussion

Au-CdS hybrid heterostructures used here were synthesized according to modified literature procedures (see details in Supplementary Information).[36,37] Figure 1a shows a transmission electron microscopy (TEM) image of single CdS nanorods densely decorated with Au nanoparticles (‘high’ surface-Au density). The diameter of the Au nanoparticles ranged from 2 nm to 7 nm, and the Au loading on the CdS nanorod was calculated to be about 10.8 wt%. The mean length and diameter of CdS nanorods used in this study were 186(±56) nm and 6.0(±0.9) nm, respectively (Figures S1 and S2).

In Au-CdS hybrid heterostructures, the optical properties of the original components are essentially retained.[38] Hence, the optical absorption spectra of Au-CdS heterostructures exhibit both the characteristic excitonic and continuous absorption of the CdS nanorods below 480 nm (*Eg*: 2.58 eV), together with an additional broad absorption centered around 532 nm due to the plasmonic Au nanoparticles (Figure 1b). This can be ascribed to the separate optical excitations of the semiconductor and metal components in the hybrid material. This is advantageous because it enables selective excitation of each material, and allows because it allows to separately probe each one of the two heterostructure components using two different incident light wavelengths.

Because of the separation of the plasmonic and excitonic features in Au-CdS hybrid heterostructures, two distinct photo-induced charge separation mechanisms are expected to exist depending on the incident excitation energy as shown in Figure 1c. Mechanism A starts with 532-nm absorption by the gold metal, followed by formation of d-band electron-hole pairs excited above the Fermi level upon decay of surface plasmons in the metal. Excited plasmonic nanoparticles that are much smaller than their plasmon resonance wavelength, can be an efficient source of hot electrons (e^-) and holes (h^+).[39,40] The hot electrons have energies between vacuum level and the work function of gold metal (4.83 eV).[39,41] These energetic electrons could be potentially used in photochemistry.[39,40,42-44] For example, Mukherjee *et al.* recently demonstrated that hot electrons formed on Au nanoparticles can be used for the room temperature dissociation of H_2, which requires a dissociation enthalpy of 436 kJ/mol (4.51 eV).[39] A significant fraction of the energetic electrons in Au nanoparticles can either overcome the energy barrier (Schottky junction) at the metal-semiconductor interface or tunnel through it to become conduction electrons in the semiconductor.[32,45,46] This results in a spatially-separated electron-hole pair where the electron resides in the semiconductor (CdS), whereas the hole remains in the metal (Au). Mechanism B starts with 405-nm absorption by the semiconductor, followed by charge transfer of photo-excited electrons to the metal. In contrast to the previous mechanism, mechanism B (405-nm excitation) charges the gold negatively and the CdS semiconductor positively. In other words, mechanisms A and B result in two different charge-separated Au-CdS species of completely opposite polarity. So far, mechanism B is well established and widely used in photocatalytic chemistry,[3,15] however mechanism A is still poorly understood in nanocatalysis. Therefore, in the present study, we first try to experimentally verify the existence of mechanism A in these Au-CdS hybrid heterostructures using 532-nm excitation, and further investigate the capability to optically control the direction of energy flow together with the catalytic activity and selectivity offered by these two mechanisms as depicted in Figure 1c.

To test and study the two aforementioned charge separation mechanisms in Au-CdS hybrid heterostructures, we used the fluorogenic oxidation reaction of non-fluorescent amplex red (10-acetyl-3,7-dihydroxyphenoxazine) to produce highly fluorescent resorufin (λ_{exc} = 563 nm; λ_{em} = 587 nm, at pH 7.2).[30,31] In an aqueous environment, photo-generated energetic electrons (e^-) are known to reductively react with adsorbed oxygen (O_2) as the primary electron acceptor to generate surface-bound superoxide anion radicals ($O_2^{\bullet -}$).[47-50] In addition, photo-generated energetic holes (h^+) oxidatively react with adsorbed water (H_2O) to generate surface-bound hydroxyl radicals ($HO^{\bullet}$).[48,49] Both of these two surface-bound oxygen radicals are known to be very reactive towards non-fluorescent amplex red, catalyzing its fluorogenic oxidation to fluorescent resorufin.[50,51]

Experimentally, we first tested if high Au-CdS heterostructures (Figure 1a) were active in catalyzing the oxidation of amplex red to resorufin by ensemble-averaged measurements. An aliquot of a solution containing Au-CdS heterostructures was injected into a cuvette containing a solution of 1 μM amplex red, 20 mM H_2O_2, and 10 mM phosphate buffer with pH = 7.2. The cuvette was illuminated at 532 nm (±25 nm band-pass filter), and the fluorescence intensity was measured every 30 s of continuous illumination. As shown in Figure S3, the fluorescence intensity arising from resorufin increases as a function of time in the presence of high Au-CdS heterostructures, but remains constant in the absence of high Au-CdS heterostructures under the same conditions. This indicates that the Au-CdS heterostructures are highly active for the fluorogenic oxidation reaction under the mechanism A at 532 nm.

Zhou *et al*. have demonstrated that isolated, unmodified (CdS-free) Au nanoparticles mediate the oxidation of amplex red to resorufin by simple catalysis on some of their surface facets.[31] Therefore, it was important to ensure that photocatalytic mechanism A, involving excited surface plasmons on Au followed by charge separation into the CdS semiconductor, was actually operating and was responsible for activity under 532-nm illumination. For this purpose, we performed several additional ensemble experiments to verify that Au-CdS heterostructures were operating *via* mechanism A (see more details in Supplementary Information). Among key results from these experiments, we found that the absorbance due to resorufin product builds up about 4 times faster under continuous 532-nm illumination (photocatalysis) than it does in the dark (surface catalysis, Figure S4). We also corroborated that 532-nm green light cannot excite pure (metal-free) CdS nanorods; this supports a null (zero) contribution to activity from the CdS nanorods alone *via* mechanism A at 532 nm in the presence of the heterostructures (Figures S5 and S6). These results clearly show that the surface-bound Au nanoparticles become excited and make the Au-CdS heterostructures distinguishably more active under 532-nm illumination, verifying the existence of photocatalytic mechanism A in the oxidation reaction of amplex red to resorufin.

To better understand the photocatalytic properties of the Au-CdS hybrid heterostructures, we performed the same fluorogenic oxidation reaction at the single-particle level. A sample was prepared by spin casting Au-CdS heterostructure solution on a positively functionalized quartz slide. The concentration of the Au-CdS heterostructures immobilized on the quartz slide was controlled to be ~1 μm^{-2} for single-particle photocatalysis and was checked using a differential interference contrast (DIC) microscope (Figure S7). The sample slide was then measured under a prism-type dual-color total internal reflection fluorescence (TIRF) microscope (Figure S8). A 532-nm green laser was used to excite both the metal in Au-CdS heterostructures and the fluorescent resorufin product. Before initiating the fluorogenic oxidation reaction, we first shined the 532-nm laser beam onto the sample for 20 min to remove possible fluorescent dusts or impurities. We then introduced the reactant-containing solution (1 μM amplex red, 20 mM H_2O_2, 10 mM pH 7.2 phosphate buffer) over the Au-CdS heterostructures within a flow chamber. A highly fluorescent resorufin product was formed at one of many possible active sites on a single Au-CdS heterostructure (Figure 2a), and was detected by an electron-multiplying charge-coupled device (EMCCD) camera (Figure S8b). The resorufin product (pKa = 5.8) is deprotonated and negatively charged in the solution with pH = 7.2. We recorded movies of stochastic fluorescence bursts at many localized spots on the quartz surface with a time resolution of 50 ms (Figure 2b). Figure 2c shows a segment of a typical fluorescence intensity trajectory from one spot squared in red in Figure 2b containing stochastic fluorescence ON–OFF signals. If these signals were produced from multiple resorufin molecules we would expect a distribution of variable intensity fluorescent signals, but the consistent height of the two-state ON-level in Figure 2c indicates that each fluorescence burst comes from a single resorufin molecule. Figure 2d is a fluorescence image of a single resorufin molecule during one burst circled in green in Figure 2c and the fluorescence intensity of a single resorufin molecule spread over a few pixels as a point spread function (PSF). The center position of this PSF can be determined with nanometer accuracy by two-dimensional (2D) Gaussian fitting of its fluorescence profile (Figure 2e). This enables us to localize the position of every resorufin molecule on a single Au-CdS heterostructure during the catalytic reactions. In this study, red-fluorescent beads with a diameter of 100 nm were used as position markers to correctly localize the position of each resorufin molecule (Figures S9 and S10).

To further confirm that each fluorescence burst comes from a single turnover catalytic reaction of amplex red over Au-CdS heterostructures, we carried out further control experiments at the single-particle level. We found that no stochastic fluorescence bursts are observed over pure CdS nanorods and that no fluorescence bursts are observed over Au-CdS heterostructures in the absence of amplex red reactant under the same conditions. In addition, we found that no digital fluorescence bursts are observed over Au-CdS heterostructure with resorufin product in solution under the same conditions. There are three important findings from these control experiments. First, a 532-nm green laser does not excite isolated metal-free CdS nanorods, which means that the intensity signal observed during catalysis is only contributed from Au-modified heterostructures under mechanism A at 532 nm. This is also consistent with ensemble experiments done with pure CdS nanorods at 532 nm (Figure S6). Second, our Au-CdS heterostructures do not exhibit any time-dependent emission fluctuations (or blinking) that could affect fluorescence bursts or our data analysis (See more detailed discussion on blinking in Supplementary Information). This is further verified by our previous report to show no fluorescence emissions of CdS nanorods with aspect ratio (AR) greater than 3 due to exciton quenching by surface defects.[52] Third, our results indicate that diffusion of free resorufin in solution does not yield any significant fluorescence bursts through its binding to the nanoparticles under our experimental conditions (See more details in Supplementary Information). This is also verified by previous reports carried out under similar experimental conditions.[28,30] Furthermore, every product formation (or dissociation) event in each single-molecule fluorescence trajectory (Figure 2c), appears as a sudden increase (or decrease) in intensity. In contrast, Xu *et al.* demonstrated that photobleaching of single resorufin molecules happens on much longer time scales (~25 s) under similar 532-nm laser intensities.[28] This strongly indicates that each observed sudden decrease in intensity is attributed to the dissociation of adsorbed resorufin from the active site where it is produced. Therefore, the fluorescence bursts observed in this study are attributed to the oxidation of amplex red to fluorescent resorufin at active sites on single Au-CdS heterostructures, and each fluorescence burst corresponds to a single catalytic turnover that results in the formation of one resorufin molecule at an active site, followed by its subsequent dissociation away from that active site on a Au-CdS heterostructure.

In the fluorescence intensity trajectory, photocatalytic events have two important characteristic durations, τ_{off} and τ_{on}, (Figure 2c); τ_{off} is the characteristic time before the formation of a fluorescent product on the Au-CdS heterostructure, and τ_{on} is the characteristic time related to the dissociation of the product molecule from the nanocatalyst surface. The inverse of the values of τ_{off} and τ_{on} represent the single-active site rates of product formation and of product dissociation, respectively. Therefore, a higher value of τ_{on}^{-1} indicates faster dissociation of the resorufin product, while a higher value of τ_{off}^{-1} indicates faster formation of the resorufin product.

It is important to note that some fluorescence bursts show long τ_{on} values of 2 to 6 s, while other fluorescence bursts show short τ_{on} values of 0.3 to 1.2 s (Figure 2c). We believe that these two distinct τ_{on} values can be ascribed to two charge-separated species containing photo-generated carriers at different locations and microenvironments (Figure 3a). In this experiment, photo-generated carriers (electrons, e^- and holes, h^+) form two surface-bound reactive oxygen radicals ($O_2^{\bullet -}$ and $HO^{\bullet}$) that act as catalytic active sites on the nanocatalyst surfaces.[30,47-50] Active sites around photo-generated electrons have a negatively charged microenvironment, while active sites around photo-generated holes have a positively charged microenvironment (Figure 3a).

To clearly verify and identify the aforementioned sites and active species, we used dimethyl sulfoxide (DMSO, 20 mM) to selectively quench the $h^+/HO^\bullet$ active sites, which allowed us to separately measure the catalytic reactivity of the $e^-/O_2^{\bullet-}$ active sites. DMSO is known to get oxidized by $HO^\bullet$ radicals to form the stable compound methanesulfinic acid (MSIA, CH_4O_2S).[53,54] Figure S11a shows a segment of a fluorescence intensity trajectory over one Au-CdS heterostructure in the absence of DMSO and the time profile for the two rates for each fluorescence burst. We observe that the rates of product formation and product dissociation over the same heterostructure vary at different times. Figure S11b shows a segment of a fluorescence intensity trajectory over one Au-CdS heterostructure in the presence of DMSO and the time profile for the two rates for each fluorescence burst. From these experiments, it is clear there is heterogeneity in catalytic activity among the $e^-/O_2^{\bullet-}$ active sites on the same Au-CdS heterostructure. This previously unobserved trait is always masked in the ensemble-averaged measurements. More importantly, as compared to the fluorescence bursts in the absence of DMSO (Figure S11a), all the fluorescence bursts in the presence of DMSO (Figure S11b) show τ_{on}^{-1} values higher than 0.6 s^{-1}, where the averaged rate of product dissociation $<\tau_{on}>^{-1}$ is 1.18 s^{-1} over a single Au-CdS heterostructure. This suggests that the lower τ_{on}^{-1} value of around ~0.25 s^{-1} in Figure S11a could be ascribed to the $h^+/HO^\bullet$ active sites. Nevertheless, the individual τ_{on}^{-1} and τ_{off}^{-1} values in single-molecule events are stochastic and, hence, their statistical properties, such as average values and distributions, are required to draw a more concrete and meaningful conclusion about the distinct dissociation kinetics in single-molecule experiments.

To more clearly elucidate the distinct dissociation kinetics between the two different active sites, we further measured many more Au-CdS hybrid heterostructures for both cases (with and without DMSO). In each case, we collected many fluorescence bursts from over 100 individual nanoparticles for a statistical analysis. Figure 3b shows a histogram of the rate of product formation for all the fluorescence bursts. We found that the averaged rate of product formation $<\tau_{\text{off}}>^{-1}$ is 0.0168 s^{-1} in the absence of DMSO, while $<\tau_{\text{off}}>^{-1}$ in the presence of DMSO is 0.00403 s^{-1}. This difference in the averaged rate of product formation can be explained by the effect of DMSO competing with, and hindering amplex red near the nanocatalyst surface, thus quenching the h^+/HO$^\bullet$ active sites. This DMSO effect is further verified by ensemble experiments (Figure S12). In addition, Figure 3c shows a histogram of the rate of product dissociation for all the fluorescence bursts. Interestingly, we find that the rate of product dissociation τ_{on}^{-1} obtained without DMSO has two distinct distributions (or peaks) for individual fluorescence bursts (Figure 3c), which is not observed in the presence of DMSO. Therefore, Figure 3c verifies that the fluorescence bursts yielding the lower τ_{on}^{-1} of around 0.25 s^{-1} on the left side of the distribution come from the h^+/HO$^\bullet$ active sites, while the fluorescence bursts yielding the higher τ_{on}^{-1} around 1.2 s^{-1} on the right side of the distribution arise from the e^-/$O_2^{\bullet -}$ active sites. The distinct dissociation kinetics for the two different active sites are further supported by a recent report.[30] These two distinct dissociation kinetics can be explained by the fact that the positively charged microenvironment around the photo-generated holes enhances the adsorption of the negatively charged resorufin product, while the negatively charged microenvironment around photo-generated electrons promotes quicker dissociation of negatively charged resorufin molecule due to the repulsive electrostatic force.[30] It should be noted that these results reveal the formation and separation of plasmon-induced hot electrons and holes initially formed in gold metal (Figure 1c, Mechanism A) during the photocatalytic oxidation reaction at the single-particle level.

This finding is important because we can directly distinguish catalytic fluorescence bursts caused by the h^+/HO$^\bullet$ active sites from those by the e^-/$O_2^{\bullet-}$ active sites in a fluorescence intensity trajectory. More importantly, this allows for resolving individual electron and hole transfer events following photo-induced charge separation in single Au-CdS hybrid heterostructures. We thus tried to map the individual active sites on a single high Au-CdS heterostructure (10.8 wt% Au) under 532-nm laser excitation for 60 min through localizing the position of every resorufin molecule with nanometer accuracy (Figure 4). Figure 4a shows TEM images of typical single Au-CdS heterostructures with high metal loading, showing that the Au nanoparticles are deposited and distributed along the length of the CdS nanorod. Figure 4b is a super-resolution image mapping single surface active sites during the photocatalytic oxidation reaction on a Au-CdS hybrid heterostructure with a similarly high metal loading. Plasmon-induced energetic electrons (encircled-marked as red-minuses), initially created in the metal particles, are injected into the conduction band of the CdS semiconductor nanorod. Therefore, our experimental results are consistent with the existence of mechanism A involving photo-induced charge transfer from the gold metal to the CdS semiconductor under 532-nm light. To the best of our knowledge, this is the first report resolving and mapping individual active sites on single Au-CdS hybrid heterostructured photocatalysts using a high-resolution super-localization imaging technique.

We then tried to verify the existence of mechanism B involving electrons and holes photo-generated in CdS nanorods at the ensemble level. We first checked if pure, metal-free CdS nanorods can oxidize amplex red, which is necessary to support the fact that mechanism B exists (See more details in Supplementary Information). In the presence of CdS nanorods (blue-curve), the resorufin product's absorption maximum at 571 nm increased with an interval of 30 s, while it remained constant in the absence of CdS nanorods under identical conditions (Figure S13). This result shows that the resorufin product is also formed through photocatalysis under mechanism B (Figures S13d and S14).

To clearly demonstrate the existence of two distinct photocatalysis mechanisms having the opposite direction of energy flow (*i.e.*, having the opposite polarity after photo-induced charge separation) at the single-particle level, we further synthesized Au-tipped CdS heterostructures (Figures 5a and S1a). An absorption spectrum of Au-tipped CdS heterostructures is provided in Figure S15. These Au-CdS heterostructures differed from those mentioned above in that they have a very low metal loading (0.54 wt% Au on CdS). As depicted in Figure 5b, we can selectively excite either the gold metal domains at 532 nm to turn ON mechanism A, or the CdS semiconductor nanorod domains at 405 nm to turn ON mechanism B. We note however, that under single-molecule experiments presented here, a 532-nm laser was always needed to excite resorufin product, and both 405 nm and 532 nm lasers were used in our study of mechanism B. Figure 5c shows a super-resolution image mapping the active sites during the same amplex red to resorufin oxidation reaction taken at 532 nm over 1 h. Interestingly, we find that holes (h^+, circled blue-cross) are positioned at the gold tips on both ends of the heterostructures, while electrons (e^-, circled red-minus) are located along the inside length of the CdS nanorods within a distance of a few tens of nanometers from the gold tips. Interestingly, a few electrons are also positioned at the heterostructure's tip, which indicates that energetic electrons can also be transferred directly to the molecules adsorbed on the gold metal. Therefore, this result reveals that at 532 nm we turned ON mechanism A, which proceeds by charge (electron) transfer from the gold metal to the CdS semiconductor nanorod. This is consistent with our observations described above for the CdS nanorods with high Au loading (Figure 4b). In addition, Figure 5d shows a super-resolution image mapping the active sites obtained after turning on the 405 nm laser in addition to the 532 nm laser (the latter needed to excite the resorufin product). We ensured that CdS nanorods in this study are excited at 405 nm under a dual-color TIRF microscope (Figure S16). Critically, in this case the holes (h^+, encircled blue-crosses) are distributed along the inside length of the CdS nanorod, while electrons (e^-, encircled red-minuses) are located at both ends. Efficient charge separation by the CdS nanorods could lead to a heterogeneous carrier distribution and compact location along the tips. However, the photo-generated carriers can travel along the CdS semiconductor nanorods,[14] followed by their reaction with oxygen and water to create and localize surface-bound radicals. It should be noted that although both mechanisms A and B are turned ON when using both 405 nm and 532 nm lasers, the super-resolution image (Figure 5d) clearly differs from the super-resolution image when using the 532 nm laser only (Figure 5c), revealing the existence of mechanism B: Charge (electron) transfer from the CdS semiconductor nanorod to the gold metal at the tip. We are unclear, at this time, about why Mechanism B dominates when both lasers are used; however, given the similar power intensities, this observation indicates that photo-generated electrons appear to be more active when generated at CdS than when generated at Au (see below). Therefore, we have disclosed the existence of two distinct photocatalysis mechanisms in Au-CdS heterostructures. The photo-induced redox activity of these Au-CdS heterostructures can be selectively turned ON by two different mechanisms using two different wavelengths of incident light.

We also compared the rates of product formation and dissociation for mechanism A (532 nm) and mechanism B (405 nm and 532 nm) in Au-tipped CdS heterostructures during the photocatalytic oxidation reaction. We found that the averaged rate of product formation $<\tau_{\mathrm{off}}>^{-1}$ for mechanism B was about 6 times higher than that of mechanism A (Figure S17). This can be ascribed to the formation of photocarriers primarily in CdS nanorod under mechanism B at both 405 nm and 532 nm. This result shows that mechanism B confirms in higher activity than mechanism A. In addition, we found two distinct dissociation kinetics in Au-tipped CdS heterostructures for both mechanisms A and B (Figure S18). The averaged rate of product dissociation $<\tau_{\mathrm{on}}>^{-1}$ for $e^-/O_2^{\bullet -}$ active sites in mechanism A was 1.46 s^{-1}, while $<\tau_{\mathrm{on}}>^{-1}$ in mechanism B was 1.57 s^{-1}. The averaged rate of dissociation $<\tau_{\mathrm{on}}>^{-1}$ for $h^+/HO^{\bullet}$ active sites in mechanism A was 0.41 s^{-1}, while $<\tau_{\mathrm{on}}>^{-1}$ in mechanism B was 0.32 s^{-1}.

There is an important point that needs to be further discussed in Figure 5. Our results show the existence of two fundamentally distinct charge separation mechanisms together with the capability to optically control the direction of charge transfer on the heterostructures at the nanoscale. Our finding is of great importance because we are capable of controlling the catalytic selectivity for charged reactant molecules with two different wavelengths of light. For example, as demonstrated in Figure 5, we can selectively make either the metal at the tip or the CdS semiconductor nanorod more active while keeping the other one less active. This is a great advantage when using the Au-CdS heterostructures in photocatalysis, which cannot be achieved separately by the individual metal and semiconductor components.

Besides the capability of tuning their photocatalytic selectivity, another advantage of hybrid metal-semiconductor heterostructures such as Au-CdS over its separate components is that we can control the photocatalytic activity by two methods. First, the photocatalytic activity in these hybrid heterostructures can be controlled by varying the metal (Au) loading on the semiconductor (CdS) nanorod under mechanism A at 532 nm. Specifically, we find that the rate of resorufin product formation rises fast when increasing the Au loading on the CdS nanorods at 532 nm (Figure S19). Mukherjee *et al.* have also demonstrated a steady increase of photocatalytic rate of HD molecule production with increasing Au loading on TiO_2.[39] Second, the photocatalytic activity can also be controlled by varying the wavelength of incident light, as supported by the spectra of Au-CdS hybrid heterostructures (Figure 1b, Figures S15 and S17). Therefore, it should be noted that Au-CdS hybrid heterostructures enable an efficient way to study and overcome important challenges in photocatalysis, such as providing synthetic and optical handles to control activity and perhaps, selectivity, in nanocatalysis.

The stability of Au-CdS heterostructures over our experimental time and conditions needs to be discussed. We recently demonstrated that metallic nanoparticles decorated on the CdS semiconductor surface significantly enhance activity and also greatly stabilize the CdS semiconductor nanorods against photo-induced degradation.[14] To clearly elucidate the stability of our Au-CdS heterostructures, we carried out ensemble measurements in the photocatalytic oxidation of amplex red to resorufin (See more details in Supplementary Information). We used a halogen lamp (150 W) to excite the Au-CdS heterostructures, and this lamp produces a continuous spectrum of light from 360 nm to 2000 nm. Therefore, under this illumination, both mechanisms are turned ON and operating in these heterostructures. We found that Au-CdS heterostructures are stable under our experimental conditions (Figures S20 and S21).

Because sunlight contains a wide range of wavelengths between the ultraviolet, visible and near-infrared spectral regions, we expect both mechanisms (A and B) to be active under direct sunlight illumination. Distinguishing between these two mechanisms and separating their individual contributions to overall photocatalytic activity (turnover) and selectivity is thus critical to fully understand, improve and devise new solar-to-chemical energy conversion technologies. We predict this model will enable engineering the direction of energy flows through heterostructured nanomaterials at the nanoscale, and expect these results will have an enormous positive impact in the development of better photocatalytic structures for solar-to-chemical energy conversion.

Conclusions

We report on the first direct measurements to resolve the nature and characteristic activities of two fundamental surface active sites ($e^-/O_2^{\bullet-}$ and $h^+/HO^\bullet$) generated by photo-induced charge separation in single Au-CdS hybrid heterostructures during photocatalytic oxidations as models for other solar-to-chemical energy conversion reactions. Single-molecule photocatalysis with high-resolution super-localization imaging allows us to reveal two distinct, incident energy-dependent charge separation mechanisms that result in completely opposite energy flows and polarities on single Au-

CdS heterostructures. This finding is very important for the following reasons. First, it can help us design and develop better metal-semiconductor heterostructures that are highly active for photocatalytic reactions under visible light. Second, it enables a better understanding of the nature and catalytic properties of single catalyst active sites in these heterostructures. Third, it permits us to potentially engineer the direction of energy flows on the heterostructured nanomaterials at the nanoscale. We therefore expect that our results have an enormous potential impact on the development of better photocatalyst structures.

References

1. Fujishima, A.; Honda, K. Electrochemical photolysis of water at a semiconductor electrode. *Nature* **1972**, *238*, 37–38.
2. Gratzel, M. Photoelectrochemical cells. *Nature* **2001**, *414*, 338–344.
3. Cho, I. S. *et al.* Branched TiO_2 nanorods for photoelectrochemical hydrogen production. *Nano Lett.* **2011**, *11*, 4978–4984.
4. Shankar, K. *et al.* Recent advances in the use of TiO_2 nanotube and nanowire arrays for oxidative photoelectrochemistry. *J. Phys. Chem. C* **2009**, *113*, 6327–6359.
5. Walter, M. G. *et al.* Solar water splitting cells. *Chem. Rev.* **2010**, *110*, 6446–6473.
6. Lewis, N. S. Toward cost-effective solar energy use. *Science* **2007**, *315*, 798–801.
7. Sunada, K.; Kikuchi, Y.; Hashimoto, K.; Fujishima, A. Bactericidal and detoxification effects of TiO_2 thin film photocatalysts. *Environ. Sci. Technol.* **1998**, *32*, 726–728.
8. Kumar, S.; Jones, M.; Lo, S. S.; Scholes, G. D. Nanorod heterostructures showing photoinduced charge separation. *Small* **2007**, *3*, 1633–1639.
9. Wu, K.; Zhu, H.; Liu, Z.; Rodriguez-Cordoba, W.; Lian, T. Ultrafast charge separation and long-lived charge separated state in photocatalytic CdS-Pt nanorod heterostructures. *J. Am. Chem. Soc.* **2012**, *134*, 10337–10340.

10. Bao, N. Z.; Shen, L. M.; Takata, T.; Lu, D. L.; Domen, K. Highly ordered Pt-loaded CdS nanowire arrays for photocatalytic hydrogen production under visible light. *Chem. Lett.* **2006**, *35*, 318–319.

11. Peng, X. G. *et al.* Shape control of CdSe nanocrystals. *Nature* **2000**, *404*, 59–61.

12. Mokari, T.; Rothenberg, E.; Popov, I.; Costi, R.; Banin, U. Selective growth of metal tips onto semiconductor quantum rods and tetrapods. *Science* **2004**, *304*, 1787–1790.

13. Alemseghed, M. G.; Ruberu, T. P. A.; Vela, J. Controlled fabrication of colloidal semiconductor-metal hybrid heterostructures: site selective metal photo deposition. *Chem. Mater.* **2011**, *23*, 3571–3579.

14. Ruberu, T. P. A.; Nelson, N. C.; Slowing, I. I.; Vela, J. Selective alcohol dehydrogenation and hydrogenolysis with semiconductor-metal photocatalysts: toward solar-to-chemical energy conversion of biomass-relevant substrates. *J. Phys. Chem. Lett.* **2012**, *3*, 2798–2802.

15. Berr, M. *et al.* Colloidal CdS nanorods decorated with subnanometer sized Pt clusters for photocatalytic hydrogen generation. *App. Phys. Lett.* **2010**, *97*, 093108.

16. Janet, C. M.; Viswanath, R. P. Large scale synthesis of CdS nanorods and its utilization in photo-catalytic H_2 production. *Nanotechnology* **2006**, *17*, 5271.

17. Menagen, G.; Macdonald, J. E.; Shemesh, Y.; Popov, I.; Banin, U. Au growth on semiconductor nanorods: photoinduced versus thermal growth mechanisms. *J. Am. Chem. Soc.* **2009**, *131*, 17406–17411.

18. Amirav, L.; Alivisatos, A. P. Photocatalytic hydrogen production with tunable nanorod heterostructures. *J. Phys. Chem. Lett.* **2010**, *1*, 1051–1054.

19. Dukovic, G.; Merkle, M. G.; Nelson, J. H.; Hughes, S. M.; Alivisatos, A. P. Photodeposition of Pt on colloidal CdS and CdSe/CdS semiconductor nanostructures. *Adv. Mater.* **2008**, *20*, 4306–4311.

20. Murdoch, M. *et al.* The effect of gold loading and particle size on photocatalytic hydrogen production from ethanol over Au/TiO_2 nanoparticles. *Nat. Chem.* **2011**, *3*, 489–492.

21. Xiao, X.; Pan, S.; Jang, J. S.; Fan, F.-R. F.; Bard, A. J. Single nanoparticle electrocatalysis: effect of monolayers on particle and electrode on electron transfer. *J. Phys. Chem. C* **2009**, *113*, 14978–14982.

22. Novo, C.; Funston, A. M.; Mulvaney, P. Direct observation of chemical reactions on single gold nanocrystals using surface plasmon spectroscopy. *Nat. Nanotechnol.* **2008**, *3*, 598–602.

23. Tang, M. L.; Liu, N.; Dionne, J. A.; Alivisatos, A. P. Observations of shape-dependent hydrogen uptake trajectories from single nanocrystals. *J. Am. Chem. Soc.* **2011**, *133*, 13220–13223.

24. Liu, N.; Tang, M. L.; Hentschel, M.; Giessen, H.; Alivisatos, A. P. Nanoantenna-enhanced gas sensing in a single tailored nanofocus. *Nat. Mater.* **2011**, *10*, 631–636.

25. De Cremer, G.; Sels, B. F.; De Vos, D. E.; Hofkens, J.; Roeffaers, M. B. J. Fluorescence micro(spectro)scopy as a tool to study catalytic materials in action. *Chem. Soc. Rev.* **2010**, *39*, 4703–4717.

26. Chen, P. *et al.* Single-molecule fluorescence imaging of nanocatalytic processes. *Chem. Soc. Rev.* **2010**, *39*, 4560–4570.

27. Tachikawa, T.; Majima, T. Single-molecule, single-particle fluorescence imaging of TiO_2-based photocatalytic reactions. *Chem. Soc. Rev.* **2010**, *39*, 4802–4819.

28. Xu, W.; Kong, J. S.; Yeh, Y.-T.; Chen, P. Single-molecule nanocatalysis reveals heterogeneous reaction pathways and catalytic dynamics. *Nat. Mater.* **2008**, *7*, 992–996.

29. Xu, W.; Kong, J. S.; Chen, P. Probing the catalytic activity and heterogeneity of Au-nanoparticles at the single-molecule level. *Phys. Chem. Chem. Phys.* **2009**, *11*, 2767–2778.

30. Xu, W.; Jain, P. K.; Beberwyck, B. J.; Alivisatos, A. P. Probing redox photocatalysis of trapped electrons and holes on single Sb-doped titania nanorod surfaces. *J. Am. Chem. Soc.* **2012**, *134***,** 3946–3949.

31. Zhou, X. *et al.* Quantitative super-resolution imaging uncovers reactivity patterns on single nanocatalysts. *Nat. Nanotechnol.* **2012**, *7*, 237–241.

32. Tachikawa, T.; Yonezawa, T.; Majima, T. Super-resolution mapping of reactive sites on titania-based nanoparticles with water-soluble fluorogenic probes. *ACS Nano* **2012**, *7*, 263–275.
33. De Cremer, G. *et al.* High-resolution single-turnover mapping reveals intraparticle diffusion limitation in Ti-MCM-41-catalyzed epoxidation. *Angew. Chem. Int. Ed.* **2010**, *49*, 908–911.

34. Roeffaers, M. B. J. *et al.* Super-resolution reactivity mapping of nanostructured catalystparticles. *Angew. Chem. Int. Ed.* **2009**, *48*, 9285–9289 .

35. Shaviv, E. *et al.* Absorption properties of metalsemiconductor hybrid nanoparticles. *ACS Nano* **2011**, *5*, 4712–4719.

36. Robinson, R. D. *et al.* Spontaneous superlattice formation in nanorods through partial cation xxchange. *Science* **2007**, *317*, 355–358.

37. Saunders, A. E.; Popov, I.; Banin, U. Synthesis of hybrid CdS-Au colloidal nanostructures. *J. Phys. Chem. B* **2006**, *110*, 25421–25429.

38. Mongin, D. *et al.* Ultrafast photoinduced charge separation in metal-semiconductor nanohybrids. *ACS Nano* **2012**, *6*, 7034–7043.

39. Mukherjee, S. *et al.* Hot electrons do the impossible: plasmon-induced dissociation of H2 on Au. *Nano Lett.* **2012**, *13*, 240–247.

40. Moskovits, M. Hot electrons cross boundaries. *Science* **2011**, *332*, 676–677.

41. Anderson, P. A. Work function ofgold. *Physical Review* **1959**, *115*, 553–554.

42. Frischkorn, C.; Wolf, M. Femtochemistry at metal surfaces: nonadiabatic reaction dynamics. *Chem. Rev.* **2006**, *106*, 4207–4233.

43. Christopher, P.; Xin, H.; Linic, S. Visible-light-enhanced catalytic oxidation reactions on plasmonic silver nanostructures. *Nat. Chem.* **2011**, *3*, 467–472.

44. Mubeen, S. *et al.* An autonomous photosynthetic device in which all charge carriers derive from surface plasmons. *Nat. Nanotechnol.* **2013**, *8*, 247–251.

45. Mubeen, S.; Hernandez-Sosa, G.; Moses, D.; Lee, J.; Moskovits, M. Plasmonic photosensitization of a wide band gap semiconductor: converting plasmons to charge carriers. *Nano Lett.* **2011**, *11*, 5548–5552.

46. Lee, J.; Mubeen, S.; Ji, X.; Stucky, G. D.; Moskovits, M. Plasmonic photoanodes for solar water splitting with visible light. *Nano Lett.* **2012**, *12*, 5014–5019.

47. Ishibashi, K.-I.; Fujishima, A.; Watanabe, T.; Hashimoto, K. Generation and deactivation processes of superoxide formed on TiO_2 film illuminated by very weak UV light in air or water. *J. Phys. Chem. B* **2000**, *104*, 4934–4938.

48. Hoffmann, M. R.; Martin, S. T.; Choi, W.; Bahnemann, D. W. Environmental applications of semiconductor photocatalysis. *Chem. Rev.* **1995**, *95*, 69–96.

49. Thompson, T. L.; Yates, J. T. Surface science studies of the photoactivation of TiO_2-new photochemical processes. *Chem. Rev.* **2006**, *106*, 4428–4453.

50. Chih, T.; Jao, H.-J.; Wang, C. M. Glucose sensing based on an effective conversion of O_2 and H_2O_2 into superoxide anion radical with clay minerals. *J. Electroanal. Chem.* **2005**, *581*, 159–166.

51. Gorris, H. H.; Walt, D. R. Mechanistic aspects of horseradish peroxidase elucidated through single-molecule studies. *J. Am. Chem. Soc.* **2009**, *131*, 6277–6282.

52. Ruberu, T. P. A.; Vela, J. Expanding the one-dimensional CdS–CdSe composition landscape: axially anisotropic $CdS_{1-x}Se_x$ nanorods. *ACS Nano* **2011**, *5*, 5775–5784.

53. Baptista, L.; Clemente da Silva, E.; Arbilla, G. Oxidation mechanism of dimethyl sulfoxide (DMSO) by OH radical in liquid phase. *Phys. Chem. Chem. Phys.* **2008**, *10*, 6867–6879.

54. Popham, P.; Novacky, A. Use of dimethyl sulfoxide to detect radical during bacteria-induced hypersensitive reaction. *Plant Physiol.* **1991**, *96*, 1157–1160.

Figures and Captions

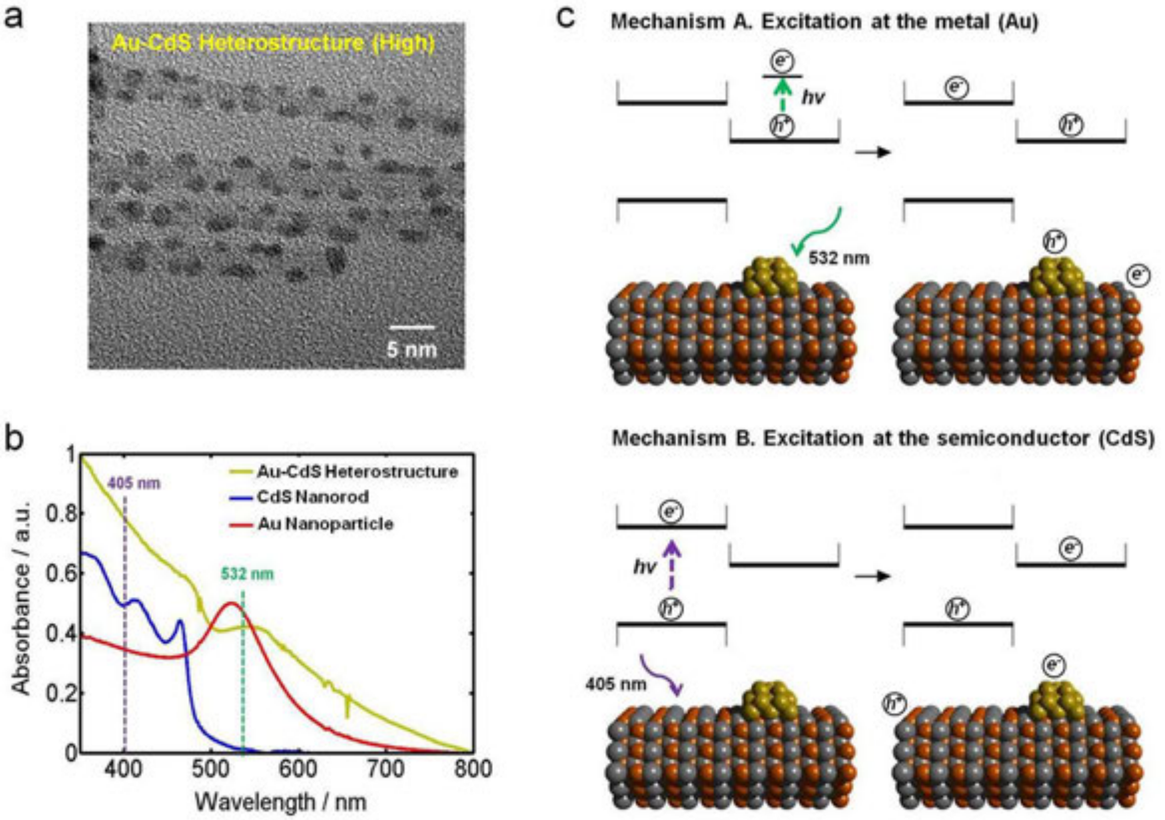

Figure 1. Photocatalytic Au-CdS hybrid heterostructures reveal two distinct photo-induced charge separation mechanisms. (a) TEM image of single high Au-CdS heterostructures (10.8 wt%). The CdS nanorods are 186(±56) nm long and 6.0(±0.9) nm wide. The diameter of Au nanoparticles ranges from 2 nm to 7 nm. (b) UV-Vis absorption spectra of pure CdS nanorods (blue-curve), Au nanoparticles (red-curve) and high Au-CdS heterostructures (10.8 wt%, yellow-curve). The green- and purple-dotted lines indicate the excitation source of a 532-nm laser and a 405-nm laser, respectively. (c) Two charge separation mechanisms in these hybrid heterostructures. Mechanism A starts by excitation at the metal at 532 nm, thus forming hot electrons (e^-) and holes (h^+) in the metal. The hot electrons are then transferred to the semiconductor's conduction band. Mechanism B starts with excitation at the semiconductor at 405 nm, thus forming electron-hole pairs at the semiconductor. Photo-generated electrons are then trapped by the gold metal.

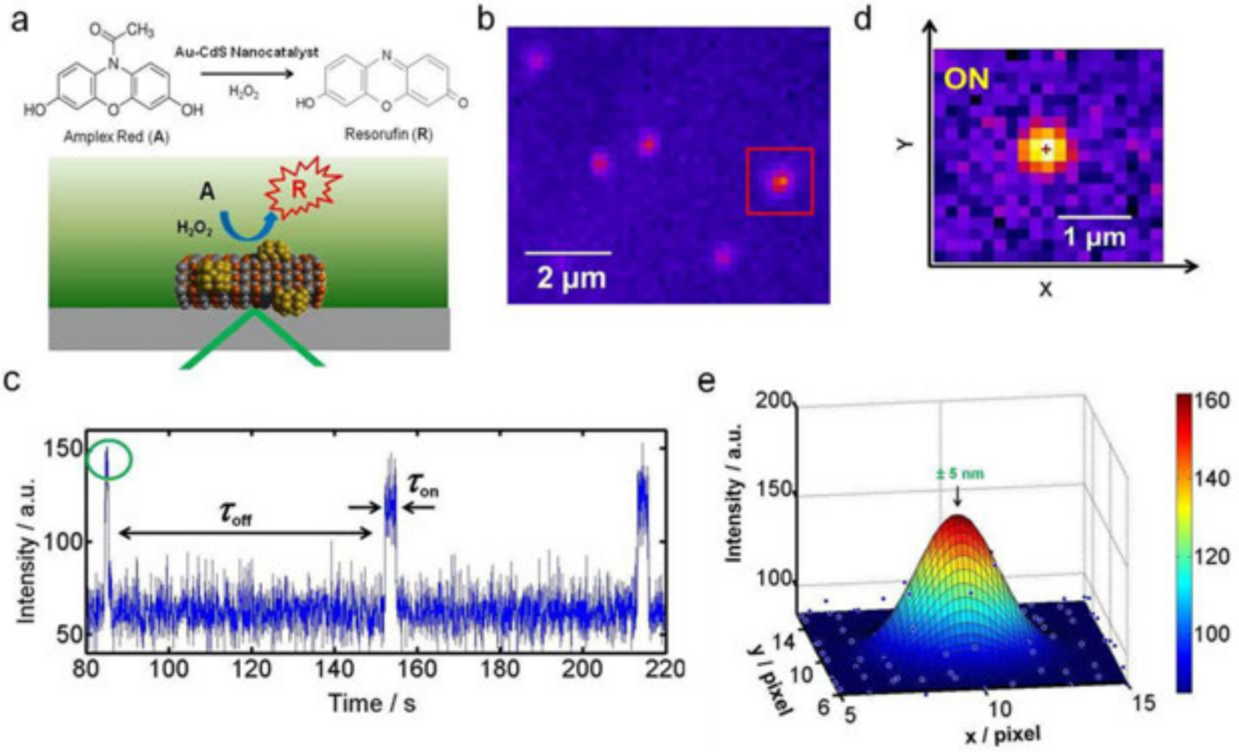

Figure 2. Single-molecule super-localization fluorescence imaging over single Au-CdS heterostructures during a photocatalytic oxidation reaction. (a) Experimental scheme using total internal reflection fluorescence microscopy to probe the fluorogenic oxidation reaction of non-fluorescent amplex red (A) to highly-fluorescent resorufin (R) by a Au-CdS nanocatalyst. (b) Typical image of fluorescent products at localized spots during the catalytic reaction under 532-nm illumination. (c) Segment of a typical fluorescence intensity trajectory from the fluorescent spot squared in red in b with 1 μM amplex red, 20 mM H_2O_2, and 10 mM phosphate buffer (pH 7.2). Temporal resolution is 50 ms. (d) Fluorescence image of a single resorufin molecule during one burst circled in green in c. (e) Three-dimensional representation of the image in d. The center position of the fluorescence image can be determined with nanometer accuracy (±5 nm) and is marked as a red-cross in d.

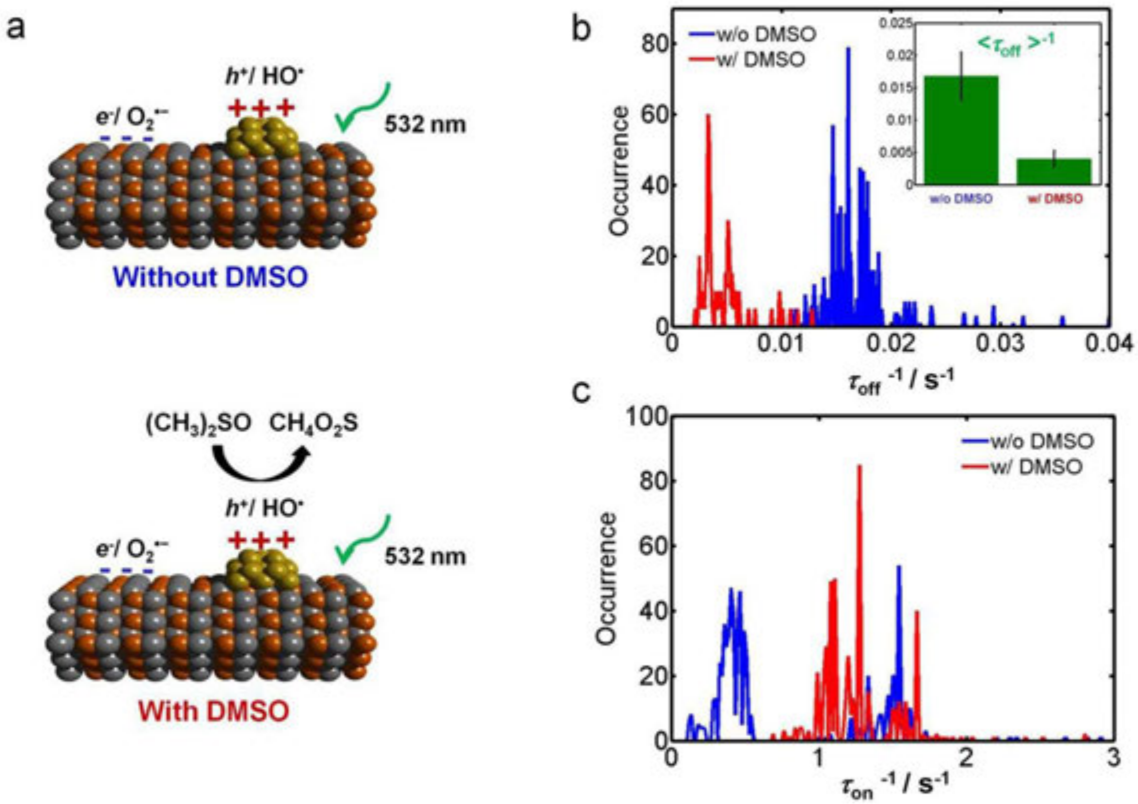

Figure 3. Heterogeneous and distinct photocatalytic activity of active sites on Au-CdS heterostructures. (a) Two distinct microenvironments around the active sites ($e^-/O_2^{\bullet-}$ and $h^+/HO^\bullet$) under 532-nm excitation. Active sites around photo-generated holes have a positively charged microenvironment, while active sites around photo-generated electrons have a negatively charged microenvironment. Dimethyl sulfoxide (DMSO) is used to quench the $h^+/HO^\bullet$ active sites. DMSO is oxidized by the $HO^\bullet$ radicals to methanesulfinic acid (MSIA, CH_4O_2S). (b) Histogram of the rate of product formation τ_{off}^{-1} for the fluorescence bursts obtained from over 100 individual nanoparticles in the absence of DMSO (blue-curve) or in the presence of DMSO (red-curve). (c) Histogram of the rate of product dissociation τ_{on}^{-1} for the fluorescence bursts obtained in the absence of DMSO (blue-curve) or in the presence of DMSO (red-curve). The distinct dissociation kinetics of the two basic active sites are observed because of the differently charged microenvironments as depicted in a.

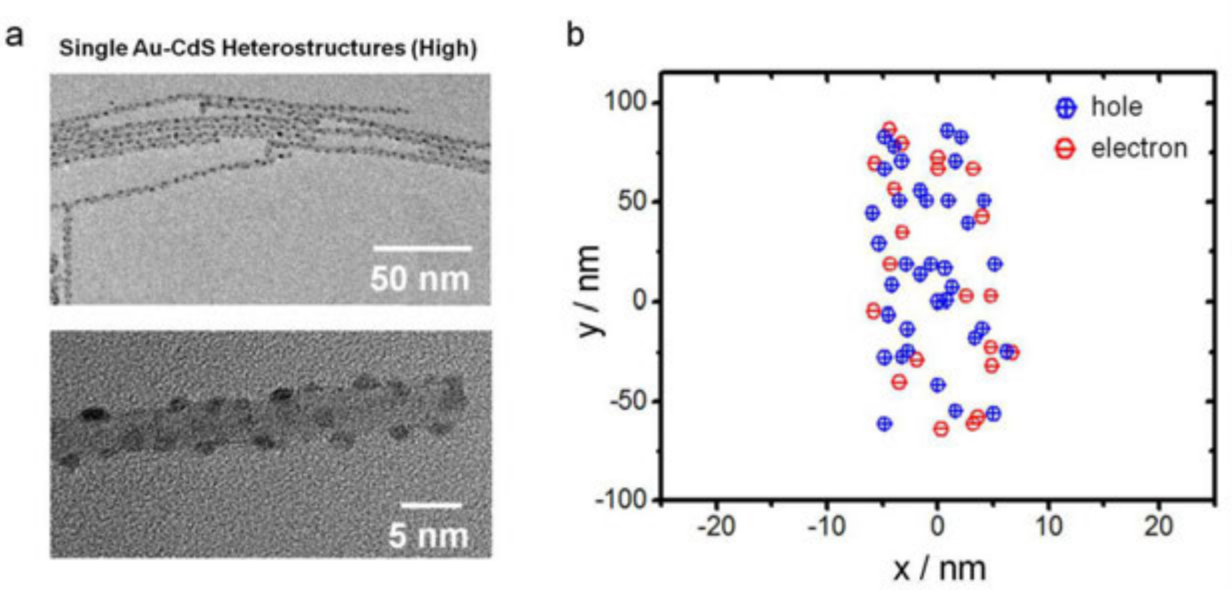

Figure 4. Super-localization of single surface active sites on a high Au-CdS heterostructure during photocatalysis. (a) TEM image of typical single high Au-CdS heterostructures (top). Enlarged TEM image (bottom) shows high density of Au nanoparticles. (b) Super-resolution mapping of individual active sites on a high metal loading Au-CdS heterostructure at 532 nm. Each one of the circled cross or minus signs corresponds to one resorufin product molecule. The circled blue-crosses show a product molecule caused by h^+/HO$^\bullet$ active sites, while the circled red-minuses shows a product molecule from e^-/$O_2^{\bullet-}$ active sites. The catalytic reaction was carried out with 1 μM amplex red and 20 mM H_2O_2 in 10 mM pH 7.2 phosphate buffer.

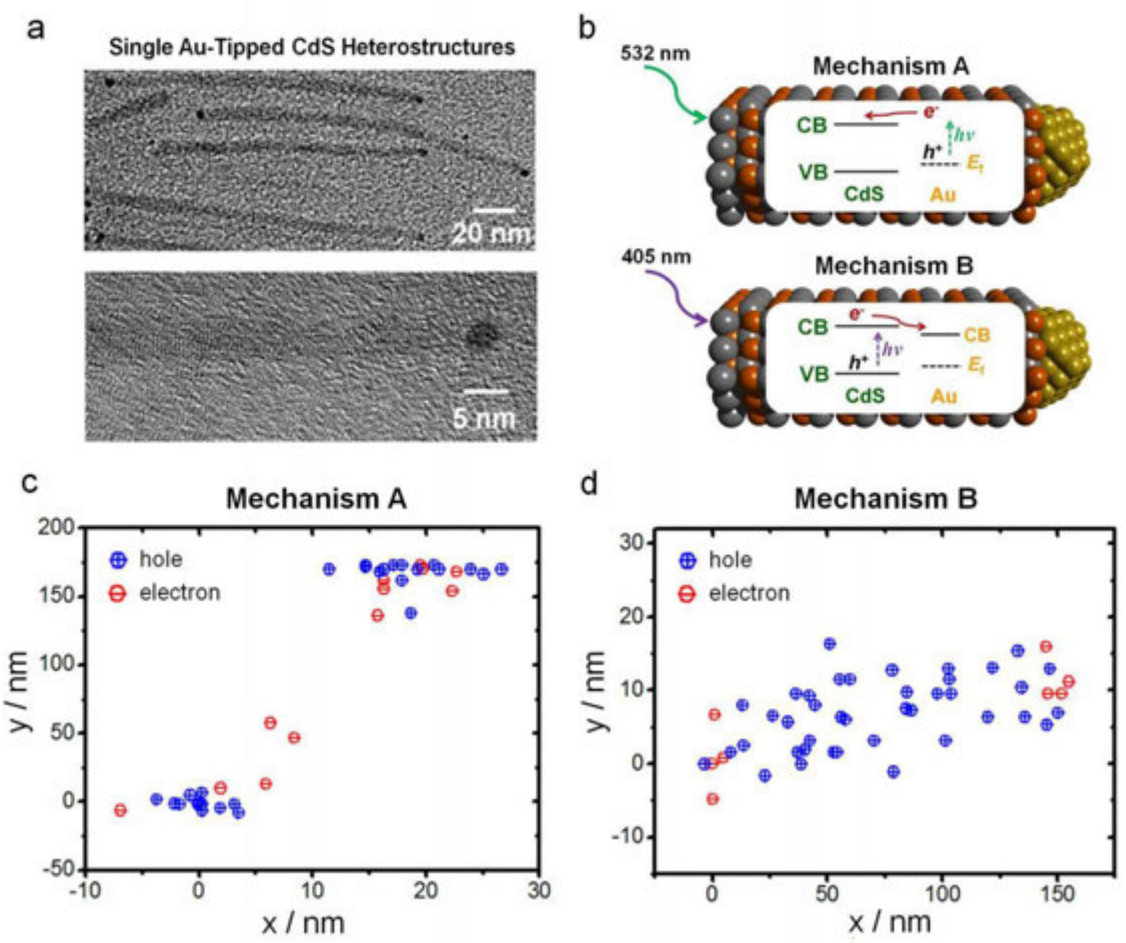

Figure 5. Engineering energy flows on single Au-tipped CdS nanorod heterostructures. (a) TEM image of typical single Au-tipped CdS nanorod heterostructures (top). Enlarged TEM image (bottom) shows a Au nanoparticle at the tip. (b) Schematic illustrating two distinct photocatalysis mechanisms with the opposite direction of energy flow (opposite polarity after photo-induced charge-separation). In mechanism A at 532 nm, the photo-generated energetic electrons in the gold metal are injected to the conduction band (CB) of the semiconductor. In mechanism B at 405 nm, the photo-generated electrons in the CB of the semiconductor are rapidly trapped by the gold metal. (c) Super-resolution mapping of single active sites on a Au-tipped CdS nanorod heterostructure during the oxidation reaction at 532 nm (mechanism A). (d) Super-resolution mapping of single active sites on a Au-tipped CdS nanorod heterostructure during the same oxidation reaction after turning on the 405 nm laser (in addition to the 532 nm laser, needed to excite the resorufin product) (mechanism B).

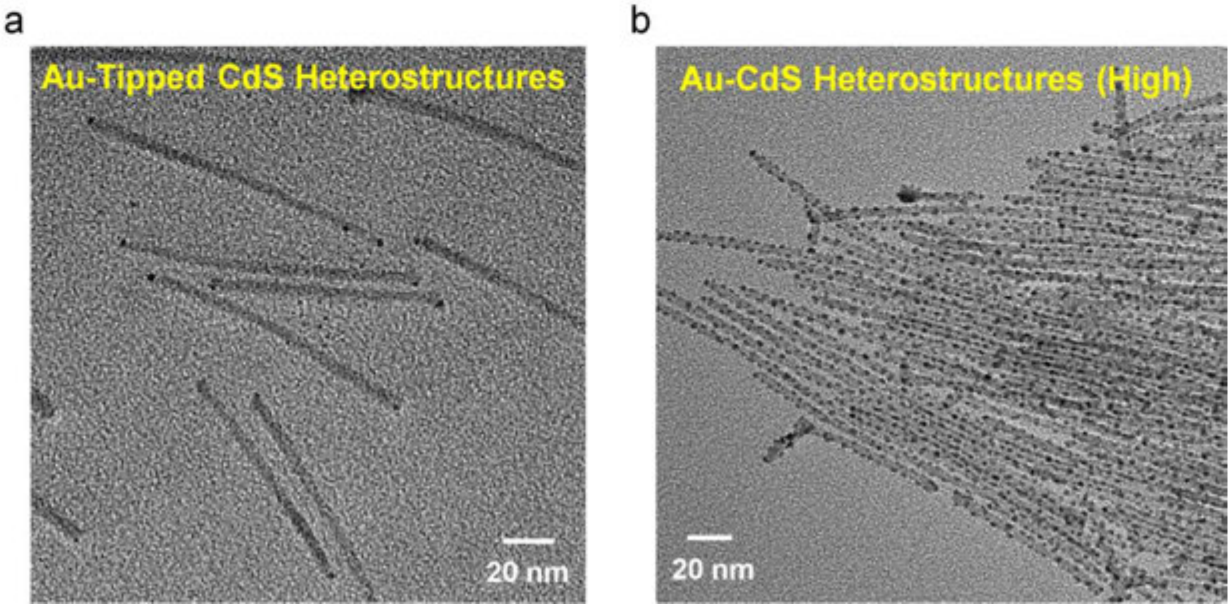

Figure S1. TEM images of Au-CdS hybrid heterostructures. (a) TEM image of CdS nanorods with Au nanoparticles at both ends (0.54 wt%). (b) TEM image of CdS nanorods with high density of Au nanoparticles (10.8 wt%).

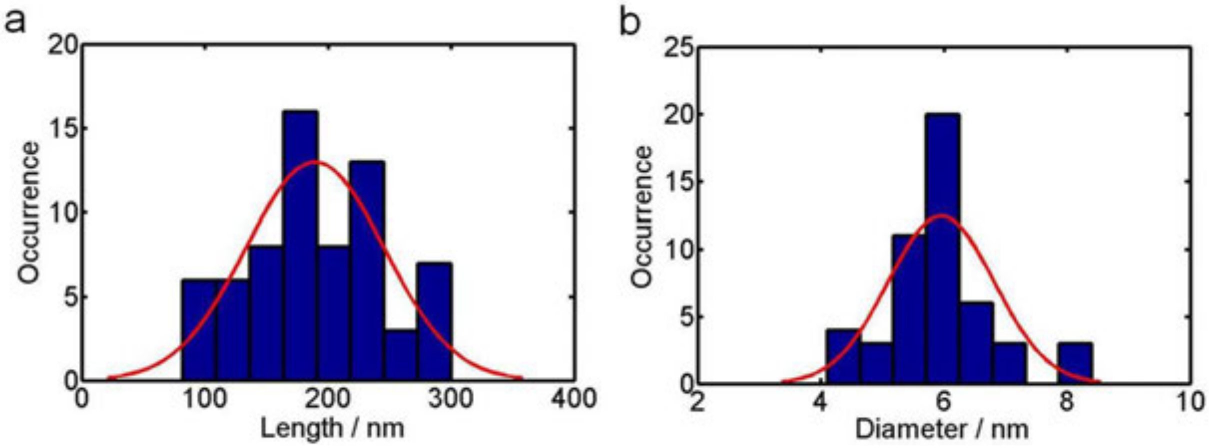

Figure S2. Size distribution of CdS nanorods. (a) Histogram to show the length of CdS nanorods used in this study. The red-curve is a Gaussian-fit to the histogram. The mean length of CdS nanorods is 186(±56) nm. (b) Histogram to show the diameter of CdS nanorods. The diameter of CdS nanorods is 6(±0.9) nm.

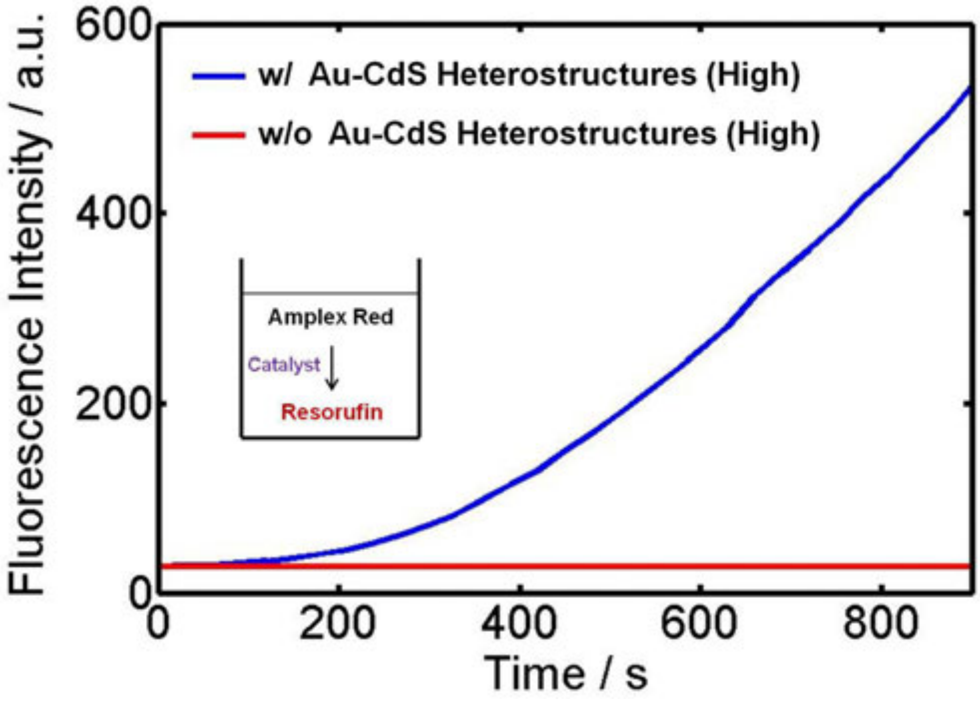

Figure S3. Ensemble fluorescence measurements of the fluorogenic oxidation reaction. The catalytic reactions were initiated by adding an aliquot of high Au-CdS heterostructure solution into a cuvette containing 1 μM amplex red and 20 mM H_2O_2 in 10 mM pH 7.2 phosphate buffer. A fluorescence intensity was measured after every 30 sec of illumination of the cuvette at 532 nm (±25 nm).

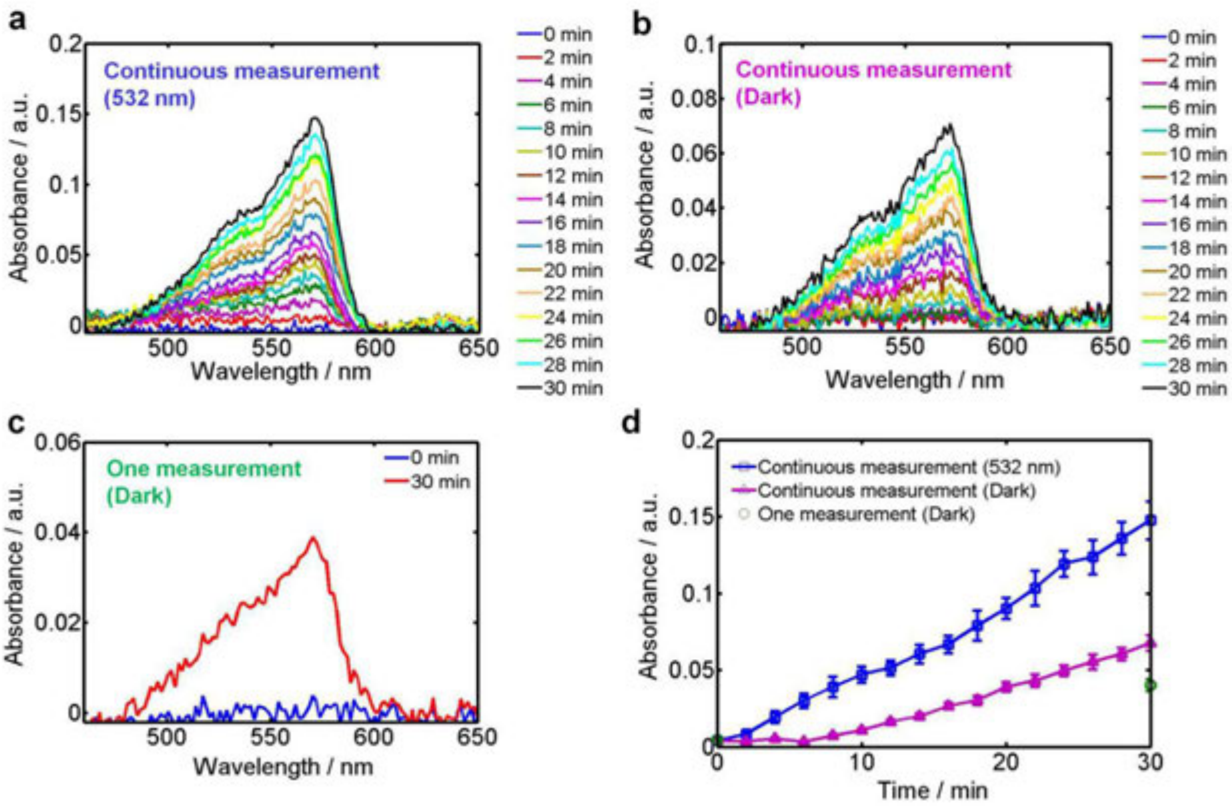

Figure S4. Photocatalysis in Au-CdS hybrid heterostructures under mechanism A at 532 nm. (a) Change in the absorbance measured after every 2 min of continuous illumination at 532 nm. (b) Change in the absorbance with an interval of 2 min under dark condition. (c) Change in the absorbance which is measured once after 30 min under dark condition. (d) The effect of light on the absorbance in Au-CdS heterostructures. We repeated three measurements for each case under the same conditions.

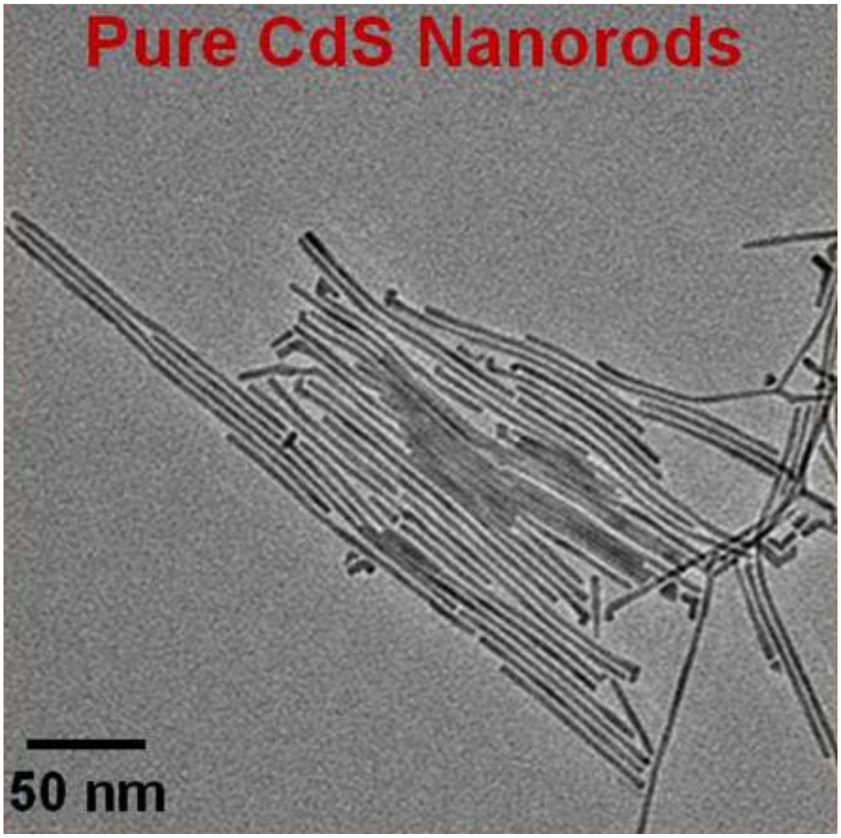

Figure S5. TEM image of pure CdS nanorods without Au nanoparticles. The average length and diameter of pure CdS nanorods used in this study are 183 nm and 6 nm, respectively.

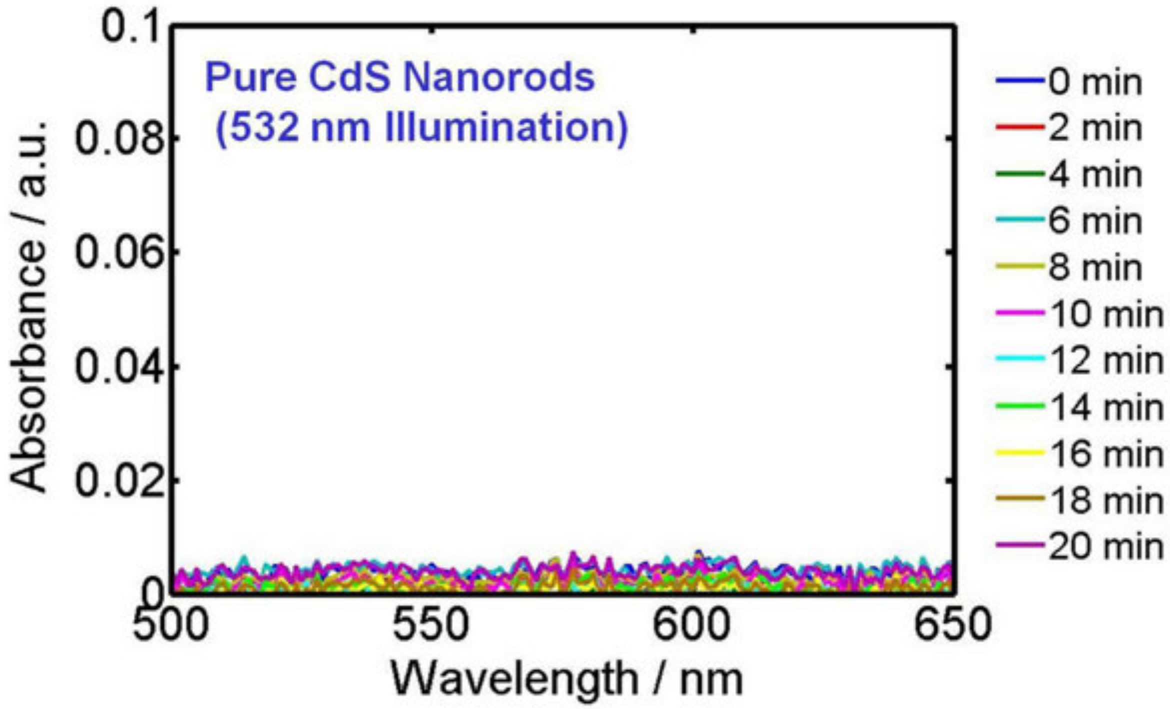

Figure S6. The effect of 532-nm illumination on pure CdS nanorods. The absorption spectra were taken after every 2 min of illumination at 532 nm. There is no formation of resorufin product in pure CdS nanorods at 532 nm. This verifies that a 532-nm green laser does not excite CdS nanorods.

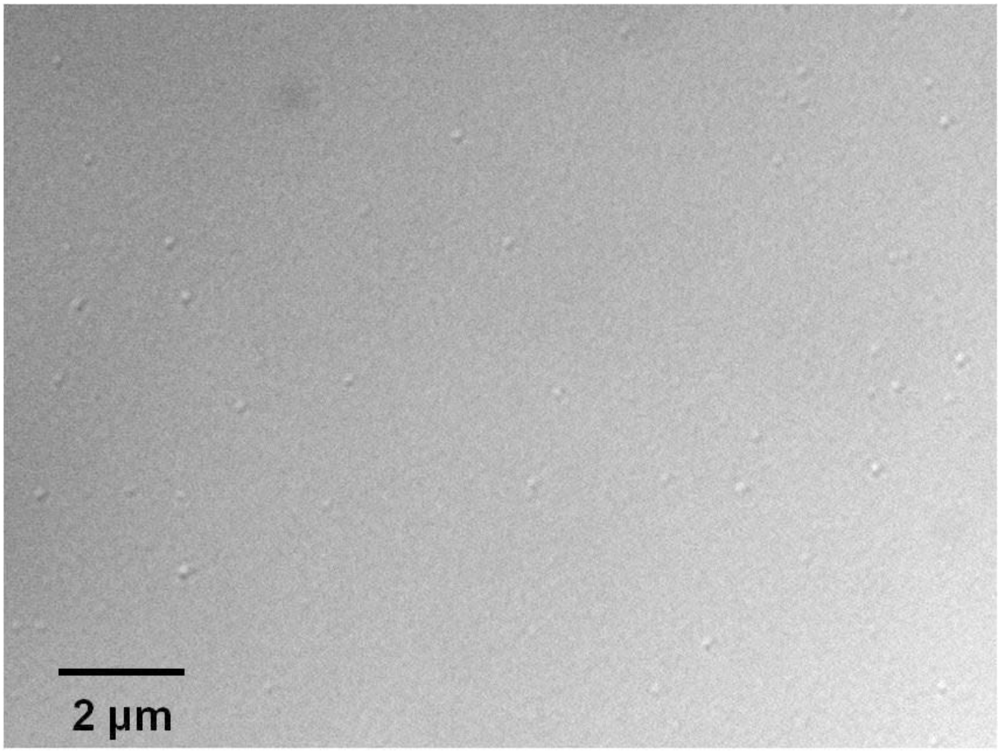

Figure S7. DIC image of high Au-CdS heterostructures. The DIC imaging was carried out by inserting a 547-nm band-pass filter into the light path in the microscope. The spots in the image indicate the Au-CdS heterostructures that are separated.

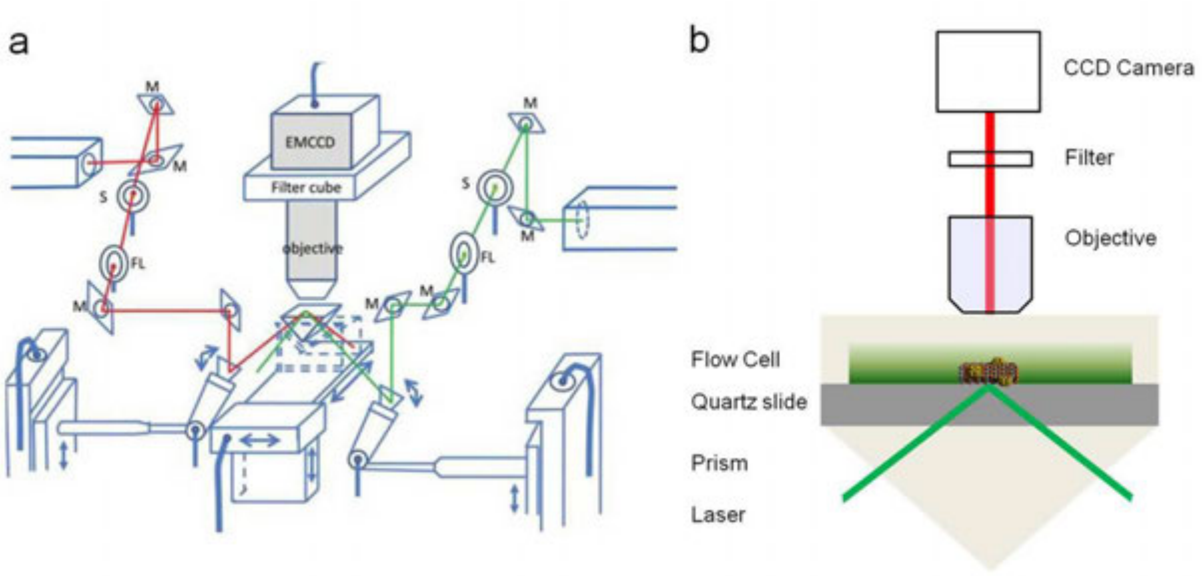

Figure S8. Experimental schematic diagrams for single-particle single-molecule photocatalysis. (a) Schematic diagram of the automated prism-type dual-color scanning-angle total internal reflection microscope: M, mirror; S, mechanical shutter; FL, focusing lens. A 532-nm laser was used as excitation source in this study. (b) Schematic diagram showing total internal reflection fluorescence microscopy to detect the fluorogenic oxidation reaction of amplex red to resorufin catalyzed by individual Au-CdS heterostructures within a flow cell.

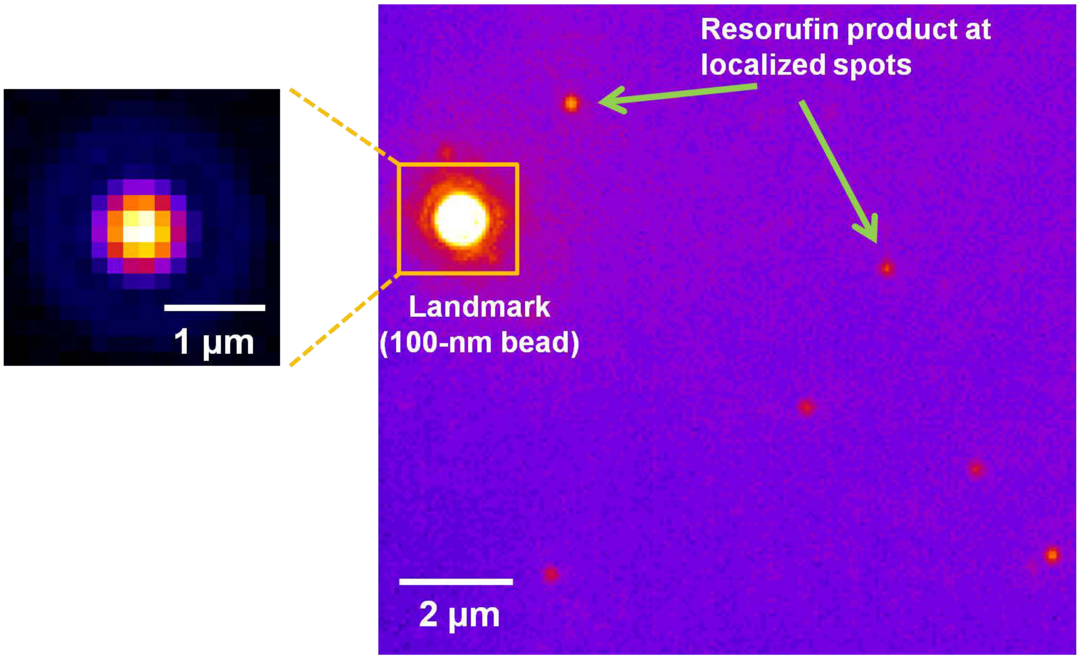

Figure S9. Position marker to correct for sample drifting. The intensity averaged image was obtained from 100 frames. A red-fluorescent bead (R100) squared with yellow was used as a position marker to correct for sample drifting. The green arrows indicate the resorufin product at localized spots in the image.

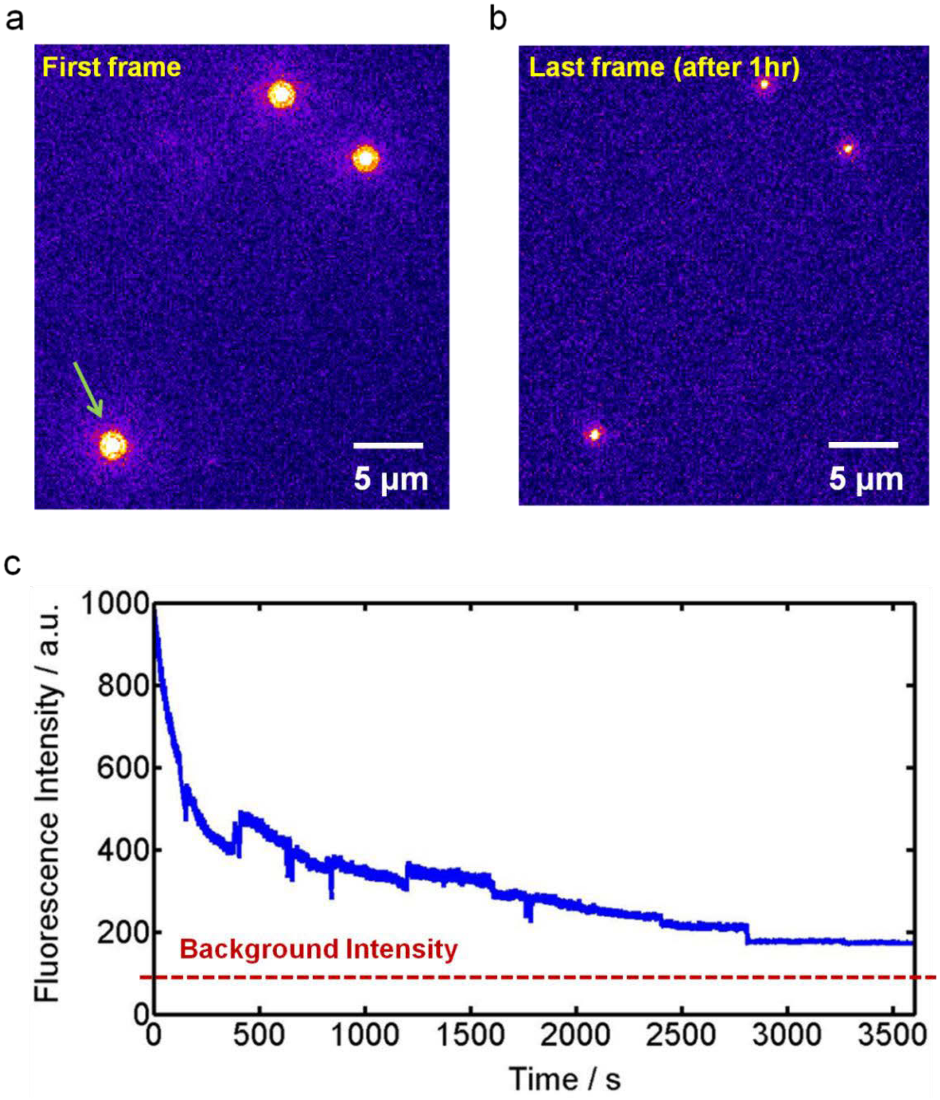

Figure S10. Photo-bleaching of the red-fluorescent beads. (a) Fluorescence image of three red-fluorescent beads (R100) used as position markers in the first frame taken under 532-nm excitation (28.24 W/cm^2). (b) Fluorescence image of the same beads in the last frame after 1 hr illumination. (c) Fluorescence intensity profile of a bead (green arrow in a) as a function of time. The red-dotted line shows a background intensity. The fluorescent bead is photo-bleached over time, but the intensity of the bead after 1 hr was about 2 times higher than the background intensity.

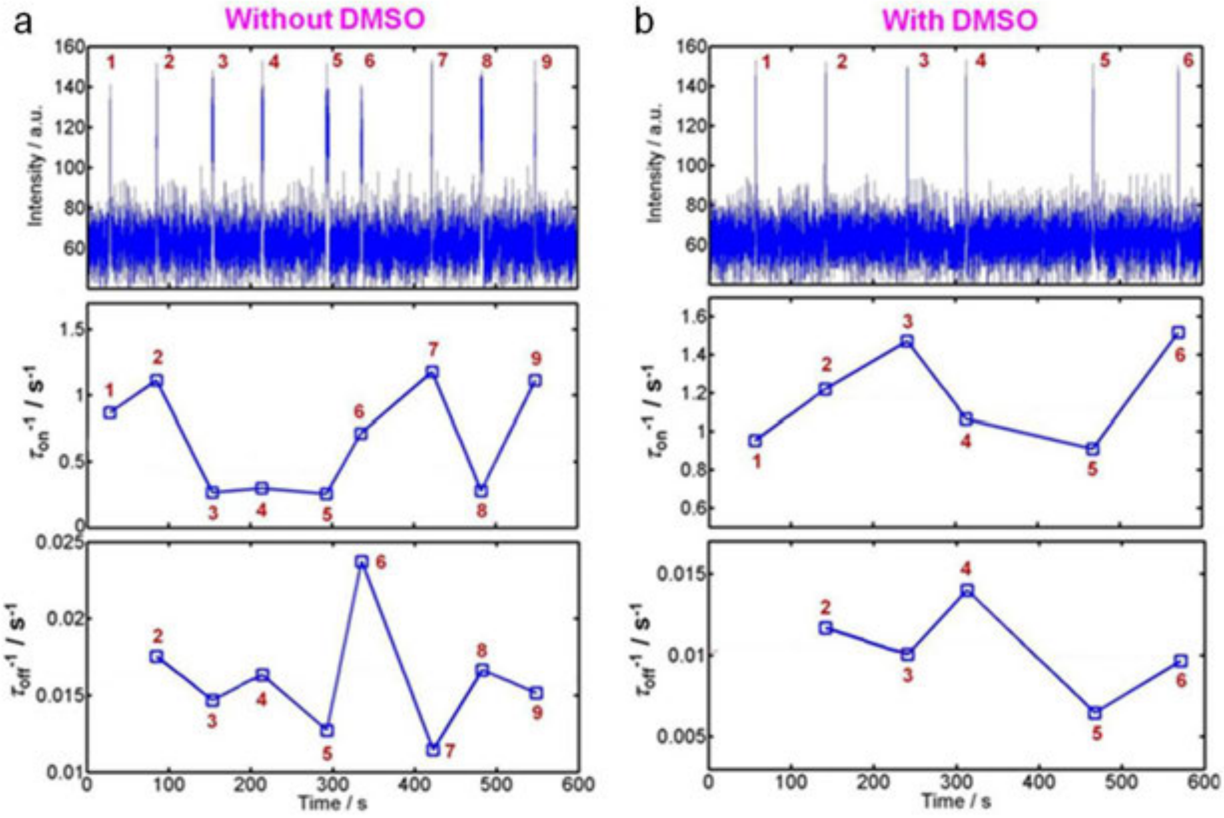

Figure S11. Reactivity of the two basic active sites on high Au-CdS heterostructures. (a) Segment of a fluorescence intensity trajectory over one Au-CdS heterostructure measured in the absence of DMSO and the time profile for the two rates for each fluorescence burst. In this case, fluorescence bursts come from both types of active sites. (b) Segment of a fluorescence intensity trajectory over one Au-CdS heterostructure measured in the presence of DMSO and the time profile for the two rates for each fluorescence burst. DMSO is used to quench all the $HO^{\bullet}$ radicals. It is oxidized by the $HO^{\bullet}$ radicals to methanesulfinic acid (MSIA, CH_4O_2S). In this case, fluorescence bursts are only produced at the $e^-/O_2^{\bullet-}$ active sites.

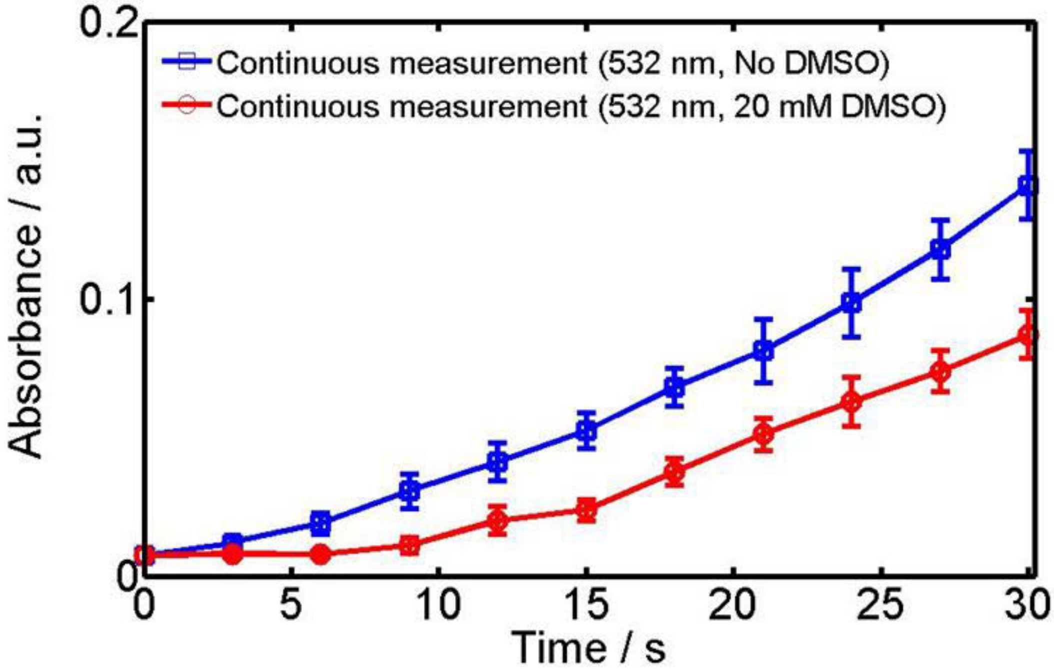

Figure S12. The effect of DMSO on the photocatalytic oxidation reaction of amplex red in Au-CdS heterostructures. An aliquot of high Au-CdS heterostructure solution was injected into a cuvette containing a solution (14 µM amplex red, 20 mM H_2O_2, and 0.5 µM catalysts in 50 mM pH 7.2 phosphate buffer). The blue-curve shows the change in the absorbance measured after every 3 min of illumination at 532 nm in the absence of DMSO. The red-curve shows the change in the absorbance measured after every 3 min of illumination at 532 nm in the presence of DMSO (20 mM). We repeated three times for each case under same experimental conditions.

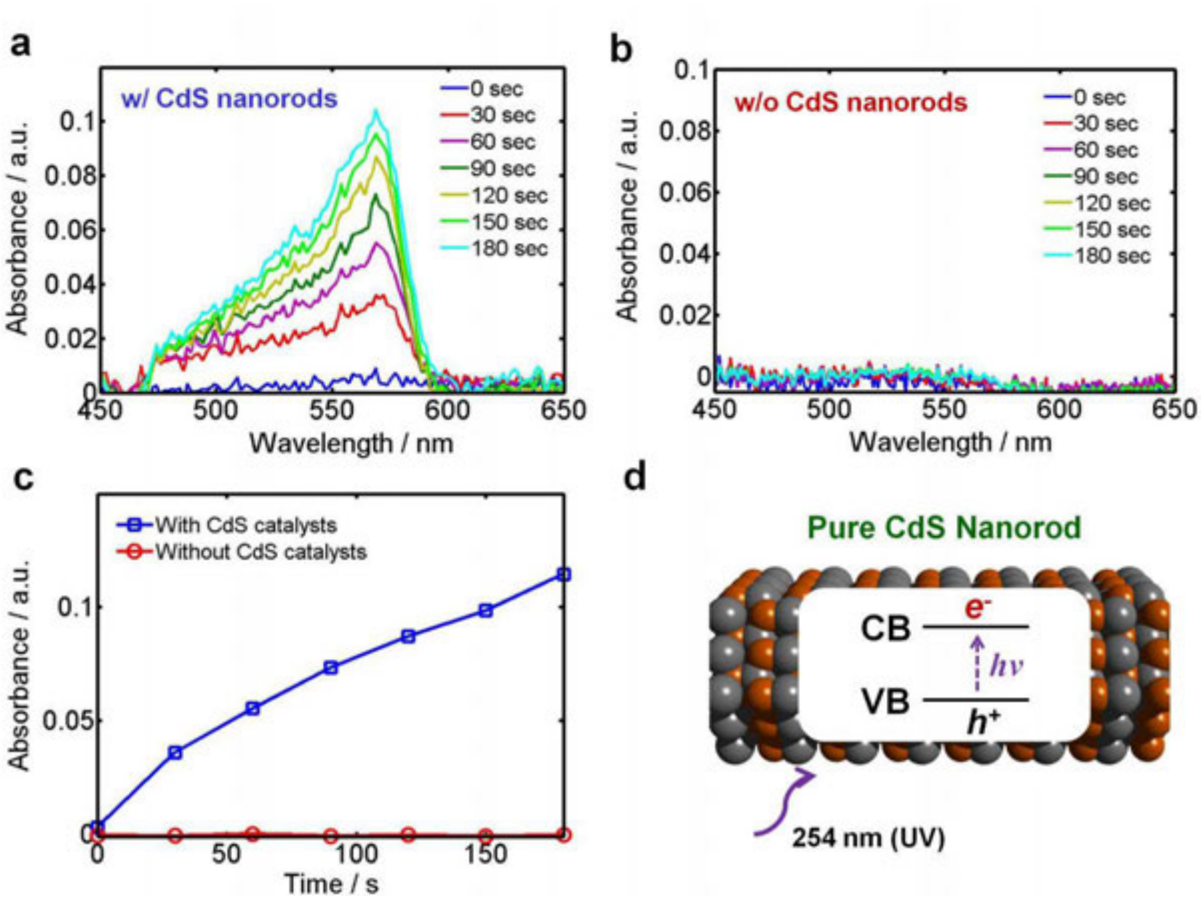

Figure S13. Ensemble experiments to support mechanism B involving the photo-generated carriers in pure CdS nanorods. (a) Change in the absorbance measured after every 30 sec of illumination at 254 nm in the presence of pure CdS nanorods. The absorbance increases with an interval of 30 sec. (b) Change in the absorbance measured after every 30 sec of illumination at 254 nm in the absence of pure CdS nanorods. The absorbance remained constant. There is no effect of solution on the formation of resorufin product under 254-nm illumination (1.93 mW/cm^2). (c) Comparison of the absorbance in both cases of w/ CdS nanorods (blue-curve) and w/o CdS nanorods (red-curve). (d) Schematic diagram to depict the formation of electrons and holes in CdS nanorods under 254-nm excitation.

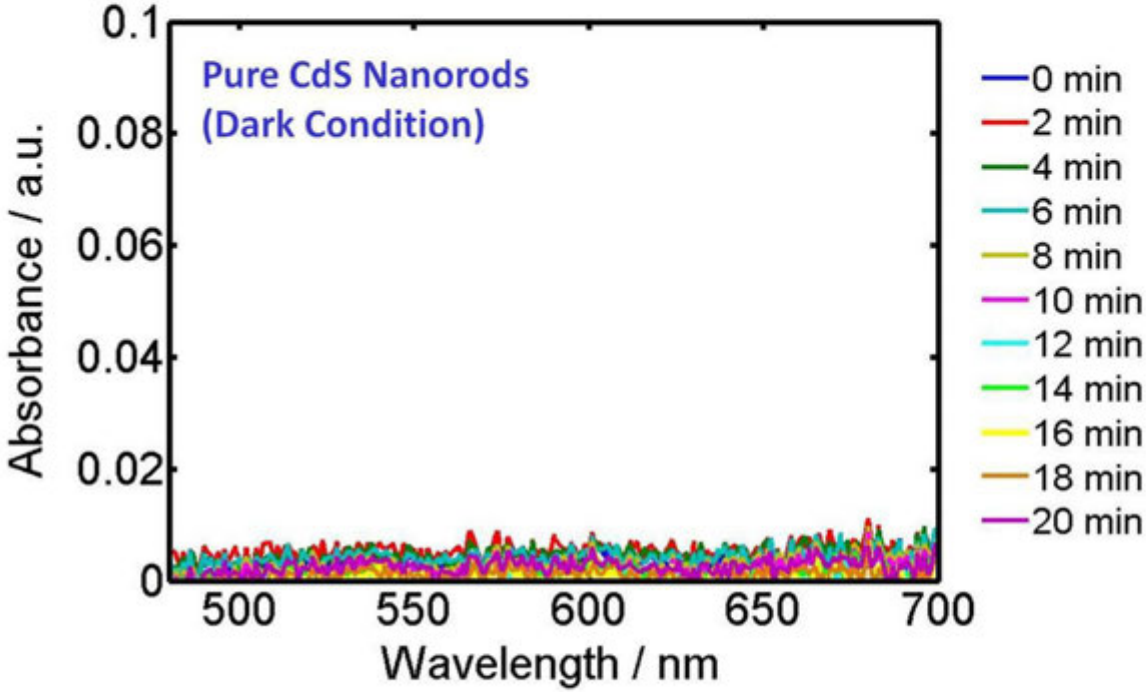

Figure S14. The effect of surface catalysis on pure CdS nanorods. These experiments were done under dark condition, and we found that there is no formation of resorufin product, which verifies no surface catalysis going on the pure CdS nanorods.

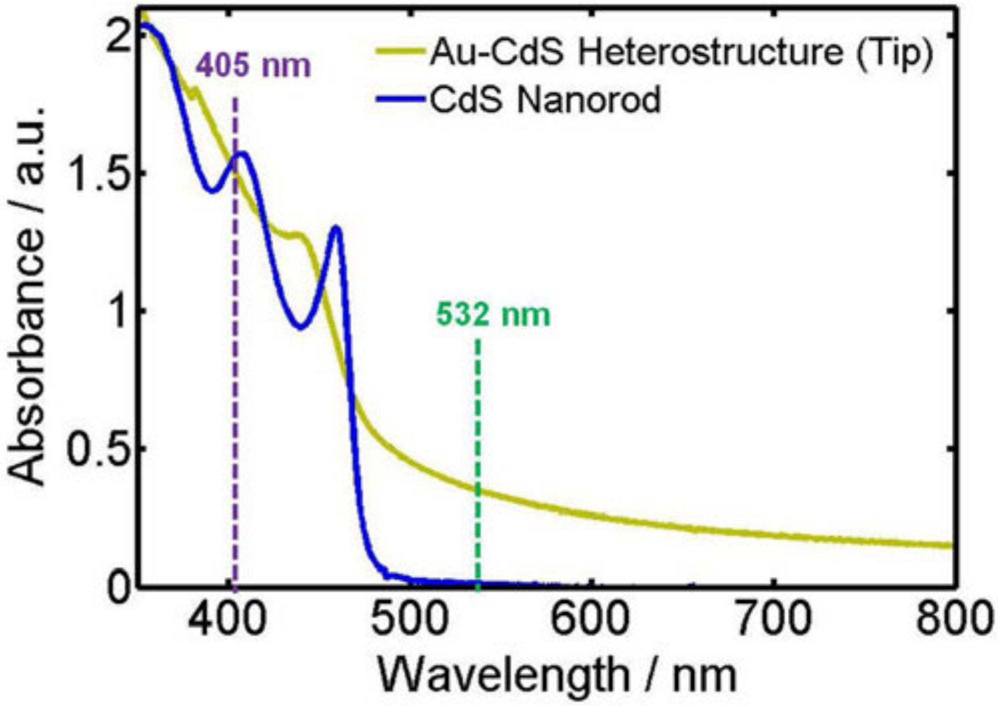

Figure S15. UV-Vis absorption spectra of pure CdS nanorods and Au-tipped CdS nanorod heterostructures. The green- and purple-dotted lines indicate the excitation source of a 532-nm laser and a 405-nm laser, respectively.

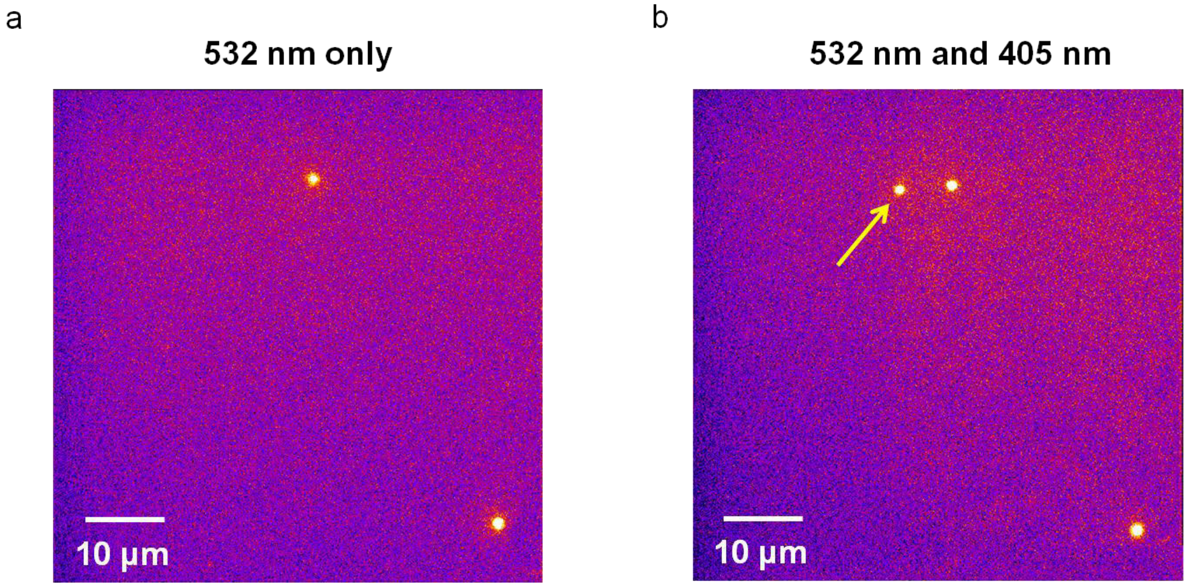

Figure S16. Two kinds of fluorescent beads (R100, B100) were mixed and deposited on the quartz slide. (a) Fluorescence image of two red-fluorescent beads (R100) excited at 532 nm. (b) Fluorescence image of beads in the same area after turning on a 405-nm laser. A blue-fluorescent bead (B100, yellow arrow) is shown in the image, which means that a evanescent field at 405 nm is generated at the interface and it excites the blue-fluorescent bead (R100). A 532-nm LP filter was inserted into the beam path before a CCD camera. The emission maximum of the blue-fluorescent beads excited at 412 nm is 473 nm, and portions of the fluorescence light with high intensity can pass the 532-nm LP filter.

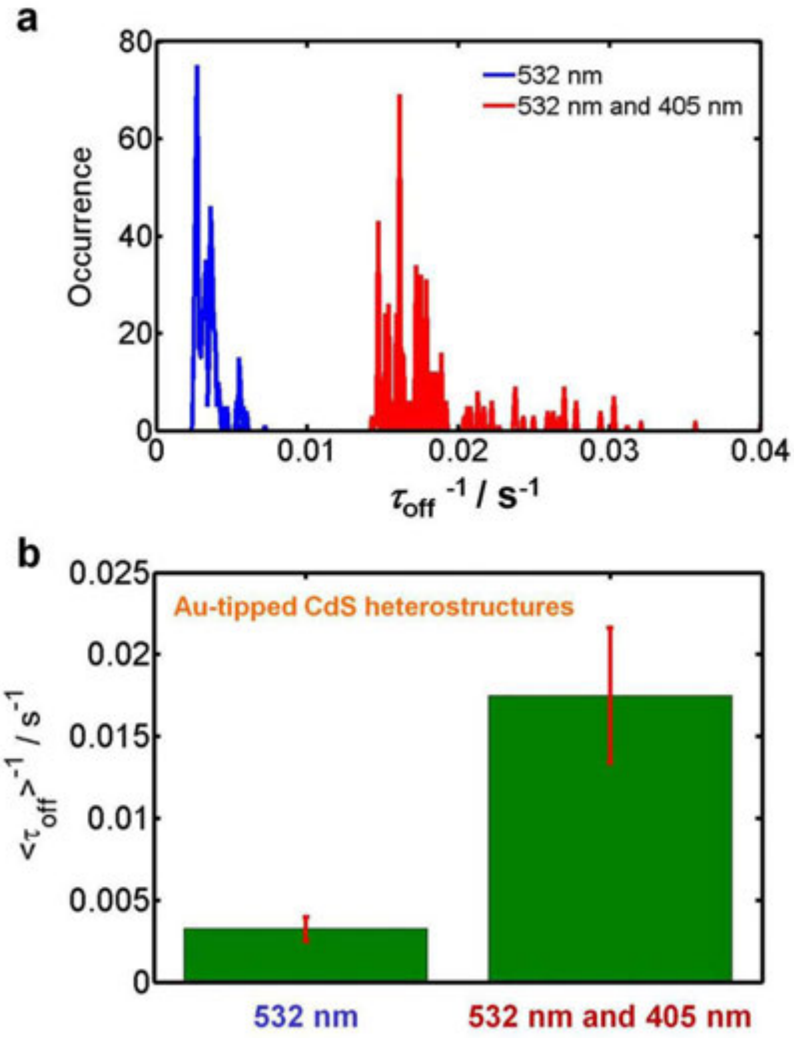

Figure S17. Comparison of the rate of product formation between two mechanisms (A and B) in Au-tipped CdS heterostructures. (a) Histogram of the rate of product formation τ_{off}^{-1} for the fluorescence bursts obtained under mechanism A at 532 nm (blue-curve) or under mechanism B at both 405 nm and 532 nm (red-curve). (b) The averaged rate of product formation $<\tau_{off}>^{-1}$ in each mechanism.

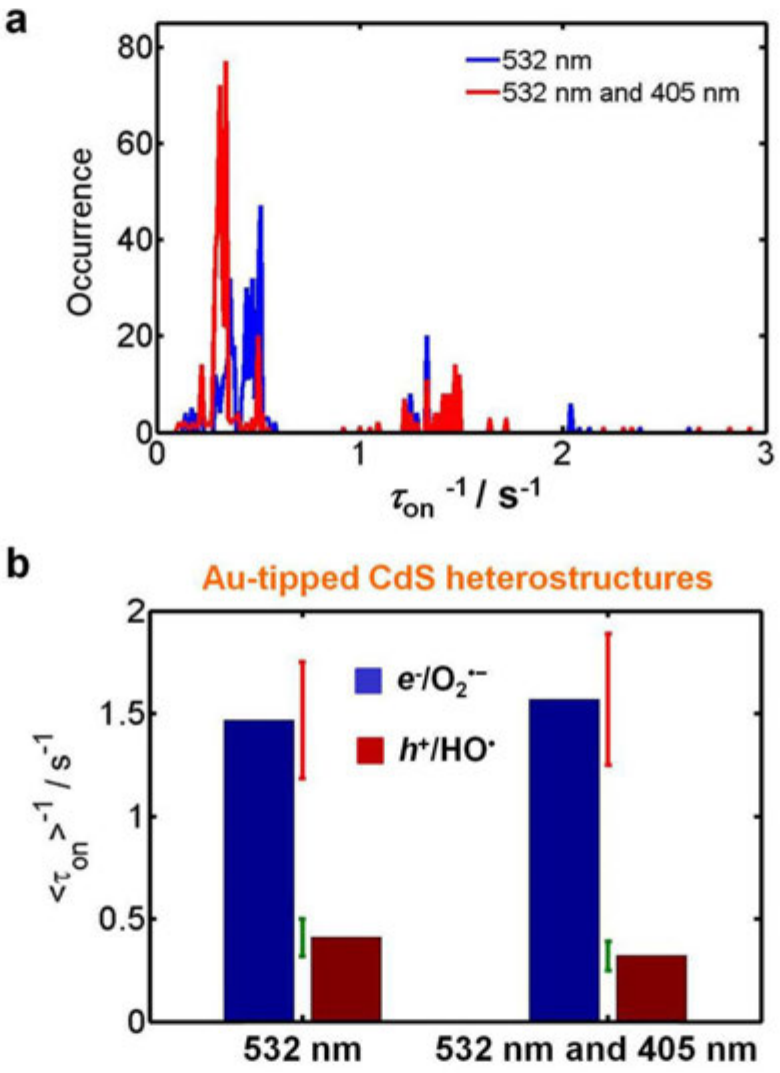

Figure S18. Comparison of the rate of product dissociation between two mechanisms (A and B) in Au-tipped CdS heterostructures. (a) Histogram of the rate of product dissociation τ_{on}^{-1} for the fluorescence bursts obtained under mechanism A at 532 nm (blue-curve) or under mechanism B at both 405 nm and 532 nm (red-curve). Two distinct dissociation kinetics (or distributions) of the two basic active sites are observed in both cases. (b) The averaged rate of product dissociation $<\tau_{on}>^{-1}$ for the two basic active sites in each mechanism.

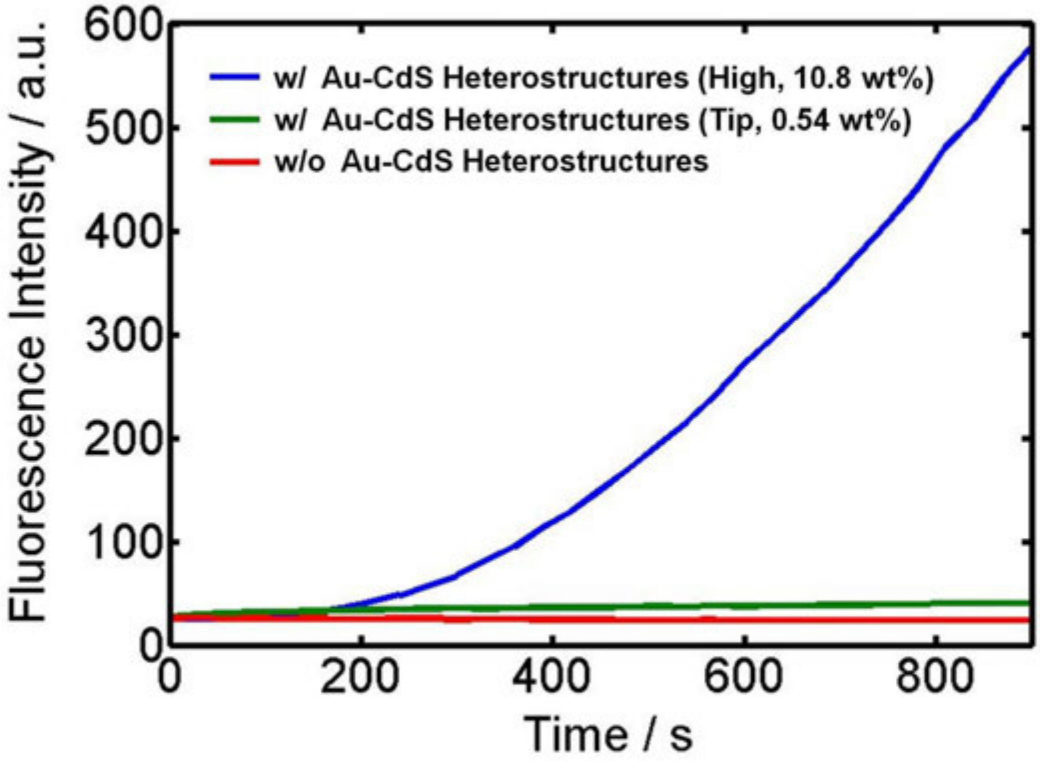

Figure S19. The effect of Au loading on the catalytic activity under 532-nm excitation (Mechanism A). The catalytic reactions were initiated by adding an aliquot of the catalyst solution into a cuvette containing 1 µM amplex red and 20 mM H_2O_2 in 10 mM pH 7.2 phosphate buffer. The fluorescence intensity was measured every 30 sec of continuous illumination at 532 nm (±25 nm). The blue-curve shows a change in the fluorescence intensity for high Au-CdS heterostructures (10.8 wt%) as a function of time. The green-curve shows a variation of the fluorescence intensity for Au-tipped CdS nanorod heterostructures (0.54 wt%). The concentration of CdS nanorods are calculated to be same in these reactions.

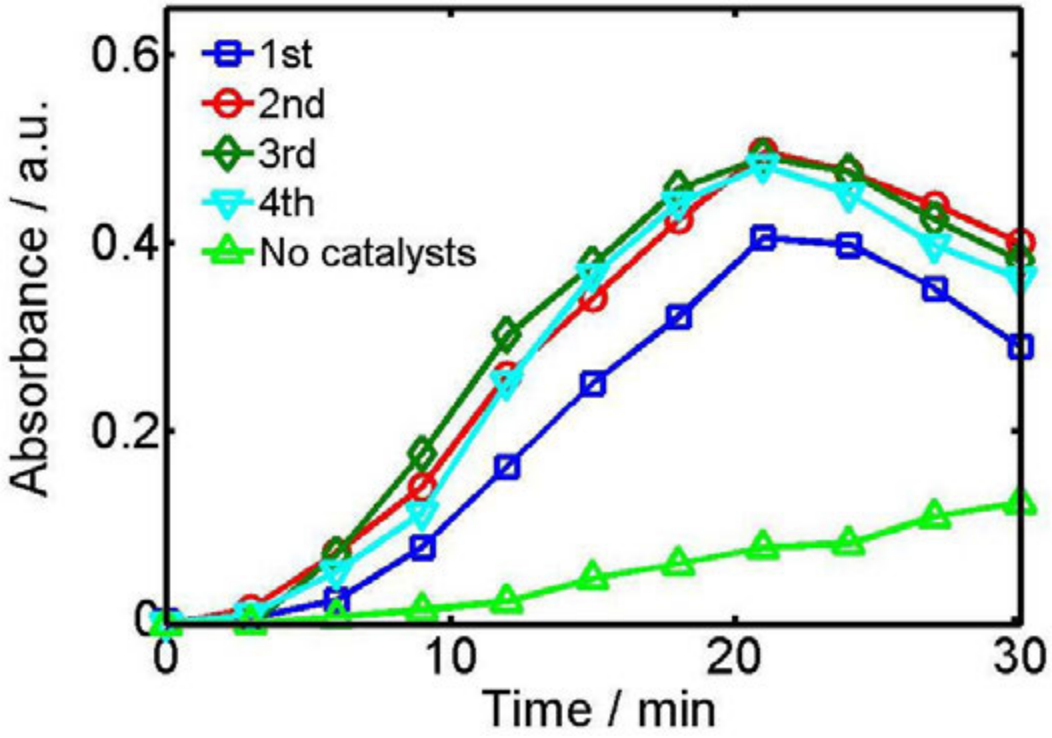

Figure S20. The stability of Au-CdS heterostructures during the photocatalytic oxidation reactions. The spectra in the first trial were taken after every 3 min of illumination with a halogen lamp (150 W) in the presence of Au-CdS heterostructures. After the first trial, we collected the Au-CdS heterostructures for reuse, the same Au-CdS heterostructures were used for the second trial. We repeated this procedure up to 4 trials to verify the stability of Au-CdS heterostructures under our experimental conditions. It is found that our Au-CdS heterostructures are stable for 2 hours of illumination with the intense lamp that contains continuous wavelengths from 360 nm to 2000 nm. In addition, the nanoparticles retained their photocatalytic activity. Note that both mechanisms will be active under this illumination.

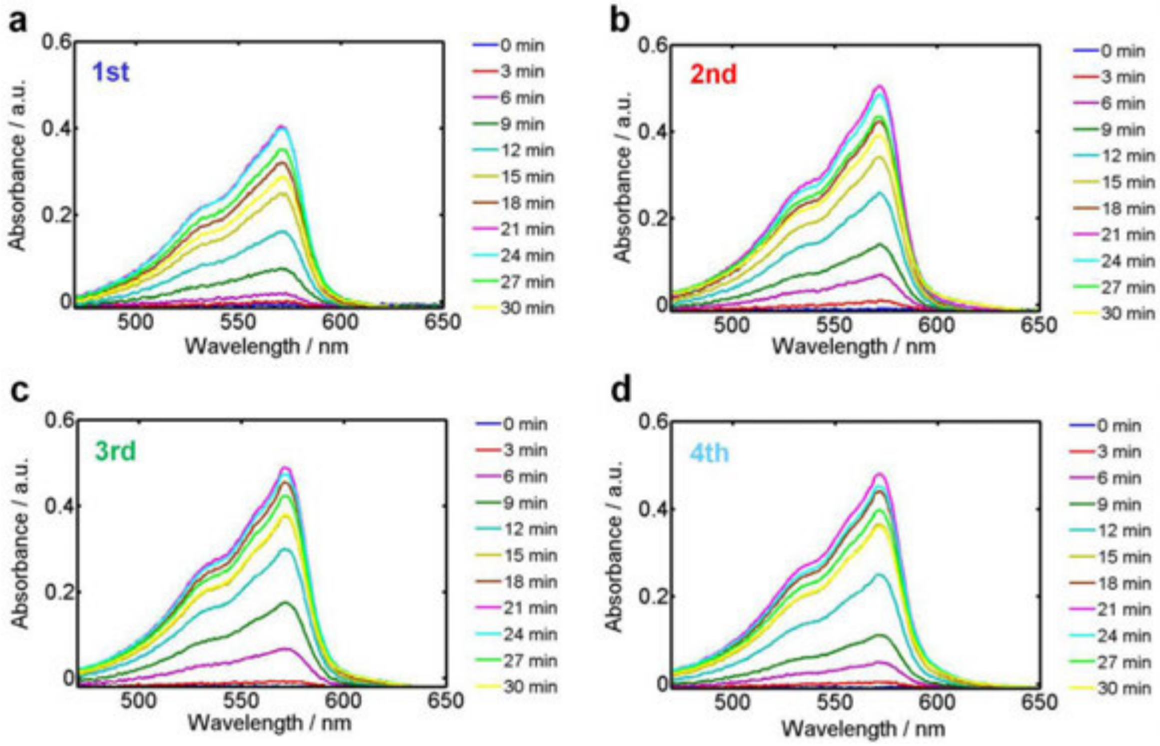

Figure S21. UV-Vis spectra for each trial in Figure S20. (a) UV-Vis spectra for 1st trial taken after every 3 min of illumination. (b) UV-Vis spectra for 2nd trial. (c) UV-Vis spectra for 3rd trial. (d) UV-Vis spectra for 4th trial.

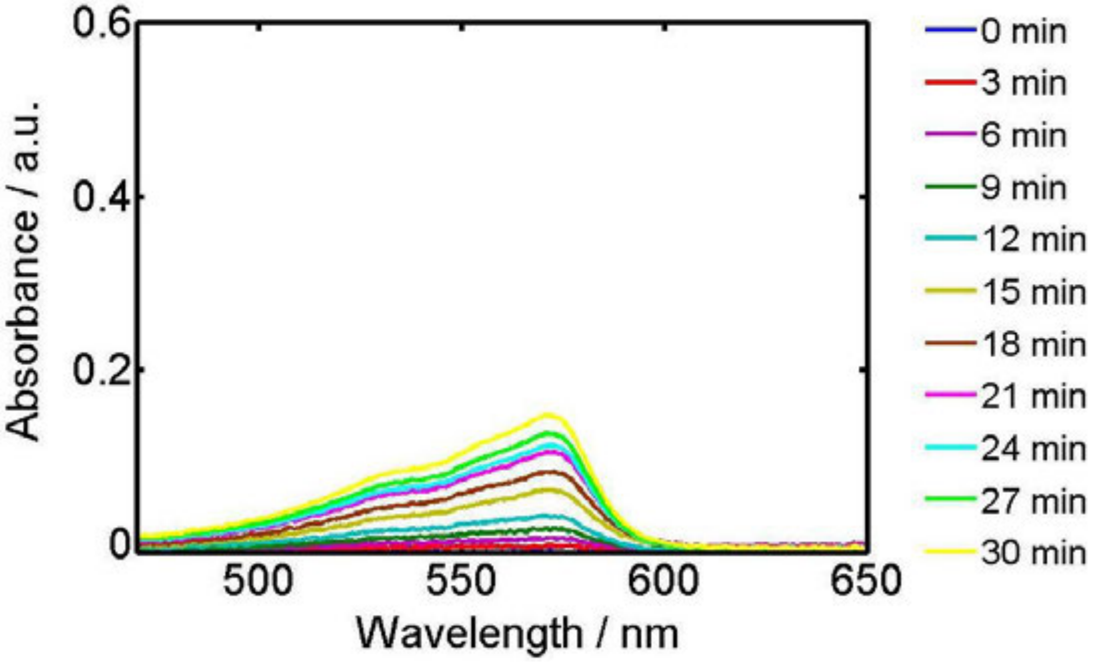

Figure S22. UV-Vis spectra for the trial without nanocatalysts in Figure S20. The spectra were taken after every 3 min of illumination with a halogen lamp in the absence of Au-CdS heterostructures. It is found that the absorbance at 571 nm increases with an interval of 3 min, which shows that resorufin molecules are slowly produced in solution under the intense illumination (150 W) of continuous wavelengths from 360 nm to 2000 nm.

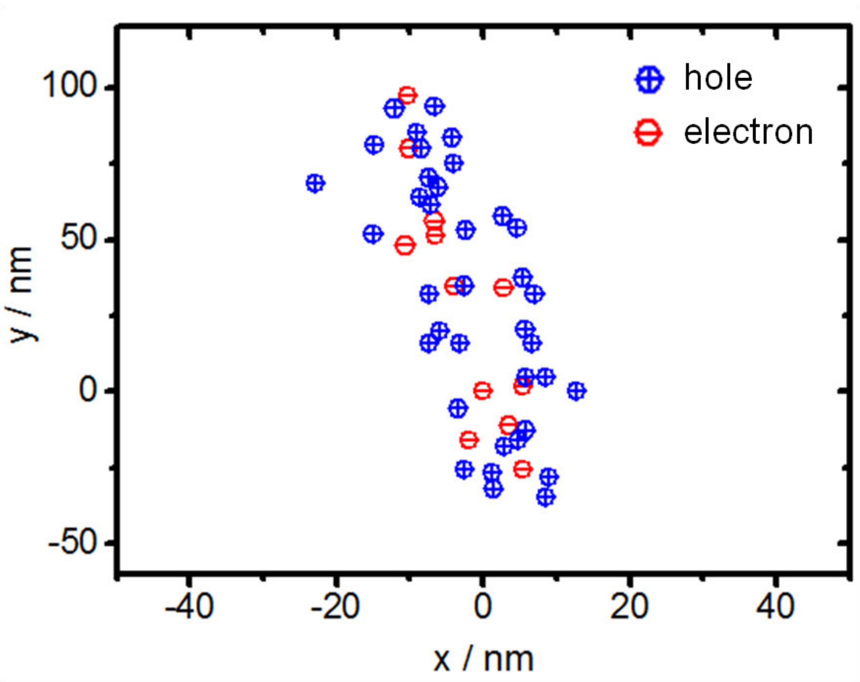

Figure S23. Another example of super-resolution mapping of active sites on a high Au-CdS heterostructure. The circled blue-crosses show resorufin molecules produced at $h^+/HO^\bullet$ active sites, while the circled red-minuses show resorufin molecules at $e^-/O_2^{\bullet-}$ active sites. The catalytic reaction was carried out under 532-nm excitation with 1 µM amplex red and 20 mM H_2O_2 in 10 mM pH 7.2 phosphate buffer.

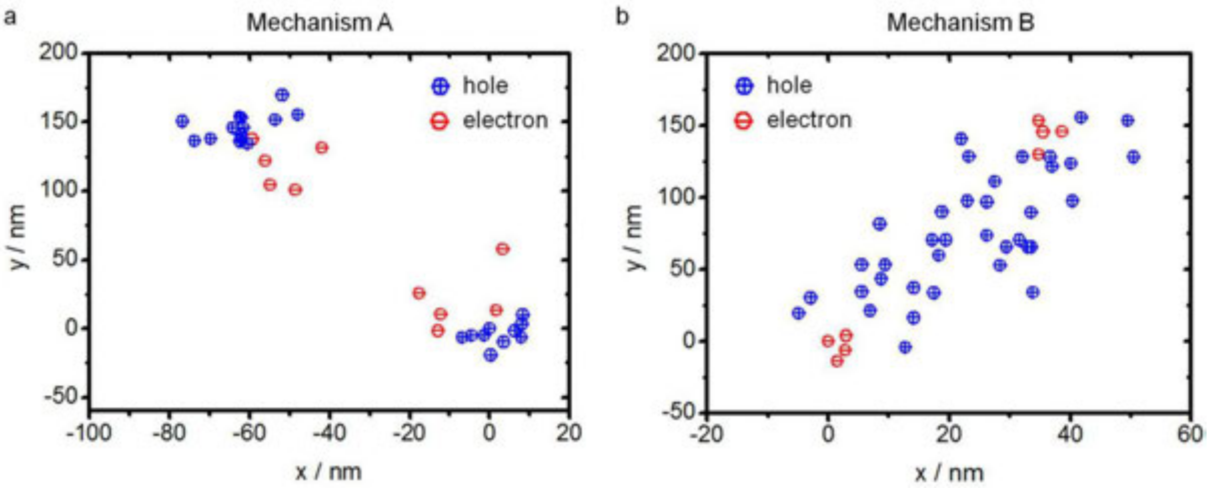

Figure S24. Another example of engineering energy flows on single Au-tipped CdS nanorod heterostructures. (a) Super-resolution mapping of single active sites on a Au-tipped CdS nanorod heterostructure during the oxidation reaction at 532 nm (mechanism A). Holes (circled blue-cross) are positioned at both ends, while electrons (circled red-minus) are located on the CdS nanorod. (b) Super-resolution mapping of single active sites on a Au-tipped CdS nanorod heterostructure during the same oxidation reaction at both 405 nm and 532 nm. Holes (circled blue-cross) are distributed along the CdS nanorod, while electrons (circled red-minus) are positioned at both ends.

Supplementary Materials

Preparation of Au-CdS Hybrid Heterostructures

Materials. Cadmium oxide (99.998%), sulfur (99.999%) and tetramethylammonium hydroxide pentahydrate (98%) were purchased from Alfa Aesar. Octadecylphosphonic acid (ODPA) was purchased from PCI Synthesis. Trioctylphosphine oxide (TOPO) (99%), dodecylamine (98%) and didodecyldimethylammonium bromide (98%) were purchased from Sigma-Aldrich. Trioctylphosphine (TOP) (97%) and gold (III) chloride (99%) were purchased from Strem. All chemicals were used as received unless specified otherwise. *Caution*: Appropriate personal protective equipment and engineering control must be in place before the use of cadmium, a toxic heavy metal.

Synthesis of Colloidal CdS Nanorods. CdS nanorods were prepared according to a reported literature procedure.[1] Briefly, CdO (105 mg, 0.81 mmol), TOPO (1.375 g, 3.56 mmol), and ODPA (535 mg, 0.94 mmol) were weighed onto a three-neck round-bottomed flask. The flask was fitted with a glass-coated magnetic stir bar, condenser, and stainless steel thermocouple. The apparatus was sealed and brought onto an Schlenk line. Using a heating mantle, the mixture was heated to 100 °C and evacuated under vacuum for 15 min, and then it was refilled with argon and heated to 320 °C to form a completely colorless solution. The solution was then allowed to cool to 120 °C and evacuated under vacuum for 15 min, and then refilled with argon and heated back to 320°C. When the temperature reached 300°C, TOP (1.20 mL, 2.7 mmol) was injected into the flask. When the temperature reached 320°C, a solution containing an air-free 2.25 M TOPS (1.00 mL, 2.2 mmol) was rapidly injected, causing a gradual color change. Upon injection, the temperature was allowed to equilibrate at 315 °C and kept constant for a total reaction time of 85 min. The reaction mixture was then removed from the heating mantle and allowed to cool to room temperature. After dilution with toluene (5 mL), the nanorods were isolated by the addition of a 1:1 v/v iso-propanol/nonanoic acid (24 mL) mixture, followed by centrifugation (5000 rpm for 10 min).

Synthesis of Colloidal Au-CdS Hybrid Heterostructures. Au-CdS hybrid heterostructures were synthesized by modifying reported procedure.[2] CdS nanorods were dissolved in toluene to give an optical density (OD) of 1.2 at 470-nm. A 15mL volume of this solution was degassed, refilled with dry argon, and stored in the dark for 12 hr in a sealed three neck round bottom flask. Under a dry atmosphere, gold (III) chloride ($AuCl_3$) (28 mg, 0.08 mmol), dodecylamine (117 mg, 0.63 mmol) and didodecyl dimethyl ammonium bromide (74 mg, 0.16 mmol) were dissolved in 18 mL of anhydrous toluene and sonicated for 20 min. This gold solution was injected dropwise to the CdS solution that is equilibrated in an oil bath at 40 °C under an argon atmosphere. (Note-injection was performed under dark conditions to avoid the preferential deposition of gold at the tip of the CdS nanorods) The reaction was allowed to proceed for 15 min after the complete of addition of the gold solution. The nonvolatile products were purified by precipation with a 1:1 mixture of acetone and methanol (30 mL) and centrifugation (4200 rpm for 10 min). The product is readily redisperse in toluene.

Transfer of Au-CdS Hybrid Heterostructures to Water. The product was dissolved in 10 mL of toluene and was added with 10 mL of distilled water. This was added with tetramethyl ammonium hydroxide penta hydrate (300 mg, 1.65 mmol) and DL-mercaptosuccinic acid (50 mg, 0.33 mmol). The mixure was allowed to stir overnight covered with an aluminium foil. The aqueous layer was separated and was washed with acetone to remove excess ligands. The product is readily redisperse in water.

Characterization of Au-CdS Hybrid Heterostructures. In the present study, we used two kinds of Au-CdS hyrbid heterostructures: Au-tipped CdS nanorod heterostructures (0.54 wt%) and high Au-CdS heterostructures (10.8 wt%). Figure S1 shows transmission electron microscopy (TEM) images of Au-tipped CdS nanorod heterostructures (Figure S1a) and high Au-CdS heterostructures (Figure S1b). The mean length and diameter of CdS nanorods synthesized for this study are 186(±56) nm and 6(±0.9), respectively (Figure S2). The diameter of Au nanoparticles decorated on single CdS nanorods ranges from 2 nm to 7 nm.

We employed a UV-Vis spectrophotometer (Varian Cary 300) to characterize the optical properties of the Au-CdS hybrid heterostructures used in this study. The absorption spectrum of high Au-CdS hybrid heterostructures is provided in Figure 1b, and it shows both the characteristic excitonic and continuous absorption of the CdS nanorods below 480 nm (*Eg*: 2.58 eV), together with an additional broad absorption centered around 532 nm due to high loading of gold nanoparticles. An absorption spectrum of Au-tipped CdS nanorod heterostructures is provided in Figure S15. As expected, the spectrum of Au-tipped CdS heterostructures shows weaker absorption around 532 nm than that of high Au-CdS heterostructures.

DIC Imaging of Au-CdS Hybrid Heterostructures. A DIC microscope was used to check the concentration of Au-CdS heterostructures deposited on a quartz slide for single-particle catalysis. An upright Nikon Eclipse 80i microscope was used in this study. The DIC mode used a pair of Nomarski prisms, two polarizers, a quarter-wave plate, a Plan Apo oil-immersion objective (100×, N.A. = 1.40) to collect the signals from the samples, and an oil-immersion condenser (N.A. = 1.40). The DIC imaging was carried out by inserting a 547-nm band-pass filter into the light path in the microscope. The band-pass filter was obtained from Thorlabs (Newton, NJ) and it has central wavelength of 547 nm and a full width at half-maximum (FWHM) of 10 nm. A Hamamatsu complementary metal oxide semiconductor (CMOS) camera was employed to record highly detailed DIC images of Au-CdS hybrid heterostructures.

Fluorescence Ensemble Measurements in Photocatalytic Oxidation Reactions. In the present study, we used fluorescence ensemble measurements to test the photocatalytic activity of Au-CdS hybrid heterostructures in catalyzing the oxidation of non-fluorescent amplex red to highly-fluorescent resorufin. We further used the fluorescence ensemble measurements to compare photocatalytic activity of high Au-CdS heterostructures with that of Au-tipped CdS heterostructures. The fluorescence measurements provide fast and sensitive measurements, and they require smaller amount of amplex red sample than the absorption measurements.

An aliquot of Au-CdS heterostructure solution was injected into a cuvette containing a solution (1 μM amplex red and 20 mM H_2O_2 in 10 mM pH 7.2 phosphate buffer). A fluorescence intensity was measured by a fluorescence spectrophotometer (Agilent/Varian Cary Eclipse). In these ensemble experiments, a band-pass filter of 532 nm (±25 nm) was inserted into the light path from a halogen lamp (Techniquip Corp, Model R150A2, 150 W). The excitation and emission wavelengths were set to 532 nm and 587 nm, respectively, and the integration time was 1 sec.

Absorbance Ensemble Measurements in Photocatalytic Oxidation Reactions. We also employed absorbance measurements to study photocatalytic activity and stability of Au-CdS hybrid heterostructures in photocataltic oxidation reactions at the ensemble level. The absorbance measurements allow us to determine the concentration (or formation) of resorufin product molecules during a photocatalytic oxidation reaction, and they are more reliable than the fluorescence measurements that could suffer from photobleaching of the resorufin molecules, etc.

A cuvette contains a sample solution (14 µM amplex red, 20 mM H_2O_2, and 0.5 µM catalysts in 50 mM pH 7.2 phosphate buffer), and an absorption spectrum was measured by a UV-Vis absorption spectrophotometer (Varian Cary 300, CA). The scan rate was set to 300 nm/min.

Instrumentation for Single-Molecule Fluorescence Experiments. Single-molecule fluorescence measurements were performed on a homebuilt prism-type dual-color total internal reflection fluorescence (TIRF) microscope. Figure S8a shows the schematic representation of the apparatus. In order to reduce the sample drifting, the original microscope stage was replaced with a Sutter MP-285 motorized 3D translational stage (Novato, CA). An equilateral fused silica prism (Melles Griot, Albuquerque, NM) was housed in a homemade prism holder that was fixed on the Sutter stage. Both a 532-nm laser and a 405-nm laser were employed for this study to selectively excite either the gold

(532 nm) or the CdS semiconductor nanorod (405 nm) in Au-CdS heterostructures. The excitation laser beam was first pointed to a periscope, passed through a Uniblitz mechanical shutter (model LS2Z2, Vincent Associates, Rochester, NY) and a focusing lens (15-cm focal length), and then directed toward the mirror of a galvanometer optical scanner (model 6220, Cambridge Technology, Cambridge, MA). The focusing lens was used to control the laser spot size in the imaging area. The mirror galvanometer is coupled to a high precision motorized linear stage (model MAA-PP, Newport, Irvine, CA) and directs the focused laser beam through the equilateral prism to the interface at different incident angles.

Sample Preparation for Single-Molecule Fluorescence Measurements. A flow chamber was formed by double-sided tapes sandwiched between a quartz slide and a borosilicate coverslip for single-molecule fluorescence measurements. The quartz slide was positively functionalized with poly-L-lysine prior to the assembly into a flow chamber. The Au-CdS heterostructure colloidal solution was diluted with 18.2-MΩ pure water. The diluted solution was sonicated for 20 min at room temperature. Then, the Au-CdS heterostructures were deposited on the pre-cleaned functionalized quartz slide by spin casting the diluted solution. The concentration of Au-CdS heterostructures immobilized on the quartz surface was controlled to be 1 μm^{-2} for single-particle catalysis.

Single-Molecule Measurements in Au-CdS Heterostructure Photocatalysis. Single-molecule fluorescence experiments were carried out on a prism-type dual-color total internal reflection fluorescence (TIRF) microscope. A 532-nm laser beam (28.24 W/cm^2)

was focused onto the sample to directly excite both Au-CdS heterostructures and the resorufin product molecules. Besides the 532-nm laser, a 405-nm laser beam (15.3 W/cm^2) was also used to excite the Au-CdS heterostructures in this study. Before initiating the fluorogenic oxidation reaction, we first shined the 532-nm laser beam onto the sample for 30 min to remove possible fluorescent dusts or impurities. We then introduced a solution (1 μM amplex red and 20 mM H_2O_2 in 10 mM pH 7.2 phosphate buffer) over the Au-CdS heterostructures within a flow chamber. A highly fluorescent resorufin product was collected by a Nikon Plan Fluor 100× oil objective (NA=1.4) and filtered through a filter (532 LP, Chroma Technology Corp). All the fluorescence images were captured with an Andor iXonEM+ 897 CCD camera (Belfast, Northern Ireland). We recorded movies of stochastic fluorescence bursts at many localized spots on the quartz surface with time resolution of 50 ms. The collected movies and images were analyzed by MATLAB and NIH ImageJ (http://rsbweb.nih.gov/ij/).

Super-Localization of the Center Position of Resorufin Product Molecules. We recorded movies of fluorescence bursts at many localized spots on the quartz surface over 1 hr. Then, the fluorescence intensity trajectories were extracted from localized fluorescence spots individually across the entire movie. Each trajectory from a Au-CdS heterostructure contains many stochastic fluorescence bursts over time. We identify the corresponding image frames of each burst in the trajectory. For each burst, all image frames contributing to the fluorescence burst were combined to form a single image. We then determined the center position of the product molecule by 2D Gaussian fitting of the single image. The accuracy of the center position was determined according to Thompson and co-workers.[3]

During the catalytic reactions, the sample drifted over several hundred nanometers. Therefore, we used position markers to correct for this drifting in localizing the center position of the resorufin molecules. Fluorescent beads with a diameter of 100 nm (R100, Duke Scientific Corp.) were used as position markers (Figure S9). The emission maximum of the red-fluorescent beads (R100) excited at 542 nm is 612 nm. The positions of the beads were determined by PSF fitting of their fluorescence images. An intensity averaged image from 20 frames was used to improve the accuracy of the center position. It is found that the fluorescent beads are photo-bleached over time, but the intensity of the beads after 1 hr was about 2 times higher than the background intensity (Figure S10).

Experimental Evidence to Support Mechanism B in CdS Nanorods. It is important to check if pure CdS nanorods without Au nanoparticles (Figure S5) can oxidize amplex red, which is necessary to support mechanism B in CdS nanorods. We performed ensemble measurements to elucidate the ability of pure CdS nanorods in oxidizing amplex red to resorufin under mechanism B. If photocatalysis involving the photo-induced charge carriers in CdS nanorods is really going on here, the resorufin product molecules will be produced from amplex red. We used a UV lamp (λ: 254 nm, 1.93 mW/cm^2) to excite pure CdS nanorods in these ensemble experiments. Since the band-gap energy (E_g) of CdS nanorod is about 2.58 eV (480 nm), the photo-generated carriers will be formed in CdS nanorods under 254-nm illumination.

We employed a UV-Vis spectrophotometer (Varian Cary 300) to measure the production of resorufin molecules during a photocatalytic oxidation reaction. A pure CdS nanorod solution (0.5 μM catalysts) was injected into a cuvette containing a solution (14 μM amplex red and 20 mM H_2O_2 in 50 mM pH 7.2 phosphate buffer). An absorption spectrum was taken after every 30 sec of illumination of the cuvette at 254 nm (Figure S13a). In addition, we further carried out a control experiment without CdS nanorods to verify that the production of resorufin molecules is resulted from the photocatalytic oxidation of amplex red by CdS nanorods (Figure S13b). It is found that an absorbance at 571 nm corresponding to the maximum absorption wavelength of resorufin increases with an interval of 30 sec in the presence of CdS nanorods (blue-curve), while it remained constant in the absence of CdS nanorods at the same condition (Figure S13c). Furthermore, we found that there is no production of resorufin molecules under dark condition, which supports no surface catalysis on pure CdS nanorods (Figure S14). Therefore, the results clearly suggest that the photo-generated electrons and holes are formed in CdS nanorods under 254-nm illumination as depicted in Figure S11d, and the resorufin molecules are produced through photocatalysis under mechanism B.

Experimental Evidence to Support Mechanism A at 532 nm in the Heterostrucutres.

Zhou *et al.* demonstrated that Au nanoparticles can catalyze the oxidation of amplex red to resorufin in the presence of H_2O_2 through simple chemical catalysis on their straight surfaces under a 532-nm laser to excite fluorescent resorufin product.[4] Besides the surface catalysis, photocatalysis with the effect of the excited surface plasmons of Au nanoparticles is also expected to exist in the oxidation reaction under

532-nm illumination. It is worthwhile to note that a 532-nm laser can excite both surface plasmon resonance of spherical Au nanoparticles and the resorufin product molecules. Therefore, we tried to verify the existence of photocatalysis (or mechanism A) during the fluorogenic oxidation reaction.

More recently, several groups have reported that the energetic electrons and holes are efficiently produced from plasmon decay in Au nanoparticles excited at 532 nm, and they could be potentially used in photochemistry.[5-8] For a nanoparticle much smaller than the wavelength of the plasmon resonance, all energy absorbed by the nanoparticle results in the formation of hot electrons and holes. Therefore, it is expected that the photo-excited carriers produced from the excited surface plasmons in the nanoparticle can play an important role in the fluorogenic oxidation reactions.

To better understand this, we carefully carried out more experiments to investigate the light effect on the fluorogenic oxidation reaction at the ensemble level. A high Au-CdS nanorod solution (0.53 μM catalyst) was injected into a cuvette containing a solution of 14 μM amplex red and 20 mM H_2O_2 in 50 mM pH 7.2 phosphate buffer. An absorption spectrum was measured after every 2 min of illumination of the cuvette at 532 nm by a UV-Vis spectrophotometer (Figure S4a). A band-pass filter of 532 nm (±25 nm) was inserted into the light path from a halogen lamp (150 W). As a control experiment, we further repeated the exactly same experiment under dark condition to verify the effect of the excited surface plasmons at 532 nm (Figure S4b). It is notable that in this case the sample is also exposed to light when it is scanned every 2 min for taking a UV-Vis spectrum. Therefore, we performed another control experiment under dark condition, and we measured the absorbance once after 30 min. We found that an absorbance under dark condition increases as a function of time, which supports the surface catalysis going on the Au nanoparticles (Figure S4c). This is consistent with the previous finding.[4] However, it should be noted that an absorbance from continuous measurement at 532 nm (total 30 min illumination) is about 4 times higher than that from one measurement after 30 min under dark condition (Figure S4d). Therefore, the result strongly supports that the photocatalysis with the plasmonic effect is operating on Au-CdS heterostructures under mechanism A at 532 nm.

In this study, we further measured 2-nm Au nanoparticles (BBI, WI, USA) to test if they are active for the oxidation of amplex red to resorufin at the ensemble level. We found that 2-nm Au nanoparticles are inactive for catalyzing the oxidation of amplex red to resorufin, which is consistent with the previous report.[9] This can be explained by our photocatalysis mechanism. The 2-nm Au nanoparticles compared to larger particles (e.g., 6 nm) are not active because they are too small to efficiently generate the photo-excited surface plasmons that can result in the energetic electrons and holes. It is notable that the 2-nm Au nanoparticle solution is clear. In summary, we find that the photo-excited charge carriers generated from decay of the excited surface plasmons play a crucial role in nanocatalysis of plasmonic Au nanoparticles much smaller than the wavelength of light, and we must consider the photocatalysis together with surface catalysis in the nanocatalysis.

The Formation of Two Different Oxygen Radicals in Plasmonic Au Nanparticles under 532-nm Excitation. In the previous section, we demonstrated the existence of photocatalysis based on the formation of the photo-generated electrons and holes. It is necessary to further discuss the formation of surface-bound oxygen radicals ($O_2^{\bullet-}$ and $HO^{\bullet}$, active sites) on plasmonic Au nanoparticles under 532-nm excitation (mechanism A). It is well known that oxygen radicals can be formed by photocarriers in wide band-gap semiconductors such as TiO_2 (*Eg*: 3.2 eV).[10,11] Besides the TiO_2 semiconductors, we found that CdS nanorods (*Eg*: 2.58 eV) can also oxidize amplex red to fluorescent resorufin under 254-nm illumination (Figure S13). This result suggests that the photo-generated electrons and holes are formed in CdS nanorods, followed by the reduction and oxidation reactions, respectively, to make surface-bound oxygen radicals.

Here, we provide three evidences to support the formation of the surface-bound oxygen radicals in Au nanoparticles deposited on the CdS nanorod under mechanism A at 532 nm. First, very recently, Lee *et al*. reported a plasmonic Au nanorod-based water splitting cell.[12] Illuminating the Au nanorods (AuNRs) with visible light excited surface plasmons that rapidly produce many hot electron−hole pairs above the Fermi level through plasmon decay. The energetic electrons were used for hydrogen evolution, while the energetic holes were used for water oxidation. Furthermore, Mukherjee *et al.* reported the room temperature dissociation of H_2 on Au nanoparticles using visible laser excitation (2.4 W/cm^2).[5] Surface plasmons excited in the Au nanoparticle decay into d-band electron-hole pairs excited above the Fermi level. The energetic electrons have energies between the vacuum level and the work function of the gold metal. The work function (ϕ) of gold is about 4.83 eV and the Fermi energy (E_F) is 5.53 eV. Therefore, they demonstrated that the energetic electrons can transfer into a Feshbach resonance of an H_2 molecule adsorbed on the Au nanoparticle surface, triggering dissociation. The dissociation enthalpy of H_2 is 436 kJ/mol (4.51 eV). Therefore, it is expected that the energetic electrons formed in Au nanoparticles under 532-nm excitation (28.24 W/cm^2) could be used for the reduction of oxygen to form surface-bound $O_2^{\bullet-}$ radicals in this study. Moreover, the photo-generated energetic holes above the Fermi energy could be used for the oxidation of water to form surface-bound $HO^{\bullet}$ radicals. Note that it is possible that a few or tens of holes could be used to oxidize water to form a surface-bound $HO^{\bullet}$ radical. Further theoretical experimental studies are needed to better understand and clarify this.

Second, the formation of surface-bound oxygen radicals is supported by our ensemble experiments, described in the previous section (2-2), using Au-CdS heterostructures under 532-nm excitation (Figure S4). We found that the absorbance under 532-nm illumination is about 4 times higher than that from one measurement under dark condition (Figure S4d). The increase in the activity suggests the existence of photocatalysis, and it could be ascribed to the formation of many surface-bound oxygen radicals very reactive toward amplex red substrate.

Last, the formation of surface-bound oxygen radicals is also supported by our single-molecule single-particle experiments. In this study, we found the distinct dissociation kinetics for two different active sites in Au-CdS heterostructures under mechanism A at 532 nm (Figure 3c). The result strongly suggests the formation of two different oxygen radicals ($O_2^{\bullet-}$ and $HO^{\bullet}$) with different rate of product dissociation, which can be explained by a model involving the charged microenvironments around the active sites. In this experiment, photo-generated carriers (electrons, e^- and holes, h^+) form two surface-bound reactive oxygen radicals that act as catalytic active sites on the nanocatalyst surfaces. As shown in Figure 5, super-resolution images mapping the active sites either at 532 nm or at both 405 nm and 532 nm further support the formation of two different oxygen radicals that are localized with the accuracy of ±5 nm.

The Stability of Au-CdS Hybrid Heterostructures in Photocatalysis. It is very important to verify if Au-CdS hybrid nanocatalysts are stable in the photocatalytic oxidation reaction of amplex red to resorufin under our experimental conditions. CdS nanorods are unstable photocatalysts in aqueous solutions. But, recently, we have demonstrated that metal-semiconductor heterostructures are much more stable photocatalysts than unmodified semiconductor nanorods.[13] Under continuous illumination Pt-CdS heterostructure solutions retained their activity for several days, while CdS nanorod solutions became inactive. In order words, metallic nanoparticles decorated on the CdS semiconductor surface significantly enhance activity and also greatly stabilize the semiconductor nanorods against photo-induced degradation.

To clearly elucidate the stability of our Au-CdS heterostructures, we further carried out ensemble measurements in the photocatalytic oxidation of amplex red to resorufin. We used a halogen lamp (150 W) to excite the Au-CdS heterostructures, and the lamp produces a continuous spectrum of light from 360 nm to 2000 nm. Note that under this illumination both mechanisms (A and B) are active and turned ON. A cuvette containing a solution (14 µM amplex red, 20 mM H_2O_2, and 0.53 µM catalysts in 50 mM pH 7.2 phosphate buffer) was placed in front of the halogen lamp without any filters in between the lamp and the sample. An absorption spectrum was measured after every 3 min of illumination of the cuvette. We found that the absorbance at 571 nm increased with an interval of 3 min (1st trial, blue-curve) in Figure S20. That indicates the formation of resorufin product molecules.

After the first trial, we collected the Au-CdS heterostructures in solution by centrifugation (5000 rpm for 6 min) for reuse, and the same Au-CdS heterostructures were used for the second trial under the same conditions. We repeated this procedure up to 4 trials corresponding to 2 hours of illumination with the lamp in order to verify the stability of Au-CdS heterostructures under our experimental conditions. It is observed that the absorbance of the second trial (red-curve) is a little higher than that of the first trial (blue-curve) as shown in Figure S20. This can be explained by the fact that some of surface ligands on the nanocatalysts could be removed by centrifugation after the first trial, making them more active. It is worthwhile to note that the last three trials (2-4) show very good agreement (Figures S20 and S21), which indicates that our Au-CdS heterostructures are stable and retain their activity for 2 hr of illumination with the intense lamp (150 W) that contains continuous wavelengths. We also find that the resorufin product molecules can be produced in solution under the intense illumination of continuous wavelengths (Figure S22), which needs to be carefully considered in the experiments using amplex red. But, it is notable that the rate of product formation in the absence of nanocatalysts is much lower than that with nanocatalysts (Figure S20). In addition, it should be noted that such increase in the absorbance (Figure S22) was not observed under the illumination at only 532 nm (±25 nm) or only 254 nm. Therefore, we confirmed that our Au-CdS heterostructures are stable under our experimental condition and time (~2 hr).

The Blinking of Au-CdS Hybrid Heterostructures under Single-Molecule Experimental Conditions. We checked the blinking of Au-CdS heterostructures that could influence fluorescence bursts under our single-molecule experimental conditions. Very recently, Sagarzazu *et al.* reported that single Au-CdSe heterostructures with aspect ratio of ~3 and Au size of ~2 nm in diameter can exhibit blinking dynamics.[14] But, the blinking of such heterostructures is strongly dependent on both aspect ratio and size of Au particles.[14] Khon *et al.* demonstrated that the excitonic feature in Au-CdS heterostructures is totally suppressed for Au nanoparticles larger than 5 nm while it remains for Au nanoparticles less than 2.5 nm in diameter.[15] Furthermore, we also demonstrated that CdS heterostructures with aspect ratio greater than 3 show no fluorescence emissions because of surface defects to quench (or trap) excitons.[16] Therefore, it is expected that our Au-CdS heterostructures (*AR*: ~30, Au size: 2 nm - 7 nm) will exhibit no blinking dynamics that could affect our data analysis of single-molecule fluorescence bursts.

To clearly confirm this, we further performed a control experiment using the same fluorogenic oxidation reaction at the single-particle level to check the blinking of Au-CdS heterostructures. A sample was prepared by spin casting high Au-CdS heterostructure solution on a positively functionalized quartz slide. The sample slide was then measured under a prism-type dual-color TIRF microscope. A 532-nm green laser was used to excite both the metal in Au-CdS heterostructures and the fluorescent resorufin product. Before initiating the fluorogenic oxidation reaction, we first shined the 532-nm laser beam onto the sample for 30 min to remove possible fluorescent dusts or impurities. We then introduced the buffer solution without reactant molecules over the Au-CdS heterostructures within a flow chamber. Then, we checked if fluorescent bursts are observed over the Au-CdS heterostructures for 1 hr. We found no stochastic fluorescence bursts, indicating that there is no blinking of our Au-CdS heterostructures. In addition, this further indicates that our fluorescence bursts come from the fluorogenic oxidation reaction of amplex red over the Au-CdS heterostructures. Therefore, we ensured that the Au-CdS heterostructures do not exhibit any time-dependent emission fluctuations that could affect our fluorescence bursts and data analysis under our single-molecule experimental conditions.

Interaction of the Probe Molecule (Resorufin) with Au-CdS Heterostructures in Solution. The using of the probe molecule (resorufin in this work) could introduce specific interaction (or non-photocatalytic reaction) with the Au-CdS photocatalysts. Thus, the precise assignment of fluorescence signal to photo-generated charge carriers should be done very carefully. To check the effect of binding or unbinding of the resorufin molecule to the Au-CdS heterostructures in solution, we performed more control experiments with only resorufin in solution at 10^{-2} μM (~1% of the substrate solution) at the single-particle level. We found that there is no fluorescence signal observed over time. This indicates that at this resorufin concentration, binding of free resorufin in solution to Au-CdS heterostructure surface is insignificant in our single-particle photocatalysis experiments. This also indicates that diffusion of free resorufin does not yield fluorescence bursts. Therefore, it should be noted that in the single-nanoparticle photocatalysis experiment, the resorufin is only generated in situ through photocatalysis of amplex red, which does not involve a resorufin-binding process. Please note that this is consistent with the previous report.[9]

Pure CdS Nanorods under 532-nm Illumination. It is necessary to check if a 532-nm laser can excite CdS nanorods in our Au-CdS heterostructures. To verify this, we synthesized pure CdS nanorods with an average size of 183 nm × 6 nm (Figure S5), and a UV-Vis absorption spectrum of these CdS nanorods is provided in Figure S15. We carried out single-molecule fluorescence experiments on a TIRF microscope. A 532-nm laser beam (28.24 W/cm^2) was focused onto the sample to directly excite both CdS nanorods and the resorufin product molecules. We first deposited pure CdS nanorods on a quartz slide by spin casting. Before initiating the fluorogenic oxidation reaction, we shined the 532-nm laser beam onto the sample for 30 min to remove possible fluorescent dusts. We then introduced a solution (1 μM amplex red and 20 mM H_2O_2 in 10 mM pH 7.2 phosphate buffer) over the pure CdS nanorods within a flow chamber. We found no fluorescence bursts resulted from photocatalysis of CdS nanorods, which indicates that a 532-nm laser beam does not excite CdS nanorods. This is further verified by our ensemble experiments with pure CdS nanorods at 532 nm (Figure S6).

The Effect of Au Loading on Photocatalytic Activity under 532-nm Excitation. An advantage of the Au-CdS hybrid heterostructures over the separate components is that we can tune the photocatalytic activity by varying the Au loading on the CdS nanorod under the mechanism A at 532 nm. To demonstrate this, we carried out ensemble-averaged measurements using two kinds of Au-CdS hybrid heterostructures with different Au loading (10.8 wt% and 0.54 wt%) used in this study. We performed the same oxidation reaction at same conditions. A cuvette was filled with a solution containing 1 μM amplex red and 20 mM H_2O_2 in 10 mM pH 7.2 phosphate buffer. We added an aliquot of high Au-CdS heterostructure (10.8 wt%) solution into the cuvette. A fluorescence intensity was measured after every 30 sec of illumination of the cuvette at 532 nm (±25 nm). We then performed the same experiment for Au-tipped CdS nanorod heterostructures (0.54 wt%) to compare the photocatalytic activity. The concentration of the CdS nanorods in each cuvette was calculated to be same. We found that both high Au-CdS heterostructures and Au-tipped CdS nanorod heterostructures are active for the oxidation of amplex red to resorufin at same conditions (Figure S19). Furthermore, the fluorescence intensity for Au-tipped CdS nanorod heterostructures increased slowly, while the fluorescence intensity for high Au-CdS heterostructures increased rapidly over time. Therefore, the result suggests that we can control the photocatalytic activity through varying Au loading in Au-CdS heterostructures, which cannot be achieved by separate.

CHAPTER 8. GENERAL CONCLUSION

Single molecule and nanoparticle imaging has become a very important tool to investigate many biological and chemical processes. This dissertation presents the applications of single molecule and nanoparticle imaging in biophysical, surface, and photocatalysis studies using far-field optical microscopy. The work was mainly carried out under a DIC microscope and a total internal reflection (TIR) microscope.

First, a DIC microscopy-based single particle orientation and rotational tracking technique that allows for resolving the full 3D orientation of single AuNR probes has been developed. The angular degeneracy was overcome by combining DIC polarization anisotropy with the image pattern recognition technique. The usefulness of this technique in biophysical studies was further verified by real time tracking of rotational motions of single AuNRs rotating on live cell membranes. Therefore, it is expected that this method will enable us to elucidate the comprehensive interaction mechanisms between the functionalized nanocargoes and the membrane receptors in live cells. Detailed in situ conformational information on how they bind on the cell membrane and how they move and rotate in live cells at single particle level would provide new avenues for the development of new generation of high efficient drug and gene delivery carriers.

Second, a high-throughput focused orientation and position imaging (FOPI) technique with 3D orientation resolvability for single AuNRs deposited on a gold film has been developed for surface studies. The FOPI method presented in this dissertatoin provides a new approach using the interaction of AuNRs with their surrounding environment for resolving the 3D orientation of single AuNRs. Therefore, it is expected that this method can be used as a tool to study interactions of functionalized nanoparticles with functional gold surfaces.

Last, single molecule TIRF imaging was successfully employed in photocatalysis study to reveal the nature and photocatalytic properties of the surface active sites on single Au-CdS hybrid nanocatalysts. Single-molecule photocatalysis with high-resolution super-localization imaging allowed us to reveal two distinct, incident energy-dependent charge separation mechanisms in single Au-CdS heterostructures. This finding will help us design and develop better metal-semiconductor heterostructures that are highly active for photocatalytic reactions under visible light. Furthermore, the finding will enable us to potentially engineer the direction of energy flows on the heterostructured nanomaterials at the nanoscale. Therefore, it is expected that the results presented in this dissertation have a potential impact on the development of better photocatalyst structures.

ACKNOWLEDGEMENTS

"We know that God is always at work for the good of everyone who loves him.

They are the ones God has chosen for his purpose"

- Romans 8: 28 -

This work was supported by the U.S. Department of Energy, Office of Basic Energy Sciences, Division of Chemical Sciences, Geosciences, and Biosciences through the Ames Laboratory. The Ames Laboratory is operated for the U.S. Department of Energy by Iowa State University under contract no. DE-AC02-07CH11358.

First, I would like to thank Dr. Ning Fang for guiding my research and scientific development while at Iowa State University. I would like to thank my committee members for their efforts and contribution to this thesis: Dr. Jacob Petrich, Dr. Emily Smith, Dr. Ian Schneider, and Dr. Wenyu Huang. I also want to thank Dr. Javier Vela for his guidance and advice on my research on single nanoparticle photocatalysis. I would also like to thank all past and present Fang Group members for not only their help in my research endeavors but also for their friendship.

I would like to thank my parents who have always supported me in every aspect of my life. I would not be the person I am today if it wasn't for their unending love and guidance. They are truly great parents who showed me the importance of education, hard work, respect, and love of family and friends which are now attributes that help me in every aspect of my life.